Research in Optoelectronics (A)

Reprints published in 2006

by

Professor Larry A. Coldren

and Collaborators

Published as

Technical Report # ECE 07-01

of

The Department of Electrical & Computer Engineering

The University of California

Santa Barbara, CA 93106

Phone: (805) 893-4486

Fax: (805) 893-4500

E-mail: coldren@ece.ucsb.edu

www.ece.ucsb.edu/Faculty/Coldren

Introduction:

Conference and Journal papers published by Prof. Coldren, together with his students, post docs, and other collaborators in 2006, are contained in this edition of Research in Optoelectronics (A). These generally focus on III-V semiconductor lasers and related photonic integrated circuits. The work spans efforts from basic materials and processing technology, through device physics and design, to device formation, characterization, and insertion into systems demonstrations.

The reprints have been grouped into four areas: **I. Photonic IC Technology & Devices; II. Photonic IC Wavelength Converters; III. MBE Technology & Devices; and IV. Spin-Wave Physics of Quantum Structures.** The majority of the work is in the first area, which has been further subdivided into *A. PIC Technology; B. PIC Transmitters and Receivers;* and *C. Analog PICs and RF-Photonics.* In the second, Wavelength Converter group we have the subdivisions: *A. Photo-Current Driven Wavelength-Converters and B. "All-Optical" Wavelength-Converters and Buffers@ 40Gb/s.* The MBE work contains *A. GaAs-based Vertical-Cavity Lasers and Technology; B. InP-based Vertical-Cavity Lasers and Technology;* and *C. In-plane Short-Cavity Lasers.* All of the epitaxial wafers for this work except for the MBE group are grown on InP by MOCVD. The epitaxial growth activity is strongly supported by Prof. DenBaars (MOCVD) and Prof. Gossard (MBE), who co-advise the students involved in these areas. Thus, their contributions have been invaluable to the research, even when they do not appear as co-authors on the device oriented papers.

The work was performed with funding from several grants from industry and government, some gift funds from industry, and support from the Kavli Endowed Chair in Optoelectronics and Sensors. Specific projects included one on wavelength converters and photonic networks under the DARPA DoDN program (Prof. Blumenthal, PI); an analog receiver project sponsored by DARPA Phorfront (Prof. Bowers, PI); two projects to create very high-efficiency optical interconnects for ICs using either edge-emitting short-cavity laser-modulators (supported by the DARPA C2OI program) or directly-modulated vertical-cavity surface-emitting lasers (supported by a UC-MICRO with IBM).

The first group of reprints (*IA. PIC Technology*) summarizes efforts to make highly-functional and efficient widely-tunable transmitters, receivers and transceivers using the integration platforms recently developed at UCSB. Most of the publications describe the quantum-well intermixing (QWI) technique, which involves post-growth processing to selectively alter the bandgap or absorption edge across the wafer. As described in previous years, waveguides with several bandgaps can be integrated together in this way to provide for gain, modulator, passive, and tuning regions without any additional regrowths. Devices using this technology are included in the transmitter and wavelength converter sections as well. With the addition of offset gain and absorber regions for high-saturation power SOAs and photodetectors, receivers have also been integrated together with transmitter sections on a single chip.

Figure 1 gives both transmitter and wavelength converter results from an InP transceiver chip that uses QWI. It contains a high-gain, high-saturation power optical receiver, which incorporates a two-stage SOA and a UTC detector, as well as a widely tunable transmitter, which integrates a quantum-well EA-modulator with a Sampled-grating DBR (SGDBR) laser. The results show both the transmitter stage modulation bandwidth as well as wavelength conversion with the receiver connected to the transmitter.

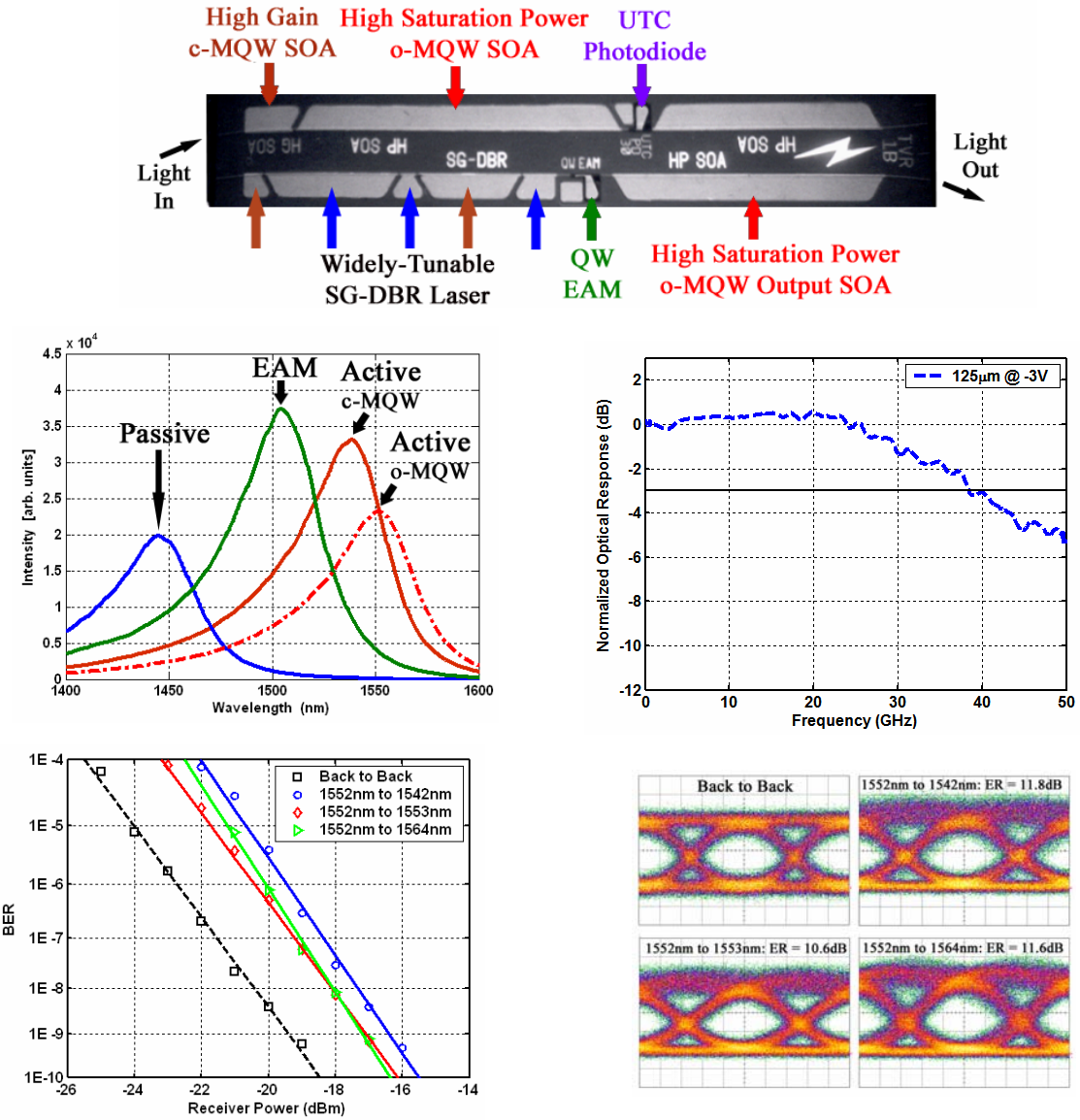

Figure 1. (top) Schematic of Photonic IC formed with quantum-well intermixing (QWI) and MOCVD regrowth. (center-left) Photoluminescence of several regions on the chip showing the various bandgaps. (center-right) Small-signal frequency response of transmitter stage. (bottom-left) Bit-error-rate (BER) for 40 Gb/s NRZ wavelength conversion to several output wavelengths. (bottom-right) Associated eye diagrams for the BER measurements.

A second widely-tunable 40 Gb/s transmitter result is shown in Fig. 2. In this case the integration platform does not involve QWI, but it uses an offset gain layer that is grown

on top of the interconnecting waveguide, which also contains quantum-wells. This gain layer is removed prior to regrowth of the upper waveguide cladding in regions where modulators, splitters, or passive interconnects are desired. In this case a series-connected Mach-Zehnder modulator (MZM) follows the widely-tunable SGDBR laser. Photocurrent-driven wavelength converters have also been made with this chip by incorporating an SOA-PIN receiver beside the transmitter.

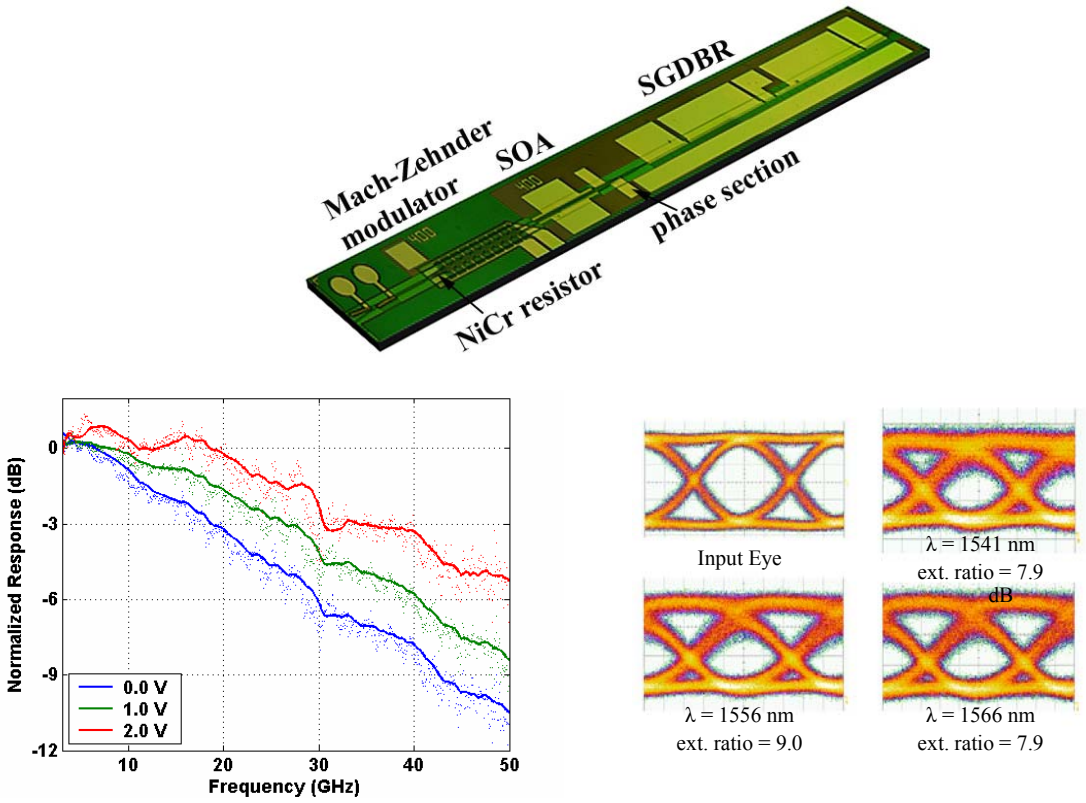

Figure 2. (top) Schematic of a widely-tunable transmitter that integrates an SGDBR laser with a series-connected MZM. (bottom-left) small-signal frequency response, and (bottom-right) 40Gb/s NRZ eye-diagrams.

As an example of work in the Analog PICs and RF-Photonics area we show some results from an integrated phase demodulator chip in Fig. 3. In this case there is no integrated transmitter, but a local reference oscillator (LO) must supply a second cw input in addition to the modulated signal to be received. The demodulator is a receiver for phase modulated optical signals, which converts the phase modulation to intensity modulation. Feedback from a balanced heterodyne detector pair to a tracking modulator is used to reduce the output swing to enable linear demodulation with phase modulation depths of many radians. A small portion of the feedback signal is also used as the received output. The figure shows how the two detectors are series connected to form the balanced heterodyne receiver as well as two-tone linearity measurements.

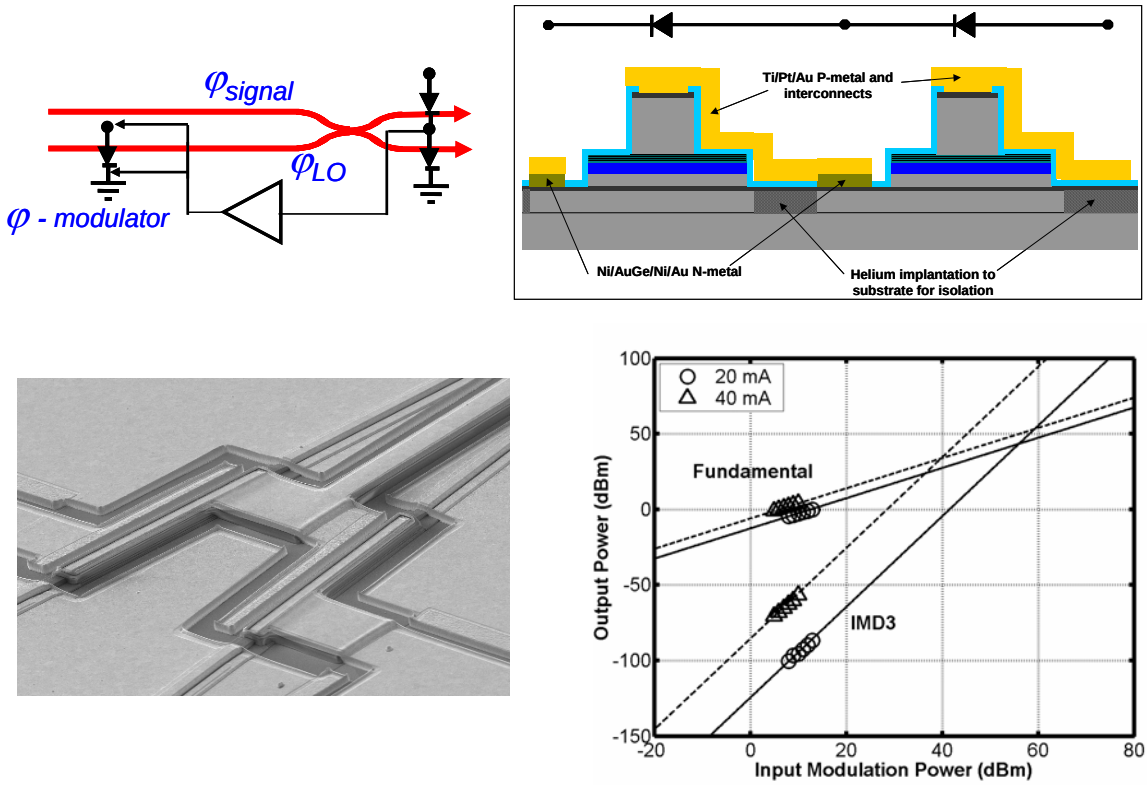

Figure 3. (top) Schematic of linear phase demodulator and cross section of series-connected waveguide detectors. (bottom) Two-tone Spur-free dynamic range (SFDR) measurements illustrating the level of the 3rd order intermodulation distortion term (IMD3) relative to the fundamental as a function of input modulation power.

Figure 4 shows some results from our work on in-plane short-cavity laser-transmitters. The objective here is to make a relatively high-power, high-speed, high-efficiency transmitter within a small footprint. The goal is to out-perform VCSELs which are limited in output power and direct modulation speed. We show a short-cavity laser integrated with an EA-modulator together with an integrated output deflection mirror and collimating lens to provide for vertical emission if desired. The output mirror for the in-plane laser is a short relatively-strong grating. We are also exploring the use of second order gratings for surface emission. Initial results have given single-mode output powers up to 10 mW with modulation bandwidths exceeding 20 GHz both at 1550 nm and 980 nm. The results shown are for the more recent results at 980 nm. Although initial digital results were taken at 10 Gb/s, the modulation bandwidth suggests that operation up to 40 Gb/s should be possible.

Figure 5 shows recent 980 nm VCSEL results. In this case we are attempting to actually demonstrate direct modulation of the vertical-cavity laser to 40 Gb/s. The results indicate a new record in modulation bandwidth for a given current and power dissipation. More recent results (to be published in 2007) show significant increases above even this record result.

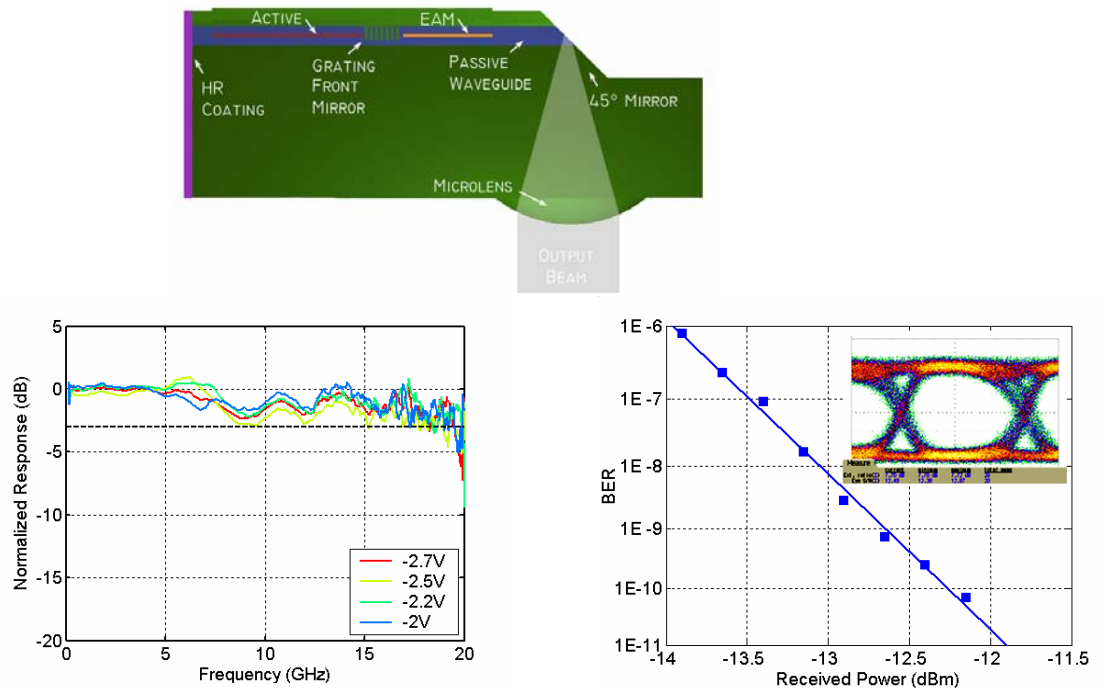

Figure 4. In-plane short-cavity laser-transmitter results. (top) Schematic; (bottom) EAM frequency response and bit-error rate at 10 Gb/s.

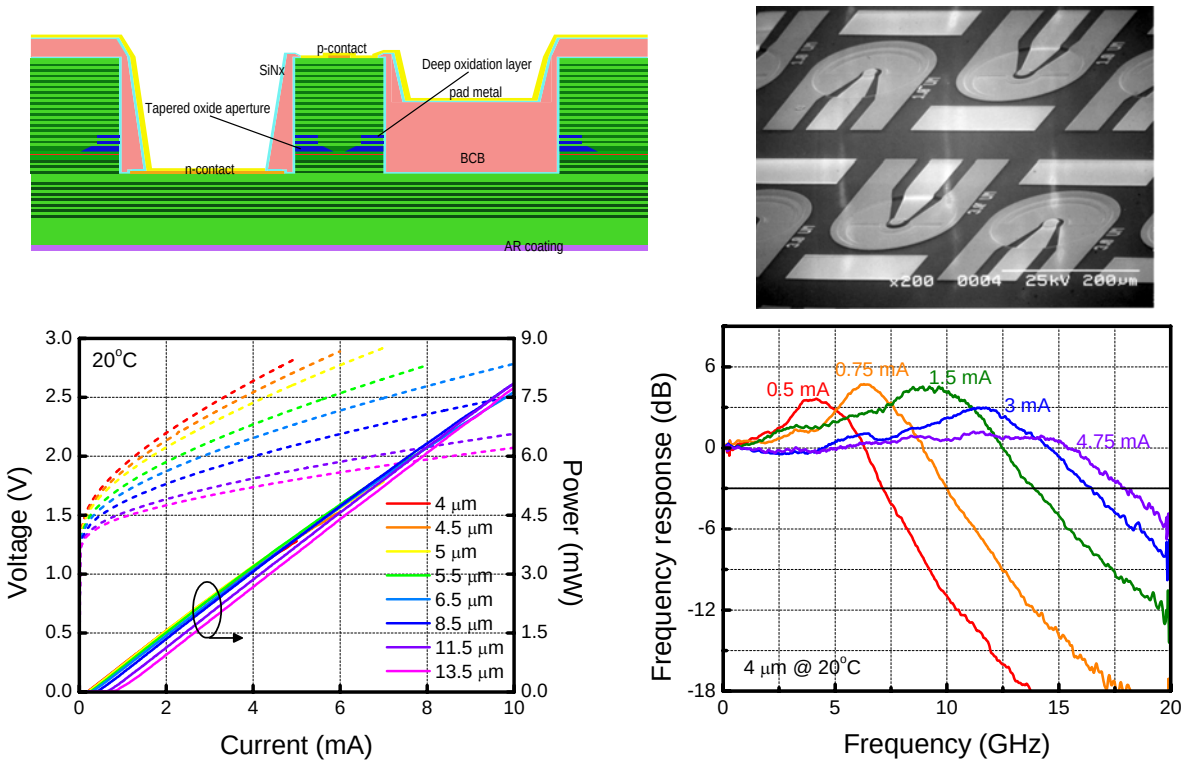

Figure 5. 980 nm VCSEL results. (top) Cross-sectional schematic and SEM of top of wafer. (bottom) Power out and voltage vs. dc current and small-signal frequency response for various bias currents.

The final group of papers, **IV. Spin-Wave Physics of Quantum Structures,** lists two papers that utilized GaAs-based MBE material grown by Prof. Coldren's group. This supported two separate research efforts on spin waves. We continue to be receptive to outside collaborations that can use our expertise in materials growth to some advantage.

Professor Coldren's Group

(*From Left*) **Back Row: Leif Johansson, Jon Klamkin, Chin-Han Lin, Matt Sysak, Steve Nicholes, Uppili Krishnamachari, Matt Dummer**
Middle Row: Chad Wang, Jon Barton, Larry Coldren, Anna Tauke-Pedretti, Janet Chen, Abbey Keck, Yan Zheng
Front Left: Joseph Chang

Professor Coldren's Group

I. *Researchers*

J. Barton	Post Doctoral Researcher, UCSB (Blumenthal)
L. Johansson	Post Doctoral Researcher, UCSB

II. *Students*

Y. Chang	Ph.D. Program
C. Chen	Ph.D. Program
M. Dummer	Ph.D. Program
J. Klamkin	Ph.D. Program
J. Raring	Ph.D. Program, now at Sandia National Laboratories
N. Stoltz	Ph.D. Program
A. Tauke-Pedretti	Ph.D. Program
C. Wang	Ph.D. Program

III. *Staff*

D. Cohen	Principal Development Engineer
A. Keck	Project Manager, OTC

Collaborators

I. *Faculty*

D. Awschalom	UCSB
D. Blumenthal	UCSB
D. Bouwmeester	UCSB
J. Bowers	UCSB
S. DenBaars	UCSB
P. Petroff	UCSB
M. Rodwell	UCSB
E. Yablonovitch	UCLA

II. *Researchers*

Y. Akulova	Agility Communications, Inc., now JDSU
D. Buell	CNRS, France
S. Carter	NIST
Z. Chen	NIST
S. Cundiff	NIST
J. English	UCSB (Gossard)
D. Feezell	Post Doctoral Researcher, UCSB (Nakamura)
B. Fimland	Norwegian University of Science and Technology
A. Huntington	Voxtel
A. Jackson	UCSB (Gossard)
P. Koh	Agility Communications, Inc., now JDSU
D. Lofgreen	Raytheon
M. Mašanović	Post Doctoral Researcher, UCSB (Blumenthal)
M. Mehta	Post Doctoral Researcher, University of Mexico (Huffaker)
G. Morrison	Apogee Photonics
H. Poulsen	Post Doctoral Researcher, UCSB (Blumenthal)
E. Skogen	Sandia National Laboratories
S. Strauf	Post Doctoral Researcher, UCSB (Bouwmeester)
M. Sysak	Post Doctoral Researcher, UCSB (Bowers)
D. Wolfson	Post Doctoral Researcher, UCSB (Blumenthal), now at Ipitek

Collaborating Students

J. Berezovsky	UCSB (Awschalom)
H. Chou	UCSB (Bowers), now at Luminent
S. Demiguel	University of Texas, Austin (Campbell)
O. Gywat	UCSB (Awschalom)
V. Lal	UCSB (Blumenthal), now at Infinera
M. Mikkelsen	UCSB (Awschalom)

N. Parthasarathy	UCSB (Rodwell)
M. Rakher	UCSB (Bouwmeester)
A. Ramaswamy	UCSB (Bowers)
S. Sahni	UCLA (Yablonovitch)
J. Summers	UCSB (Blumenthal)
D. Zibar	UCSB (Bowers), now at Com-DTU, Institute for Communication, Optics and Materials; Denmark

Table of Contents:

I. Photonic IC Technology & Devices Page

IA. PIC Technology

IB. PIC Transmitters and Receivers

J.W. Raring, L.A. Johansson, E.J. Skogen, M.N. Sysak, H.N. Poulsen, S.P. DenBaars, and L.A. Coldren, "Single-Chip 40Gb/s Widely-Tunable Transceivers with Integrated SG-DBR Laser, QW EAM, UTC Photodiode, and Low Confinement SOA," *Proc. International Semiconductor Laser Conference,* paper no. TuA1, Waikoloa Beach, HI (September 17-21, 2006)

M.N. Sysak, J.W. Raring, G.P. Morrison, D.J. Blumenthal, and L.A. Coldren, "Monolithically Integrated, Sampled Grating DBR Laser Transmitter with an Asymmetric Quantum Well Electroabsorption Modulator," *Proc. International Semiconductor Laser Conference,* paper no. TuB6, Waikoloa Beach, HI (September 17-21, 2006)

IC. Analog PICs and RF-Photonics

L.A. Johansson and L.A. Coldren, "Baseband Optical Down-Sampling for High-Performance Analog Links," *Proc. OFC 2006,* paper no. JThB30, Anaheim, CA (March 5-10, 2006)

M.N. Sysak, L.A. Johansson, J.W. Raring, M. Rodwell, L.A. Coldren, and J.E. Bowers, "A High Efficiency, Current Injection Based Quantum-Well Phase Modulator Monolithically Integrated with a Tunable Laser for Coherent Systems," *Proc. Coherent Optical Technologies and Applications,* paper no. CFC6, Whistler, BC, Canada (June 28-30, 2006)

H.-F. Chou, A. Ramaswamy, D. Zibar, L.A. Johansson, J.E. Bowers, M. Rodwell, and L.A. Coldren, "SFDR Improvement of a Coherent Receiver Using Feedback," *Proc. Coherent Optical Techniques and Applications (COTA),* paper no. CFA3, Whistler, British Columbia, (June 28-30, 2006)

L.A. Johansson, Y.A. Akulova, P.C. Koh, and L.A. Coldren, "Integrated Adaptively Predistorted Analog Optical Transmitter," *Proc. European Conference Optical Communication (ECOC)*, paper no. We1.6.3, Cannes, France (September 2006)

M.N. Sysak, L.A. Johansson, J. Klamkin, L.A. Coldren, and J.E. Bowers, "Characterization of Third Order Distortion in InGaAsP Optical Phase Modulator Monolithically Integrated with Balanced UTC Photodetector," *Proc. Lasers and Electro-Optics Society (LEOS)*, paper no. TuU 2, Montreal, Canada (October 2006)

J. Klamkin, L.A. Johansson, A. Ramaswamy, H.-F. Chou, M.N. Sysak, J.W. Raring, N. Parthasarathy, S. P. DenBaars, J.E. Bowers, and L.A. Coldren, "Monolithically Integrated Balanced Uni-Traveling-Carrier Photodiode with Tunable MMI Coupler for Microwave Photonic Circuits," *Proc. Conference on Optoelectronic and Microelectronic Materials and Devices (COMMAD)*, paper no. TO-B2, Perth, Australia (December 5-9, 2006)

II. Photonic IC Wavelength Converters

IIA. Photo-Current Driven Wavelength-Converters

J.S. Barton, M.N. Sysak, A. Tauke-Pedretti, M.M. Dummer, J.W. Raring, L.A. Johansson, M.L. Mašanović, D.J. Blumenthal, and L.A. Coldren, "Field Modulated Wavelength Converters," *Proc. SPIE,* paper no. 6124 -17, San Jose, CA (January 23-25, 2006) INVITED PAPER

M.N. Sysak, J.W. Raring, J.S. Barton, M.M. Dummer, A. Tauke-Pedretti, H.N. Poulsen, D.J. Blumenthal, and L.A. Coldren, "10 Gb/s Monolithically Integrated, Photocurrent Driven Wavelength Converter with Widely Tunable SGDBR Laser and Optical Receiver," *Proc. Integrated Photonics Research and Applications,* paper no. ITuC5, Uncasville, CT (April 24-28, 2006)

M.N. Sysak, J.W. Raring, J.S. Barton, M.M. Dummer, A. Tauke-Pedretti, H.N. Poulsen, D.J. Blumenthal, and L.A. Coldren, "Single-Chip, Widely-Tunable 10 Gbit/s Photocurrent-Driven Wavelength Converter Incorporating a Monolithically Integrated Laser Transmitter and Optical Receiver," *Electronics Letters,* **42**, (11), pp. 657-658 (May 25, 2006)

M.M. Dummer, M.N. Sysak, J.W. Raring, A. Tauke-Pedretti, and L.A. Coldren, "Widely Tunable Single-Chip Transceiver for 10 Gb/s Wavelength Conversion," *Proc. Device Research Conference,* paper no. II.A-3, University Park, PA (June 26-28, 2006)

M.N. Sysak, J.W. Raring, L.A. Johansson, H.N. Poulsen, J.S. Barton, D.J. Blumenthal, and L.A. Coldren, "Optical 2R and 3R Signal Regeneration in Combination with Dynamic Wavelength Switching Using a Monolithically Integrated, Widely Tunable Photocurrent Driven Wavelength Converter," *Proc. European Conference Optical Communication (ECOC),* paper no. Th3.4.1, Cannes, France (September 2006)
INVITED PAPER

M.N. Sysak, J.W. Raring, J.S. Barton, H.N. Poulsen, D.J. Blumenthal, and L.A. Coldren, "Extinction Ratio Regeneration, Signal Re-amplification (2R), and Broadband Wavelength Switching using a Monolithically Integrated Photocurrent Driven Wavelength Converter," *Optics Express*, **14**, (23), pp. 11348-11353, (November 2006)

M.N. Sysak, L.A. Johansson, J.W. Raring, H.N. Poulsen, D.J. Blumenthal, and L.A. Coldren, "Broadband Return to Zero (RZ) Wavelength Conversion and Signal Regeneration Using a Monolithically Integrated, Photocurrent-Driven Wavelength Converter," *Electronics Letters,* **42**, (25), pp. 1479-1481 (December 7, 2006)

IIB. "All-Optical" Wavelength-Converters and Buffers @ 40Gb/s

V. Lal, M.L. Mašanović, J.A. Summers, L.A. Coldren, and D.J. Blumenthal, "Performance Optimization of an InP-Based Widely Tunable All-Optical Wavelength Converter Operating at 40 Gb/s," *IEEE Photonics Technology Letters,* **18**, (4), pp. 577-579 (February 15, 2006)

C.-H. Chen, D. Wolfson, L.A. Johansson, D.J. Blumenthal, and L.A. Coldren, "Demonstration of 40 Gbit/s Optical Packet Synchronization Using Fiber Bragg Gratings and Fast-Tunable Wavelength Converters," *Electronics Letters,* **42**, (6), pp. 367-369, (March 16, 2006)

III. MBE Technology & Devices

IIIA. GaAs-based Vertical-Cavity Lasers and Technology

Y.-C. Chang, C.S. Wang, J.H. English, and L.A. Coldren, "Accurate Carbon Doping System for Low-Voltage and Low-Loss VCSELs," *Proc. Electronic Materials Conference*, paper no.Y8, University Park, PA (June 2006)

N.G. Stoltz, M. Rakher, S. Strauf, D. Bouwmeester, P.M. Petroff, and L.A. Coldren, "Quantum Dot Spontaneous Emission Lifetime Modification in Optical Microcavities using Oxide Apertured Micropillars," *Proc. SPIE Photonics West,* paper no. 6101, San Diego, CA (August 13-17, 2006)

Y.-C. Chang, C.S. Wang, L.A. Johansson, and L.A. Coldren, "High-Efficiency, High-Speed VCSELs with Deep Oxidation Layers," *Electronics Letters*, **42**, (22), pp. 1281-1282 (October 26, 2006)

IIIB. InP-based Vertical-Cavity Lasers and Technology

S. Sahni, E. Yablonovitch, D.A. Buell, and L.A. Coldren, "Optically Pumped Silicon Laser Based on Evanescent Coupling of Si Micro-Disk to III-V DBR Stack," *Proc. Conference on Lasers and Electro-Optics Quantum Electronics and Laser Science Conference,* paper no. CMBB2, Long Beach, CA (May 21-26, 2006)

D. Feezell, D.A. Buell, D. Lofgreen, M. Mehta, and L.A. Coldren, "Optical Design of InAlGaAs Low-Loss Tunnel-Junction Apertures for Long-Wavelength Vertical-Cavity Lasers," *IEEE Journal of Quantum Electronics,* **42**, (5), pp. 494-499, (May 2006)

D.A. Buell, D. Feezell, B.-O. Fimland, and L.A. Coldren, "Molecular Beam Epitaxy of InP-Based Alloys for Long-Wavelength Vertical Cavity Lasers," *Journal of Vacuum Science and Technology B,* **24**, (3), pp. 1544-1547 (May/June 2006)

M. Mehta, D. Feezell, D.A. Buell, A.W. Jackson, L.A. Coldren, and J.E. Bowers, "Electrical Design Optimization of Single-Mode Tunnel-Junction-Based Long-Wavelength VCSELs," *IEEE Journal of Quantum Electronics*, **42**, (7), pp. 675-682 (July 2006)

IIIC. In-plane Short-Cavity Lasers

C.S. Wang, G.B. Morrison, E.J. Skogen, and L.A. Coldren, "Fabrication and Molecular Beam Epitaxy Regrowth of First-Order, High Contrast AlGaAs/GaAs Gratings," *Journal of Vacuum Science and Technology B,* **24**, (3), pp. 1559-1563 (May/June 2006)

C.S. Wang, Y.-C. Chang, J.W. Raring, and L.A. Coldren, "Short-Cavity 980 nm DBR Lasers with Quantum Well Intermixed Integrated High-Speed EA Modulators," *Proc. International Semiconductor Laser Conference,* paper no. WC8, Waikoloa Beach, HI (September 17-21, 2006)

IV. Spin-Wave Physics of Quantum Structures

S.G. Carter, Z. Chen, S.T. Cundiff, A.S. Huntington, and L.A. Coldren, "Transient Spin-Gratings of Itinerant Electrons in Lightly-Doped GaAs Quantum Wells," *Proc. Conference on Lasers and Electro-Optics Quantum Electronics and Laser Science Conference,* paper no. QME6, Long Beach, CA (May 21-26, 2006)

J. Berezovsky, M.H. Mikkelsen, O. Gywat, N.G. Stoltz, L.A. Coldren, and D.D. Awschalom, "Non-destructive Optical Measurements of a Single Electron Spin in a Quantum Dot," *Science*, **314**, (5807), pp. 1916-1920 (December 22, 2006)

I. Photonic IC Technology & Devices

A. PIC Technology

Advanced Integration Schemes for High-Functionality/High-Performance Photonic Integrated Circuits

James W. Raring, Matthew N. Sysak, Anna Tauke-Pedretti, Mathew Dummer, Erik J. Skogen, Jonathon S. Barton, S. P. DenBaars, and Larry A. Coldren

Materials and Electrical and Computer Engineering Depts.,
University of California, Santa Barbara, 93106
jraring@engineering.ucsb.edu

ABSTRACT

The evolution of optical communication systems has facilitated the required bandwidth to meet the increasing data rate demands. However, as the peripheral technologies have progressed to meet the requirements of advanced systems, an abundance of viable solutions and products have emerged. The finite market for these products will inevitably force a paradigm shift upon the communications industry. Monolithic integration is a key technology that will facilitate this shift as it will provide solutions at low cost with reduced power dissipation and foot-print in the form of highly-functional optical components based on photonic integrated circuits (PICs). In this manuscript, we discuss the advantages, potential applications, and challenges of photonic integration. After a brief overview of various integration techniques, we present our novel approaches to increase the performance of the individual components comprising highly functional PICs.

Keywords: Semiconductor lasers, semiconductor optical amplifiers, electroabsorption modulators, metalorganic chemical vapor deposition, photodetectors, wavelength-division multiplexing.

1 INTRODUCTION

TERAHERTZ carrier frequencies characteristic of lightwave communication systems have enabled the necessary bandwidth to meet the increasing demand for higher data rates. Furthermore, optical communication systems in the 1.30μm to 1.55μm wavelength range offer desired low dispersion and loss characteristics allowing for high-bit-rate long-distance transmission with reduced repeater spacing over that of electrical coaxial lines[1]. The finite market in the telecommunications industry coupled with an abundance of chip vendors offering unique solutions creates intense competition[2]. The prevailing technology in this competition will not only fulfill the required performance specifications for the application, but will also be low cost and possess additional desired characteristics such as a compact foot print and low power consumption. Monolithic integration of optoelectronic components is the answer to this challenge. The generation, detection, modulation, switching, and transport of light on chip not only enables cost reduction, but also allows for a new generation of high functionality photonic integrated circuits (PICs) with reduced size and power dissipation.

The majority of optoelectronic components comprising modern day communications systems are discrete in nature. Several of these discrete components with differing functions are then interconnected using fiber splices in a configuration to provide the required system functionality. The underlying advantage of this method is that each component is optimized for one specific function, enabling deployment of state of the art components. However, there are several shortcomings involved with this method. The difficulty in efficiently coupling light on and off each discrete chip is great. Advances in the coupling between the semiconductor chip and optical fiber using mode converters is a significant step in reducing the coupling loss, yet coupling is still a dominant source of optical loss. Another draw back

Nanophotonic Packaging, edited by Allen M. Earman, Ray T. Chen,
Proc. of SPIE Vol. 6126, 61260H, (2006) · 0277-786X/06/$15 · doi: 10.1117/12.655999

to discrete components is the expense involved with packaging each component individually. This is the major expense as devices are taken from fabrication to deployment. A reduction of the packaging cost can be accomplished by using co-packaging of optoelectronic components although device-to-device coupling is still an issue.

The monolithic integration of the optoelectronic devices on a single chip offers the potential to completely eliminate the device-to-device coupling problem. This can provide a significant reduction in packaging cost and package size as well as increased reliability and reduced power dissipation. Increased reliability results from the elimination of possible mechanical movements amongst the elements of an optical train and the reduced driving currents allowed by the reduction in optical coupling loss between elements. The reduction in required drive currents subsequently results in decreased device power consumption.

1.1 The Challenge of Monolithic Integration

There are several examples of high functionality PICs where multiple active components are placed on a common chip. Widely-tunable transmitters, photocurrent driven wavelength converters (PD-WC), and transceivers are three such examples, as these devices will facilitate enabling technologies in wavelength division multiplexing (WDM) applications such as dynamic provisioning, reconfigurable optical add/drop multiplexers (ROADMs), wavelength routing, and optical packet switching[3]. The latter two devices require the monolithic integration of widely tunable light sources such as the sampled-grating DBR laser (SG-DBR) with modulators, semiconductor optical amplifiers (SOA), and photodiodes.

The widely-tunable electroabsorption modulator (EAM) based PD-WC making using of a receiver ridge parallel to a transmitter ridge is a viable architecture for single chip wavelength conversion[3,4]. The PD-WC is a particularly challenging device since the individual components comprising the PIC necessitate unique waveguide architectures for optimum performance. Low threshold, high efficiency lasers require high optical confinement QW active region architecture for maximized modal gain[5]. Integrated QW EAMs utilizing the quantum confined stark effect (QCSE) for high efficiency, necessitate a QW band-edge that is blue-shifted from that of the laser or SOA operation wavelength for reasonable insertion loss/extinction properties. State of the art SOAs employ measures for reduced photon density in gain region such as low optical confinement QWs, so high saturation powers can be achieved[6]. Finally, high performance photodiodes employ a bulk absorber region and can make use of unique waveguide or internal structure design for high photocurrent/high speed operation[7]. The unique characteristics required by each component for optimum performance clearly poses significant difficulty in realizing a high performance single-chip wavelength converter.

1.2 Guidelines for Monolithic Integration

There are some general requirements that must be fulfilled when monolithically integrating optoelectronic components. First, each integrated component must function as intended. The performance of each integrated component must operate at a level that will enable the PIC as a whole to achieve its specified performance level. Clearly, as these levels are increased, the performance demands of the individual integrated components will also be increased. The second requirement is that the operation of one component must not adversely effect the operation of another. That is, each component should be isolated from the other components on chip and function as if it were discrete. These requirements allow for the design of PICs using an optoelectronic building blocks approach such that discrete components sharing a common growth and processing platform can be combined in a way that creates a higher functionality device or PIC. When implementing a method for monolithic integration, the trade-off between fabrication difficulty and device optimization capabilities should be carefully weighed since added processing steps and growth complexity can lead to increased manufacturing costs and yield reduction. Additionally, the method should not be prohibitively time consuming or expensive. A review of some of some integration methods are given in the following section.

2 INTEGRATION TECHNOLOGIES

When selecting the appropriate integration method for the specific device, the strengths and weaknesses of the candidate methods should be carefully considered with the understanding that the design flexibility of the integration scheme must be increased as the PIC functionality and performance demands are increased. The butt-joint regrowth method is an example of an integration scheme offering a high degree of versatility[8]. This method involves the selective removal of the as-grown waveguide/MQW region followed by the non-planar selective regrowth of waveguide/MQW material with the desired band edge and waveguide architecture. The butt-joint regrowth process, depicted in Fig. 1a, is highly-flexible as it enables the use of a centered QW (c-MQW) active region for maximized modal gain and allows each integrated component to possess a unique band edge or waveguide architecture. Once all desired structures are realized on chip with the butt-joint method, an additional regrowth is performed for the upper cladding. This technique allows for a high degree of separate optimization of the individual components within the PIC. However, the difficulty associated with matching thickness and achieving the desired composition to avoid reflection and loss at the interface is great[8]. Furthermore, the complexity of this process is compounded as the number of desired band edges and waveguide architectures is increased since each will require an additional regrowth.

Selective area growth (SAG) has been shown to be useful in providing multiple band edges across the wafer in a single growth step[9]. In this method a dielectric mask is patterned on the wafer, which is then subjected to MOCVD growth. Growth is limited to regions between the dielectric mask, where thickness and composition of the growing layers are modified based on the adjacent mask pattern. Following the selective growth, the dielectric mask is removed and an additional regrowth is performed for the upper cladding. A schematic diagram illustrating this method is shown in Fig. 1b. This technique provides the capability to realize c-MQW active regions for maximized modal gain and QW EAMs on the single chip with a single growth. However, since this technique exploits the contrast in surface kinetics of the growth constituents on the semiconductor and dielectric, a high degree of calibration/optimization is required to tightly control the reactor conditions. Surface diffusion lengths limit the abruptness of the transition region, which may be on the order of tens of microns. Additionally, the optical mode overlap with the MQW may not be ideal in all sections due to the thickness variation.

An established and very simple integration platform is based on the use of offset QWs, where the multi-quantum well (MQW) active region is grown above a passive bulk waveguide. This allows for the selective etching of the MQW in regions where gain is not required, leaving the non-absorbing waveguide. Once the active and passive regions have been defined, the upper cladding is regrown[10]. A schematic of this method is shown in Fig. 1c. Although this is a relatively simple process and does not add significant processing steps in the case of the widely-tunable SG-DBR laser, it allows for only two band edges on a single chip, one from the MQW and one from the waveguide. Not only is the modal gain in the offset QW design less than optimal since the peak of the optical mode is offset from the QWs, but also when integrating an EAM with the SG-DBR laser the trade off between loss, tuning, and absorption may lead to reduced performance of one or more components. Furthermore, this scheme forces the use bulk Franz Keldysh (FK) type EAMs,

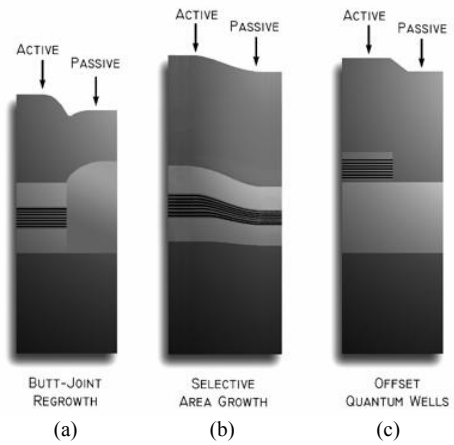

Fig. 1. Various techniques for achieving active and passive sections orthogonal to the growth direction.

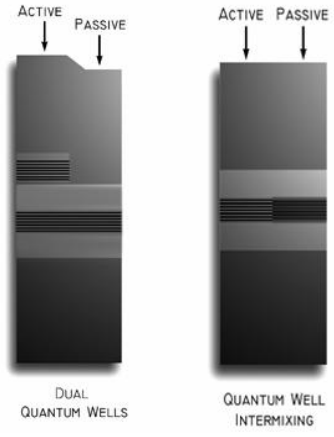

Fig. 2. Foundational integration techniques explored in this work for enhanced high-functionality PIC performance

which are not as efficient as QW EAMs based on the Quantum Confined Stark Effect (QCSE)[11].

3 BACKGROUND: INTEGRATION FOUNDATIONS

Although there has been some great success in producing PICs based on the various methods discussed above, these fabrication schemes require a significantly increased level of growth complexity as the PIC functionality is elevated. These techniques rely on butt-joint regrowth or SAG to realize blue-shifted QWs on the same chip as a laser for use in an EAM. Furthermore, aside from the butt-joint method, these schemes provide little flexibility in the cross-sectional waveguide architectures. This has limited the performance of previous single-chip EAM-based PD-WCs since they were fabricated using the offset QW platform in which inefficient FK type EAMs were employed[3]. In other work, it was the common QW stack used in the laser, SOA, and photodetector, that ultimately limiting the linearity of the receiver and hence the overall device performance[4]. Thus a key challenge of the PIC designer has been to allocate the trade-offs in such a way that the overall performance of the device is sufficient for the intended application. With this, there is clearly a demand for integration solutions that provide greater design flexibility without significant increase in fabrication complexity.

3.1 Dual QW Platform for Integrated QW EAM

Electroabsorption modulators can greatly benefit from the presence of QWs in the absorption region since the QCSE can be exploited to enable higher absorption efficiency and lower insertion losses[11]. However, as mentioned above, achieving multiple QW band edges on the same chip for the integration of a QW EAM with a laser often includes added growth/processing complexities, which makes simple solutions offering these characteristics attractive. The simple offset QW method discussed above has been used with great success in fabricating various integrated structures: SG-DBR lasers with integrated EAMs[12], SG-DBR lasers with integrated semiconductor optical amplifiers (SOAs)[13], SG-DBR lasers with integrated Mach-Zehnder modulators[14], optical receivers[15], and wavelength converters[3,16]. However, in addition to the non-optimal modal gain, the main drawback of the offset QW method is the limitation of each integrated component to one of two band edges, the active QWs or the bulk waveguide. Thus, this scheme does not allow for the flexibility necessary for the fabrication of PICs requiring multiple QW bandedges for use in lasers and EAMs.

In recent progress we have demonstrated the capability to realize a second MQW band-edge on chip using the same simple processing scheme employed in the offset QW method. This is accomplished by growing an MQW centered within the bulk waveguide below the offset MQW. The waveguide MQW is blue shifted from the bandedge of the active offset QWs to be used in gain regions. Since the resulting structure contains two stacks of QWs, this scheme is called the dual QW platform and is depicted in Fig. 2a. With only a moderate increase in the base structure growth complexity, QW EAMs can now be realized on the same chip as widely-tunable lasers using the identical simple processing steps as in the offset QW method. This scheme offers a large degree of EAM design freedom since the MQW design can be tailored without disruption of the laser active region. This freedom opens new avenues for the use of specially designed wells for optimum modulator performance in terms of well depth, well/barrier width, and well symmetry.

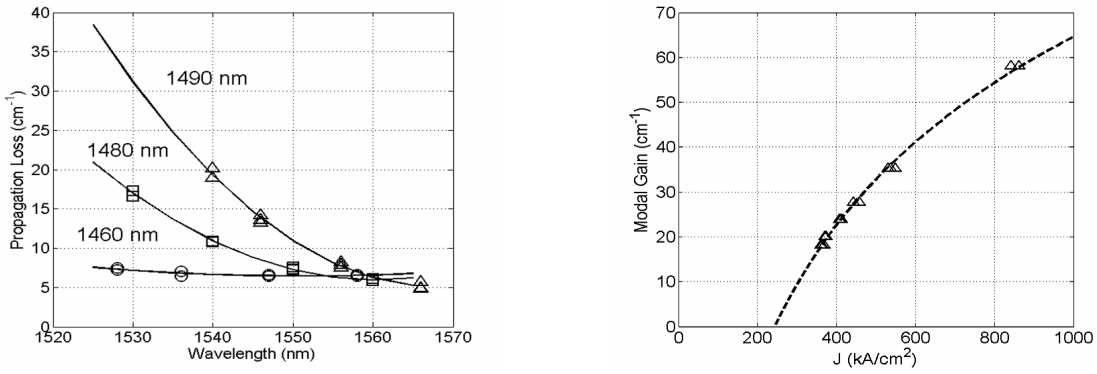

(a) (b)

Fig. 3. (a) Propagation loss versus operating wavelength for three different waveguide MQW designs employed in the dual QW platform. (b) Two parameter fit of modal gain versus current density for broad area lasers fabricated from dual QW design with a waveguide MQW PL peak placed at 1480 nm demonstrating a transparency current of 270 kA/cm^2 and material gain parameter of 764 cm^{-1}.

Furthermore, for the bulk FK EAMs, relatively high waveguide doping levels (~2E17 cm^{-3}) have been incorporated in the past to achieve large peak electric fields in order to maximize device efficiency. This is not conducive to high speed operation due to the large associated capacitance associated with the structure. For the dual QW platform, it is actually detrimental to performance to have high waveguide doping levels. Since doping that is above the QW active region will lower the electric field, and reduce the device efficiency. As a result, the doping in the waveguide portion of the structure has been lowered significantly (5E16 cm^{-3}). This allows for lower EAM capacitance and hence higher bandwidths along with enhanced EAM efficiency when compared with the more traditional offset QW EAMs.

To maintain high device output powers, it is critical that the unbiased absorption edge of the MQW centered in the waveguide not provide unreasonable amounts of loss since these QWs will be present throughout all passive components and mirror sections in addition to the EAMs. The propagation loss versus wavelength was measured for different waveguide MQW designs possessing photoluminescence (PL) peaks of 1460nm, 1480nm, and 1490nm using an integrated tunable laser and passive photocurrent taps placed at various propagation distances. The results of this study, shown in Fig. 3a, demonstrate the trade-off in passive loss versus decreasing absorption edge of the EAM wells, which results in high EAM absorption efficiencies. From this data, the design employing waveguide QWs with a PL peak of 1480nm was used for PIC fabrication as the propagation loss across the full optical communication C-Band remains below 17 cm^{-1} and is not unreasonable for the applications discussed in this work. The epitaxial base structure of this design used a standard active offset MQW with seven 6.5 nm compressively strained QWs and eight 8.0 nm barriers with a peak photoluminescence wavelength of 1550nm. The MQW centered within the waveguide consisted of seven 9.0 nm compressively strained wells and six 5.0 nm tensile strained barriers. As shown in Fig. 3a, the loss

A necessary characterstic of the dual QW platform is that the presence of the QWs in the waveguide not hinder carrier transport to the offset MQW used in the laser active regions and/or SOAs. More specifically, electrons must now traverse the waveguide MQW before arriving at the offset MQW for recombination with injected holes. Fabry Perot (FP) broad area laser (BAL) devices were fabricated using the dual QW platform and were subjected to pulse testing. The inverse differential efficiency versus FP laser length was plotted to extract the injection efficiency and modal loss. The injection efficiency was found to be 73% and the modal loss was found to be ~6 cm^{-1}, which are both in close correlation to the 73-76% injection efficiency and ~6cm^{-1} loss observed for BAL devices fabricated on the standard offset QW platform. By using a two parameter fit to plot the BAL device modal gain versus current density as shown in Fig. 3b, a transparency current density of 270 kA/cm^2 and material gain parameter of 764 cm^{-1} was extracted. The close correlation of all material properties extracted from dual QW BALs with those previously extracted from BAL devices fabricated using the standard offset QW platform demonstrates efficient electron transport through the waveguide wells and into the offset wells.

3.2 Quantum Well Intermixing for Centered Quantum Well Active Regions and Integrated QW EAM

Another method to realize multiple QW bandedges is through quantum well intermixing (QWI), which allows for the strategic, post growth, tuning of the QW band edge using a relatively simple procedure. As this technique enables the employment of centered MQW active regions for maximized modal gain lasers and blue shifted QWs for use in EAMs, QWI breaks the trade-off associated with the simple fabrication scheme offered by the offset QW method and the design flexibilities offered by butt-joint regrowth and SAG. QWI makes use of the metastable nature of the compositional gradient found at heterointerfaces. The natural tendency for materials to interdiffuse is the basis for the intermixing process. Also, because QWI does not change the average composition, but only slightly changes the compositional profile, there is a negligible index discontinuity at the interface between adjacent sections. This eliminates parasitic reflections that can degrade performance.

There are several methods to accomplish QWI[17,18,19]. In this work we employ the implant-enhanced interdiffusion technique, which relies on the diffusion of point defects created during an ion implantation into an InP implant buffer layer grown above the MQW active region. This method has been shown to have good spatial resolution, and be controllable using anneal time, temperature, and implant dose[5]. Furthermore, we have developed a method to further control the QWI process by achieving any number of QW band edges in the structure using selective removal of the catalyst. This method requires a single ion implant followed by a rapid thermal anneal step. The extent of intermixing is precisely controlled using the anneal time. Once the desired band edge is reached for a given region, the anneal is stopped and the point defects are removed in that region by selective removal of the InP implant buffer layer. The anneal is then continued until the desired band edge in another section is reached, at which point the point defects are removed in this section. The process, illustrated in Fig. 4a, can be repeated to achieve any number of band edges across the wafer as demonstrated in Fig. 4b with a plot of photoluminescence peak versus anneal time for samples with and without implantation and samples with the implant buffer layer removed.

Several aspects of the QWI material are crucial for the successful operation of PICs incorporating SG-DBR lasers and QW EAMs and required characterization. The loss in the passive and mirror regions must be made low such that high device output powers can be achieved. To characterize the loss properties of intermixed material, active/passive buried ridge stripe (BRS) Fabry-Perot (FP) with different magnitudes of photoluminescence shift were pulse tested using the cleave back method. The FP laser devices possessed an active length of 500 μm and an initial passive waveguide length of 2500 μm, The passive region loss was plotted as a function of photoluminescence peak wavelength at an operation wavelength of 1570nm, as shown in Fig. 5a. An exponential curve provides a good fit with the data. As evident from the figure, the passive region modal loss is strongly dependent on the relative position of the intermixed band edge.

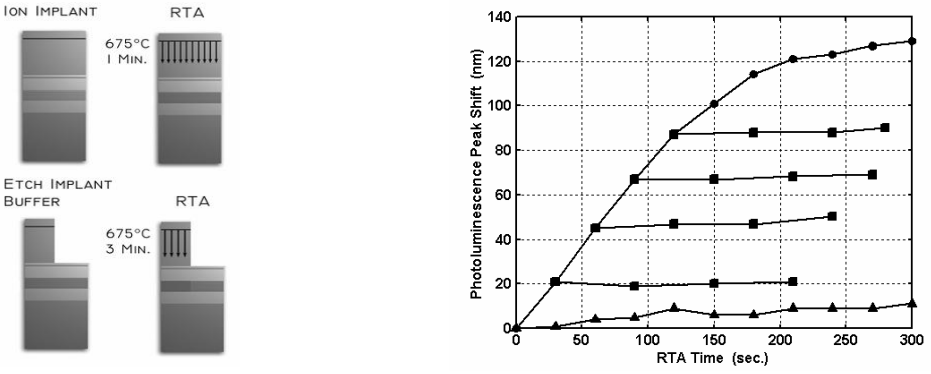

(a) (b)

Fig. 4. (a) Schematic of the intermixing process. From left to right on top; ion implantation followed by rapid thermal annealing. From left to right on bottom; selective removal of vacancy point defects required for blue-shifting, followed by an additional anneal (b) Peak photoluminescence peak shift as a function of anneal time, showing the initial linear increase in the peak shift and the complete halting of the peak shift for samples for which the implant buffer layer has been etched. Symbols indicate nonimplanted (triangles), implanted (circles), and samples with partial anneal followed by the removal of the implant buffer layer (squares).

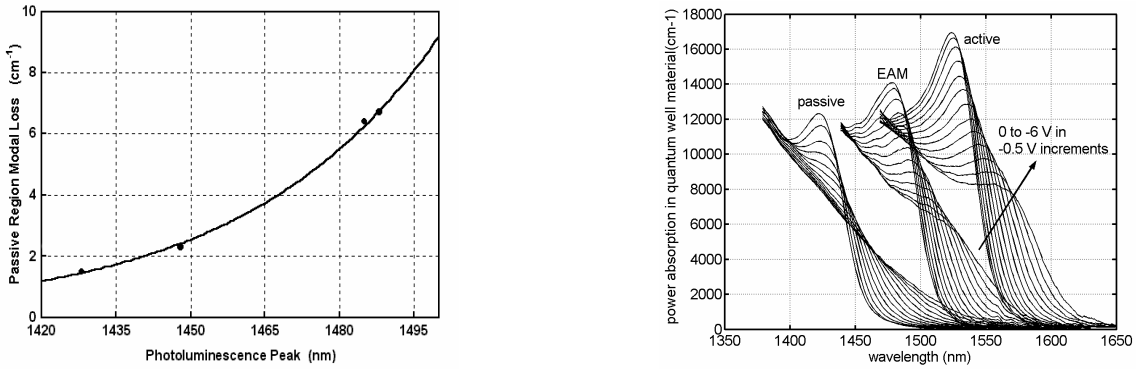

(a) (b)

Fig. 5. (a) Passive region modal loss as a function of photoluminescence peak wavelength at a wavelength of 1570nm. Solid line indicates an exponential curve fit, while symbols indicate modal loss data extracted from active/passive lasers. (b) Power absorption vs. wavelength measured using photocurrent spectroscopy for as-grown and two regions whose quantum wells are intermixed to different levels.

Maximizing the magnitude of intermixing can minimize the modal loss in the passive region.

As mentioned in the introduction, QW EAMs are desirable over bulk FK EAMs due to performance enhancement resulting from the QCSE, which gives rise to a strong exciton peak in the material absorption spectrum and can result in low and even negative chirp behavior in an EAM[20]. Thus for the realization of an optimum EAM, it is crucial that the QWI process does not severely degrade the absorption characteristics of the as-grown material. This effect was studied using photocurrent spectroscopy on diodes fabricated with as-grown (λ_{pl} = 1537) and material intermixed to two levels (λ_{pl} = 1483 and λ_{pl} = 1429) at bias levels from 0 to -6 V in -0.5 V increments. The results of this study are shown in Fig. 5b. The devices used in this study contained seven 6.5 nm compressively strained QWs and eight 8.0 nm barriers placed between two 120 nm bulk waveguides. The effect of QWI on the exciton peak is made clear by comparison of the band edges for the as-grown and intermixed regions of the photodiodes. As the degree of intermixing increases, and the exciton peaks shift to shorter wavelengths, the exciton magnitude decays. With increased intermixing, the exciton peaks also decay more rapidly as a function of applied bias voltage. Although there is some degree of exciton degradation with intermixing, the exciton remains the dominant characteristic of the absorption spectra, especially for intermixing levels required for EAM employment.

This method of QWI has been further qualified through the successful fabrication of short-cavity distributed Bragg reflector (DBR) lasers with integrated EAMs[21], widely-tunable multi-section sampled-grating (SG) DBR lasers with integrated EAMs[22], and chip-scale wavelength converters[4,23]. A detailed review of these devices fabricated using our QWI method along with a thorough description of the fabrication process can be found elsewehere[24].

4 CHALLENGES OF INCREASED FUNCTIONALITY PIC

Although both of the foundational integration technologies discussed above enable the use of QWs in the EAM regions and QWI provides maximized modal gain in the lasers, significant limitations are imposed as higher PIC functionality is required. This is a result of the limited waveguide architecture options for use in the integrated components. In the case of the widely-tunable EAM based PD-WC, the integration of SOAs and photodetectors with the SG-DBR laser and EAM is required. When employing the simple yet versatile dual quantum well or QWI schemes for device fabrication, the SOA gain region must make use of the same MQW active region as used in the laser. Since these components have different functionalities, it is clear that they will also require different considerations when designing the MQW active region.

High modal gain is desired in the laser such that low threshold currents, high wall plug efficiency, and high output powers can be achieved. The threshold modal gain (Γg_{th}) is governed by Eq. 1, where Γ is the optical confinement factor, g_{th} is the threshold material gain, α_i is the optical loss in the cavity, and α_m is the mirror loss. From Eq. 1 it is clearly advantageous to maximize the optical confinement factor within the laser to achieve high modal gain. The

output saturation power, P_{OS}, defined as the output power at which the gain drops by 3 dB, is a critical consideration in SOA design. The output saturation power can be approximated by Eq. 2[25] , where G_o is the unsaturated gain, *w* is the width of the gain region, *d* is the thickness of the gain region, *a* is the differential gain of the material, τ is the carrier lifetime, and again Γ is the optical confinement factor. From Eq. 2, it is clear that for the realization of high saturation power SOAs, a low optical confinement factor is desirable. Thus, there is clear performance trade-off between the integrated laser and SOA imposed by the optical confinement properties of the device architecture.

Since the core component of the PICs discussed in this work is the widely-tunable SG-DBR laser, the first design consideration of the MQW active region must be given to the laser performance. Thus, the confinement factors in the base structure MQW active regions are designed to be relatively high at ~6% and ~9.5% for seven active QWs employed in the dual QW and QWI platforms, respectively. Without modifications for enhanced SOA performance, the saturation power of the SOAs is expected to be on the order of 11-13 dBm at current densities in the range of 10 kA/cm^2.

$$\Gamma g_{th} = \alpha_i + \alpha_m \qquad Eq.1 \qquad P_{os} = \left(\frac{G_o Ln(2)}{G_o - 2}\right)\left(\frac{wd\,h\nu}{a\Gamma\tau}\right) \qquad Eq.2$$

Another limitation imposed on highly functional PICs such as the PD-WC when using the dual quantum well or QWI integration platforms pertains to photodetectors. In the dual QW platform, the photodetector absorption region must utilize either the offset MQW used in the laser or the higher energy bandedge centered MQW used in the EAMs and passive components as shown in Fig. 2b. In the QWI platform, the photodetector is forced to use the centered MQW with any of the available bandedges rendered with QWI. In both cases, the best choice is the as-grown active QWs, since these wells have the lowest energy absorption edge resulting in the highest absorption coefficient and least wavelength dependence. Since this structure sandwiches intrinsic QWs between the p and n-type cladding layers, the resulting photodetector structure is classified as a p-i-n photodiode which employs QWs in the absorbing medium. While the active QWs are the best available option on these platforms, they are definitely not the optimum choice for use in a photodetector. The reasons for this are threefold: The potential barriers introduced by the QWs in the absorbing region hinder carrier escape, which results in premature saturation properties. The high confinement factor leads to a steep exponential absorption profile that results in a front-end-concentrated current density, again leading to saturation. Finally, since the thickness of the intrinsic region is set by the MQW active region design, the PIC designer has little freedom to tailor the electric field strength and profile in the photodetectors. Conventional p-i-n photodiodes operating in the 1.55 μm range employ a bulk absorber such as InGaAs with a lower energy bandgap than that of the operating wavelength to avoid complications associated with QWs and minimize wavelength dependent absorption properties. More advanced devices employ special architectures such as evanescently coupled waveguide schemes to create a uniform absorption profile along the detector and minimize front-end saturation[26]. In the following sections we will explore techniques to improve integrated SOA and photodetector performance.

5 TECHNIQUES FOR ENHANCED PIC PERFORMANCE

5.1 2-Dimensional Solutions: Flared Waveguide

By inspection of Eq. 2, it is clear that there are several possible approaches to increasing the saturation power within an SOA. Reduction of the carrier lifetime and/or differential gain through the use of a differing gain material such as quantum dots or through higher current density operation would both be beneficial to the SOA performance[27]. Another approach would be to reduce the photon density over the gain medium, which can be accomplished by reducing the optical confinement factor or by increasing the cross-sectional area of the active region to expand the optical mode[28]. Perhaps the latter of the two options would be the simplest method to increase the saturation power. When increasing the cross-sectional area of the active region, one has the option to increase the thickness (d) and/or the width (w) of the gain material in the active region. However, in typical waveguide configurations such as the surface-ridge architecture, an increase in thickness of the active material also leads to an increase in the confinement factor and is actually detrimental

to the saturation power. However, the optical confinement factor is relatively insensitive to the waveguide width, such that the width can be increased without significant increase in confinement factor. Furthermore, the width of the waveguide is simply controlled with the lithographic mask design such that waveguide flares can be implemented without any increase in fabrication or growth complexity.

In order to study the saturation power benefits offered by simple waveguide flares, photoreceivers consisting of SOAs and QW p-i-n detectors with various waveguide flare/taper schemes were fabricated using the offset QW process[15]. The SOAs were designed as two-stage amplifiers. The first stage uses 200-μm-long by 3-μm-wide waveguide to provide unsaturated gain for low input powers while keeping amplified spontaneous emission noise to a minimum. The second stage employs a linearly flared waveguide from 3 μm to between 6 μm and 12 μm. Curved and flared input waveguides were used for reduced parasitic reflections. The devices were soldered to Cu blocks for continuous wave (CW) testing at an input wavelength of 1548nm in the TE polarization state. A scanning electron micrograph of the photoreceivers is shown in Fig. 6a.

The output power at which the gain rolls off by 1dB is plotted versus input power at a current density of 8.3 kA/cm^2 for the different SOA designs in Fig. 6b. From this plot it is seen that the 1dB compression point can be increased from the 10-11 dBm range with no flare to nearly 16 dBm at a final flare width of 12 μm. The result is a 3-4X increase in power handling capabilities of the SOA through the use of simple waveguide flares. Furthermore, as shown by the plot of device gain versus length in Fig 7a, with the proper choice of device length, the SOA gain can be on the order of 20 dB.

The saturation point of a photodetector can be classified by the photocurrent density at which the power out versus power in response compresses by a specified value. With this in mind, the goal was to improve the performance of QW p-i-n type photodetectors such that the offset active MQW could be employed in the photodetector regions with sufficient performance. The QW p-i-n detectors provide high absorption coefficients due to the high modal confinement and material absorption associated with the waveguide structure and QWs, respectively. These properties coupled with the characteristic exponential absorption profile in the detector results in a majority of the photocurrent generated in the front-end. While this allows for short detector lengths it also causes front end photodetector saturation. This saturation is evident in the degradation of small signal bandwidth with increased photocurrent densities. Since wider waveguides result in lower current densities for a fixed input power, the saturation power of a photodetector can be increased with the use of wide waveguides. As mentioned above, this is attractive since it requires only changes to the lithographic mask design and no processing or growth deviations are necessary. However, the effects of having a larger device area increases the capacitance and in turn decreases the bandwidth. Therefore, the best bandwidth versus increased saturation power trade-off is a waveguide scheme in which the width is tapered from large to small. In order to study the potential benefits of such schemes, three detector designs were fabricated on the same chip as the SOAs and tested. The first detector design had a length of 150-μm with a straight 3-μm-wide ridge. The first 50 μm of the detector employed bulk waveguide material (passive material) as the absorber followed by 100 μm of offset MQW active material. The second

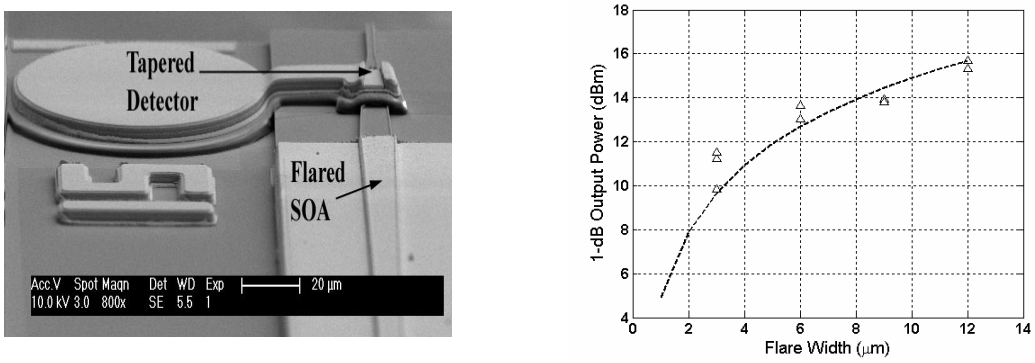

(a) (b)

Fig. 6 (a) SEM of photoreceiver employing flared/tapered waveguides for improved saturation performance. (b) 1dB compression point of output power as a function of final flare width for SOA operating at 8.3 kA/cm^2.

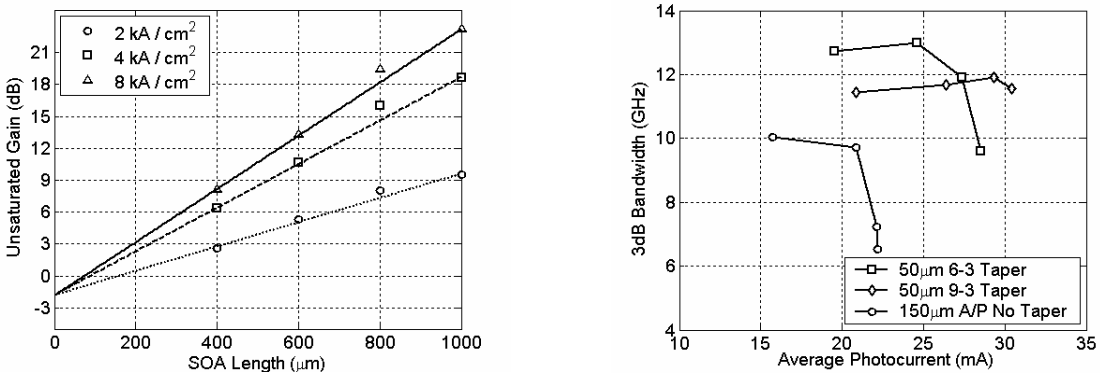

(a) (b)

Fig. 7. (a) Unsaturated gain versus SOA length for various operation current densities and (b) 3dB photodetector bandwidth versus average photocurrent for various taper schemes demonstrating the benefits from widening the front-end waveguide width of the photodetector.

and third designs were 50-μm in length and used a linear ridge taper from 6 μm to 3 μm and 9 μm to 3 μm, respectively.

In Fig. 7b, the small-signal 3dB bandwidths versus average photocurrent are plotted for the different detector designs at a reverse bias of 4V using a termination load of 50Ω. The key aspect of this plot is not the magnitude of the unsaturated bandwidth since the total diode area and hence capacitance of the various designs are different, but rather the photocurrent at which the bandwidth begins rolling off. The 3 μm wide non-tapered device demonstrates bandwidth degradation at ~20mA of average photocurrent. However, the tapered designs do not begin degrading until photocurrent levels of >25mA and >30mA for the 6 μm and 9 μm wide front-ends, respectively. Thus, through the use of simple waveguide tapers, the saturation power levels was increased by 50% in a photodetector with 2/3 the total diode area.

5.2 3-Dimensional Solutions: QWI and MOCVD Regrowth

In the previous section, we presented recent progress in which significant improvements to SOA and photodetector performance were made through simple waveguide flares. Although this technique is elegant in that it does not require any additional processing or growth steps for the integration of these components with SG-DBR lasers and EAMs, the possible performance improvements are limited. In the case of the SOA, simply increasing the width can reduce the heat dissipation efficiency due to the device aspect ratio. Since gain and saturation power are dependent on the operation current density and it is this current density generating heat, insufficient heat dissipation can lower the optimum operation current density and hence degrade performance. This effect counteracts the benefits of decreased photon density provided by the flares.

State of the art high saturation power SOAs employ a drastically different gain region design than the MQW designs employed in the SG-DBR lasers of this work. These gain region schemes include quantum dots, low optical confinement (LOC) QW active regions, or slab coupled optical waveguide architectures. The LOC configuration is an attractive choice since the photon density within the QWs can be kept relatively low. Using the LOC-QW scheme, impressive saturation powers of +23 dBm and +28 dBm have recently been demonstrated[6,28].

The photocurrent handling capabilities of the QW p-i-n type photodetector is intrinsically limited for three reasons. Saturation in a p-i-n photodetector can be explained by the classic space charge effect, which is a result of the slow escape time of holes from the absorbing layer[7]. The spatial distribution of photogenerated carriers in the absorbing medium effectively reduces the applied electric field due to screening effects. Once the field drops below a critical value, the holes can no longer maintain their saturation velocity and the power in versus power out response of the device begins to roll-off. Furthermore, the presence of quantum wells in the absorbing region introduces potential barriers, which impede carrier escape and hence compound the saturation issue[29]. The third issue, front-end saturation, can be dealt with by evanescent coupling schemes or simple waveguide flares as discussed above[15,26].

The uni-traveling carrier (UTC) photodiode has been designed specifically to circumvent the influence of hole transport on the performance of the detector by making the total charge transit time heavily dominated by electrons. The active layers of the UTC are the neutral InGaAs:Zn absorption layer and the adjacent depleted wide bandgap InP electron collection layer. Under normal operation of the photodiode, carriers are photogenerated in the absorber layer. The minority carriers, electrons, diffuse towards the collector layer where they accelerate to their overshoot velocity and drift across the collector layer. The escape time of the majority carriers, holes, from the absorption layer is negligible since it is set by their dielectric relaxation time[7]. Since the overshoot velocity of electrons is an order of magnitude higher than the saturation velocity of holes, the UTC can achieve saturation current densities 4-6 times higher than that in p-i-n photodiodes[7].

With the above discussion, the intrinsic difficulties of achieving high performance SOAs and photodetectors integrated with SG-DBR lasers and QW EAMs on the dual QW quantum or 2-dimensional QWI platform should be clear. In order for PICs to compete with their discrete counterparts, the necessity for a break-through technology that will circumvent these trade-offs is essential. This technology is further exploitation of QWI. By using QWI to render the as-grown c-MQW passive and then performing straightforward, blanket MOCVD regrowth, state of the art SOA and photodetector architectures can be integrated.

The proposed novel integration procedure is initially identical to that of the 2-dimensional single regrowth QWI process for the realization of multiple c-MQW band-edges to be employed in the laser, EAM, and passive sections[5]. However, upon removal of the InP buffer layer and 1.3Q stop etch layers, a blanket MOCVD regrowth is performed for the growth of a thin InP:Si layer followed by a 1.3Q:Si stop etch layer, an InP:Si confinement tuning layer (CTL), an offset low-confinement MQW (o-MQW) SOA gain region with similar compositions and thicknesses to that of the standard c-MQW active region sandwiched between 25nm barriers, 50nm InP, and a 200nm InP:Zn cap layer. Since the CTL layer functions to remove the active wells from the peak of the optical mode, the choice of the thickness is a key aspect in the design and will be discussed in detail below. The proof of concept and key growth aspects were previously reported[30,31]. Following the regrowth, the sample is patterned with Si_xN_y and a wet chemical selective etch process is carried out such that the o-MQW structures remain in regions where low optical confinement active regions are desired with intermixed c-MQW regions below. A second blanket MOCVD regrowth for the realization of UTC photodiode structures is performed. Again, the regrowth initiates with a thin InP:Si regrowth layer and a 1.3Q:Si stop etch layer, but is then followed by the growth of the InP collector, conduction band smoothing layers, the InGaAs:Zn absorber layer, and a 150nm InP:Zn cap layer. The thickness and doping of both the collector and absorber layers have a great impact on the expected device performance and will be discussed further below. The epitaxial structure of the UTC was based largely off of the structure employed by Ishibashi et al[7]. The sample is then patterned with Si_xN_y and a wet etch is performed such that the UTC structure remains only where detectors are desired. A final blanket MOCVD regrowth is performed to grow the p-type InP:Zn cladding and p-contact InGaAs:Zn layers to yield four distinct regions remain on a single chip: The as-grown c-MQW active regions to be used for high gain lasers and SOA sections, the partially intermixed c-MQW regions for use in high efficiency QW-EAMs, low confinement o-MQW regions grown above intermixed wells for high saturation power SOAs, and finally UTC structures grown over intermixed wells for high-saturation power high-bandwidth photodiodes. A complete and labeled schematic of the resulting regions on a single chip is shown in Fig. 8.

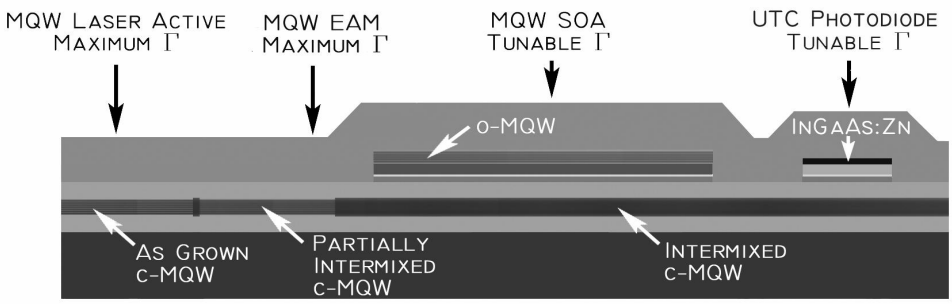

Fig. 8. Side-view schematic of QWI and MOCVD regrowth integration scheme enabling the integration of high gain lasers, QW EAMs, high saturation power amplifiers, and high saturation power photodetectors.

In Fig. 9a, a schematic side-view of the SOA is presented. By growing the o-MQW active region above the intermixed c-MQW, the active wells are taken off the peak of the optical mode and hence the confinement factor is reduced. A finite difference technique was used to solve the wave equation and compute the optical confinement within the active QWs for both the c-MQW and o-MQW regions. The base structure consists of ten 6.5 nm compressively strained QWs and eleven 8.0 nm barriers sandwiched between two 1050 nm waveguide layers. The refractive index and simulated optical modes are plotted in Fig. 9b for the c-MQW and Fig. 9c for an o-MQW consisting of five wells with a CTL thickness of 150nm. To show how the optical confinement in the o-MQW is influenced by the CTL thickness and number of offset QWs, the finite difference technique was used to solve for the optical confinement as a function of the CTL thickness for three different numbers of offset QWs. The simulation, shown in Fig. 10a, assumes a ridge waveguide architecture with a ridge width of 5μm. According to the simulations, confinement factors in the vicinity of 1% can be achieved.

The saturation power and chip gain can be predicted using Eq. 2 and material gain data from previous BAL devices, respectively. These simulations are shown in Fig. 10b, which plots chip saturation power and chip gain versus CTL thickness for 3-5 offset QWs. The simulations assume a current density of 2.5 kA/cm^2/well, a radiative recombination coefficient of B = 0.3x10^{-10} cm^3/s, an Auger recombination coefficient, C = 6x10^{-29} cm^6/s, and a device length of 1500μm. According to Fig. 10b, saturation powers >20dBm with chip gains in the 7-15 dB range can be simultaneously achieved for such a device with the proper choice of CTL thickness and number of offset QWs.

To demonstrate the viability of QWI plus offset QW growth for the realization of low confinement and high confinement active regions on the same chip, 3μm wide ridge type FP devices of both active region types were fabricated on the same chip. The o-MQW consisted of 5 QWs with a CTL thickness of 1450nm, yielding a confinement factor of ~1.5%. The cleave back method was used to plot the inverse differential efficiency versus FP laser length to extract the injection efficiency and optical loss of both active region types. The injection efficiency was found to be 70% and 73 % in the c-MQW and o-MQW active regions, respectively. The optical loss was found to be 20 cm^{-1} and 3 cm^{-1} in the c-MQW and o-MQW active regions, respectively. A two-parameter fit was used to plot the threshold modal gain

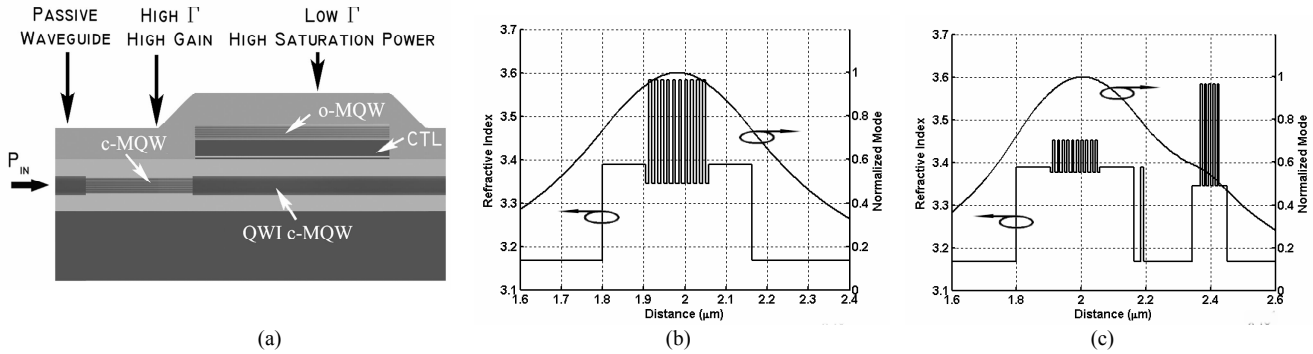

(a) (b) (c)

Fig. 9. (a) Side view schematic of SOA with high gain c-MQW section and high saturation power o-MQW section. In (b) and (c) the refractive index and mode profile are plotted versus waveguide position illustrating the drastic reduction in confinement factor that can be achieved in the o-MQW.

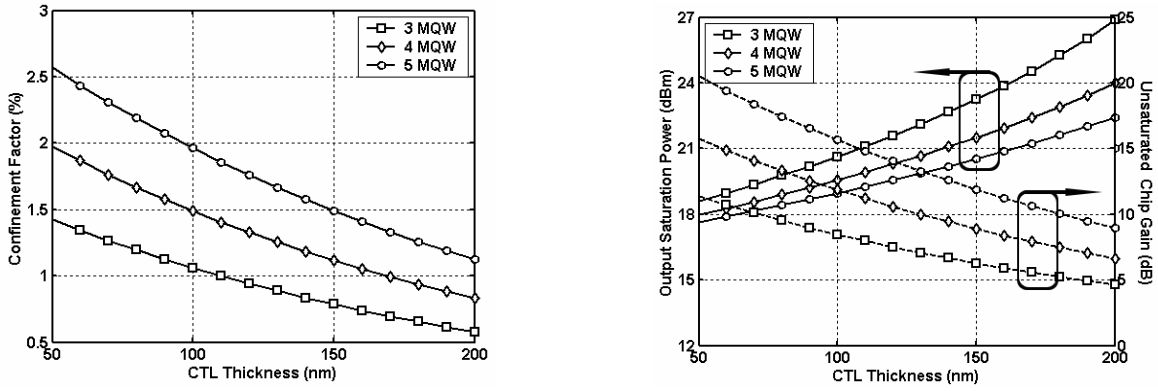

(a) (b)

Fig. 10. Simulated (a) optical confinement factor and (b) saturation power/ unsaturated chip gain versus CTL thickness in the o-MQW for 3, 4, and 5 offset QWs. The simulations assume a current density of 2.5 kA/cm^2/well, a radiative recombination coefficient of B = 0.3x10^{-10} cm^3/s, an Auger recombination coefficient, C = 6x10^{-29} cm^6/s, and a device length of 1500μm.

versus current density. The fit yielded a modal gain parameter of 94.1 cm^{-1} in the c-MQW active region and 9.1 cm^{-1} in the o-MQW active region, which is in good agreement with the simulated difference in optical confinement factor.

The separate growth for the realization of the UTC structure enables a high level of detector design freedom. However, the choice of the InGaAs:Zn absorber layer thickness and InP collector layer thickness is crucial. Since the integrated UTC photodetector of this work will use an edge-coupled architecture, the internal quantum efficiency is not largely dependent on the absorber thickness. Thus, we employ a thin 50nm absorber, such that the diffusion component of the electron transport does not dominate the total transport time. Since the collector layer functions to space the InGaAs:Zn absorber layer from the core waveguide consisting of an intermixed c-MQW, the choice of the collector thickness will influence the absorption profile and hence the internal quantum efficiency of the detector.

Beam propagation simulations were performed using commercially available software from Rsoft in order to predict the absorption profile. The simulated absorption profile for our integrated UTC structure with varying collector thicknesses along with that expected in a p-i-n detector formed from the as-grown c-MQW stack consisting of ten 6.5nm wells is shown in Fig. 12a. The loss values of 6800 cm^{-1} used for the InGaAs:Zn and 5000 cm^{-1} used for the p-i-n QWs was extracted experimentally with photocurrent spectroscopy. The three collector thicknesses used in the simulation were 150nm (squares), 200nm (triangles), and 250nm (circles) with an absorber thickness of 50nm. As shown in Fig. 11a, with proper design the absorption profile can be tuned in the UTC device to take on a more linear shape opposed to the fixed steep exponential profile exhibited by the QW-p-i-n. This feature of the integrated UTC structure enables the

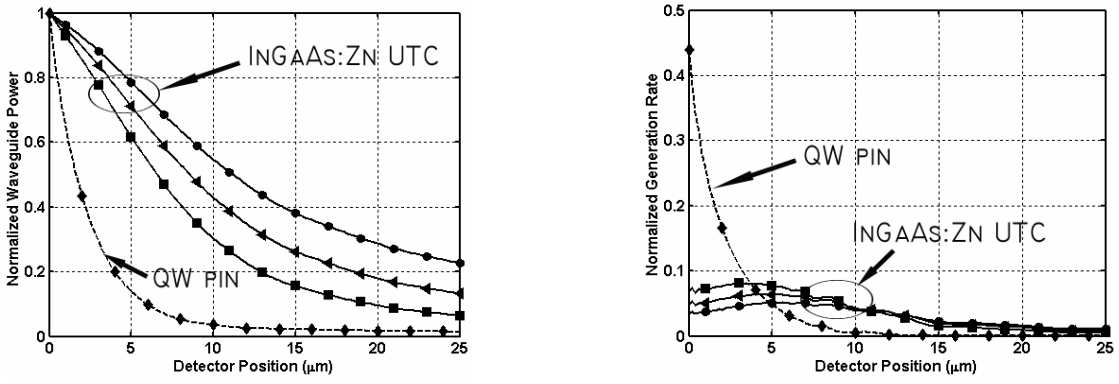

(a) (b)

Fig. 11 (a) Simulated waveguide power along photodetector for a QW p-i-n (dashed line) and UTC photodiodes (solid lines). The simulations use a 50nm thick absorber and collector thicknesses of 100nm (squares), 150nm (triangles), and 200nm (circles). (b) Simulated carrier generation rate along detector for a QW p-i-n (dashed line) and UTC photodiode (solid lines). The simulations use a 50nm thick absorber and collector thicknesses of 100nm (squares), 150nm (triangles), and 200nm (circles).

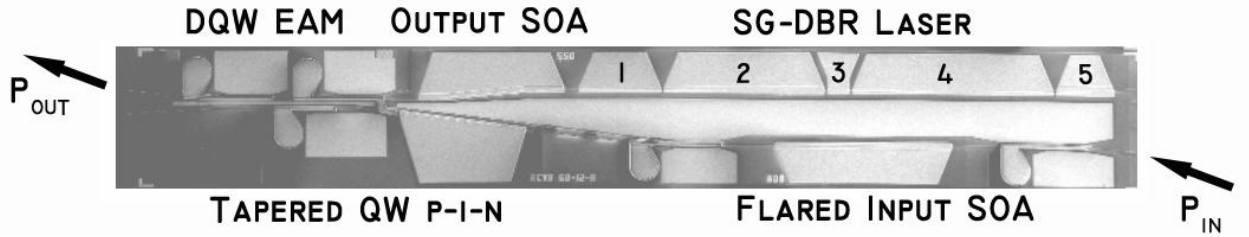

Fig. 12 Top view SEM of PD-WC device fabricated using the dual QW platform incorporating flared/tapered waveguide schemes for enhanced receiver performance.

control over the carrier generation profile since this profile is governed by the slope of the absorption profile. The normalized carrier generation rates along the detector lengths resulting from the absorption profiles are shown in Fig. 11b. The UTC type detectors demonstrate a radically more uniform generation rate along the length of the device than does the c-MQW p-i-n detector, with an ~8X reduction in front-end photocurrent generation. This implies that the front-end saturation characteristics plaguing traditional waveguide photodiodes can be avoided using the regrowth scheme. Since the collector layer also sets the detector capacitance as it is the intrinsic layer, careful consideration of the trade-off between bandwidth and desired absorption profile must be taken.

6 PIC RESULTS

In the following sections results are presented from PICs fabricated on the dual QW and on the QWI platform. First we report the performance 10 Gb/s widely-tunable transmitters monolithically integrated with photoreceivers employing waveguide flares for both the SOA and the detector for the realization of a 10 Gb/s PD-WC. In the following section results are shown for a 10 Gb/s widely-tunable negative-chirp transmitter fabricated using QWI. Finally, the results from SOAs and UTC photodiodes fabricated using the novel QWI and MOCVD regrowth scheme are presented.

6.1 Dual QW 10 Gb/s Transmitter with Integrated Receiver

In some of our most recent progress we have monolithically integrated SG-DBR lasers with QW EAMs and SOA/QW p-i-n receivers employing flares and tapers for improved saturation characteristics using the dual QW platform. This device, shown in Fig. 12, was the first single chip widely tunable EAM based 10 Gb/s PD-WC providing 10 dB of output signal extinction and a net conversion gain. Further details and performance characteristics of the PD-WC device can be found elsewhere[32]. Here we focus on the transmitter portion of the device which is comprised of a five section SG-DBR laser followed by an SOA for output amplification and a QW EAM consisting of seven 9.0 nm compressively strained wells and six 5.0 nm tensile strained barriers. The 5 sections of the SG-DBR laser are, from front to back of the laser: front mirror, gain, phase, rear mirror, and backside absorber, as depicted in Fig. 12. The phase and mirror sections function to tune the wavelength of the laser[10].

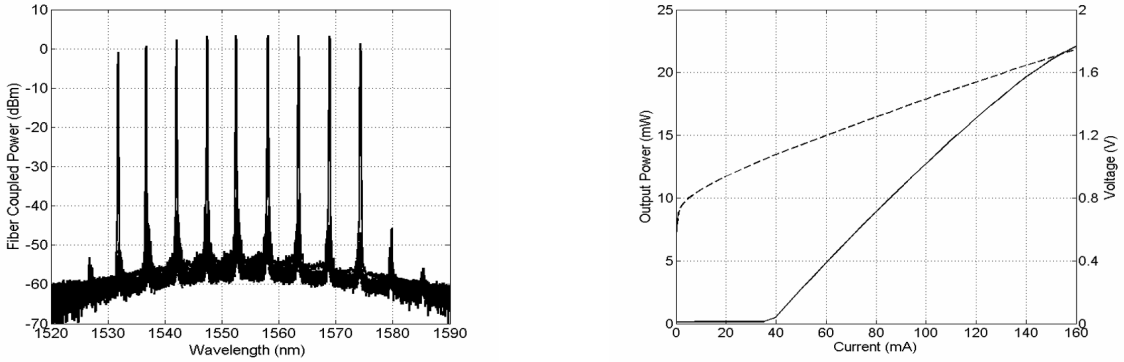

(a) (b)

Fig. 13. (a) Tuning spectra and (b) light/voltage characteristics versus current for SG-DBR fabricated on dual QW platform.

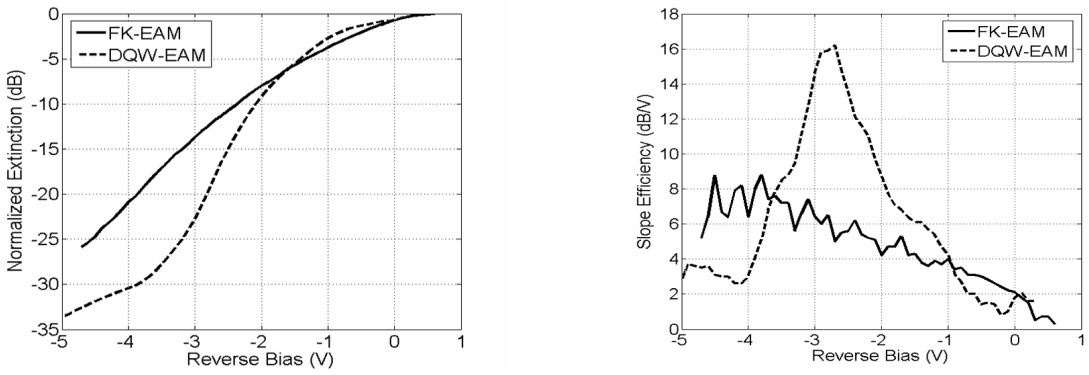

(a) (b)

Fig. 14 (a) Extinction and (b) slope efficiency versus reverse bias for 400µm long EAMs employing the FK absorption mechanism fabricated on the offset QW platform and employing the QCSE absorption mechanism fabricated using the dual QW platform.

The output tuning spectra of the transmitter, Fig. 13a, demonstrated over 40nm of continuous tuning with a side mode suppression ratio (SMSR) of > 35 dB at all wavelengths. The SG-DBR lasers demonstrated threshold currents of under 40mA with over 20 mW of output power at a gain current of 160 mA as shown in the plotted LIV of Fig. 13b. There is no significant degradation in the laser performance over that of SG-DBRs fabricated using the offset QW platform, and in fact, there is a slight enhancement in the tuning efficiency of the lasers due to the addition of the QWs in the waveguide.

The benefits offered by the dual QW platform over that of the standard offset QW can be clearly seen when comparing the efficiencies of 400µm long EAMs fabricated with each platform. In Fig. 14a, EAM extinction versus bias, and in Fig. 14b, EAM slope efficiency versus bias are presented for both bulk FK type EAMs fabricated using the offset QW method and QW EAMs fabricated using the dual QW method. The QW EAM provides up to 2.5X the efficiency than that of the FK device. Furthermore the QW EAM has an optimal operating bias regime in the 2.5 to 3.5V with respect to the extinction efficiency. The FK EAM demonstrates an increase in extinction efficiency with an increase in reverse bias. This indicates that in order to achieve maximum extinction efficiency in the EAM, high insertion losses will be suffered.

The reduced doping levels in the EAM required for optimized efficiency in the dual QW platform over that of the offset QW platform enables a significantly lowered device capacitance. In Fig. 15a, a plot of capacitance versus reverse bias is shown for 40 µm by 40µm capacitor structures fabricated from both bulk FK material and dual QW material. As can be seen from the figure, with the reduction in doping, the capacitance is decreased by a factor of 2 and depletes more rapidly with reverse bias in the QW EAM. The frequency response enhancement is shown in Fig. 15b, with a 400 µm

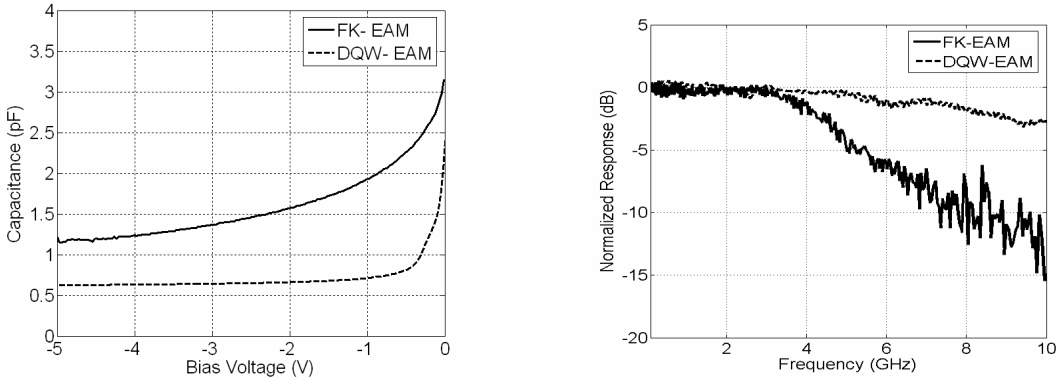

(a) (b)

Fig. 15 (a) Capacitance versus reverse bias for 40µm by 40µm capacitors fabricated from both bulk FK material and DQW material. (b) Normalized frequency response of 400µm long FK EAM and dual QW EAM.

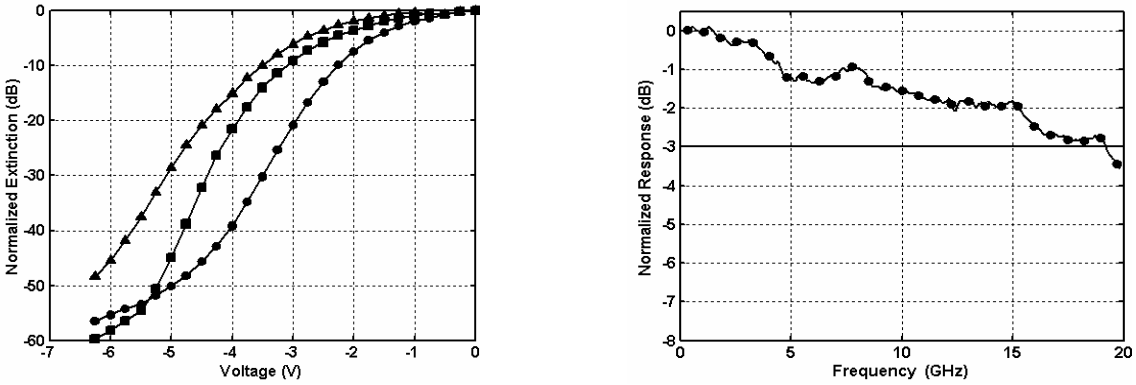

(a) (b)

Fig. 16 (a) DC Extinction of a 175 μm EAM fabricated with QWI for wavelengths of 1558 nm (circles), 1570 nm (squares), and 1580 nm (triangles). And (b) electrical to optical frequency response of the same EAM. The circular markers represent every 30th data point.

long dual QW EAM demonstrating 10 GHz of 3 dB bandwidth, which is a factor of 2 better than the FK EAM response shown on the same plot. Thus, with the dual QW platform we have demonstrated a 2X improvement in EAM efficiency and bandwidth without any degradation to the laser performance or additional fabrication steps than those associated with the offset QW platform.

6.2 SG-DBR /EAM 10 Gb/s Transmitter Fabricated with QWI

With the use of QWI, we have for the first time, fabricated a widely-tunable transmitter demonstrating negative chirp characteristics at 10 Gb/s over its entire tuning range[22] .The transmitter device consists of an SG-DBR laser followed by an EAM. The SG-DBR laser demonstrated a threshold current of 13mA, with an output power of 10mW at a gain section current of 100mA. At this operating point, a side mode suppression ratio (SMSR) greater than 35 dB was achieved. The EAM (175 μm) demonstrated over 40 dB of DC extinction for wavelengths of 1558, 1570, and 1580 nm, with efficiencies greater than 20 dB/Volt as shown in Fig. 16a. The efficient extinction properties are due to the combination of the centered quantum well design and the intermixing process that allows for precise placement of the modulator band edge. The 3dB bandwidth, shown in Fig. 16b, of the same modulator was greater than 19 GHz. Eye diagrams, shown in Fig. 17a, were taken at wavelengths of 1558 nm, 1564 nm, 1571 nm, and 1578 nm with DC biases ranging from -2.1 to -3.8 V and peak to peak voltage swings ranging from 2.2 V to 3.4 V. Greater than 10 dB extinction was achieved at all wavelengths.

Transmission experiments at 10 Gb/s were performed using a non-return to zero (NRZ) pseudo-random-bit-sequence (PRBS) of 2^{31}-1 through Corning SMF-28 fiber. BER curves through 25, 50, and 75 km of fiber at a wavelength of

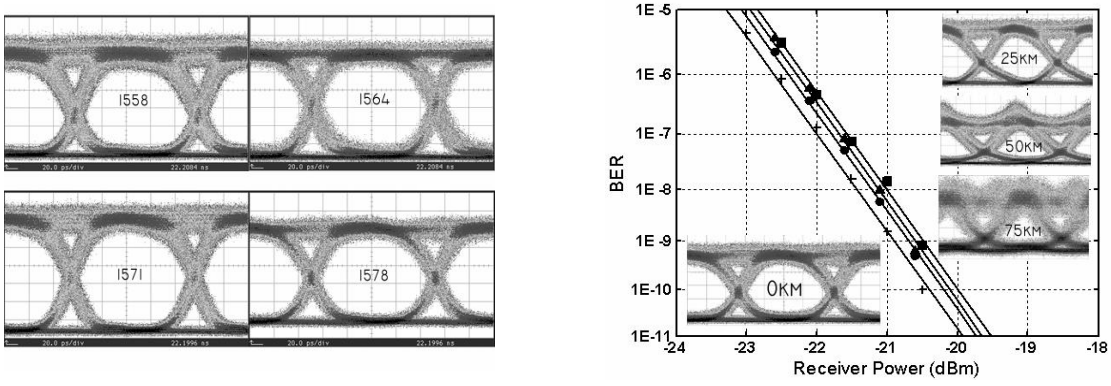

(a) (b)

Fig. 17 (a) 10Gb/s back-to-back eye diagrams from transmitter at wavelengths of 1558 nm, 1564 nm, 1571 nm, and 1578 nm and (b) BER curves/eye diagrams for back-to-back (cross), and transmission through 25 km (circles), 50 km (triangles), and 75 km (squares) of fiber.

1564 nm are shown in Fig. 17b. The EAM was biased at -3.5 V with a 2.0 V peak-to-peak swing. Error-free operation was achieved through 75km of fiber with a power penalty of less than 0.5 dB. The low power penalty transmission is indicative of negative chirp operation, which was confirmed with further testing[20]. The shaping of the eye diagrams due to dispersion is clearly seen in the insets of Fig. 17b where the optical eye diagrams are shown after transmission through fiber.

6.3 High Saturation Power SOAs and Photodiodes Fabricated with QWI and MOCVD Regrowth

The high flexibility QWI and regrowth scheme was used to fabricated high saturation power SOAs and UTC photodiodes. The processing sequence is completely compatible with that used for the fabrication of the SG-DBR/EAM transmitter presented in the previous section. The ridge waveguide SOA chips were soldered to AlN carriers, wirebonded, and placed on a copper stage cooled to 18˚C for characterization. The three characterized SOA designs used a waveguide width of 5μm. The first two designs employed single section low confinement o-MQWs with lengths of 1000μm and 1500μm and the third design used a dual section scheme containing 150μm high optical confinement c-MQW front-end followed by 1350μm of low optical confinement o-MQW. A continuous wave (CW) 1550 nm light source was fed through a polarization controller to maintain the TE polarization state and coupled into the SOA waveguide using a tapered fiber.

The chip gain versus input power and output power versus input power characteristics are shown for the three SOA types in Fig. 18a and Fig. 18b, respectively. In all figures, the operating electrode current density was 9 kA/cm^2 in the o-MQW regions and 20 kA/cm^2 in the c-MQW regions. As can be seen in the figures, a 1000μm long single section o-MQW device provides 6 dB of gain with a saturation output power of over 20 dBm while a 1500μm long single section device provides over 9 dB of chip gain with a saturation output power of 19.5 dBm. By placing a 150μm c-MQW high gain section in front of a 1350μm o-MQW section, the device gain is increased to nearly 15 dB while maintaining a saturation output power of over 19 dBm at 1550nm. Over 13.5 dB of gain was maintained for wavelengths from 1530 to 1560nm.

UTC photodiodes with a waveguide width of 3 μm and length of 25 μm employing an absorber thickness of 50nm and a collector thickness of 150nm were characterized in terms of the internal quantum efficiency, small signal response, and output eye diagrams. The internal quantum efficiency using a 1550nm CW input source was measured to be ~90% in the reverse bias range of 1-4V.

The frequency response of the photodiodes was characterized for various levels of generated photocurrent using a 20 GHz Agilent Lightwave Component Analyzer (LCA). The AlN carrier possessing a matched 50Ω load was probed with ground-signal-ground probes to extract the electrical signal from the photodiode with an effective termination load of

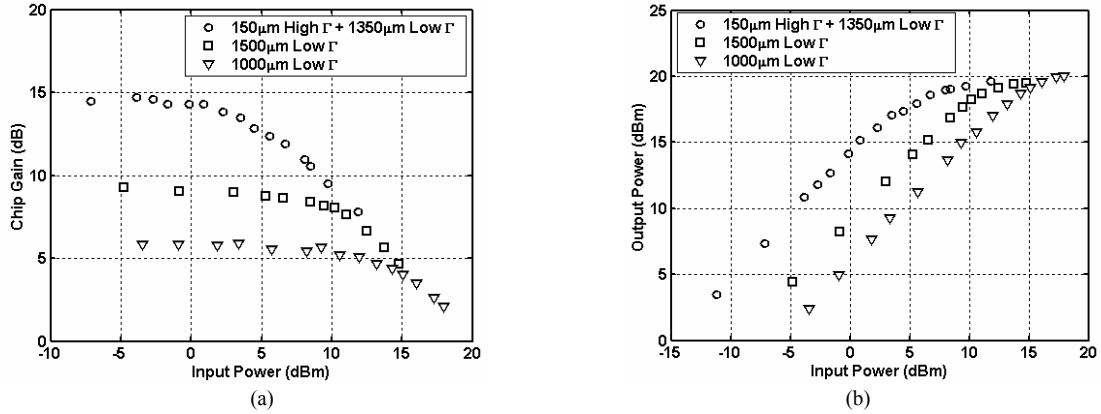

(a) (b)

Fig. 18 (a) Chip gain versus input power and (b) output power versus input power for SOA devices at 1550nm. The applied current density was 9 kA/cm^2 in the low-Γ o-MQW sections and 20 kA/cm^2 in the high-Γ c-MQW sections.

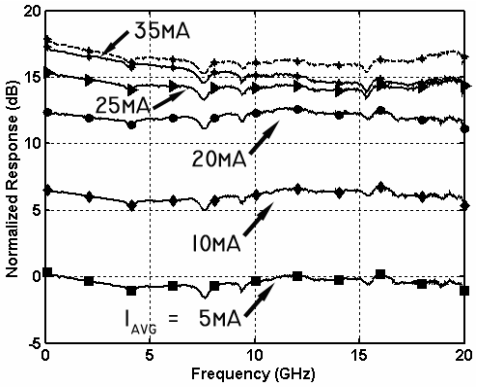

Fig. 19 Optical to electrical response of a 25μm long detector for average photocurrents of 5 (squares), 10 (diamonds), 20 (circles), 25 (triangles), and 35 mA (stars) with a 3V reverse bias and 35 mA at a –4V reverse bias (dashed line).

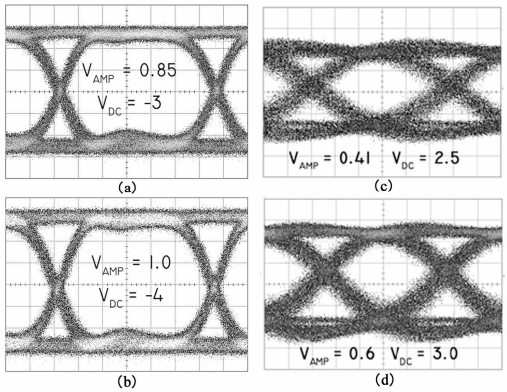

Fig. 20 (a,b) 10 Gb/s and (c,d) 40 Gb/s eye diagrams from a 3 by 25 μm^2 photodetector.

25Ω. The optical to electrical response of a 25 μm long photodiode is shown for various average detected photocurrent levels at a reverse bias of 3V in Fig. 19. The response curves are normalized to the 5mA curve such that they are easily differentiated. As can be seen in the figure, the 20 GHz response demonstrates under 0.5 dB of roll-off with average photocurrents up to 20 mA. At an average photocurrent of 25mA, the roll off is somewhat increased to 0.75 dB and at 35mA the 20 GHz roll-off is increased to slightly over 2 dB. When increasing the reverse bias to 4V at an average photocurrent of 35 mA, the roll-off is decreased to below 1dB.

In Fig. 20a and 20b we present 10 Gb/s eye diagrams taken from a 25 μm long detector at a given input power at reverse biases of 3V and 4V with an effective termination load of 25Ω. The voltage amplitude provided by the photodiode at a reverse bias of 3V was 0.85V and at a reverse bias of 4V it was 1.0V. These amplitudes are indicative of minimum peak currents of 34 and 40 mA, respectively, since the voltage drop was obtained over a 25Ω effective load. In Fig. 20c and 20d we present 40 Gb/s eye diagrams taken from a 25 μm long detector with two different input power levels at a reverse bias of 2.5V and 3.0V. The voltage amplitude of these eyes was measured at 0.41V and 0.6V. As can be seen from the figure, the eye diagrams are open and clear. The 0.6V amplitude provided by the photodiode at 3V is indicative of a minimum peak current of 24mA in the photodiode.

7 CONCLUSION

The monolithic integration of optoelectronic components supporting modern day communication systems will provide solutions at low cost with a reduction of space requirements and device power dissipation. However, as the functionality of the PIC is increased, the challenge of realizing a high performance integrated circuit is great due to the unique characteristics required by the individual components for optimum performance. To meet the increasing performance demands placed upon the PICs, novel integration platforms must be developed such that the design space is increased without significant increase in processing and growth requirements that can raise cost and lower yields.

In this manuscript we have presented two viable integration technologies, which provide the foundation for the monolithic integration of QW EAMs with widely tunable SG-DBR lasers. By growing a blue-shifted MQW in the bulk waveguide below the active MQW in the base structure, etching the active MQW in regions where gain is not required and performing a regrowth of the upper cladding, the dual QW platform requires the same simple processing/growth steps as the well-established offset QW platform with the added flexibility of a second MQW bandedge. By using our implant enhanced QWI scheme, any number of MQW band-edges can be realized on the same chip for the fabrication of high-functionality PICs. Furthermore, this method enables the use of a centered MQW active region for maximized modal gain lasers. Through the use of QWI, we have demonstrated the first widely-tunable negative chirp EAM based transmitter.

Building off these foundational platforms for the integration of lasers and QW EAMs, further techniques were demonstrated as a means for the integration of enhanced performance SOAs and photodiodes. Simple waveguide flares and tapers were shown to increase the 1 dB compressed output power of SOAs by 3-4X up to the 16 dBm range and increase the photocurrent handling capabilities of the integrated QW p-i-n photodetectors by over 50%. These flare/taper techniques were employed in a photoreceiver that was monolithically integrated with a widely-tunable SG-DBR/QW EAM transmitter using the dual QW platform for the realization of a 10 Gb/s PD-WC[33]. The transmitters simultaneously demonstrated high output powers, high side-mode suppression, and wide-tunability. The integrated QW EAMs possessed over 2X the efficiency and bandwidth of equal length FK devices fabricated on the offset QW platform.

For further increased SOA and photodetector performance we have developed a novel QWI and MOCVD regrowth scheme for the integration of low optical confinement factor SOAs and UTC photodiodes with high gain lasers and QW EAMs. Using this scheme, SOAs were fabricated that facilitate saturation output powers in the 19-20 dBm range while providing ~15 dB of gain. The fabricated UTC photodiodes showed excellent photocurrent handling capabilities with a 25 μm by 3 μm detector demonstrating only minimal bandwidth degradation out to 20 GHz while driving 35 mA of average photocurrent. As these components have been developed using processing and growth schemes completely compatible with that of the SG-DBR/QW EAM transmitter, current work is focused on the integration of widely-tunable SG-DBR lasers, negative chirp QW EAMs, high saturation power SOAs, and high saturation power UTC photodiodes.

8 REFERENCES

[1] G. P. Agrawal, Fiber Optic Communication Systems, New York: John Wiley & Sons, Inc., 1997, pp. 3-7.

[2] M. Hatcher and M. Libby, "Foundry model could be key to InP industry future," *Compound Semiconductor,* Vol. 11 no. 7 pp17-19. Aug. 2005.

[3] M. Sysak, J. Barton, L. Johansson, J. Raring, E. Skogen, M. Mašanović, D. Blumenthal, and L. Coldren, "Single Chip Wavelength Conversion using a Photocurrent Driven (PD) EA Modulator integrated with a Widely Tunable Sampled Grating DBR (SGDBR) Laser," IEEE Photon. Technol. Lett., vol. 16, pp. 2093-2095, 2004.

[4] J. Raring, E. Skogen, L. Johansson, M. Sysak, J. Barton, Milan L. Mašanović, and L. Coldren, "Quantum Well Intermixing for Monolithic Integration: A Demonstration of Novel Widely-Tunable 10Gb/s Transmitters and Wavelength Converters," Integrated Photonics Research Conf., San Francisco 2004.

[5] E. Skogen, J. Raring, J. Barton, S. DenBaars, and L. Coldren, "Post-Growth Control of the Quantum-Well Band Edge for the Monolithic Integration of Widely-Tunable Lasers and Electroabsorption Modulators," IEEE J. Sel. Topics in Quantum Electron., vol. 9, pp. 1183-1190, September/October.

[6] K. Morito, S. Tanaka, S. Tomabechi, and A. Kuramata, "A broadband MQW semiconductor optical amplifier with high saturation output power and low noise figure". Semiconductor Optical Amplifiers and their Applications Meeting. PD1-1. San Francisco, CA June 30 2004

[7] T. Ishibashi, T. Furuta, H. Fushimi, and H. Ito, "Photoresponse characteristics of uni-traveling-carrier photodiodes" Invited paper. Proceedings of SPIE Vol. 4283 (2001).

[8] J. Binsma, P. Thijs, T. VanDongen, E. Jansen, A. Staring, G. VanDenHoven, and L. Tiemeijer, "Characterization of Butt-Joint InGaAsP Waveguides and Their Application to 1310 nm DBR-Type MQW Ganin-Clamped Semiconductor Optical Amplifiers," IEICE Trans. Electron., vol. E80-C, pp. 675-681, 1997.

[9] M. Aoki, M. Suzuki, H. Sano, T. Kawano, T. Ido, T. Taniwatari, K. Uomi, and A. Takai, "InGaAs/InGaAsP MQW Electroabsorption Mofulator Integrated with a DFB Laser Fabricated by Band-Gap Energy Control Selective Area MOCVD," IEEE J Quantum Electron., vol. 29, pp. 2088-2096, 1993.

[10] B. Mason, G. Fish, S. DenBaars, and L. Coldren, "Ridge Waveguide Sampled Grating DBR Lasers with 22-nm Quasi-Continuous Tuning Range," IEEE Photon. Technol. Lett., vol. 10, pp. 1211-1213, 1998.

[11] M.K. Chin, "Comparative Analysis of the performance analysis of Franz Keldysh effect and quantum confined stark effect electroabsorption waveguide modulators," IEE Proc. Optoelectron, vol. 142, pp. no. 2. pp. 109-114. 1995

[12] B. Mason, G. Fish, S. DenBaars, and L. Coldren, "Widely Tunable Sampled Grating DBR Lasers with Integrated Electroabsorption Modulator," IEEE Photon. Technol. Lett., vol. 11, pp. 638-640, 1999.

[13] B. Mason, J. Barton, G. Fish, and L. Coldren, "Design of Sampled Grating DBR Lasers with Integrated Semiconductor Optical Amplifiers," IEEE Photon. Technol. Lett., vol. 12, pp. 762-764, 2000.

[14] J. Barton, M. Mašanovic, E. Skogen, and L. Coldren, "Widely-Tunable High-Speed Transmitters Using Integrated SGDBRs and Mach-Zehnder Modulators," IEEE J. Sel. Topics in Quantum Electron., vol. 9, pp. 1113-1117, September/October, 2003.

[15] A. Tauke-Pedretti, M. Dummer, J.S. Barton, M.N. Sysak, J.W. Raring, and L.A. Coldren, "High Saturation Power and High Gain Integrated Photoreceivers," IEEE Photon. Technol. Lett., vol. 17, pp. 2167-2169, 2005.

[16] J.S. Barton, A. Tauke-Pedretti, M. Dummer, M.N. Sysak, M.L. Mašanović, J.W. Raring, E.J. Skogen, and L.A. Coldren, "10Gbit/s Wavelength Conversion Using a Widely-Tunable Series Push-Pull Photocurrent-Driven Transmitter," IEEE Photon. Technol. Lett., vol. 17, pp. 1902-1904, 2005.

[17] S. McDougall, O. Kowalski, C. Hamilton, F. Camacho, B. Qiu, M. Ke, R. De La Rue, A. Bryce, and J. Marsh, "Monolithic Integration via a Universal Damage Enhanced Quantum-Well Intermixing Technique," IEEE J. Sel. Topics in Quantum Electron., vol. 4, pp. 636-646, 1998.

[18] S. Charbonneau, E. Kotels, P. Poole, J. He, G. Aers, J. Haysom, M. Buchanan, Y. Feng, A. Delage, F. Yang, M. Davies, R. Goldberg, P. Piva, and I. Mitchell, "Photonic Integrated Circuits Fabricated Using Ion Implantation," IEEE J. Sel. Topics in Quantum Electron., vol. 4, pp. 772-793, 1998.
[19] D. Hofstetter, B. Maisenholder, and H. Zappe, "Quantum-Well Intermixing for Fabrication of Lasers and Photonic Integrated Circutis," IEEE J. Sel. Topics in Quantum Electron., vol. 4, pp. 794-802, 1998.
[20] G. B. Morrison, J.W. Raring, E.J. Skogen, C.S. Wang, and L.A. Coldren, Photocurrent Spectroscopy Analysis of Widely Tunable Negative-Chirp Quantum Well Intermixed Laser-Modulator Transmitters. Applied Physics Letts. vol. 86, Feb, 2005.
[21] C. Wang, E. Skogen, J. Raring, G. Morrison, and L. Coldren, "Short-Cavity 1.55μm DBR Lasers Integrated with High-Speed EAM Modulators," Proc. IEEE International Semiconductor Laser Conf., paper no. WB1, Matsue-shi, Japan (Sept. 21-25, 2004).
[22] J. Raring, E. Skogen, L. Johansson, M. Sysak, S. Denbaars, and L. Coldren: " Widely-Tunable Negative-Chirp SG-DBR Laser/EA-Modulated Transmitter", IEEE Journal of Lightwave Technology. vol. 23 no.1, pp. 80-86, Jan. 2005
[23] V. Lal, M. L. Masanovic, E. J. Skogen, J. W. Raring, J. A. Summers, L. A. Coldren, and D. J. Blumenthal, "Quantum Well Intermixed Monolithically-Integrated Widely-Tunable All-Optical Wavelength Converter Operating at 10Gbps Across the C-band," IEEE Photon. Technol. Lett., vol. 17, pp. 1689-1691, 2005.
[24] E. Skogen, J. Raring, G. Morrison, C. Wang, V. Lal, M. Masonovic, and L. Coldren, "Monolithically Integrated Active Components: A Quantum Well Intermixing Approach," IEEE J. Sel. Topics in Quantum Electron., vol. 11, pp. 343-355, March/April, 2005
[25] L. Coldren, and S. Corzine, Diode Lasers and Photonic Integrated Circuits, New York: John Wiley & Sons, Inc., 1995, pp. 456.
[26] S. Demiguel, L. Giraudet, L. Joulaud, J. Decobert, F. Blache, V. Coupe, F. Jorge. P. Pagnod-Rosiaux, E. Boucherez, F. Devaux. "Evanescently Coupled Photodiodes Integrating a Double Stage Taper for 40Gb/s Applications – Compared Performance With Side-Illuminated Photodiodes" IEEE J. Lightwave Technol.., vol. 20, no. 12, pp. 2004 2014. Dec. 2002.
[27] T. W. Berg and J. Mork, "Saturation and Noise Properties of Quantum-Dot Optical Amplifiers" .IEEE J. Quantum Electronics. Vol. 40 NO. 11, November 2004.
[28] P. W. Juodawlkis, J. J. Plant, R. K. Huang, L. J Missaggia, and J. P. "High Power 1.5μm InGaAsP-InP Slab-Coupled Optical Waveguide Amplifier," IEEE Photon. Technol. Letts. vol. 17, Feb, 2005.
[29] T H. Wood, J. Z. Pastalan, C. A. Burrus, Jr., B. C. Johnson, B. I. Miller, J. L. deMiguel, U. Koren, and M. G. Young "Electric field screening by photogenerated holes in multiple quantum wells: A new mechanism for absorption saturation" Applied Physics Letts. vol. 57, no. 11, pp. 1081-1083 Sept. 1990.
[30] E. Skogen, J. Raring, S. DenBaars, and L. Coldren, "Integration of High-Gain and High-Saturation Power Active Regions using Quantum Well Intermixing and Offset-Quantum Well Regrowth," Electron. Lett., Vol. 40, pp. 993-94, 2004.
[31] J. Raring, E. Skogen, S. Denbaars, and L. Coldren: "A Study of Regrowth Interface and Material Quality for a Novel InP Based Architecture," Journal of Crystal Growth. vol. 273/1-2 pp. 26-37 Dec. 2004
[32] J. S. Barton, A. Tauke-Pedretti, M. Dummer, M. N. Sysak, J. W. Raring, L. A. Coldren, "Field modulated wavelength conversion , *Invited,* 6124 -42. San Jose, CA, January 21-26, 2006

Design and Demonstration of Novel QW Intermixing Scheme for the Integration of UTC-Type Photodiodes With QW-Based Components

James W. Raring, *Student Member, IEEE*, Erik J. Skogen, *Member, IEEE*, Chad S. Wang, *Student Member, IEEE*, Jonathon S. Barton, *Member, IEEE*, Gordon B. Morrison, Stephane Demiguel, *Member, IEEE*, Steven P. DenBaars, *Member, IEEE*, and Larry A. Coldren, *Fellow, IEEE*

***Abstract*—We present the design and demonstration of unitraveling carrier (UTC) photodiodes fabricated using a novel quantum-well (QW) intermixing and metal–organic chemical vapor deposition (MOCVD) regrowth fabrication platform. The photodiodes discussed here were realized on the same chip as high gain centered QW active regions, intermixed passive centered well waveguides, and low optical confinement offset QW active regions regrown over intermixed wells. This demonstration lifts previous constraints imposed on high functionality photonic circuits, which forced a common waveguide architecture in the detector, laser, and amplifier by validating a platform suited for the monolithic integration of UTC photodiodes into photonic integrated circuits comprised of widely tunable high gain laser diodes, high efficiency modulators, and low optical confinement high saturation power semiconductor optical amplifiers. In this manuscript we focus on the design and performance of UTC photodiodes fabricated on intermixed QWs using this novel scheme. The photodiodes exhibit ∼90% internal quantum efficiency, excellent photocurrent handling capabilities, and minimal response roll-off over the 20 GHz of our testing capability. The 40 Gb/s operation was achieved with the demonstration of open eye diagrams.**

***Index Terms*—Electro-absorption modulators, metal–organic chemical vapor deposition (MOCVD), monolithic integration, quantum-well intermixing (QWI), semiconductor lasers, semiconductor optical amplifier (SOA), unitraveling carrier (UTC) photodiodes.**

I. Introduction

A. Photodiodes

FUNCTIONING to convert signals from the optical to the electrical domain, photodiodes are the core element of optical receivers and are thus key components in optical networks. In conventional receivers, the photodetector is followed by a transimpedence electrical amplifier for signal amplification. The sensitivity of this configuration is limited by the front-end noise of the electrical amplifier. The emergence of fiber amplifiers and the development of semiconductor amplifiers for pre-detection amplification has enabled the realization of significantly higher signal-to-noise ratios [1]. In this configuration, the demands on the photodetector are drastically increased since they are forced to handle the higher photocurrents generated in the detectors with the larger incident optical powers. It is essential that the detectors maintain high speed and high efficiency operation at high power levels.

High-speed high-efficiency p-i-n photodiodes have been developed with the use of a side illuminated waveguide structure and traveling wave electrodes [2]. However, the photocurrent handling capabilities of this type of photodetector is intrinsically limited for two reasons. Saturation in a p-i-n photodetector can be explained by the classic space charge effect, which is a result of the slow escape time of holes from the absorbing layer. The spatial distribution of photogenerated carriers in the absorbing medium effectively reduces the applied electric field due to screening effects. Once the field drops below a critical value, the holes can no longer maintain their saturation velocity and the power in versus power out response of the device begins to roll-off. The second source of low saturation current densities in side-illuminated p-i-n detectors is the nonuniform generation of carriers along the length of the detector. The exponential absorption profile leads to significantly greater current densities at the front-end of the diode, and thus degrades the overall performance of the detector. However, this front-end saturation can be greatly reduced without altering the internal physics within the photodetector by evanescently coupling the optical power from the core waveguide into the absorbing layer [2].

The unitraveling carrier (UTC) photodiode has been designed specifically to circumvent the influence of hole transport on the performance of the detector by making the total charge transit time heavily dominated by electrons. The theory outlined in [3] offers an expression for carrier transport times entirely governed by electrons. Since the overshoot velocity of electrons is an order of magnitude higher than the saturation velocity of holes, the UTC can achieve saturation current densities four to six times higher than that in p-i-n photodiodes [3]. Due to the superior photocurrent handling capabilities, the UTC photodiode has received a great deal of recent attention. The theory of operation and demonstration of such photodiodes have been extensively reported [3], [4]. As the technology has matured over

Manuscript received June 28, 2005; revised September 19, 2005.

J. W. Raring, C. S. Wang, J. S. Barton, and S. P. DenBaars are with the Materials Department, University of California, Santa Barbara, CA 93106 USA (e-mail: jraring@engineering.ucsb.edu; cswang@engineering.ucsb.edu; jsbarton@engineering.ucsb.edu; denbaars@engineering.ucsb.edu).

E. J. Skogen is with the Sandia National Laboratories, Albuquerque, NM 87123 USA (e-mail: ejskoge@sandia.gov).

G. B. Morrison is with ThreeFive Photonics, 3994 DB Houten, The Netherlands.

S. Demiguel is with the University of Texas at Austin, Austin, TX 78758 USA (e-mail: stephane_demiguel@yahoo.com).

L. A. Coldren are with the Electrical and Computer Engineering Department, University of California, Santa Barbara, CA 93106 USA (e-mail: tallest_dwarf@hotmail.com; coldren@ece.ucsb.edu).

Digital Object Identifier 10.1109/JQE.2005.862030

the past several years, further advances have been made such as charge compensated UTCs and most recently, nearly ballistic UTCs [4], [5]. To the best of our knowledge, there have been no reports presenting a UTC photodiode fabricated using an integration platform specifically designed for extremely high functionality monolithic integration. Previous reports have focused on discrete UTC photodiodes or photodiodes integrated with one other active component such as a modulator [6].

B. Monolithic Integration

Monolithic integration of photonic circuits offers tremendous advantages in optical network applications such as high functionality, improved efficiency, decreased size, and lower costs. As the functionality demands on photonic integrated circuits (PIC) continues to increase, the circuits will inevitably require higher levels of integration complexity. With this complexity, the realization of an optimally performing device becomes a far more arduous task due to the design constraints often imposed by monolithic integration.

There are several examples of high functionality PICs in which a photodiode must be monolithically integrated with other active components such as semiconductor optical amplifiers (SOA), the widely tunable sampled-grating DBR laser (SG-DBR), and quantum-well (QW) electroabsorption modulators (EAM). Photocurrent-driven wavelength converters (PD-WC) and transceivers are two such examples, as these devices will facilitate enabling technologies such as dynamic provisioning and wavelength routing [7].

The PD-WC is a particularly challenging device since the individual components necessitate unique waveguide architectures for optimum performance. Low threshold, high efficiency lasers require high optical confinement QW active region architecture for maximized modal gain. Integrated QW EAMs necessitate a QW band-edge that is blue-shifted from that of the laser or SOA operation wavelength for reasonable insertion loss/extinction properties. State of the art SOA's employ a low optical confinement QW active region architecture such that the photon density over the active QWs can be kept low and high saturation powers can be achieved [8]. Finally, as discussed above, a photodiode designed for high photocurrent/high speed operation should employ a unique internal structure such as the UTC-type photodiode, which mitigates the saturation effects induced by hole transport and/or employs a waveguide architecture designed to minimize front-end saturation.

Conventional fabrication schemes offer little flexibility in the cross-sectional waveguide architectures within the individual components of highly complex devices such as single-chip PD-WCs. This has resulted in individual components sharing the same waveguide architecture such as a common QW stack in the laser, SOA, and photodetector, ultimately limiting the device performance as reported in [9]. Thus, a key challenge of the PIC designer has been to allocate the tradeoffs in such a way that the overall performance of the device is sufficient for the intended application.

C. Integration Technology

With the growing performance demands and increasing data rates of PICs, the design space will be exhausted on conventional integration platforms and next generation platforms will be essential. Various methods for manipulating the material properties to achieve multiple QW band edges within a single PIC have been reported such as butt-joint growth, selective area growth (SAG), and QW intermixing (QWI) [10]–[12]. In the butt-joint scheme, the optical waveguide is selectively removed in regions where a different band-edge material or alternative waveguide structure is desired. This is followed by a nonplanar regrowth in which the alternative desired material is deposited. The difficulty with this scheme resides in the high degree of thickness and material composition matching required at the waveguide interfaces such that reflections and loss are minimized [10]. In SAG, a carefully designed dielectric mask is defined on the sample prior to growth such that the growth rate and hence the QW band-edge adjacent to the mask is controlled. Since this technique exploits the contrast in surface kinetics of the growth constituents on the semiconductor and dielectric, a high degree of calibration/optimization is required to tightly control the reactor conditions. The abruptness of the transition regions is limited by the surface diffusion length of the growth constituents, which may be on the order of tens of microns. Additionally, the optical mode overlap with the mulitple QW (MQW) may not be ideal in all sections due to the thickness variation [11].

Here we use a simple and robust QWI method to precisely control the QW band-edge orthogonal to the growth direction without any disruption of the waveguide in the axial direction. In the QWI process detailed in [12], point defects are created by ion implantation into an InP buffer layer over the MQW active region. During a high temperature anneal, the point defects are diffused through the MQW region, promoting the interdiffusion of group V-atoms between the wells and barriers. The interdiffusion reshapes the QW profile by distorting the QW–barrier interface. The result is a shift in the quantized energy levels in the well, and hence a shift in the band edge energy. Following the QWI process, we use MOCVD regrowth to realize unique waveguide architectures such as low optical confinement QW active regions and UTC photodiode structures. The blanket regrowth performed here is relatively straightforward and does not require the additional growth precision necessary for butt-joint growth or sample patterning in SAG [13].

In previous work, we have demonstrated viable 10 Gb/s, high efficiency, negative-chirp, widely tunable SG-DBR/EAM transmitters employing a high optical confinement centered MQW (c-MQW) active region fabricated using our simple and robust QWI process [14]. In [13] we propose and demonstrate the proof of concept for a novel QWI and MOCVD regrowth scheme for the integration of low confinement/high saturation power offset MQW (o-MQW) active regions on the same chip as the high optical confinement c-MQW active regions used in the SG-DBR/EAM transmitters. In this work, we expand on the integration scheme with the design and demonstration of UTC type photodiodes realized on the same chip as both high optical confinement c-MQWs for use in high gain lasers or high gain SOA sections, low optical confinement o-MQWs for use in high saturation power SOA sections, and intermixed c-MQW sections for low loss passive waveguides. With the successful placement of these three unique waveguide architectures on a

TABLE I
EPTIAXIAL STRUCTURE EMPLOYED IN UTC REGION (Absorber thickness = WA, Collector thickness = WC)

Layer	*Material*	*Thick (nm)*	*Doping (cm^{-3})*	*Function*
1.	InGaAs:Zn	100	5E19	p-Contact Layer
2.	InP:Zn	1700	5E17-1E18	p-Clad
3.	InGaAs:Zn	WA	2E18	Absorber
4.	InGaAs	8	NID	Cond. Band Smooth
5.	1.24Q	16	NID	Cond. Band Smooth
6.	InP	6	NID	Cond. Band Smooth
7.	InP:Si	7	1E18	Cond. Band Smooth
8.	InP	WC	NID	Collector
9.	InP:Si	30	1E18	Subcollector
10.	1.3Q:Si	15	2E17	Etch Stop
11.	InP:Si	25	8E16	Regrowth Layer
12.	1.3Q:Si	105	5E16	Waveguide
13.	QWI cMQW	153	NID	Waveguide
14.	1.3Q:Si	105	1E17	Waveguide
15.	InP:Si	2000	1E18	n-Clad

single chip and since the definition of widely tunable lasers and QW EAMs only requires the addition of two processing steps to define mirror gratings and an intermediate EAM band-edge, the QWI/MOCVD based processing/growth scheme is completely suited UTC photodiode integration with the previously reported high performance SG-DBR/EAM transmitters. Here we focus on UTC type photodiodes fabricated on top of intermixed QWs, which exhibited high quantum efficiency, excellent photocurrent handling capabilities, minimal response roll-off over the 20 GHz of our testing capability, and open eye diagrams at 40 Gb/s.

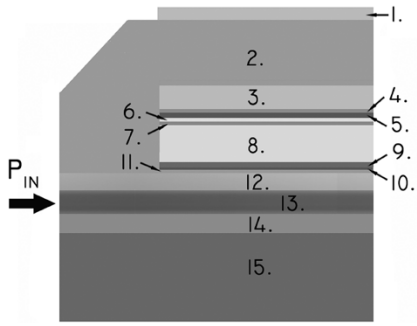

Fig. 1. Side view schematic of UTC structure grown above intermixed QWs.

II. PHOTODIODE DESIGN

By using QWI to render the as-grown base structure QWs transparent, performing an MOCVD regrowth of the appropriate photodiode epitaxial structure, and then using wet chemical selective etching, we demonstrate the first photodetectors fabricated on top of QWI material. The benefits of this photodiode structure over the alternative of using the as-grown c-MQW stack as a p-i-n photodiode are three-fold. First, the use of QWs, which act as potential barriers and hinder carrier escape, can be avoided in the absorber region. Second, since the waveguide core composed of intermixed QWs is set below the absorbing region of the UTC, the absorption profile along the photodiode can be carefully controlled through the choice of collector and absorber layer thicknesses for maximized photocarrier generation uniformity. Finally, since the regrowth of the detector structure is independent of all other components, there are no design constraints on the choice of internal layer structure. With this flexibility, we employ a UTC photodiode structure for its established superior photocurrent handling capabilities [3], [4], [15]. By avoiding the classic space charge saturation effects that plague p-i-n photodiodes, higher saturation current densities are possible allowing for smaller diode areas and hence higher bandwidths. Furthermore, the processing and growth sequence for the integrated UTC structure offers no further difficulty over that of an integrated p-i-n structure, indicating no increase in manufacturing costs.

The epitaxial structure employed in the UTC portion of the device is shown in Fig. 1 with the corresponding layer specifications presented in Table I. The structure was based on that presented in [15] by Ishibashi *et al.* with a few modifications necessary to accommodate our integration scheme. The active layers of the UTC are the neutral InGaAs:Zn absorption layer (#3) and the depleted wide bandgap InP electron collection layer (#8). Under normal operation of the photodiode, carriers are photogenerated in the absorber layer. The minority carriers, electrons, diffuse toward the collector layer where they accelerate to their overshoot velocity and drift across the collector layer. The escape time of the majority carriers, holes, from the absorption layer is negligible since it is set by their dielectric relaxation time [3]. Thus, the carrier transport properties are governed solely by electron transport and the classic space charge effect associated with p-i-n photodiodes is avoided.

The nonbiased band diagram for our proposed structure was simulated with SimWindows software and is shown in Fig. 2. Layers 4–7 function to smooth conduction band discontinuities at the heterointerface and remove potential barriers that could impede electron transport as described in [15]. The most notable differences in our structure compared to that of [15] are the upper p-InP clad (#2), the 1.3Q:Si stop etch (#10), and the intermixed c-MQW region below (#12–14). The use of p-InP cladding above the absorber has been previously employed with no reported performance degradation resulting from hindered carrier transport [4]. The conduction band discontinuities imposed by the 1.3Q:Si stop etch layer between the InP:Si subcollector and InP:Si regrowth layer should not impede the carrier transport properties since at this position electrons should be

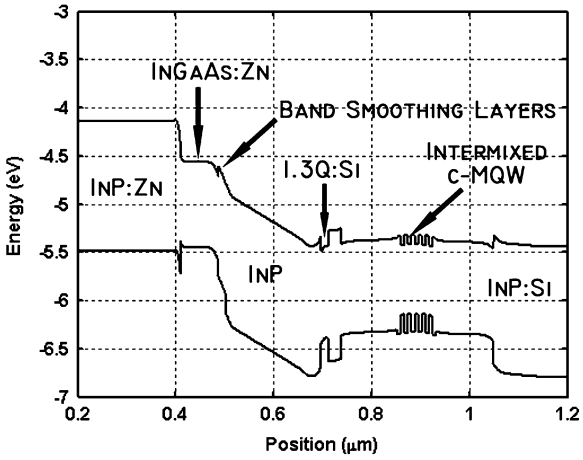

Fig. 2. Simulated 0-V band diagram for our proposed integrated UTC structure.

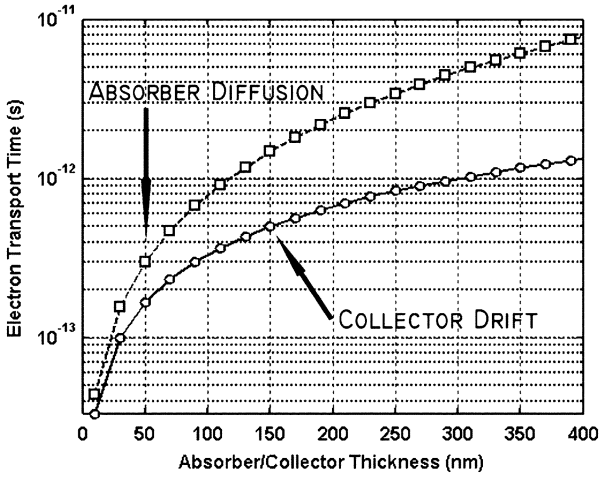

Fig. 3. Calculated electron transport time across collector (circles) and absorber (squares) using (1) and (2), an electron diffusivity of 86 cm^2/s, and carrier velocities given in [3].

collected and governed by majority carrier transport. The thick (1.7 μm) p-cladding and the intermixed active region present in our UTC structure are necessary for the high functionality integration scheme and are expected to result in a somewhat higher series resistance compared to widely reported discrete UTC photodiodes.

III. Photodiode Optimization

In the proposed integrated UTC photodiode structure we must consider the effects imposed by the thickness of the absorber and collector regions on the quantum efficiency, bandwidth, and photocurrent handling capabilities. As discussed above, the total carrier transport time in a UTC photodiode is comprised of two components. Electron drift across the collector and electron diffusion across the absorber. Using the theory outlined in [3], the drift dependent electron transport time from the collector region of the UTC photodiode can be given by (1) and the diffusion time across the absorber by (2). In these expressions, W_C is the collector thickness, W_A is the absorber thickness, $V_e^{\rm os}$ is the electron over shoot velocity in InP, $V_{\rm th}$ is the thermionic emission velocity of electrons in InGaAs, and D_e is the electron diffusivity of electrons in p-InGaAs. Using carrier velocities given in [3] and an electron diffusivity of 86 cm^2/s extracted in [16], we plot the calculated transport times for electrons across the absorber and collector for various layer thicknesses in Fig. 3. As can be seen in the figure, for absorber layer thicknesses greater than 100 nm, the diffusion transport time will dominate the total transport time for reasonable collector thickness of over 100 nm

$$\tau_C = W_C/V_e^{\rm os} \tag{1}$$

$$\tau_A = W_A^2/3D_e + W_A/V_{\rm th}. \tag{2}$$

One key benefit to waveguide photodiodes is that the internal quantum efficiency can be much higher than in typical surface illuminated photodiodes [17]. This is easily explained by the differences in the absorption path for the two photodiode geometries. The total detector absorption can be approximated by an exponential decay governed by the product of the material absorption coefficient (α), the optical confinement (Γ) in the absorber layer, and the dimension (L) of the absorption layer normal to optical incidence. In a conventional waveguide photodiode, optical absorption occurs parallel to the growth plane, such that the absorption length (L) is set by the length of the photodiode, which is usually on the order of tens of microns. In a surface illuminated device, absorption occurs normal to the growth direction such that the absorption length (L) is set by the absorber layer thickness, which is usually on the order of 200–500 nm. Although Γ can be close to unity in a surface normal device compared to typical values of 0.1–0.4 for a waveguide device, the extreme contrast in absorption lengths results in higher internal quantum efficiencies for a waveguide photodiode. Using $\alpha = 6800$ cm^{-1} for InGaAs at a wavelength of 1550 nm, $L = 500$ nm and $\Lambda = 1$ for a surface-normal photodiode, the internal efficiency of the device is estimated at 29%. However, for a waveguide photodiode, if we assume an identical absorption coefficient, $L = 25$ μm, and $\Gamma = 0.2$, an internal efficiency of 96% is estimated. With this flexibility in our waveguide photodiode, we choose an absorber thickness of 50 nm such that the electron diffusion component of the carrier transport time is expected to be less than the drift time for collector thicknesses greater than 100 nm as shown in Fig. 3.

In order to study the absorption characteristics, photocurrent generation, and internal quantum efficiency characteristics of the photodiodes, beam propagation simulations were performed using commercially available software from RSoft. The simulations were performed by exciting the fundamental mode of the passive sections comprised of an intermixed c-MQW waveguide. The mode was propagated through a short 5-μm section of lossless passive waveguide before entering the detector region such that the theoretical internal quantum efficiency could be computed most accurately. The simulated absorption profile for our integrated UTC structure with varying collector thicknesses along with that expected in a p-i-n detector formed from the as-grown c-MQW stack consisting of ten 6.5-nm wells is shown in Fig. 4. The loss values of 6800 cm^{-1} used for the InGaAs:Zn and 5000 cm^{-1} used for the p-i-n QWs was extracted experimentally with photocurrent spectroscopy. The three collector thicknesses used in the simulation were 150 (squares), 200 (triangles), and 250 nm (circles) with an absorber thickness

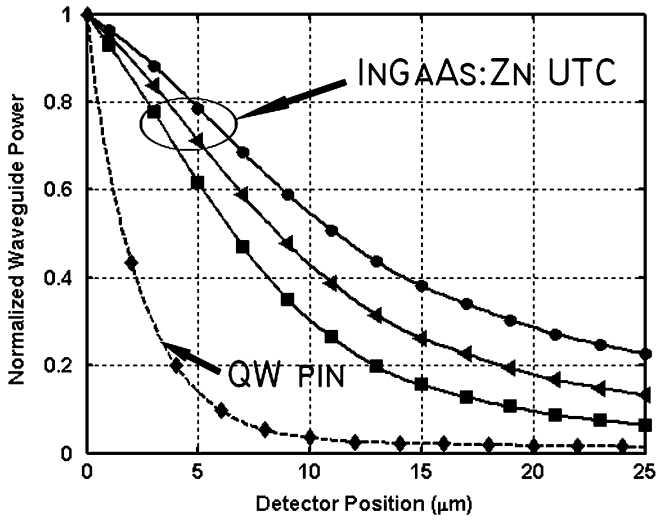

Fig. 4. Simulated waveguide power along photodetector for a QW p-i-n (dashed line) and UTC photodiodes (solid lines). The simulations use a 50-nm-thick absorber and collector thicknesses of 100 (squares), 150 (triangles), and 200 nm (circles).

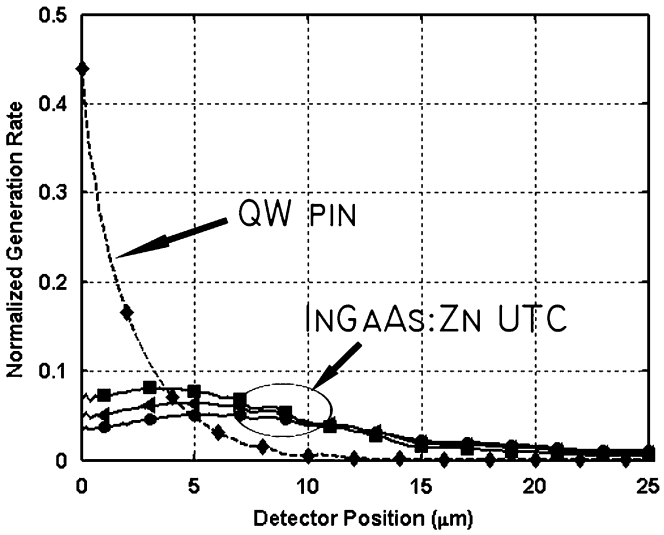

Fig. 5. Simulated generation rate along detector for a QW p-i-n (dashed line) and UTC photodiode (solid lines). The simulations use a 50 nm thick absorber and collector thicknesses of 100 (squares), 150 (triangles), and 200 nm (circles).

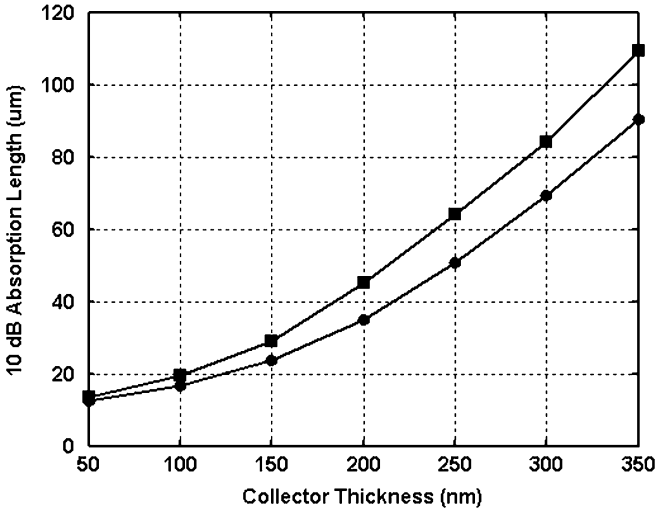

Fig. 6. Simulated 10-dB absorption length versus collector thickness for photodiodes with absorber region thicknesses of 50 (squares) and 100 nm (circles).

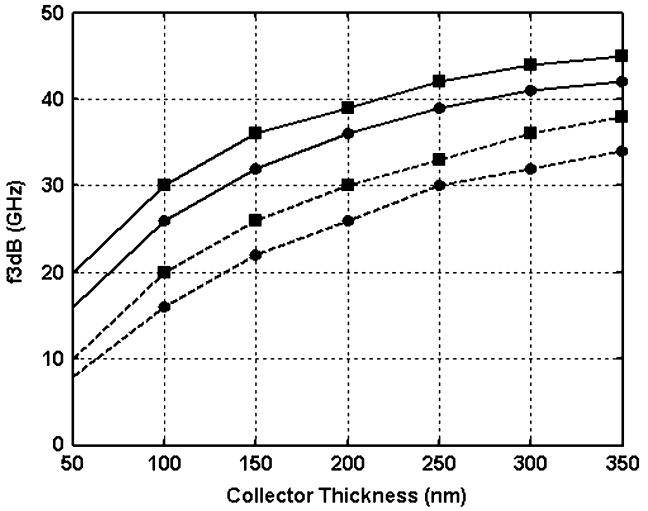

Fig. 7. Simulated *RC* limited 3-dB bandwidth of UTC photodiodes with lengths of 25 (solid lines) and 50 μm (dashed lines) for series resistance values of 30 (squares) and 40 Ω (circles) and effective termination of 25 Ω.

of 50 nm. As shown in Fig. 4, with proper design the absorption profile can be tuned in the UTC device to take on a more linear shape opposed to the fixed steep exponential profile exhibited by the QW-p-i-n. This feature of the integrated UTC structure enables the control over the generation profile since this profile is governed by the slope of the absorption profile. The normalized generation rates along the detector lengths resulting from the absorption profiles are shown in Fig. 4. The UTC type detectors demonstrate a radically more uniform generation rate along the length of the device than does the c-MQW p-i-n detector, with an $\sim 8\times$ reduction in front end photocurrent generation. This implies that the front-end saturation characteristics plaguing traditional waveguide photodiodes can be avoided using the regrowth scheme.

In Fig. 5 it is clear that the generation rate in the UTC is significantly influenced by the collector thickness, which implies an effect on the device quantum efficiency. Since the collector thickness is inversely proportional to the junction capacitance of the device, the tradeoff between projected internal quantum efficiency and 3-dB bandwidth should be characterized. Fig. 6 plots the simulated 10-dB absorption length versus collector thickness for absorber thicknesses of 50 and 100 nm. From this figure, it is apparent that for collector thicknesses over 150 nm, the diode length required for 90% internal quantum efficiency begins to rapidly increase.

The projected *RC*-limited 3-dB bandwidth versus collector thickness is shown for both the 25-μm-long (solid lines) and 50-μm-long (dashed lines) photodiodes in Fig. 7. Based on the projected absorber/collector carrier transport times shown in Fig. 3, parasitics are expected to limit the bandwidth as the devices in this work were fabricated on conducting substrates. The simulations were performed for series resistance values of 30 and 40 Ω, a pad capacitance of 53 fF, a wire bond inductance of 0.3 nH, and an effective load resistance of 25 Ω. Fig. 6 shows

that a 45-GHz 3-dB bandwidth is possible for a 25-μm long device with a series resistance of 30 Ω. For all curves of Fig. 7, the slope decreases with higher collector thicknesses as the junction capacitance becomes less significant compared to the pad capacitance. In this work we employ a collector thickness of 150 nm in attempt to achieve an internal quantum efficiency of 90% in the 25-μm-long photodiodes. From Fig. 7, a 3-dB bandwidth in the vicinity of 33–36 GHz can be expected with this collector thickness.

IV. Fabrication

The epitaxial base structure is grown on a conducting InP substrate using a Thomas Swan Scientific Equipment Ltd. horizontal-flow rotating-disc MOCVD reactor. The active region consists of ten 6.5-nm compressively strained (1.0%) QWs, separated by 8.0-nm tensile strained (0.3%) barriers, centered within two InGaAsP:Si (1.3Q:Si) layers designed to maximize the optical confinement in the QWs. Following the active region, a 15-nm InP:Si regrowth layer, a 20-nm 1.3Q:Si stop etch, and a 450-nm InP implant buffer layer is grown.

The sample is patterned with Si_xN_y and selectively implanted with P^+ for intermixing. Following the implant, the samples are subjected to our QWI process as described in detail in [12]. In the QWI process, the as grown c-MQWs are shifted in peak photoluminescence wavelength from 1530 to 1410 nm in regions where passive waveguide, low optical confinement QW active regions, or UTC type detectors are desired. Following the QWI process, the implant buffer layer and 1.3Q stop etch layers are removed using selective wet chemical etching, leaving a thin InP:Si regrowth layer on the surface. An MOCVD regrowth is then performed beginning with a 1.3Q:Si stop etch layer, followed by a InP:Si optical confinement tuning layer, an o-MQW active region, and finally a thin InP:Zn cap. The wafer was patterned and a wet chemical etch process was carried such that the o-MQW remained only in regions where low confinement active regions are desired. The sample is then subjected to a second MOCVD step in which the appropriate UTC structure listed in Table I is grown. Following the regrowth, the sample is patterned with Si_xN_y and a selective wet chemical etch process is carried out such that the UTC structure remains in regions where it is desired with the blue-shifted c-MQW below. A final MOCVD regrowth process is performed to grow p-type InP:Zn cladding and p-contact InGaAs:Zn layers. A thorough investigation of the regrowth issues associated with this scheme and with the matter of achieving good material on a surface subjected to QWI can be found in [13].

Following the growth of the p-cladding, surface ridge waveguides were defined. The input waveguide consisted of a 250-μm curved/flared section for reduction of parasitic reflections. A 3.5-μm-thick layer of photo-benzocyclobutene (BCB) was patterned such that it would remain underneath the p-contacts, vias were opened, and p-metal was deposited. A proton implant was performed to provide electrical isolation between electrodes. The wafers were thinned and back-side n-metal was deposited. The die were separated into 3×25 μm^2 and 3×50 μm^2 diodes, soldered to aluminum nitride carriers, and wire bonded (Fig. 2) to a matched load of 50 Ω on a coplanar transmission line to yield an effective termination load of 25 Ω for RF characterization. Scanning electron micrographs of the device cross section and the finished device soldered to the carrier are shown in Fig. 8(a) and (b), respectively.

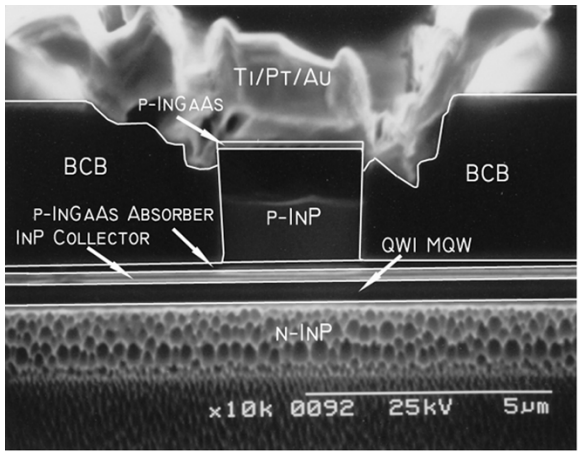

(a)

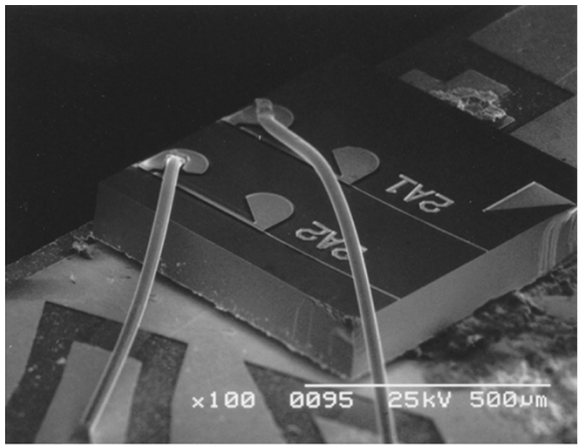

(b)

Fig. 8. Scanning electron micrographs of (a) the cross section of a UTC photodiode, and (b) a device mounted on a AlN carrier for RF testing. Note that the particular device in (b) does not possess the curve/flare input waveguide.

V. Experiment, Results, and Discussion

The passive waveguide loss on the chip was extracted using Fabry–Perot active-passive lasers and found to be $<6\,cm^{-1}$. The internal quantum efficiency of the detectors was estimated by separately reverse biasing two photodetectors configured optically in series. The first detector in the pair is the 25- or 50-μm-long detector in question. The second detector is significantly longer at 250 μm such that essentially all optical power escaping the first detector is absorbed. A 1550-nm continuous-wave (CW) optical input is then applied to the facet through a lensed fiber. The internal quantum efficiency is estimated by taking the fraction of photocurrent detected in the first detector over the sum of photocurrents in both detectors. The estimated internal quantum efficiency for both 25 μm (solid lines) and 50-μm-long (dashed lines) UTC type detectors at reverse biases of 1–4 V is shown in Fig. 9. As can be seen from the figure, the internal quantum efficiency of the 25-μm-long detector is

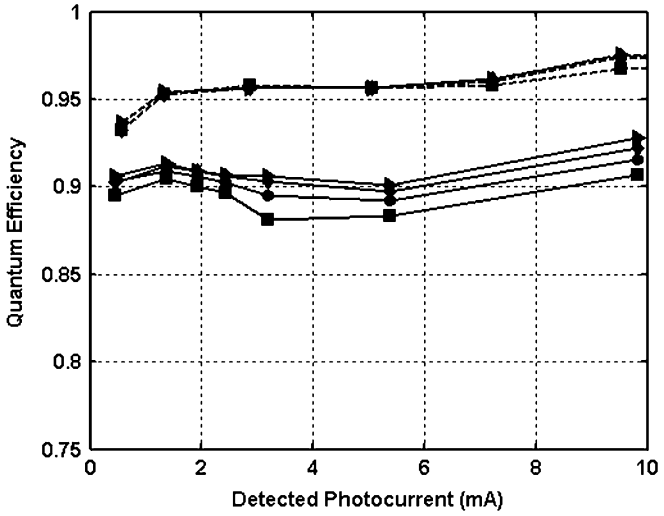

Fig. 9. Measured internal quantum efficiency for a 25 (solid lines) and 50-μm-long (dashed lines) UTC photodiodes under reverse biases of -1 V (squares), -2 V (circles), -3 V (diamonds), and -4 V (triangles).

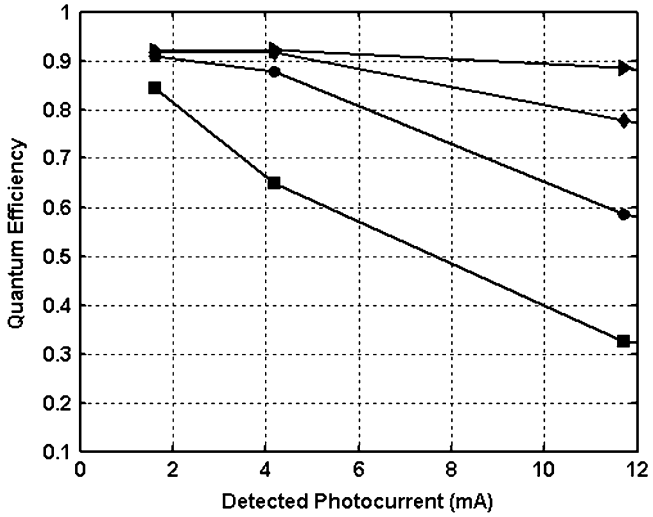

Fig. 10. Measured quantum efficiency for a 75 μm long QW p-i-n under reverse biases of -1 (squares), -2 (circles), -3 (diamonds), and -4 V (triangles).

$\sim$90% as predicted by the beam propagation simulations. The 50-μm-long detector achieves over 95% quantum efficiency. The CW responsivity was measured to be 0.20 and 0.25 A/W at a wavelength of 1550 nm for the 25- and 50-μm-long detectors, respectively. The efficiency values reported here are on the same order as those previously reported for high efficiency discrete waveguide type UTC photodiodes with an external quantum efficiency of 32% [17], however are significantly lower than the 1.14 A/W reported in [5]. With an optimized input waveguide design, a better choice of lensed fiber, and the application of an antireflective coating, the high coupling loss measured at $\sim$6 dB could be significantly reduced, resulting in an increased responsivity.

For direct comparison of the UTC photodiodes realized with the regrowth step to the QW p-i-n detectors we were previously forced to employ in high functionality PICs, QW p-i-n detectors were fabricated on the same chip. Fig. 10 shows the measured efficiency from a 75-μm-long QW p-i-n consisting of ten centered 6.5-nm-thick wells, for a total absorber thickness of 65 nm. As can be seen in the figure, the QW p-i-n detector requires a large bias of -4 V to maintain a linear internal quantum efficiency at the low power levels that these measurements were made. The decrease in quantum efficiency with increasing power at lower bias levels is indicative of space charge saturation occurring in the QW p-i-n detectors. The superior dc saturation performance demonstrated by the UTC photodiodes over the QW p-i-n detectors fabricated on the same chip further reinforces the necessity of integrating the UTC photodiode into high functionality PICs. This fabrication scheme allows the laser and EAM sections to utilize the c-MQW structure while increasing the detector performance by moving from a QW p-i-n to a UTC design [9].

A set of current versus voltage (I–V) sweeps were taken from -5 to $+1.5$ V for the photodiodes at various levels of input power. The dark current generated in a 25-μm-long devices was found to be 0.5 μA at -1 V, 3 μA at -3 V, and 10 μA at -5 V. The reverse bias series resistance for this device was estimated to be 35–40 Ω by taking the slope of an appropriately placed load line through the set of IV curves taken at various input power levels. The series resistance is over $2\times$ higher than that of high performance discrete photodiodes reported in [2] with similar diode areas. This excess resistance is likely due in part to the $\sim 2\times$ thicker p-cladding and intermixed c-MQW in our structure, which are necessary for the other waveguide architectures integrated with the photodiode.

The frequency response of the photodiodes was characterized using a 20-GHz Agilent Lightwave Component Analyzer (LCA). The optical signal from the LCA was fed through an erbium-doped fiber amplifier (EDFA) and then coupled into the photodiode waveguide using a lensed fiber. The AlN carrier possessing a matched 50-Ω load was probed with ground-signal-ground probes to extract the electrical signal from the photodiode with an effective termination load of 25 Ω. The frequency response of the photodiode was then characterized as a function of average detected photocurrent and reverse bias.

The optical to electrical response of a 25-μm-long photodiode is shown for various average detected photocurrent levels at a reverse bias of 3 V in Fig. 11. The response curves are normalized to the 5-mA curve such that they are easily differentiated. As can be seen in the figure, the 20-GHz response demonstrates under 0.5 dB of roll-off with average photocurrents up to 20 mA. At an average photocurrent of 25 mA, the roll off is somewhat increased to 0.75 dB and at 35 mA, the 20-GHz roll-off is increased to slightly over 2 dB. When increasing the reverse bias to 4 V at an average photocurrent of 35 mA, the roll-off is decreased to below 1 dB. In Fig. 12 we show the effects of reverse bias on the bandwidth of the same detector at an average photocurrent level of 10 mA. At a reverse bias of 1 V, the 3 dB bandwidth of the 25 μm long photodiode is 16.5 GHz. Upon increasing the bias to -2 V, the bandwidth increases such that there is only 0.5 dB roll-off out to 20 GHz. For reverse biases of 3 and 4 V, there is no roll-off in the response out to 20 GHz.

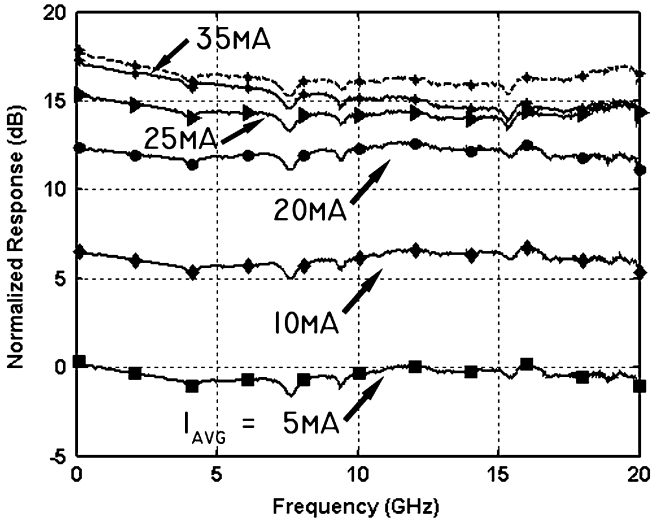

Fig. 11. Optical to electrical response of a 25-μm-long detector for average photocurrents of 5 (squares), 10 (diamonds), 20 (circles), 25 (triangles), and 35 mA (stars) with a 3 V reverse and 35 mA at a -4 V reverse bias (dashed line). Response is normalized to 5 mA data set. Markers represent every 80th data point.

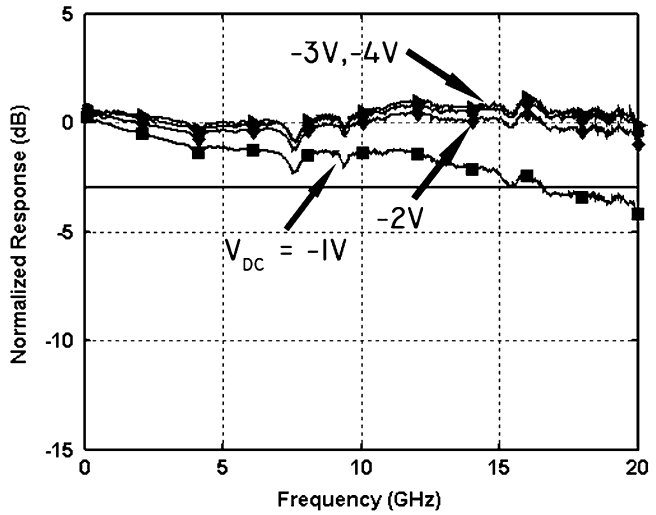

Fig. 12. Optical to electrical response of a 25-μm-long detector for reverse biases of -1 (squares), -2 (diamonds), -3 (circles), and -4 V (triangles) with an average photocurrent of 10 mA. Markers represent every 80th data point.

The optical to electrical response of a 50-μm-long photodiode is presented for various average photocurrent levels at a reverse bias of 4 V in Fig. 13. The response curves are normalized to the 20 mA curve such that they are easily differentiated. As shown in the figure, for average photocurrent levels of up to 40 mA, the roll-off at 20 GHz is under 2 dB, and at 50 mA, the roll-off at 20 GHz is 2.2 dB. The 20-GHz 3 dB photocurrent level was found to be 55 mA. Beyond this photocurrent level, the photodiode demonstrated a marked decrease in quantum efficiency due to saturation effects.

The minimal roll-off of under 0.5 dB demonstrated by the 25-μm-long photodiode and under 2.0 dB demonstrated by the 50-μm-long photodiode out to 20 GHz is in excellent agreement with our response simulations used in Fig. 7, which predicts a 3-dB bandwidth of 33–36 GHz for the 25-μm-long photodiode. The maximum 3-dB bandwidths reported in this initial

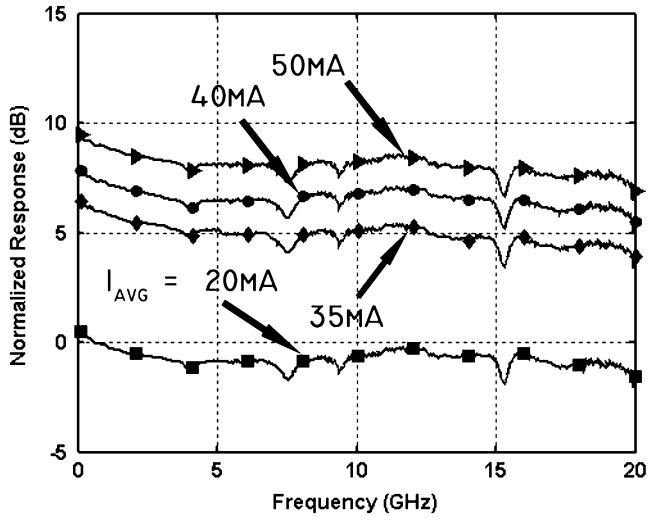

Fig. 13. Optical to electrical response of a 50-μm-long detector for average photocurrents of 20 (squares), 35 (diamonds), 40 (circles), and 50 mA (triangles) with a 4 V reverse bias). Response is normalized to 20 mA data set. Markers represent every 80th data point.

demonstration of UTC photodiodes fabricated using the integration scheme do not reach the >40-GHz levels reported for discrete waveguide type UTC photodiodes. However the reported discrete photodiodes employ semi-insulating substrates for lowered capacitance and have specially designed RF pads for low capacitance and impedance matching [5], [17]. These measures can be easily implemented into the UTC photodiodes reported here in order to greatly improve the response characteristics.

The key performance characteristic offered by the UTC photodiode over p-i-n photodiodes is the improved photocurrent handling capabilities. It can be difficult to directly compare the photocurrent handling capabilities of various detectors reported in literature due to the differences in measurement techniques. However, a special type of p-i-n photodiode to maximize bandwidth and efficiency is reported in [18] and uses similar metrics to characterize the photocurrent handling capabilities. In this report a 90-μm^2 photodiode demonstrates a 50-GHz 3-dB bandwidth at a bias of -3 V under low photocurrent operation. However, upon increasing the photocurrent to 18 mA, the bandwidth falls to under 10 GHz. Since the 75 μm^2 photodiodes reported here operating at the same bias demonstrated no bandwidth degradation up to 25 mA of average photocurrent and still maintained >20 GHz bandwidth for 35 mA of average photocurrent, the advantages offered by the UTC structure are apparent. In [5], state-of-the-art waveguide-type UTC photodiodes with a diode area of 320 μm^2 are characterized by measuring the 3-dB bandwidth at different photocurrent levels and different bias levels. At a bias level of -3 V, the 3-dB bandwidth is maintained in the 22–26-GHz range for photocurrent levels up to 30 mA. This photocurrent handling performance appears to be well inline with the performance reported here for photodiodes of 75 and 150 μm^2 operating at the same bias levels.

To examine the large signal characteristics of the photodiodes, eye diagrams were taken at 10 and 40 Gb/s in a nonreturn to zero (NRZ) format. In the test setup, a CW light source at 1548 nm was modulated using a pattern generator operating with a pseudo-random bit sequence (PRBS) of $2^{31} - 1$. The

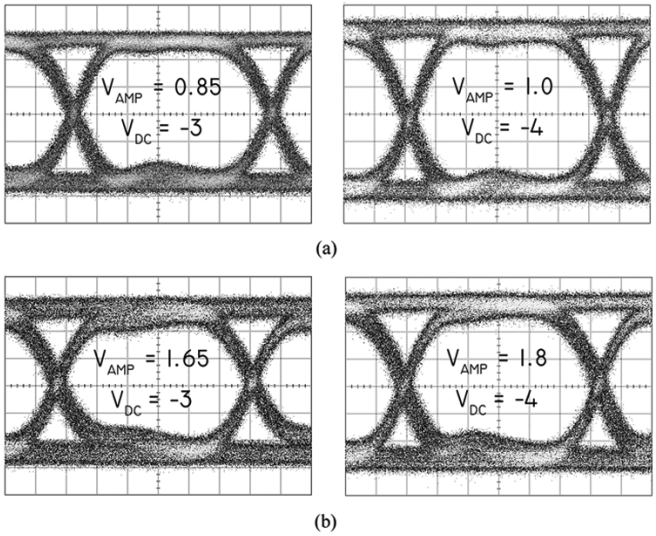

Fig. 14. 10 Gb/s eye diagrams from a (a) $3 \times 25\ \mu m^2$ and (b) $3 \times 50\ \mu m^2$ photodiode.

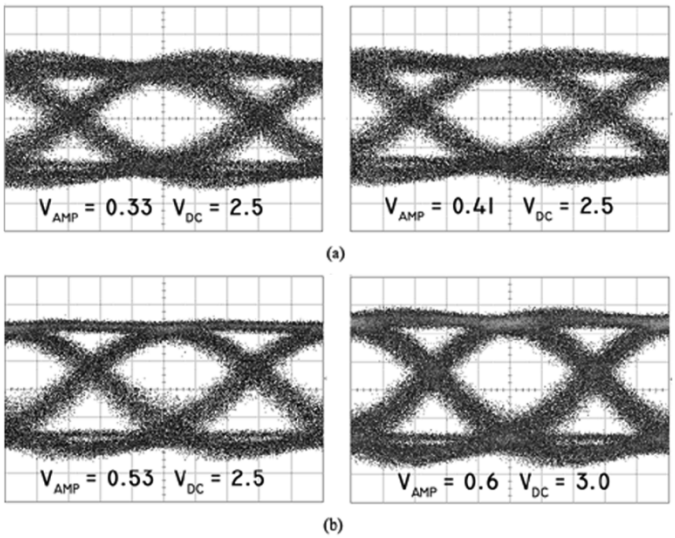

Fig. 15. 40 Gb/s eye diagrams from a $3 \times 25\ \mu m^2$ μm photodiode.

modulated light was then fed through an EDFA and into the waveguide of the photodiode using a lensed fiber. The electrical output of the device was analyzed using an Agilent DCA.

In Fig. 14(a), we present 10 Gb/s eye diagrams taken from a 25-μm-long detector at a given input power. The voltage amplitude provided by the photodiode at a reverse bias of 3 V, was 0.85 V and at a reverse bias of -4 V, it was 1.0 V. These amplitudes are indicative of minimum peak currents of 34 and 40 mA, respectively, since the voltage drop was obtained over an effective load 25 Ω due to the 50-Ω matching load on the carrier. In Fig. 13(b), eye diagrams from a 50-μm-long detector are shown for a given input power. The voltage amplitude provided by this photodiode at a reverse bias of 3 V was 1.65 V and at a reverse bias of 4 V it was 1.8 V. These amplitudes are indicative of minimum peak photocurrents of 66 and 72 mA, respectively.

In Fig. 15(a), we present 40 Gb/s eye diagrams taken from a 25-μm-long detector with two different input power levels at a reverse bias of 2.5 V. The voltage amplitude of these eyes was measured at 0.33 and 0.41 V. As can be seen from the figure, the eye diagrams are open and demonstrate no difference in shape for the two input power levels. In Fig. 14(b), eye diagrams are shown for a constant input power at reverse biases of 2.5 and 3.0 V. The higher crossing point of the eye diagram driving a voltage amplitude of 0.53 V at a reverse bias of 2.5 V is indicative of the onset of saturation. However, upon increasing the reverse bias to 3.0 V, the voltage amplitude is increased to 0.6 V and the crossing point returns to its normal position. The 0.6 V amplitude provided by the photodiode at 3 V is indicative of a minimum peak current of 24 mA in the photodiode.

VI. Conclusion

We have presented the concept and design for the realization of UTC type photodiodes fabricated using a novel QWI and MOCVD regrowth scheme. The photodiodes were fabricated on the same chip as high-gain c-MQW active regions, low optical confinement o-MQW active regions, and intermixed c-MQW passive waveguide sections. Since this scheme is an extension of and completely compatible with our established SG-DBR/EAM transmitter process, we demonstrate an extremely flexible integration technology to enable the monolithic integration of UTC photodiodes with high gain widely tunable laser diodes, high efficiency EAMs, and high saturation power SOA's.

In this first demonstration of UTC photodiodes fabricated on intermixed QWs, the UTC photodiodes exhibited greatly reduced DC saturation characteristics over the QW p-i-n photodiodes fabricated on the same chip that were previously used as detectors in high functionality PICs. The $3 \times 25\ \mu m^2$ UTC photodiodes exhibited high internal quantum efficiencies of 90% and a minimal response roll-off out to 20 GHz, which is in good agreement with simulations. No significant degradation in the bandwidth out to 20 GHz was observed for average photocurrent levels up to 25 and 50 mA for the $3 \times 25\ \mu m^2$ and the $3 \times 50\ \mu m^2$ photodiodes, respectively. Eye diagrams at 10 Gb/s demonstrated peak photocurrents of 40 and 72 mA in the $3 \times 25\ \mu m^2$ and 3 by 50 μm^2 photodiodes, respectively. Open 40 Gb/s eye diagrams were achieved with a voltage amplitude of 0.6 V. Future work will include further optimization of the UTCs for increased bandwidth.

References

[1] S. Srivastava and K. P. Roenker, "Numerical modeling study of the InP/InGaAs unitraveling-carrier photodiode," *Solid State Electron.*, vol. 48, pp. 461–470, 2004.

[2] S. Demiguel, L. Giraudet, L. Joulaud, J. Decobert, F. Blache, V. Coupe, F. Jorge, P. Pagnod-Rosiaux, E. Boucherez, and F. Devaux, "Evanescently coupled photodiodes integrating a double stage taper for 40 Gb/s applications—Compared performance with side-illuminated photodiodes," *J. Lightw. Technol.*, vol. 20, no. 12, pp. 2004–2014, Dec. 2002.

[3] T. Ishibashi, T. Furuta, H. Fushimi, and H. Ito, "Photoresponse characteristics of unitraveling-carrier photodiodes," *Proc. SPIE*, vol. 4283, pp. 469–479, 2001.

[4] D. A. Tulchinsky, X. Li, N. Li, S. Demiguel, J. C. Campbell, and K. J. Williams, "High-saturation current wide bandwidth photodetectors," *IEEE J. Sel. Topics Quantum Electron.*, no. 4, pp. 702–708, Jul./Aug. 2004.

[5] J. W. Shi, Y. S. Yu, C. Y. Wu, P. H. Chiu, and C. C. Hong, "High-speed, high-responsivity, and high-power performance of near ballistic unitraveling-carrier photodiode at 1.55 μm wavelength," *IEEE Photon. Technol. Lett.*, vol. 17, no. 9, pp. 1929–1931, Sep. 2005.

[6] T. Yoshimatsu, S. Kodama, K. Yoshino, and H. Ito, "100 Gbit/s error-free retiming operation of monolithic optical gate integrating with photodiode and electroabsorption modulator," *Electron. Lett.*, vol. 40, no. 10, pp. 626–628, 2004.
[7] M. Sysak, J. Barton, L. Johansson, J. Raring, E. Skogen, M. Mašanović, D. Blumenthal, and L. Coldren, "Single chip wavelength conversion using a photocurrent driven (PD) EA modulator integrated with a widely tunable sampled grating DBR (SGDBR) laser," *IEEE Photon. Technol. Lett.*, vol. 16, no. 9, pp. 2093–2095, Sep. 2004.
[8] K. Morito, S. Tanaka, S. Tomabechi, and A. Kuramata, "A broad-band MQW semiconductor optical amplifier with high saturation output power and low noise figure," presented at the *Semicond. Opt. Amp. Applicat. Meeting. PD1-1*, San Francisco, CA, Jun. 30, 2004.
[9] J. Raring, E. Skogen, L. Johansson, M. Sysak, J. Barton, M. L. Mašanović, and L. Coldren, "Quantum well intermixing for monolithic integration: A demonstration of novel widely tunable 10 Gb/s transmitters and wavelength converters," presented at the *Integrated Photonics Research Conf.*, San Francisco, CA, 2004, Paper IWC3.
[10] J. Binsma, P. Thijs, T. VanDongen, E. Jansen, A. Staring, G. VanDenHoven, and L. Tiemeijer, "Characterization of butt-joint InGaAsP waveguides and their application to 1310 nm DBR-type MQW Ganin-clamped semiconductor optical amplifiers," *IEICE Trans. Electron.*, vol. E80-C, pp. 675–681, 1997.
[11] M. Aoki, M. Suzuki, H. Sano, T. Kawano, T. Ido, T. Taniwatari, K. Uomi, and A. Takai, "InGaAs/InGaAsP MQW electroabsorption mofulator integrated with a DFB laser fabricated by bandgap energy control selective area MOCVD," *IEEE J. Quantum Electron.*, vol. 29, no. 6, pp. 2088–2096, Jun. 1993.
[12] E. Skogen, J. Raring, J. Barton, S. DenBaars, and L. Coldren, "Post-growth control of the quantum-well band edge for the monolithic integration of widely tunable lasers and electroabsorption modulators," *IEEE J. Sel. Topics Quantum Electron.*, vol. 9, no. 5, pp. 1183–1190, Sep./Oct. 2003.
[13] J. Raring, E. Skogen, S. Denbaars, and L. Coldren, "A study of regrowth interface and material quality for a novel InP based architecture," *J. Cryst. Growth*, vol. 273, no. 1–2, pp. 26–37, Dec. 2004.
[14] J. Raring, E. Skogen, L. Johansson, M. Sysak, S. Denbaars, and L. Coldren, "Widely tunable negative-chirp SG-DBR laser/EA-modulated transmitter," *J. Lightw. Technol.*, vol. 23, no. 1, p. 80–86, Jan. 2005.
[15] T. Ishibashi, T. Furuta, H. Fushimi, S. Kodama, H. Ito, T. Nagatsuma, N. Shimizu, and Y. Miyamoto, "InP/InGaAs unitraveling-carrier photodiodes," *IEICE Trans. Elelctron.*, vol. E83-C, no. 6, Jun. 2000.
[16] N. Shimizu, N. Watanabe, T. Furuta, and T. Ishibashi, "Electron diffusivity in p-InGaAs determined from the pulse response of InP/InGaAs unitraveling-carrier photodiodes," *Appl. Phys. Lett.*, vol. 76, no. 9, pp. 1191–1193, Feb. 2000.
[17] Y. Muramoto, K. Kato, M. Mitsuhara, O. Nakajima, Y. Matsuoka, N. Shimizu, and T. Ishibashi, "High-output, high speed, high efficiency unitraveling-carrierwaveguide photodiode," *IEE Electron. Lett.*, vol. 34, no. 1, pp. 122–123, 1998.
[18] Y. Muramoto and T. Ishibashi, "InP/InGaAs pin photodiode structure maximizing bandwidth and efficiency," *IEE Electron. Lett.*, vol. 39, no. 24, pp. 1749–1750, 2003.

James W. Raring (S'03) was born in Ramsey, NJ, in 1978. He received the B.S. degree from the Materials Engineering Department, California Polytechnic State University, San Luis Obispo, in 2001. He is currently pursuing the Ph.D. degree in materials science from the University of California, Santa Barbara.

His current research focuses on design, growth, and fabrication of wavelength-agile photonic integrated circuits. His work employs flexible quantum-well intermixing and MOCVD growth schemes for the realization of highly functional active monolithic photonic circuits.

Erik J. Skogen (M'99) was born in Minneapolis, MN, in 1975. He received the B.S. degree from Iowa State University, Ames, in 1997, and the M.S. and Ph.D. degrees from the University of California, Santa Barbara (UCSB), in 1999 and 2003, respectively. His dissertation work involved the development and application of quantum-well intermixing techniques to widely tunable sampled-grating DBR lasers and photonic integrated circuits (PIC).

He was a Postdoctoral Researcher with UCSB where he investigated advanced PICs. In 2005, he joined Sandia National Laboratories, Albuquerque, NM, as a Senior Member of Technical Staff. His current research involves advanced monolithic integration techniques for next generation PICs.

Chad S. Wang (S'99) was born in Racine, WI, in 1979. He received the B.S. degree from The University of Texas at Austin, in 2001, and the M.S. degree from the University of California, Santa Barbara, in 2002, where he is currently working toward the Ph.D. degree in electrical and computer engineering.

His research interests include the development of integrated laser-modulators for optical interconnect applications. He is also involved in molecular beam epitaxy growth of III–V semiconductor vertical-cavity lasers and avalanche photodetectors.

Jonathon S. Barton (M'00) received the B.S. degree in electrical engineering and material science at the University of California, Davis, in 1997. He received the Ph.D. degree in electronic materials from the University of California, Santa Barbara, where he was an Intel Fellow.

Currently, he is an Assistant Project Scientist for the LASOR DARPA grant working on the growth, fabrication, and high-speed testing of many monolithic optoelectronic components such as tunable lasers, modulators, and photocurrent-driven wavelength converters.

Dr. Barton is a member of IEEE LEOS, OSA, and SPIE.

Gordon B. Morrison received the B.A.Sc. (hons.) degree in engineering physics from Simon Fraser University, Vancouver, BC, Canada, in 1997 and the Ph.D. degree in engineering physics from McMaster University, Hamilton, ON, Canada, in 2002.

From 1998 to 2002, he spent more than a year as a Graduate Student Researcher at Nortel Networks, Ottawa, ON. After completing the Ph.D., he spent eight months as a Postdoctoral Researcher at McMaster University. From 2003 to 2005, he was a Visiting Assistant Research Engineer in the Department of Electrical and Computer Engineering, University of California, Santa Barbara. Since June 2005, he has been an Optical Device Engineer at Three Five Photonics BV, Houten, The Netherlands. His interests have included design of integrated laser/EAM modulators using quantum-well intermixing for both GaAs and InP material systems, as well as photocurrent spectroscopy for material characterization and device optimization. Other interests have included modeling the spectra of DFB lasers, and modeling the gain in asymmetric multiple-quantum-well lasers.

Stéphane Demiguel (M'04) was born in Gennevilliers, France, in 1971. He received the engineer degree in electrical engineering from the Ecole Supérieure d'Ingenieurs en Génie Electrique, Rouen, France, in 1996 and the Ph.D. degree in optoelectronic from Rouen University, Rouen, in 2001.

In 2000, he worked on the design and measurements of high-speed photodiodes in Alcatel Opto+, Marcoussis, France. In particular, he was involved in optical and electrical modeling for optoelectronic devices. In 2002, he joined Prof. J. Campbell's group at the University of Texas, Austin. He is currently working on high-speed PIN, APD, and high-power photodiodes utilizing an evanescently coupled approach integrating a multimode waveguide.

Steven P. DenBaars (M'91) is a Professor of Materials and Electrical Engineering at the University of California, Santa Barbara (UCSB). From 1988–1991, he was a Member of the Technical Staff at Hewlett-Packard, involved in the fabrication of high-brightness LEDs. In 1991, he joined the faculty of UCSB, where he is developing new solid-state optoelectronic devices. His research also involves MOCVD growth of GaN- and InP-based tunable lasers and detectors. Currently, he is an Associate Director of the Solid-State Lighting and Display Center (SSLDC) at UCSB, which is developing new, more energy-efficient light sources. Special interests include the effect of materials properties on device performance, blue VCSEL lasers, and microwave power transistors. He has authored over 200 technical publications, three book chapters, 100 conference presentations, and over seven patents.

Dr. DenBaars received a National Science Foundation Young Scientist Award in 1995, and the Young Scientist Award from the International Symposium on Compound Semiconductors in 1998.

Larry A. Coldren (S'67–M'72–SM'77–F'82) received the Ph.D. degree in electrical engineering from Stanford University, CA, in 1972.

After 13 years in the research area at Bell Laboratories, he was appointed Professor of Electrical and Computer Engineering at the University of California at Santa Barbara (UCSB) in 1984. At Bell Labs Coldren initially worked on waveguided surface-acoustic-wave signal processing devices and coupled-resonator filters. He later developed tunable coupled-cavity lasers using novel reactive-ion etching (RIE) technology that he created for the then new InP-based materials. At UCSB he continued work on multiple-section tunable lasers, in 1988 inventing the widely tunable multi-element mirror concept, which is now fundamental to many of Agility's products. During the late eighties he also developed efficient vertical-cavity multiple-quantum-well modulators, which led to novel vertical-cavity surface-emitting laser (VCSEL) designs that provided unparalleled levels of performance. In 1986, he assumed a joint appointment with Materials and Electrical and Computer Engineering and, in 2000, the Fred Kavli Chair in Optoelectronics and Sensors. He is also Chairman and Chief Technology Officer of Agility Communications, Inc. At UCSB, his efforts have included work on novel guided-wave and vertical-cavity modulators and lasers, as well as the underlying materials growth and fabrication technology. He is now investigating the integration of various optoelectronic devices, including optical amplifiers and modulators, tunable lasers, wavelength converters, and surface-emitting lasers. He continues to be active in developing new photonic integrated circuit (PIC) and VCSEL technology, including the underlying materials growth and fabrication techniques. In recent years, for example, he has been involved in the creation of vertical and in-plane GaN-based emitters, efficient all-epitaxial InP-based VCSEL's, and a variety of PICs incorporating numerous optical elements for widely tunable integrated transmitters, receivers, and wavelength converters. He has authored or coauthored more than 700 papers, five book chapters, one textbook, and has been issued 36 patents. He has presented dozens of invited and plenary talks at major conferences.

Prof. Coldren is a Fellow of the Optical Society of America (OSA) and the Institute of Electrical Engineers (IEE), U.K., a Member of the National Academy of Engineering, and the recipient of the 2004 John Tyndall Award, and a member of the National Academy of Engineering.

IMPROVED FUNCTIONALITY AND PERFORMANCE IN PHOTONIC INTEGRATED CIRCUITS

Larry A. Coldren, James Raring, Matt Sysak, Jonathan Barton, and Leif Johansson

Materials and Electrical and Computer Engineering Depts., University of California, Santa Barbara, 93106

Abstract

With the continued maturation of InP-based photonic ICs, improvements in their functionality, performance, and reliability are evolving. High-performance single-chip transmitters, receivers, sensors, transceivers, and wavelength converters that integrate numerous components have been demonstrated. Here we summarize results of integrated widely-tunable transmitters using two different integration platforms.

I. Introduction

The majority of optoelectronic components comprising modern day communications systems are discrete in nature. Several of these discrete components with differing functions are then interconnected using fiber splices in a configuration to provide the required system functionality. The underlying advantage of this method is that each component is optimized for one specific function, enabling deployment of state of the art components. However, there are several shortcomings involved with this method. The difficulty in efficiently coupling light on and off each discrete chip is great. Advances in the coupling between the semiconductor chip and optical fiber using mode converters is a significant step in reducing the coupling loss, yet coupling is still a dominant source of optical loss. Another draw back to discrete components is the expense involved with packaging each component individually. This is the major expense as devices are taken from fabrication to deployment. A reduction of the packaging cost can be accomplished by using co-packaging of optoelectronic components although device-to-device coupling is still an issue.

The monolithic integration of the optoelectronic devices on a single chip offers the potential to completely eliminate the device-to-device coupling problem. This can provide a significant reduction in packaging cost and package size as well as increased reliability and reduced power dissipation. Increased reliability results from the elimination of possible mechanical movements amongst the elements of an optical train and the reduced driving currents allowed by the reduction in optical coupling loss between elements. The reduction in required drive currents subsequently results in decreased device power consumption.

There are some general requirements that must be fulfilled when monolithically integrating optoelectronic components. First, each integrated component must function as intended. The performance of each integrated component must operate at a level that will enable the PIC as a whole to achieve its specified performance level. Clearly, as these levels are increased, the performance demands of the individual integrated components will also be increased. The second requirement is that the operation of one component must not adversely effect the operation of another. That is, each component should be isolated from the other components on chip and function as if it were discrete. These requirements allow for the design of PICs using an optoelectronic building blocks approach such that discrete components sharing a common growth and processing platform can be combined in a way that creates a higher functionality device or PIC. When implementing a method for monolithic integration, the trade-off between fabrication difficulty and device optimization capabilities should be carefully weighed since added processing steps and growth complexity can lead to increased manufacturing costs and yield reduction. Additionally, the method should not be prohibitively time consuming or expensive. A review of some of some integration methods are given in the following section.

II. Integration Technologies

Three established active-passive integration techniques are outlined in Fig 1. The butt-joint regrowth method is an example of an integration scheme offering a high degree of versatility, because waveguides with exactly the desired properties can be grown successively after removal of the original waveguide[1]. However, it tends to suffer from imperfect interfaces between the two guides, resulting in unwanted scattering loss and reflections. Of course, a separate

regrowth is required for each new bandgap or other waveguide property change.

Selective area growth (SAG) uses a dielectric mask to pattern the wafer, which inhibits epi-layer growth during MOCVD[2]. As a result the layers grow thicker near the dielectric mask and this can be used to tailor the waveguide properties along its length. However, waveguide properties cannot be shifted very abruptly, the waveguide thickness and confinement factor also change, and critical control of growth parameters are necessary.

An established and very simple integration platform is based on the use of offset QWs, where the multi-quantum well (MQW) active region is grown above a passive bulk waveguide that extends throughout the PIC[3]. Passive, tuning, or modulator regions are then formed by selectively etching off the MQW active prior to the single non-critical regrowth. However, here there is a slight discontinuity at the interface, the confinement factor is limited by the offset geometry in the active section, and only two possible waveguides/bandgaps are possible. Nevertheless, this platform has enjoyed commercial success with fairly complex PICs involving, for example, a five-section widely-tunable SGDBR laser, an SOA, and an EAM on a single chip. The SGDBR itself contains two tunable mirrors, a backside detector, an intracavity phase shifter, and a gain region.

In order to improve upon the above well-established integration platforms, two new platforms have been developed as shown in Fig. 2. The first, called the 'dual quantum-well' approach, is just like the offset QW platform outlined in Fig. 1 (c), with the addition of higher bandgap QWs in the common 'passive' waveguide[4]. This is very beneficial for more efficient electroabsorption and phase modulators due to the possible use of the quantum-confined Stark effect (QCSE), which provides a more abrupt absorption edge. With only a moderate increase in the base structure growth complexity, QW EAMs can now be realized on the same chip as widely-tunable lasers using the identical simple processing steps as in the offset QW method. This scheme offers a large degree of EAM design freedom since the MQW design can be tailored without disruption of the laser active region. This freedom opens new avenues for the use of specially designed wells for optimum modulator performance in terms of well depth, well/barrier width, and well symmetry.

Another method to realize multiple QW bandedges is through quantum well intermixing (QWI), which allows for the strategic, post growth, tuning of the QW band edge using a relatively simple procedure[5]. This is illustrated in Fig. 2b. As this technique enables the employment of centered MQW active regions for maximized modal gain lasers and blue shifted QWs by various amounts for use in EAMs and passive waveguides. QWI breaks the trade-off associated with the simple fabrication scheme offered by the offset QW method and the design flexibilities offered by butt-joint regrowth and SAG. QWI makes use of the metastable nature of the compositional gradient found at heterointerfaces. The natural tendency for materials to interdiffuse is the basis for the intermixing process. Also, because QWI does not change the average composition, but only slightly changes the compositional profile, there is a negligible index discontinuity at the interface between adjacent sections. This eliminates parasitic reflections that can degrade performance.

In our work we employ the implant-enhanced interdiffusion technique, which relies on the diffusion of point defects created during an ion implantation into an InP implant buffer layer grown above the MQW active region. This method has been shown to have good spatial resolution, and be controllable using anneal time, temperature, and implant dose[5]. Furthermore, we have shown that numerous QW band edges can be obtained by sequential selective removal of the vacancy source followed by a prescribed RTA. As indicated in Fig. 3a the properties of the resulting MQW regions still

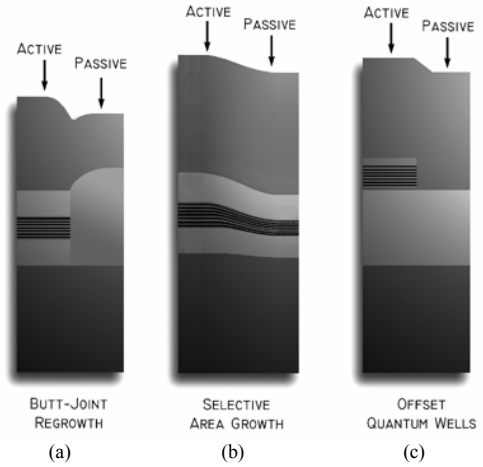

Fig. 1. Various techniques for achieving active and passive sections orthogonal to the growth direction.

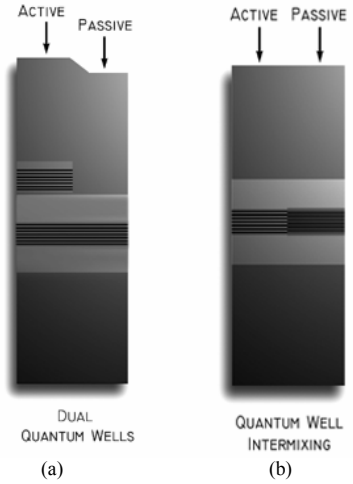

Fig. 2. Newer integration techniques for enhanced high-functionality PIC performance

have good QCSE behavior. And as shown in Fig. 3b low-loss passive waveguides are enabled by shifting the absorption edge further.

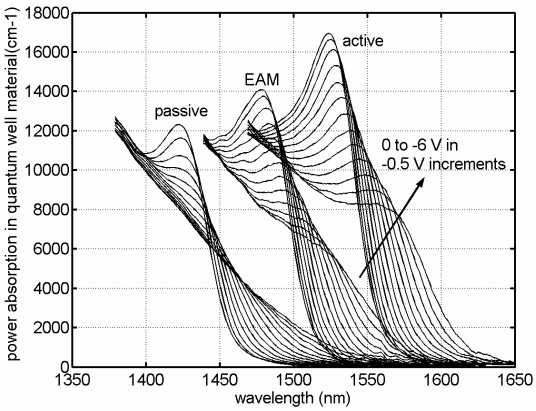

Fig. 3a. Photocurrent vs. wavelength for as grown, partially intermixed (EAM) and more fully intermixed (passive) quantum wells.

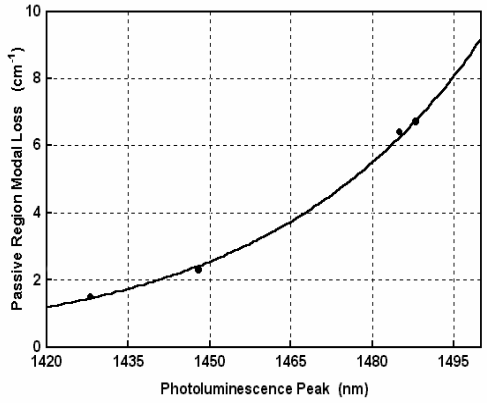

Fig. 3b. Passive region modal loss vs. photoluminescence peak wavelength measured at 1570nm.

III. PIC Results

In the following sections results are presented from PICs fabricated on the dual QW and on the QWI platform. First we report the performance 10 Gb/s widely-tunable transmitters monolithically integrated with photoreceivers employing waveguide flares for both the SOA and the detector for the realization of a 10 Gb/s photocurrent-driven wavelength converter (PD-WC). In the following section results are shown for a 10 Gb/s widely-tunable negative-chirp transmitter fabricated using QWI.

III.A. Dual QW 10 Gb/s Transmitter with Integrated Receiver

SG-DBR lasers have been integrated with QW EAMs and SOA/QW p-i-n receivers employing flares and tapers for improved saturation characteristics[6] using the dual QW platform. This device, shown in Fig. 4, was the first single chip widely tunable EAM based 10 Gb/s PD-WC providing 10 dB of output signal extinction and a net conversion gain[7]. Further details and performance characteristics of the PD-WC device can be found elsewhere[8]. Here we focus on the transmitter portion of the device which is comprised of a five section SG-DBR laser followed by an SOA for output amplification and a QW EAM consisting of seven 9.0 nm compressively strained wells and six 5.0 nm tensile strained barriers. The 5 sections of the SG-DBR laser are, from front to back of the laser: front mirror, gain, phase, rear mirror, and backside absorber, as depicted in Fig. 4. The phase and mirror sections function to tune the wavelength of the laser[3]. The output tuning spectra of the transmitter demonstrated over 40nm of continuous tuning with a side mode suppression ratio (SMSR) of > 35 dB at all wavelengths. The SG-DBR lasers demonstrated threshold currents of under 40mA with over 20 mW of output power at a gain current of 160 mA. There is no significant degradation in the laser performance over that of SG-DBRs fabricated using the offset QW platform, and in fact, there is a slight enhancement in the tuning efficiency of the lasers due to the addition of the QWs in the waveguide.

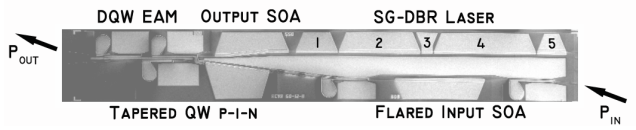

Fig. 4. Top view SEM of PD-WC using dual-QW platform and flared/tapered waveguide schemes in receiver.

In Fig. 5a, EAM extinction versus bias, and in Fig. 5b, EAM slope efficiency versus bias are presented for both bulk FK type EAMs fabricated using the offset QW method and QW EAMs fabricated using the dual QW method. The QW EAM provides up to 2.5X the efficiency than that of the FK device. Furthermore the QW EAM has an optimal operating bias regime in the 2.5 to 3.5V with respect to the extinction efficiency. The FK EAM demonstrates an increase in extinction efficiency at larger biases, requiring a larger modulation swing and resulting in relatively high on loss.

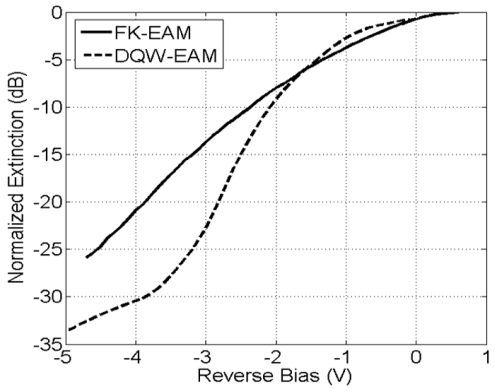

(a)

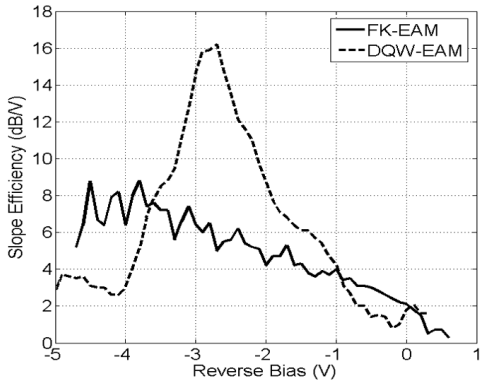

(b)

Fig.5 (a) Extinction and (b) slope efficiency versus reverse bias for 400μm long EAMs employing the FK absorption mechanism fabricated on the offset QW platform and employing the QCSE absorption mechanism fabricated using the dual QW platform.

The reduced doping levels in the EAM required for optimized efficiency in the dual QW platform over that of the offset QW platform enables a significantly lowered device capacitance. As a result, a 400 μm long dual QW EAM demonstrating 10 GHz of 3 dB bandwidth, which is a factor of 2 better than the FK EAM response shown on the same plot. Thus, with the dual QW platform we have demonstrated a 2X improvement in EAM efficiency and bandwidth without any degradation to the laser performance or additional fabrication steps than those associated with the offset QW platform.

III.B. SG-DBR /EAM 10 Gb/s Transmitter Fabricated with QWI

Figure 6 shows results from a similar SGDBR-EAM transmitter fabricated with QWI with properties outlined in Fig. 3. This is the first widely-tunable transmitter demonstrating negative chirp characteristics at 10 Gb/s over its entire tuning range[9]. The SG-DBR laser demonstrated a threshold current of 13mA, with an output power of 10mW at a gain section current of 100mA. At this operating point, a side-mode suppression ratio (SMSR) greater than 35 dB was achieved. The EAM (175 μm) demonstrated over 40 dB of DC extinction for wavelengths of 1558, 1570, and 1580 nm, with efficiencies greater than 20 dB/Volt as shown in Fig. 6a.

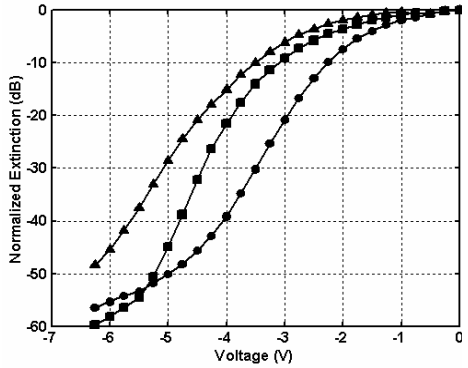

(a)

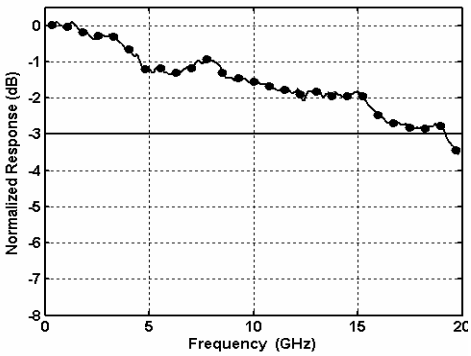

(b)

Fig. 6 (a) DC Extinction of a 175 μm EAM fabricated with QWI for wavelengths of 1558 nm (circles), 1570 nm (squares), and 1580 nm (triangles). And (b) electrical to optical frequency response of the same EAM. The circular markers represent every 30th data point.

The efficient extinction properties are due to the combination of the centered quantum well design and the intermixing process that allows for precise placement of the modulator band edge. The 3dB bandwidth, shown in Fig. 6b, of the same modulator was greater than 19 GHz. Eye diagrams, shown in Fig. 7a, were taken at wavelengths of 1558 nm, 1564 nm, 1571 nm, and 1578 nm with DC biases ranging from -2.1 to -

3.8 V and peak to peak voltage swings ranging from 2.2 V to 3.4 V. Greater than 10 dB extinction was achieved at all wavelengths.

Transmission experiments at 10 Gb/s were performed using a non-return to zero (NRZ) pseudo-random-bit-sequence (PRBS) of 2^{31}-1 through Corning SMF-28 fiber. BER curves through 25, 50, and 75 km of fiber at a wavelength of 1564 nm are shown in Fig. 7b. The EAM was biased at -3.5 V with a 2.0 V peak-to-peak swing. Error-free operation was achieved through 75km of fiber with a power penalty of less than 0.5 dB. The low power penalty transmission is indicative of negative chirp operation[20]. The shaping of the eye diagrams due to dispersion is clearly seen in the insets of Fig. 7b where the optical eye diagrams are shown after transmission through fiber.

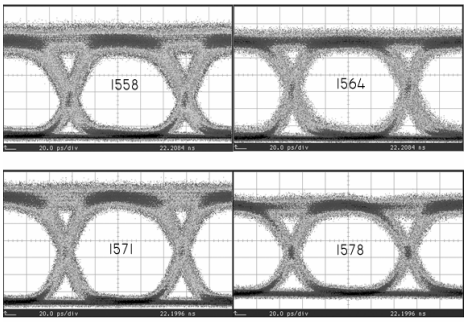

(a)

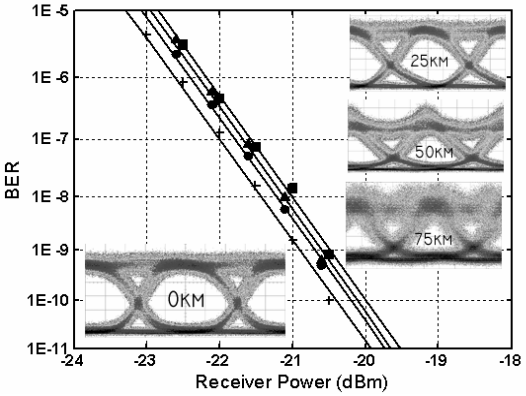

(b)

Fig. 7 (a) 10Gb/s back-to-back eye diagrams from transmitter at wavelengths of 1558 nm, 1564 nm, 1571 nm, and 1578 nm and (b) BER curves/eye diagrams for back-to-back (cross), and transmission through 25 km (circles), 50 km (triangles), and 75 km (squares) of fiber.

IV. Conclusion

The monolithic integration of optoelectronic components supporting modern day communication systems will provide solutions at low cost with a reduction of space requirements and device power dissipation. However, as the functionality of the PIC is increased, the challenge of realizing a high performance integrated is great due to the unique characteristics required by the individual components for optimum performance. To meet the increasing performance demands placed upon the PICs, novel integration platforms must be developed such that the design space is increased without significant increase in processing and growth requirements that can raise cost and lower yields.

We have reviewed two viable integration technologies, which provide the foundation for the monolithic integration of QW EAMs with widely tunable SG-DBR lasers. By growing a blue-shifted MQW in the bulk waveguide below the active MQW in the base structure, etching the active MQW in regions where gain is not required and performing a regrowth of the upper cladding, the dual QW platform requires the same simple processing/growth steps as the well-established offset QW platform with the added flexibility of a second MQW bandedge. By using our implant enhanced QWI scheme, any number of MQW band-edges can be realized on the same chip for the fabrication of high-functionality PICs. Furthermore, this method enables the use of a centered MQW active region for maximized modal gain lasers. Through the use of QWI, we have demonstrated the first widely-tunable negative chirp EAM based transmitter.

V. References

[1] J. Binsma, P. Thijs, T. VanDongen, E. Jansen, A. Staring, G. VanDenHoven, and L. Tiemeijer, "Characterization of Butt-Joint InGaAsP Waveguides and Their Application to 1310 nm DBR-Type MQW Ganin-Clamped Semiconductor Optical Amplifiers," IEICE Trans. Electron., vol. E80-C, pp. 675-681, 1997.

[2] M. Aoki, M. Suzuki, H. Sano, T. Kawano, T. Ido, T. Taniwatari, K. Uomi, and A. Takai, "InGaAs/InGaAsP MQW Electroabsorption Mofulator Integrated with a DFB Laser Fabricated by Band-Gap Energy Control Selective Area MOCVD," IEEE J Quantum Electron., vol. 29, pp. 2088-2096, 1993.

[3] B. Mason, G. Fish, S. DenBaars, and L. Coldren, "Ridge Waveguide Sampled Grating DBR Lasers with 22-nm Quasi-Continuous Tuning Range," IEEE Photon. Technol. Lett., vol. 10, pp. 1211-1213, 1998.

[4] M. N. Sysak, J. W. Raring, D. J. Blumenthal, L. A. Coldren, "A Single Regrowth Integration Platform for Photonic Circuits Incorporating Tunable SGDBR Lasers, and Quantum Well EAMs," submitted to Photonics Technology Letters, 2006.

[5] E. Skogen, J. Raring, J. Barton, S. DenBaars, and L. Coldren, "Post-Growth Control of the Quantum-Well Band Edge for the Monolithic Integration of Widely-Tunable Lasers and Electroabsorption Modulators," IEEE J. Sel. Topics in Quantum Electron., vol. 9, pp. 1183-1190, September/October, 2003.

[6] A. Tauke-Pedretti, M. Dummer, J.S. Barton, M.N. Sysak, J.W. Raring, and L.A. Coldren, "High Saturation Power and High Gain Integrated Photoreceivers," IEEE Photon. Technol. Lett., vol. 17, pp. 2167-2169, 2005.

[7] M. N. Sysak, J. W. Raring, J. S. Barton, M. Dummer, A. Tauke-Pedretti, H. N. Poulsen, D. J. Blumenthal, L. A. Coldren, "10 Gb/s Photocurrent Driven, Electroabsorption Modulator Based Wavelength Converter with Monolithically Integrated Widely Tunable SGDBR Laser and Optical Receiver," accepted for presentation at the Integrated Photonics Research Conference, 2006.

[8] J. S. Barton, A. Tauke-Pedretti, M. Dummer, M. N. Sysak, J. W. Raring, L. A. Coldren, "Field Modulated Wavelength Conversion, *Invited,* 6124 -42. San Jose, CA, January 21-26, 2006.

[9] J. Raring, E. Skogen, L. Johansson, M. Sysak, S. DenBaars, and L. Coldren, "Widely-Tunable Negative-Chirp SG-DBR Laser/EA-Modulated Transmitter," IEEE Journal of Lightwave Technology, vol. 23 no.1, pp. 80-86, Jan. 2005.

A Single Regrowth Integration Platform for Photonic Circuits Incorporating Tunable SGDBR Lasers and Quantum-Well EAMs

Matthew N. Sysak, *Member, IEEE*, James W. Raring, *Student Member, IEEE*, Jonathon S. Barton, *Member, IEEE*, Matthew Dummer, *Student Member, IEEE*, Daniel J. Blumenthal, *Fellow, IEEE*, and Larry A. Coldren, *Fellow, IEEE*

***Abstract*—A monolithic integration platform is demonstrated for high functionality photonic circuits that include quantum-well electroabsorption modulators, semiconductor optical amplifiers, and widely tunable lasers. The platform is based on the selective removal of a set of active quantum wells located above an optical waveguide layer. The waveguide layer contains a second set of quantum wells to be used in modulator regions. Fabrication requires only a single blanket InP regrowth.**

***Index Terms*—Electroabsorption modulators (EAMs), monolithic integration, quantum confined stark effect (QCSE), sampled grating distributed Bragg reflector (SGDBR) laser, semiconductor lasers, semiconductor optical amplifier (SOA).**

I. Introduction

THE development of high functionality photonic integrated circuits (PICs) is critical for reducing packaging costs and improving performance in next-generation networks. As a precursor to such devices, an integration platform must be available that requires simple fabrication and growth procedures in order to minimize processing requirements and maximize device yields. Several viable platforms have been demonstrated using the InGaAsP–InP material system. These include selective area growth, butt-joint regrowth, quantum-well intermixing, and offset quantum-well (OQW) platforms [1].

For PICs that require a tunable laser source integrated with electroabsorption modulators (EAMs) and semiconductor optical amplifiers (SOAs), the OQW platform employing sampled grating distributed Bragg reflector (SGDBR) lasers has been shown to be one of the simplest solutions [2]. A diagram of the layer structure in this platform is shown in Fig. 1(a). In this approach, quantum wells (QWs) located above a bulk InGaAsP waveguide layer are used for optical gain. To define regions where gain is not necessary, a wet selective etch is performed to remove these QWs. The etch terminates on a 15-nm InP regrowth and stop etch (SE) layer. To form the top p-contact, a blanket Zn-doped p-InP and p-InGaAs regrowth is performed. EAMs are defined by contacting and reverse biasing passive waveguide sections. Though very simple to implement, EAMs of this type are dependent on the Franz–Keldysh electroabsorption effect (FK-EAMs). This effect has limited modulation efficiency with low insertion loss, and exhibits positive chirp. In contrast, QW-EAMs employing the quantum confined stark effect (QCSE) have demonstrated large bandwidths, excellent modulation efficiency, low insertion loss, and negative chirp [3].

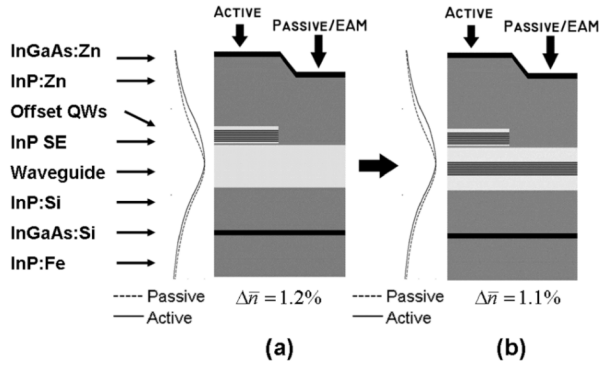

Fig. 1. Epitaxial layer structure and active/passive mode profiles for the (a) OQW and (b) DQW platforms. The modal effective index mismatch for transitions between active and passive regions is $<1.3\%$ for both approaches.

In this work, we present a newly developed dual-quantum-well (DQW) integration platform where the OQW approach is modified to obtain QCSE-based EAMs. A diagram of the DQW platform is shown in Fig. 1(b). In this new platform, the same selective etching and blanket regrowth techniques used in the OQW approach are employed to define optical gain (active) and passive/EAM regions. However, to enhance the EAM modulation efficiency, bandwidth, and chirp characteristics, a second set of QWs is placed into the center of the waveguide layer. The photoluminescence (PL) peak of the added wells is detuned from the offset QWs to balance propagation loss and laser performance with EAM efficiency.

To demonstrate the viability of the DQW platform, we have compared active region material characteristics and EAM performance for both the OQW and DQW platforms using a set of integrated widely tunable transmitters.

II. DQW Integration Platform

The offset QWs in the DQW platform are identical to those in the OQW approach. The offset QW stack consists of 7×6.5 nm compressively strained wells and 8×8.0 nm tensile strained barriers with a PL peak of 1550 nm. Below the offset wells is a 345-nm InGaAsP waveguide layer. In the center of the waveguide is the second set of QWs consisting of 7×9.0 nm compressively strained wells and 6×5.0 nm tensile strained barriers

Manuscript received March 2, 2006; revised April 20, 2006. This work was supported by the Defense Advanced Research Projects Agency (DARPA)/MTO CS-WDM under Grant N66001-02-C-8026 and by Intel Corporation under Grant TXA001630000.

The authors are with the Department of Electrical Engineering and the Department of Materials, University of California Santa Barbara, Santa Barbara, CA 93116 USA (e-mail: mnsysak@engineering.ucsb.edu).

Digital Object Identifier 10.1109/LPT.2006.878153

TABLE I
SUMMARY AND COMPARISON OF MATERIAL PARAMETERS

Platform	Injection efficiency (η_i)	Transparency current density (A/cm^2)	Material gain (cm^{-1})	Active loss (cm^{-1})
DQW	73 %	269.9	764	10
OQW	75 %	246	826.4	10

with a PL peak of 1480 nm. The conduction and valence band offsets for the waveguide QWs are 65 and 97 meV, respectively.

Above and below the waveguide QWs is a 25-nm undoped outer barrier layer. The remaining waveguide consists of high bandgap (1.3 μm) material that is lightly doped n-type (Si) at 5×10^{16} cm^{-3}. Since the waveguide doping levels are low, the electric field at the QWs with a reverse bias is almost identical to that in a standard PIN structure.

III. DQW Platform Material Parameters

When introducing a set of QWs into the waveguide layer, it is critical that the propagation loss and optical gain properties of the integrated SGDBR laser, optical amplifier, and passive waveguides are not degraded. Under forward bias operation, injected carriers must travel to the offset QWs without parasitic recombination for high laser injection efficiency. For holes, the transport path is identical to that in the OQW platform. Carriers are injected from p-cladding into the offset wells and trapped by the potential barrier created by the InP SE layer above the waveguide. The SE is thin enough to avoid vertical coupling effects in the active region, but maintain repeatability in the selective wet etch process. However, for electrons, carriers from the n-buffer layer must pass through the potential barriers associated with the waveguide QWs and over the InP SE layer before entering the OQWs for recombination.

To examine the carrier transport process in the DQW platform, pulsed differential efficiency measurements were performed on a set of 50-μm-wide Fabry–Pérot broad area lasers (BAL) and 3-μm-wide active ridge lasers (RLs) using the cleave back method. From the RLs, the injection efficiency and the modal active region propagation loss at 1550 nm was extracted. From the threshold current and differential efficiency of the BALs, a two parameter fit material gain curve was generated after accounting for the offset QW confinement factor of 6.2 %. These results are summarized in Table I and are in excellent agreement with measurements from devices fabricated on the OQW platform containing a moderately doped n-type (1.41-μm bandgap, 2×10^{17} cm^{-3} Si) waveguide. This indicates minimal or no added parasitic recombination in the waveguide QWs.

The other key material parameter that has been examined for the DQW integration platform is the passive region propagation loss over wavelengths within the telecommunications C-band. To investigate this, structures have been fabricated that contain a tunable laser source and a 3-mm-long passive waveguide. Electrical contacts are placed periodically along the passive waveguide and reverse biased to measure the photocurrent at each point along the structure. Based on the ratio of the photocurrents at each contact and the separation between pads, the propagation loss can be calculated. Results showed losses of 6 cm^{-1} at 1562 nm, 7.5 cm^{-1} at 1550 nm, 10 cm^{-1} at 1542 nm, and 16 cm^{-1} at 1530 nm. The exponential dependence of the propagation loss is expected based on an Urbach absorption tail resulting from the bandgap energy proximity between the waveguide and OQW stacks [4]. The propagation loss for the OQW waveguides was 6 cm^{-1} at 1550 nm. This is not expected to vary greatly due to the large bandgap detuning.

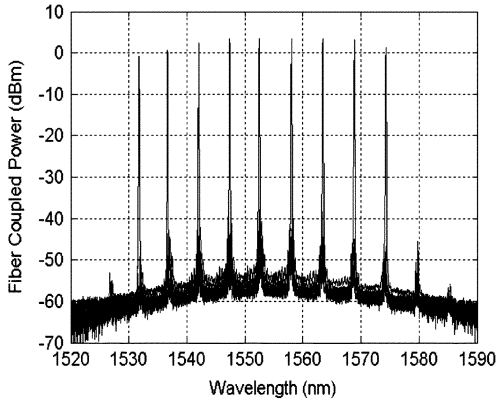

Fig. 2. Superimposed fiber coupled SGDBR spectra at various wavelengths. Laser gain and SOA postamplifier are biased at 100 mA.

IV. DQW Tunable Transmitter

To demonstrate the viability of the DQW integration platform for use in high functionality PICs and to compare performance of the QW-EAMs with OQW FK-EAMs, we have fabricated a set of widely tunable transmitters. Devices consisted of a four-section SGDBR laser, a 400-μm-long SOA and a 400-μm-long EAM. To minimize parasitic capacitance, photo-bis-benzocyclobutene was used as a low-k dielectric. The separation between the SGDBR front mirror and SOA postamplifier is 50 μm, and between the SOA postamplifier and EAM is 100 μm. Device isolation is accomplished by selective removal of the Zn : InGaAs layer and a proton implant. All transmitters were antireflection-coated, soldered on AlN carriers, and wirebonded for characterization. The temperature in the following experiments was held at 17 °C.

For the DQW SGDBR, on-chip light versus current characteristics and fiber coupled output spectra at various wavelengths have been collected. The on-chip light output–current–voltage (L–I–V) data is extracted by reverse biasing the SOA that spatially follows the front mirror of the laser, and monitoring the detected photocurrent. The threshold current for the SGDBR was 38 mA at 1550 nm and optical power levels up to 12 mW were observed at a gain region bias current of 100 mA. Superimposed fiber coupled SGDBR spectra at various wavelengths are shown in Fig. 2 with both laser gain and SOA biased at 100 mA. Output powers ranged from 0 dBm at 1532 nm to 5 dBm at 1560 nm with fiber coupling losses measured at 4.5 dB. The sidemode suppression ratio for all operating wavelengths is greater than 30 dB.

The performance of the DQW EAMs and OQW EAMs (1.41-μm bandgap, 2×10^{17} cm^{-3} Si) were evaluated based on several device characteristics. These included measurements of the broadband dc extinction, small signal 50 Ω terminated S_{21} electrical to optical response, and the large signal chirp.

Normalized dc extinction measurements are shown in Fig. 3. At wavelengths of 1532, 1545, and 1560 nm, respectively,

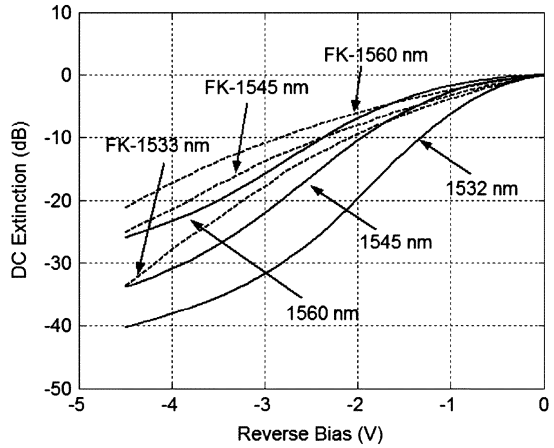

Fig. 3. Normalized dc extinction DQW (solid lines, 1532, 1545, and 1560 nm) and FK (dashed lines, 1533, 1545, 1560 nm) integrated EAMs.

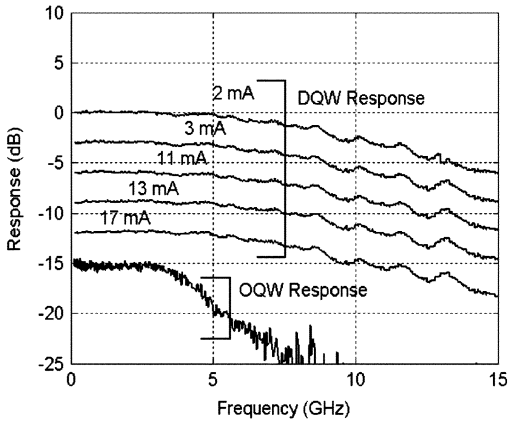

Fig. 4. S_{21} measurements for DQW and OQW EAMs. Data is spaced at 3-dB intervals for clarity Average waveguide photocurrent is indicated.

the DQW EAMs show modulation depths of −40, −33, and −26 dB, and peak modulation efficiencies of 16, 13, and 10 dB/V. Compared with FK-EAMs at similar wavelengths, this corresponds to improvements between 4 and 6 dB for the modulation depth and 4 and 3 dB/V for the modulation efficiency. The insertion loss of both EAM types is compared by combining the on-state insertion loss with the wavelength dependent propagation loss. The comparison is performed at dc bias points that maximize slope efficiency. For the QW-EAMs, the optimal slope efficiency at 1545 nm occurs at −2.4 V. With a 1-V pp modulation, the on-state loss from Fig. 3 is −5 dB. Combining this with the wavelength-dependent propagation loss for a 400-μm-long device, the total loss is −6.75 dB. A similar calculation for an FK-EAM operating at 1545 nm that has been biased for maximum slope efficiency (−4.5 V) gives a total EAM insertion loss of −18 dB.

Electrical-to-optical S_{21} measurements for OQW and DQW EAMs are shown in Fig. 4 at a bias of −3 V. The 3-dB bandwidth is improved from 4 to 10 GHz for the QW-EAMs. This result corresponds well with the larger depletion thickness that is expected using the lower waveguide doping employed in the DQW epitaxial structure. Since it is well known that

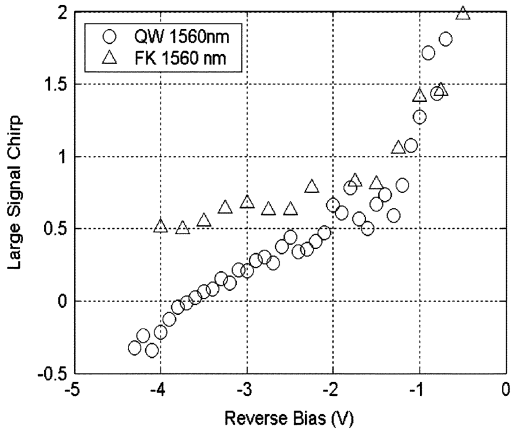

Fig. 5. The 10-Gb/s large signal time resolved chirp results at 1560 nm for integrated OQW FK-EAMs and DQW QW-EAMs under reverse bias.

QW-EAMs suffer from carrier screening effects, measurements on the DQW devices were performed for a variety of waveguide photocurrent levels. DQW EAMs show no deviation in bandwidth with up to 17 mA of photocurrent. Alternatively, similar FK-EAMs have been shown to be compatible with large optical power levels in [5].

The EAM chirp characteristics are shown in Fig. 5. This measurement was performed at 10 Gb/s using the Agilent Time Resolved Chirp (TRC) software with the SGDBR laser transmitters tuned to 1560 nm. This wavelength was selected because the large detuning between the laser wavelength and the waveguide absorption peak represents a condition where it is difficult to obtain small chirp values [3]. The DQW EAMs that employ the QCSE show lower chirp values at applied bias levels greater than −2 V, with zero chirp at −3.8 V.

V. Conclusion

We have demonstrated a DQW integration platform for advanced photonic circuits that requires a single blanket InP regrowth step to realize QW-EAMs, widely tunable lasers, and optical amplifiers. Integrated EAMs fabricated in this new platform show larger bandwidths, improved efficiency, lower insertion loss, and reduced chirp when compared with FK-EAMs that are available using a similar OQW platform.

References

[1] J. W. Raring, M. N. Sysak, A. Tauke-Pedretti, M. Dummer, E. J. Skogen, J. S. Barton, S. P. Senbaars, and L. A. Coldren, "Advanced integration schemes for high functionality/high performance photonic integrated circuits," in *Proc. Photonics West*, San Jose, CA, 2006.

[2] Y. A. Akulova, G. A. Fish, P. C. Koh, C. Schow, P. Kozodoy, A. Dahl, S. Nakagawa, M. Larsen, M. Mack, T. Strand, C. Coldren, E. Hegblom, S. Penniman, T. Wipiejewski, and L. A. Coldren, "Widely-tunable electroasbsorption-modulated sampled grating DBR laser transmitter," *IEEE J. Sel. Topics Quantum Electron.*, vol. 8, no. 6, pp. 1349–1357, Nov./Dec. 2002.

[3] G. L. Li and P. K. L. Yu, "Optical intensity modulators for digital and analog applications," *J. Lightw. Technol.*, vol. 21, no. 9, pp. 2010–2030, Sep. 2003.

[4] J. Dow and D. Redfield, "Toward a unified theory of Urbach's rule and exponential absorption edge," *Phys. Rev. B*, vol. 5, p. 594, Jan. 1972.

[5] L. A. Johansson, Y. A. Akulova, G. A. Fish, and L. A. Coldren, "High optical power electroabsorption modulator," *Electron. Lett.*, vol. 39, no. 4, pp. 364–365, Feb. 2003.

I. Photonic IC Technology & Devices

B. PIC Transmitters and Receivers

Low Drive Voltage, Negative Chirp 40 Gb/s EA-Modulator/Widely-Tunable Laser Transmitter, Using Quantum-Well-Intermixing

J.W. Raring[*], L.A. Johansson[†], E.J. Skogen[†], M.N. Sysak[†], H.N. Poulsen[†], S.P. DenBaars[*], and L.A. Coldren[*†]
[*] *Materials Dept. University of California, Santa Barbara, CA 93106*
[†] *ECE Dept. University of California, Santa Barbara, CA 93106*
Phone: 805.893.7163, Fax: 805.893.4500, Email: jraring@engineering.ucsb.edu

Abstract: We present the first 40Gb/s widely-tunable EAM/laser transmitters demonstrating 1.0-1.5V_{PtoP} drive, low-chirp, and under 0.5dB of power penalty for transmission through 2.3km of fiber. A robust quantum-well-intermixing technique was employed for the realization of these devices.

OCIS codes: (140.5960) Semiconductor lasers; (140.3600) Lasers, tunable; (250.5300) Photonic Integrated Circuits

1. INTRODUCTION

For the first time, an electroabsoprtion modulator (EAM) based widely-tunable transmitter demonstrating negative chirp performance at 40 Gb/s has been fabricated using a simple, robust quantum-well-intermixing (QWI) processing platform. The transmitter consists of a quantum-well (QW) EAM monolithically integrated with a widely-tunable sampled grating (SG) DBR laser. The EAMs demonstrated 3dB optical bandwidths of up to 39 GHz, low drive voltages (1.0-1.5 V_{PtoP}), and 0.2- 0.5 dB of power penalty for 40 Gb/s transmission through 2.3km of fiber across the wide tuning range of the SG-DBR laser. The QWI method facilitates a simple fabrication sequence avoiding the traditional processing complexity necessary for the integration of negative chirp EAMs with diode lasers.

Electroabsorption-modulated lasers are candidate sources for 40 Gb/s very-short-reach (VSR) router to router interconnect applications, as they are compact, potentially low-cost, and can facilitate low drive voltages with high bandwidth [1]. The monolithic integration of EAMs with widely-tunable lasers allows for inventory reduction and wavelength agile functionality. A QW-based EAM exploits the quantum confined stark effect resulting in increased efficiency over bulk Franz-Keldysh type EAMs, and allows for the possibility of achieving negative chirp. Previous reports of 40 Gb/s QW-EAMs either did not include an integrated laser or included a single frequency distributed feedback (DFB) laser [1, 2, 3].

Butt-joint regrowth is the traditional method implemented to monolithically integrate QW-EAMs with lasers. This method involves the selective removal of the as-grown waveguide/multiple QW (MQW) region followed by the regrowth of waveguide/MQW material with the desired band edge. Although the butt-joint regrowth process does allow each integrated component to possess a unique band edge, the difficulty associated with matching thickness and achieving the desired composition to avoid reflection and loss at the interface is great [4]. Selective area growth is another technique used to realize multiple band edges across a wafer. However, in addition to the lack of abruptness of the transition region, the thickness of the waveguide changes from one region to the next therefore modulating the optical confinement factor of the device in the axial direction. Another method uses the detuning of the DFB laser Bragg wavelength from the absorption edge of the MQW, allowing the same active layer to be used in the laser and EAM. However, this method imposes a performance trade-off between the laser and EAM [3]. The relatively simple QWI process employed in this work enables optimal placement of the QW band-edge in the laser, EAM, and passive sections without disturbing the waveguide in the axial direction [5].

2. EXPERIMENT

The transmitter used in this work was the output stage of an integrated transceiver, which also contained an SOA/photodetector receiver [6]. The receiver consists of a low-confinement semiconductor optical amplifier (SOA) for high saturation power and a uni-traveling carrier (UTC) photodiode capable of 40 Gb/s operation. Details of the receiver structures are given in [7, 8]. Here we focus on the transmitter, which contains a five section widely tunable sampled-grating (SG) distributed Bragg reflector (DBR) laser followed by an EAM. The 5 sections of the SG-DBR laser are, from back to front in Fig. 1a, backside absorber, rear mirror, phase, gain, and front mirror. The phase and mirror sections function to tune the wavelength of the laser [5]. The lithographically defined mirrors make the SG-DBR laser ideal for monolithic integration.

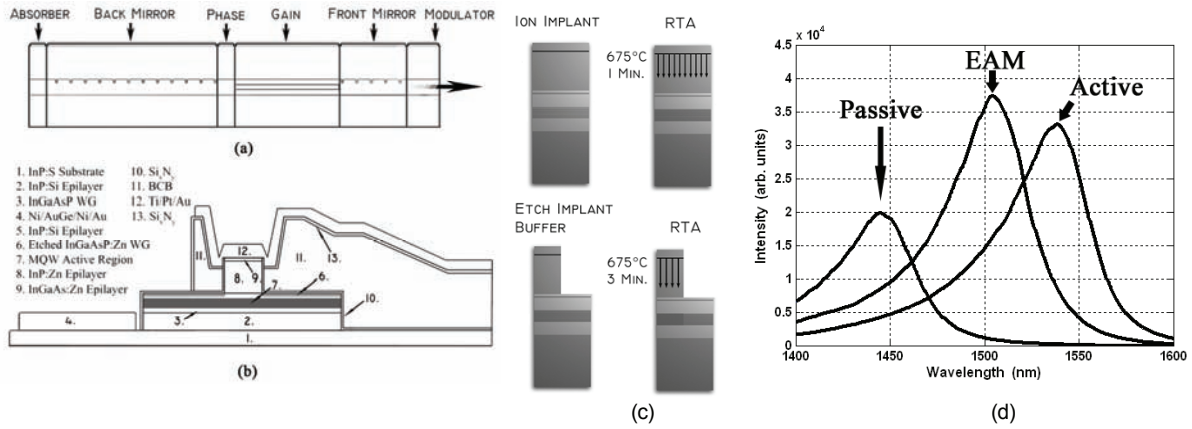

FIGURE 1. (a) Side view schematic of the SG-DBR/EAM device architecture. (b) Cross-sectional schematic of the 3 µm wide modulator sections. (c) Quantum well intermixing scheme used for device fabrication. (d) Photoluminescence of the as-grown active regions, partially intermixed EAM regions, and severely intermixed passive sections.

This work employs a modified ion-implantation enhanced QWI process described in [5]. In this process, point defects are created by ion implantation into an InP buffer layer over the MQW active region. During a high temperature anneal, the defects are diffused through the MQW region, promoting the interdiffusion of group V-atoms between the wells and barriers. The interdiffusion reshapes the QW profile resulting in a shift in the quantized energy levels in the well, and hence a shift in the band edge energy.

3. PROCESS

Two different epitaxial base structure MQW designs were explored in this work. The first consisted of 10 InGaAsP 6.5 nm compressively strained (0.9%) QWs and 8.0 nm tensile strained (0.3%) InGaAsP barriers. The second consisted of 15 InGaAsP 8.0 nm compressively strained (0.6%) QWs and 8.0 nm tensile strained (0.3%) InGaAsP barriers. Both MQW designs were centered within a 1.3Q waveguide. A standard surface ridge waveguide architecture was employed in the laser and EAM. A cross-section of the 3µm wide EAM region is shown in Fig. 1b. Using the intermixing process detailed in [5] and illustrated in Fig. 1c, the as-grown MQW band-edge (λ_{PL}= 1540nm) was blue-shifted in the EAM (λ_{PL}= 1505nm) and passive regions (λ_{PL}= 1440nm) as shown in Fig. 1d.

4. RESULTS

The surface ridge SG-DBR lasers using the 10 MQW design demonstrated over 30nm of tuning, threshold currents of 35mA, and output powers of 15-30mW at a gain section current of 150mA. At this operating point, a side mode suppression ratio (SMSR) greater than 35 dB was achieved. The EAMs with a length of 125µm demonstrated over 20 dB of DC extinction for wavelengths from 1535nm to 1560nm, with peak efficiencies of over 15 dB/V as shown in Fig. 2a for the 10 MQW device. The small signal response, shown in Fig. 2b, of the 10 and 15 MQW modulators terminated with 50Ω demonstrated 3dB optical bandwidths of 39 GHz and 35 GHz, respectively. The broadband large-signal chirp parameter was characterized using Time Resolved Chirp (TRC) software for both MQW designs with 1.5V_{PtoP} applied to the 10 MQW and 1.0V_{PtoP} applied to the 15 MQW EAM. As shown in Fig.

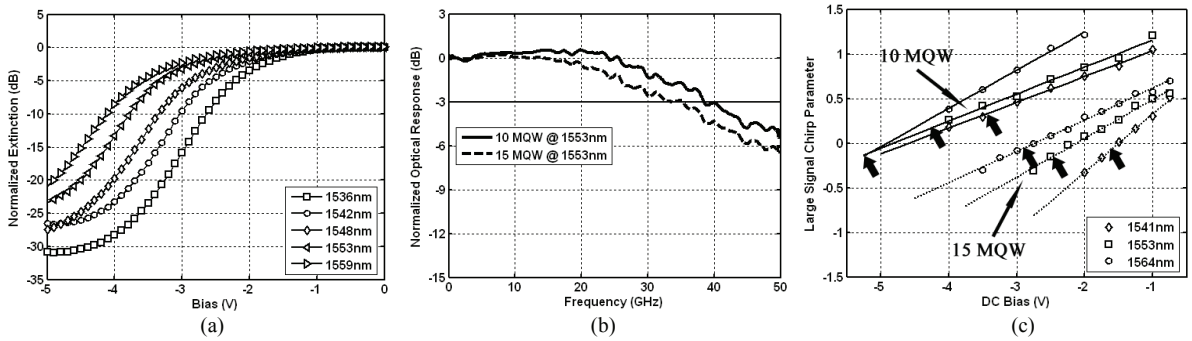

FIGURE 2. (a) Broadband DC extinction of 125µm EAM with 10 MQW design. (b) Small signal response of 125µm EAMs using 10 MQW and 15 MQW designs. (c) Broadband large signal chirp parameter of EAMs using the 10 MQW (1.5 V_{PtoP}) and 15 MQW (1.0 V_{PtoP}) designs with arrows indicating DC bias used for optimized 40 Gb/s eye diagrams shown in Fig. 3a for the 10 MQW EAM.

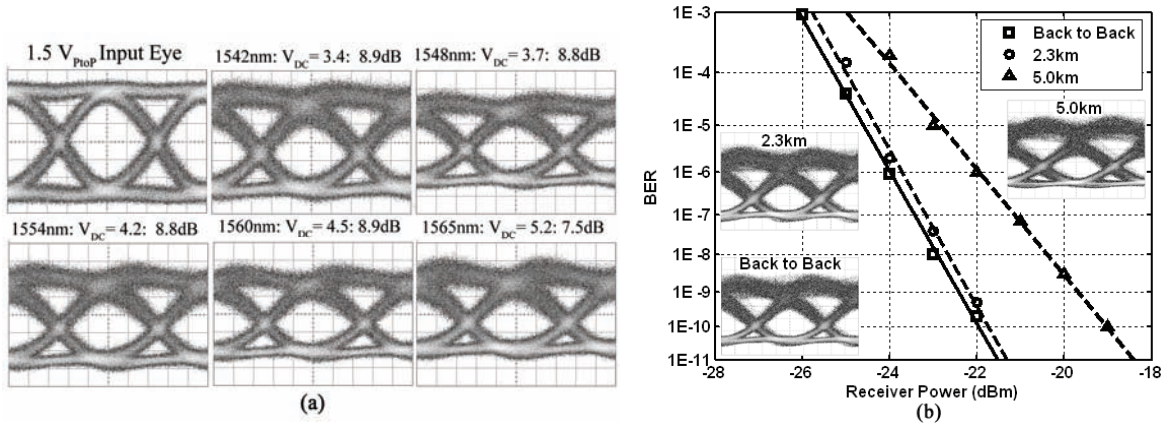

FIGURE. 3 (a) 40 Gb/s eye diagrams from 10 MQW device with a 1.5 V_{PtoP} drive and average fiber-coupled output powers of -5dBm to 0dBm. The wavelength, DC bias, and extinction ratio are depicted. (b) Bit error rate measurements from 10 MQW device at 40 Gb/s with a 1.5 V_{PtoP} drive and a wavelength of 1553nm. The back to back eye diagram along with the eye diagrams after transmission are shown as insets.

2c, the chirp parameter approaches zero and goes negative with increasing reverse bias for the QW-EAMs.

Non return to zero (NRZ) eye diagrams were taken at 40 Gb/s with a pseudo random bit sequence (PRBS) of 2^{31}-1 over the tuning range of the SG-DBR lasers for both MQW designs. In Fig. 3a, the back to back input eye along with device output eyes are shown for the 10 MQW EAM with a 1.5 V_{PtoP} drive and average fiber-coupled powers in the -5dBm to 0dBm range. Extinction ratios (ER) greater than 8.7dB are demonstrated for wavelengths up to 1560nm with DC bias levels ranging from 3.4V to 5.2V. The 15 MQW EAM required only a 1.0 V_{PtoP} drive to achieve similar values of ER across the SG-DBR tuning range. The DC bias points for optimized eye diagrams are indicated on Fig. 2c to demonstrate the expected chirp at these operating points. As can be seen, the predicted chirp for the 10 MQW EAMs ranges from -0.1 to 0.3 and for the 15 MQW the chirp parameter is negative in all cases.

40 Gb/s bit error rate (BER) testing was performed on the 10 MQW transmitter for transmission through 2.3km and 5km of standard Corning SMF-28 fiber. A PRBS of 2^7-1 was used due to a noise floor in the bit-error rate test set-up at longer word lengths. In Fig. 3, the BER results and the respective eye diagrams for transmission through fiber are shown for a wavelength of 1553nm using a 1.5 V_{PtoP} drive and a DC bias of 4.9V. The transmitter demonstrated between 0.2dB and 0.5dB of power penalty for transmission through 2.3km of fiber at wavelengths spanning from 1543nm to 1565nm. According to Fig. 2c, the operating points in this experiment were expected to provide slightly negative chirp. Upon increasing the transmission length to 5km, the power penalty increased to 3dB due to fiber dispersion.

5. CONCLUSION

For the first time, we have demonstrated high performance 40 Gb/s widely-tunable EAM/laser transmitters. The 10 MQW transmitters exhibited 39GHz of 3dB bandwidth, a 1.5 V_{PtoP} drive, negative chirp, and low power penalty transmission through 2.3km of fiber across the tuning range of the laser. The 15 MQW device required lower drive voltages (1.0 V_{PtoP}) and provided negative chirp at lower DC bias levels. This work was facilitated by a simple, robust QWI processing platform for the monolithic integration of blue-shifted QW-EAMs with SG-DBR lasers.

6. REFERENCES

[1] M. Okayasu, et al., "A 1550-nm 40-Gbit/s Electro-Absorption DFB Laser Diode Module for Transponders with Very Short Reach (<2 km) Applications" *Lasers and Electro-Optics Society, LEOS* Technical Digest paper WG2, 2004

[2] H. Fukano, et al., "Very Low Driving Voltage InGaAlAs/InAlAs Electroabsorption Modulators Operating at 40 Gbit/s," *IEE Electron. Lett*., vol. 41. No. 4, 2005.

[3] P. Gerlach, et al., " 40-Gbit/s Operation of Laser-Integrated Electroabsorption Modulator Using Identical InGaAlAs Quantum " *International Conference on Indium Phosphide and Related Materials.* Technical Digest. 2005

[4] J. Binsma, et al., "Characterization of Butt-Joint InGaAsP Waveguides and Their Application to 1310 nm DBR-Type MQW Gain-Clamped Semiconductor Optical Amplifiers," IEICE Trans. Electron., vol. E80-C, pp. 675-681, 1997.

[5] E. Skogen, et al., "Post-Growth Control of the Quantum-Well Band Edge for the Monolithic Integration of Widely-Tunable Lasers and Electroabsorption Modulators," IEEE *J. Sel. Topics Quantum Electron*. *IEEE J. Sel. Topics in Quantum Electron.*, vol. 9, pp. 1183-1190, 2003.

[6] J. Raring, et al, "Quantum Well Intermixing for Monolithic Integration: A Demonstration of Novel Widely-Tunable 10Gb/s Transmitters and Wavelength Converters," *Integrated Photonics Research Conf*., San Francisco 2004.

[7] J.W. Raring, et al., "Demonstration of high saturation power/high gain SOAs using quantum well intermixing and MOCVD regrowth," IEE Electronics Letts. vol.41, issue 24 pp. 1345-1346 Nov. 2005.

[8] J.W. Raring, et al., "Design and Demonstration of Novel Quantum Well Intermixing Scheme for the Integration of UTC–Type Photodiodes with QW–Based Components", IEEE Journal of Quantum Electronics, Vol. 42, No. 2, pp. 171-181, 2005.

A Quantum Well EAM-SGDBR Widely Tunable Transmitter Fabricated in a Novel Dual-Quantum-Well Integration Platform

Matthew N. Sysak, James W. Raring, Daniel J Blumenthal, Larry A Coldren
University of California Santa Barbara, Optoelectronic and Optical Devices, 93106 Santa Barbara, CA, USA
phone: 8058935828, fax: 8058937990, email: mnsysak@engineering.ucsb.edu

In this work we demonstrate for the first time a monolithically integrated, widely tunable, electroabsorption modulator (EAM) based sampled grating DBR (SGDBR) laser transmitter fabricated in a novel dual quantum well (DQW) integration platform that breaks the fabrication and growth barriers associated with integrating quantum well EAMs with laser sources. Compared with the well established offset quantum well (OQW) tunable transmitters [1,2], the DQW devices require no additional processing or growth steps, and demonstrate significant improvements in bandwidth, modulation efficiency, insertion loss, and chirp characteristics.

Monolithically integrated tunable transmitters containing EAMs are key components in next generation networks due their reduced packaging costs, small footprint, and their application to inventory reduction. Of particular importance are integrated transmitters with EAMs that utilize the quantum confined stark effect (QCSE) in quantum wells due to their large modulation efficiency and low chirp characteristics. Traditionally, integrated QCSE-based transmitters have required complex growth and/or processing techniques such as selective area growth (SAG), butt joint regrowth (BJG), or quantum well intermixing (QWI). As an alternative to these approaches, the OQW platform is attractive since it uses simple selective etch techniques to define active (gain) and passive (mirror tuning/EAM) regions and requires only a single blanket p-InGaAs/InP regrowth step [2]. However, until the work presented here intensity modulation in OQW integrated EAMs has been based on the Franz-Keldysh (FK) effect, which leads to limited modulation efficiency under low insertion loss conditions and positive chirp [3].

A diagram of the novel DQW platform is shown in Fig. 1. As in the OQW approach, fabrication consists of the selective removal of a set of quantum wells located above the optical waveguide layer to form gain and passive/EAM regions, followed by a blanket p-InP/InGaAs regrowth. In the DQW platform, an additional set of quantum wells consisting of 7x9 nm wells and 6x5 nm barriers is inserted into the center of the waveguide and utilized for modulation efficiency. Careful control of the emission wavelength of the waveguide wells (1480 nm) is used to manage band-tail absorption losses associated with the detuning between the waveguide and offset wells.

The DQW transmitter consists of a four section SGDBR laser [4], a 550 μm long semiconductor optical amplifier (SOA), and a 400 μm long EAM. A supermode spectrum from the transmitter along with an on-chip current versus optical power curve for the SGDBR is shown in Fig. 2 and Fig. 3 respectively. The on-chip laser power is extracted by measuring the photocurrent that was generated when the SOA that follows the SGDBR is reverse biased and the SGDBR laser is forward biased. At 1550 nm greater than 20 mW is generated from the SGDBR at 130 mA. Fiber coupled optical power levels ranged from 0 dBm at 1532 nm to 5 dBm at 1560 nm with both the SGDBR gain and SOA biased at 100 mA. Side mode suppression ratio (SMSR) measurements over 45 channels spaced at 100 GHz (Fig. 4) was > 30 dB.

Measurements of the integrated DQW EAM DC extinction, the 50 Ω terminated electrical to optical frequency response, and large signal time resolved chirp (TRC) are shown in Fig. 5, Fig. 6, and Fig. 7 respectively. DQW EAMs slope efficiencies ranged from 10 dB/V to 16 dB/V at 1560 nm and 1532 nm and modulation depths were up to 40 dB. The 3-dB bandwidth was in excess of 10 GHz and the chirp at 10 Gb/s reaches zero at a bias of -3.6 V. We have included data from the FK-EAMs in an OQW transmitter with a moderately Si-doped waveguide ($2x10^{17}$ cm^{-3}, 1.41 μm bandgap) in these Figures, along with a separate comparison of the slope efficiency at 1545 nm (Fig. 8). Using the DQW approach, EAM bandwidth is improved from 4 to 10 GHz, slope efficiency at 1545 nm is improved from 9 to 13.5 dB/V, and the chirp is clearly reduced.

In summary, we have demonstrated the first widely tunable transmitter fabricated on a DQW integration platform that utilizes the QCSE for modulation efficiency but maintains the simple fabrication requirements of the more traditional OQW approach. The DQW transmitters showed significantly improved modulation efficiency, bandwidth and chirp characteristics compared with the traditional OQW platform.

[1] Y. Akulova et al., *J. Select. Topics in Quantum. Electron.,* vol. 8, p. 1349 (2002).
[2] B. Mason et al., *IEEE Photon. Technol. Lett.*, vol. 11, p. 638 (1999).
[3] G. L. Li et al., *J. Lightwave Technol.*, vol. 21, pp. 2010 (2003).
[4] M. Sysak et al., *IEEE Photon. Technol. Lett.*, vol. 16, p. 2093 (2004).

This work was supported by DARPA/MTO CS-WDM under grant No. N66001-02-C-8026 and by Intel Corporation under grant No. TXA001630000

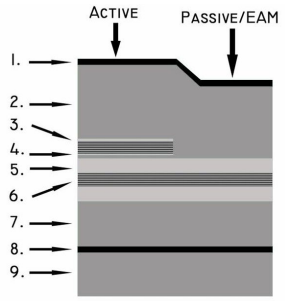

Region	Description
1	p-contact
2	p-cladding
3	Offset QWs
4	Stop Etch
5	Waveguide
6	Centered QWs
7	n-Buffer
8	n-contact
9	Fe-substrate

Fig.1. Epitaxial layer structure of the dual quantum well integration platform.

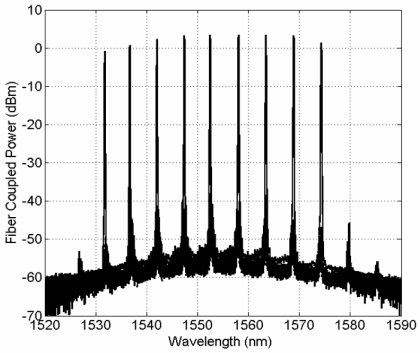

Fig. 2. Supermode spectrum of DQW SGDBR. Laser gain and SOA are at 100 mA bias.

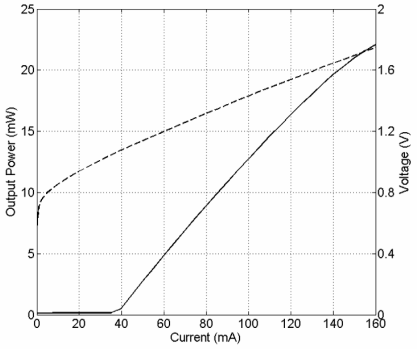

Fig. 3. Current vs. voltage (dashed line) and on-chip optical power (solid line) from the DQW SGDBR at 1550 nm.

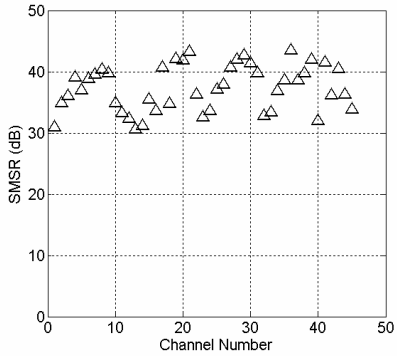

Fig. 4. SMSR measurements for DQW SGDBR over 45 channels spaced at 100 GHz. (1535 nm to 1570.2 nm)

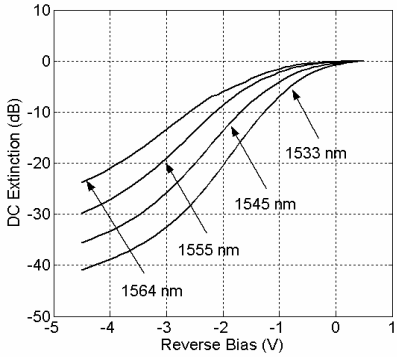

Fig. 5. DC extinction characteristics of the DQW EAM (400 μm).

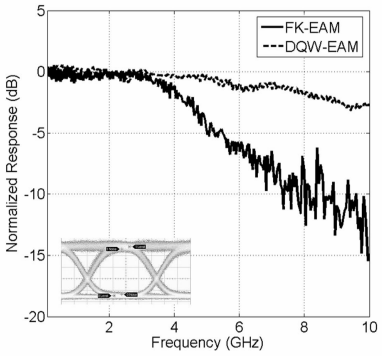

Fig 6. Frequency response of 50 Ω terminated QW-EAM and FK-EAMs. A 10 Gb/s eye diagram is embedded in the figure (1550 nm, -2 V bias, 1.2 V pp drive voltage)

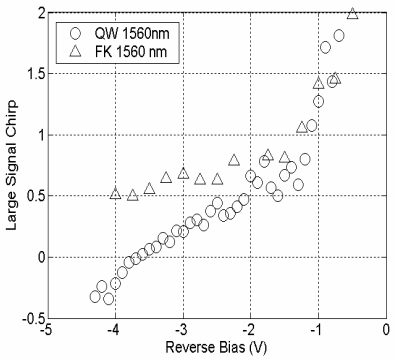

Fig. 7. Large signal chirp measured measurement for DQW-EAMs and FK-EAMs the Agilent Time resolved chirp software. Transmitter wavelength is 1560 nm.

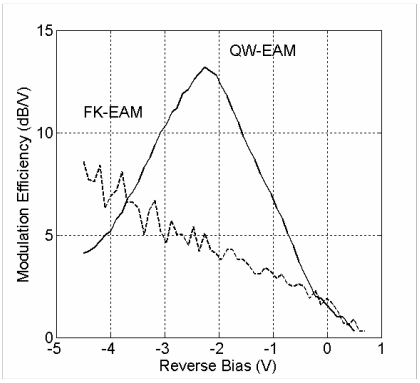

Fig. 8. Modulation efficiency comparison of OQW and DQW EAMs (1545 nm)

This work was supported by DARPA/MTO CS-WDM under grant No. N66001-02-C-8026 and by Intel Corporation under grant No. TXA001630000

40 Gbit/s photonic receivers integrating UTC photodiodes with high- and low-confinement SOAs using quantum well intermixing and MOCVD regrowth

J.W. Raring, L.A. Johansson, E.J. Skogen, M.N. Sysak, H.N. Poulsen, S.P. DenBaars and L.A. Coldren

Photonic receivers integrating unitravelling carrier (UTC) photodiodes with high saturation power/high gain semiconductor optical amplifiers (SOAs) are presented. The SOAs demonstrated up to 28 dB of gain with saturation output powers of up to 18.6 dBm, while the UTC photodiodes were capable of 40 Gbit/s operation under high photocurrent operation. The chip-coupled receiver sensitivity was better than −20 dBm at 40 Gbit/s. A high-flexibility quantum well intermixing and MOCVD regrowth integration method was used for device fabrication.

Introduction: Photonic integrated circuits (PICs) hold the potential to revolutionise the photonics industry. High-functionality PICs offering light generation, detection, modulation, amplification, switching, and transport on a single chip will facilitate reduced cost, size, and power dissipation. Optimised complex PICs will not only require multiple quantum well (QW) band edges, but will also need differing amounts of gain and optical confinement, and in some cases, a radically different internal structure. In a preamplified receiver consisting of an SOA and photodetector, a low optical confinement multiple QW (MQW) active region is attractive for high saturation power performance since the photon density within the QWs can be kept relatively low. The UTC photodiode is a unique photodetector structure developed specifically to mitigate the influence of hole transport on the operation of the detector facilitating superior photocurrent handling capabilities over conventional *pin*-type detectors.

With the addition of simple blanket regrowth steps to a robust quantum well intermixing (QWI) scheme, we have demonstrated a method to integrate UTC photodiodes and SOAs utilising gain regions of both low and high optical confinement with high performance widely-tunable transmitters [1, 2]. Here we report the results from photonic receivers comprising UTC photodiodes and SOAs fabricated on the same chip as 40 Gbit/s widely-tunable transmitters reported elsewhere [3]. The dual section SOAs contain a high optical confinement centred multiple quantum well (c-MQW) front-end for high incremental gain followed by a low optical confinement offset MQW (o-MQW) section for high saturation power. The SOAs demonstrated up to 28 dB of gain with saturation output powers of 18.2–18.6 dBm, and the photodiodes demonstrated 40 Gbit/s operation under high photocurrent operation. When combined to form photonic receivers, chip-coupled sensitivities better than −20 dBm were demonstrated at 40 Gbit/s. The fabrication method involved only simple blanket MOCVD regrowth steps.

Experiment: Device fabrication begins with MOCVD growth of the epitaxial base structure consisting of ten 6.5 nm QWs separated by 11 8.0 nm barriers centred within two InGaAsP:Si waveguide layers for maximum optical confinement in the MQW (12.6%). The samples were subjected to our QWI process described in [4] to shift the as-grown c-MQW peak photoluminescence (PL) wavelength from 1540 to 1505 nm in EAM regions, and to 1440 nm in regions where passive waveguides, low-confinement o-MQW sections, or UTC-type detectors were desired.

After completion of the QWI process, a blanket MOCVD regrowth was performed to deposit the low confinement o-MQW layer structure with a peak PL wavelength of 1550 nm. A 140 nm InP confinement tuning layer (CTL) was placed between the intermixed c-MQW and active o-MQW to yield an optical confinement factor of ∼1.4% for the five offset wells. The sample was patterned and wet etched for selective removal of the o-MQW regrowth layer stack. A second blanket MOCVD regrowth was performed for the UTC photodiode layer structure. In this work we use a 200 nm InP collector layer and a 50 nm InGaAs:Zn absorber layer. Further details of the o-MQW and UTC layer structures can be found in [1, 2]. After selective removal of the UTC regrowth layer stack, a final blanket MOCVD regrowth was performed to grow the *p*-type InP:Zn cladding and *p*-contact InGaAs:Zn layers. A schematic side view illustrating the high confinement c-MQW regions, low confinement o-MQW regions, and UTC photodiode regions used in the photonic receivers is shown in Fig. 1.

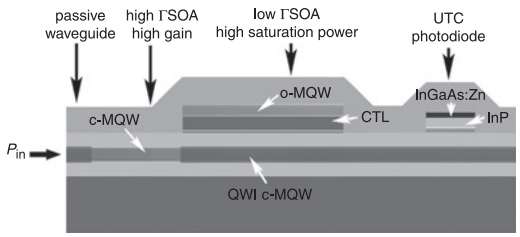

Fig. 1 *Side view schematic of device structure showing high confinement c-MQW gain region (left), low confinement o-MQW gain region (middle), UTC photodiode structure (right) grown over regions in which c-MQW has been intermixed*

Standard processing techniques were used for the definition of surface ridge waveguides and photo-benzocyclobutene was employed underneath the photodiode *p*-metal electrodes for capacitance reduction. The wafers were thinned, cleaved into bars, antireflection (AR) coated, separated into SOA/UTC receivers, soldered to AlN carriers, and wire bonded to a matched load of 50 Ω on the carrier for RF characterisation. The devices were placed on a copper stage cooled to 18°C for characterisation.

Results: The SOA/UTC receivers employed curved/flared input waveguides in addition to the AR coating to reduce facet reflections. The chip coupling loss was estimated to be ∼4 dB. Two receiver designs were explored. The first design (design 1) consisted of a dual section SOA with a 5 × 250 μm high-gain c-MQW section and a 5 × 1650 μm high-saturation-power o-MQW section followed by a 3 × 30 μm UTC photodiode. The second design (design 2) consisted of a dual section SOA with a 5 × 400 μm high-gain c-MQW section and a 5 × 1500 μm high-saturation-power o-MQW section followed by a 3 × 40 μm UTC photodiode. The TE polarisation state was used during all testing owing to the polarisation sensitivity of the integrated SOAs.

The measured chip gain against input power characteristics is shown in Fig. 2 for the two SOA types at an input wavelength of 1550 nm. As shown in the Figure, design 1, making use of the 250 μm-long c-MQW section, provides a peak gain of over 22 dB and a saturation power of 18.6 dBm while design 2 with a 400 μm-long c-MQW section provides a peak gain of over 28 dB and a saturation output power of 18.2 dBm. The SOAs demonstrated less than 1 dB of gain deviation for input wavelengths from 1535 to 1565 nm.

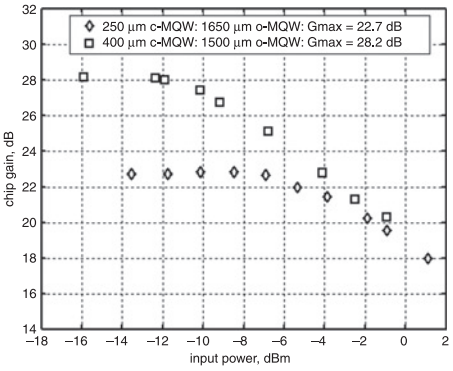

Fig. 2 *Gain against input power for dual section SOAs employing two different designs*

In both cases c-MQW sections operating at 15 kA/cm^2 and o-MQW sections operating at 6 kA/cm^2. Input wavelength 1550 nm

The internal quantum efficiency of the 30 and 40 μm-long photodiodes was measured at 28 and 32%, respectively, at an input wavelength of 1550 nm. The reduced UTC quantum efficiency from that demonstrated by previous devices reported in [1] is believed to be due to a fabrication issue. The frequency response of the UTC photodiodes was measured out to 20 GHz using an Agilent Lightwave Component Analyser (LCA). The detectors demonstrated only ∼1 dB of roll-off at the 20 GHz limit of our testing capability with a 3 V reverse bias and an average photocurrent level of 20 mA.

To demonstrate high-speed receiver functionality, eye diagrams and bit error rate (BER) measurements were performed on the two receiver designs at 40 Gbit/s. A pseudorandom bit sequence of $2^7 - 1$ was used due to a noise floor in the bit error rate test setup at longer word lengths. The 40 Gbit/s non-return-to-zero signal was fed through a bandpass filter, optical attenuator and polarisation controller before entering the input waveguide where it was amplified in the SOA and detected in the UTC photodiode. The receiver output eye diagrams shown in Fig. 3 are clear and open. The device employing design 1 (Fig. 3*a*) demonstrates up to 300 mV of output amplitude, while the device employing design 2 (Fig. 3*b*) demonstrates up to 500 mV of output amplitude. As shown in the BER results of Fig. 4, receiver design 1 demonstrated error-free operation (10^{-9}) with a chip-coupled power of −16.8 dBm while receiver design 2 required only −20.2 dBm for error-free operation. The increased sensitivity of receiver design 2 is a result of the higher gain provided by the SOA and slightly higher quantum efficiency of the photodiode within this design.

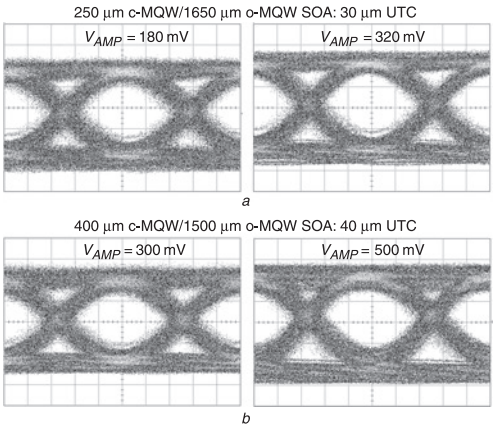

Fig. 3 *40 Gbit/s eye diagrams from receiver design 1 at c-MQW current density of 8 kA/cm² and receiver design 2 at c-MQW current density of 12 kA/cm²*

a Design 1, c-MQW current density of 8 kA/cm²
b Design 2, c-MQW current density of 12 kA/cm²
In both cases o-MQW sections operated at 5 kA/cm² and detectors biased at 3 V

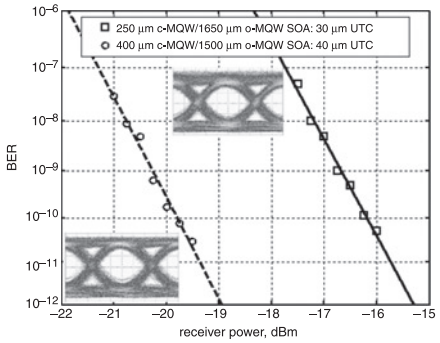

Fig. 4 *40 Gbit/s BER against received power for two dual section SOA/UTC photodiode receiver designs*

SOA operating conditions identical to those stated in Fig. 3
Insets: Eye diagrams

Conclusions: We have demonstrated 40 Gbit/s photonic receivers integrating low and high optical confinement SOAs with UTC photodiodes. The devices were fabricated on the same chip as widely-tunable 40 Gbit/s transmitters using a high-flexibility integration scheme. The SOAs within the receiver demonstrated up to 28 dB of gain with saturation output powers in the 18.5 dBm range and the UTC photodiodes were capable of 40 Gbit/s operation. BER measurements of the two receiver designs explored in this work demonstrated chip-coupled sensitivities of −16.8 and −20.2 dBm at 40 Gbit/s.

2 May 2006
Electronics Letters online no: 20061368
doi: 10.1049/el:20061368

J.W. Raring and S.P. DenBaars (*Materials Department, University of California, Santa Barbara, CA 93106, USA*)

L.A. Johansson, E.J. Skogen, M.N. Sysak, H.N. Poulsen and L.A. Coldren (*Electrical and Computer Engineering Department, University of California, Santa Barbara, CA 93106, USA*)

E-mail: jraring@engineering.ucsb.edu

References

1 Raring, J.W., *et al.*: 'Design and-demonstration of novel quantum well intermixing scheme for the integration of UTC-type photodiodes with QW-based components', *IEEE J. Quantum Electron.*, 2005, **42**, (2), pp. 171–181
2 Raring, J.W., *et al.*: 'Demonstration of high saturation power/high gain SOAs using quantum well intermixing and MOCVD regrowth', *Electron. Lett.*, 2005, **41**, (24), pp. 1345–1346
3 Raring, J.W., *et al.*: 'Low drive voltage, negative chirp 40 Gbit/s EA-modulator/widely-tunable laser transmitter, using quantum-well-intermixing'. Optical Fiber Communications Conf. (OFC'06), Postdeadline Tech. Digest Optical Society of America, PDP 26, 2006
4 Skogen, E., *et al.*: 'Post-growth control of the quantum-well band edge for the monolithic integration of widely-tunable lasers and electroabsorption modulators', *IEEE J. Sel. Top. Quantum Electron.*, 2003, **9**, pp. 1183–1190

40-Gb/s Series-Push-Pull Mach–Zehnder Transmitter on a Dual-Quantum-Well Integration Platform

Anna Tauke-Pedretti, *Student Member, IEEE*, Matthew N. Sysak, *Member, IEEE*, Jonathon S. Barton, *Member, IEEE*, James W. Raring, *Student Member, IEEE*, Leif Johansson, *Member, IEEE*, and Larry. A. Coldren, *Fellow, IEEE*

***Abstract*—A series-push-pull Mach–Zehnder modulator is integrated with a sampled-grating distributed Bragg reflector laser on a dual-quantum-well integration platform. The device exhibited greater than 7.8-dB extinction at 40 Gb/s with a 2.5-V drive voltage across a wavelength range of 1541–1566 nm. Bit-error-rate measurements at 10 Gb/s showed error-free operation and negative chirp.**

***Index Terms*—Mach–Zehnder modulator, offset quantum wells, optical modulation, optical transmitters, photonic integrated circuits (PICs), sampled-grating distributed Bragg reflector laser (SGDBR), semiconductor optical amplifier (SOA), tunable lasers.**

I. Introduction

INCREASED data volumes in next-generation networks are requiring transmission systems to embrace 40-Gb/s data rates. Such systems require transmitters with low drive voltages for minimal power consumption, high bandwidths to accommodate increased bit rates, and tailorable chirp to counteract dispersion. While some of these needs can be addressed with electroabsorption modulator (EAM)-based transmitters, it has been difficult to demonstrate an EAM-based solution with tunable chirp. As a more viable alternative, Mach–Zehnder-modulator-based transmitters are well positioned to manage the detrimental dispersion effects at these high bit rate [1].

Previously, several 40-Gb/s transmitters have been reported; these devices include discrete high-speed InP-based Mach–Zehnder modulators [1], [2] and monolithically integrated transmitters [3]. Of particular interest is a small footprint, high-speed Mach–Zehnder modulator integrated with a widely tunable laser similar to [3] that uses quantum-wells within the waveguide for highly efficient index modulation and low capacitance [4]. These broadband transmitters reduce packaging costs, decrease coupling losses, and reduce network provider inventory requirements.

This letter presents a 40-Gb/s widely tunable Mach- Zehnder transmitter fabricated on a dual-quantum-well (DQW) integration platform. This device implements a widely tunable sampled-grating distributed Bragg reflector (SGDBR) laser, two parallel semiconductor optical amplifiers (SOAs) within the interferometer and a series-push-pull Mach–Zehnder modulator with an integrated termination resistor.

Manuscript received May 11, 2006. This work was supported by Defense Advanced Research Projects Agency (DARPA) MTO-LASOR Grant W911NF-04-9-0001 and MTO-CS-WDM Grant N66001-02-C-8026.

The authors are with the Department of Electrical and Computer Engineering and the Department of Materials, University of California Santa Barbara, Santa Barbara, CA 93106 USA (e-mail: atauke@engineering.ucsb.edu).

Digital Object Identifier 10.1109/LPT.2006.881668

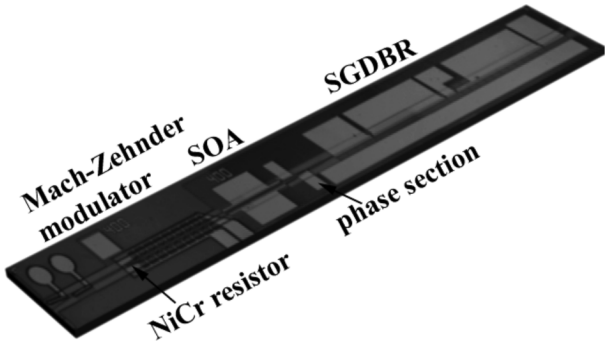

Fig. 1. Diagram of integrated widely tunable transmitter chip.

II. Device and Integration Platform

A schematic of the widely tunable Mach–Zehnder transmitter is shown in Fig. 1. The SGDBR laser consists of five sections—an active absorber, a rear mirror, a phase section, a 500-μm-long gain section, and a front mirror. This is followed by a Mach–Zehnder interferometer with a 400-μm SOA in each arm to increase the output power of the device and compensate for propagation losses. Phase sections within the interferometer arms are forward biased to achieve π-phase-shift. A flared and curved output waveguide, as well as an antireflection-coating was used to reduce optical reflections and to aid in fiber coupling.

The 400-μm-long Mach–Zehnder is operated in a series-push-pull fashion with the RF signal applied across the modulator electrode (Fig. 2). This configuration allows for small chirp values and high bandwidth due to the series connection of the two Mach–Zehnder arms. The modulator has a traveling wave electrode segmented into 8–50-μm-long T-sections to capacitively load the transmission line allowing for better impedance matching to 50 Ω [3], [5]. The ridge width is reduced from 3 μm in the laser and SOA regions to 2 μm within the modulators. In addition to the thinner ridge widths, photo-bis-benzocyclobutene (BCB) is used underneath the modulator electrode to reduce the parasitic capacitance. An integrated 50-Ω NiCr load resistor provides on chip termination, thus reducing RF losses.

The fabrication of this device requires a single blanket regrowth of the InP cladding and InGaAs contact layer following the selective removal of the set offset quantum-wells from the

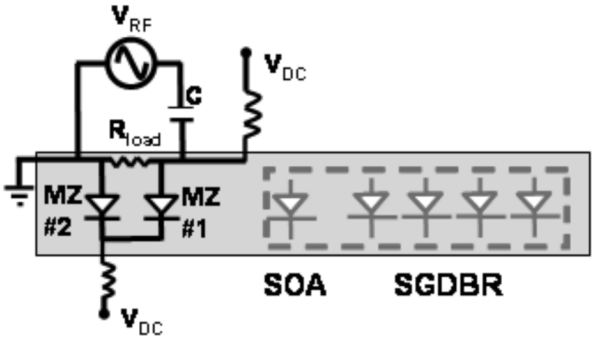

Fig. 2. Schematic of series-push-pull biasing scheme.

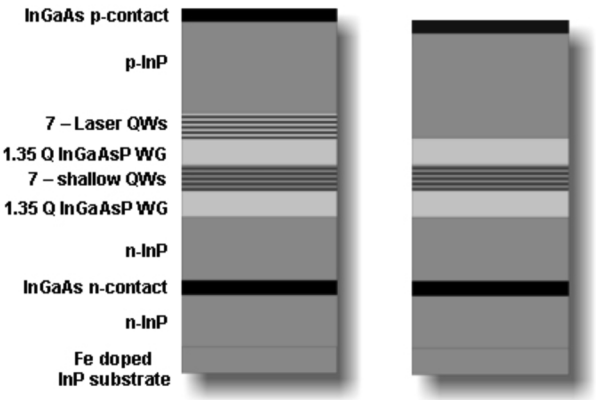

Fig. 3. Schematic of the DQW integration platform. The SOA and laser gain regions with the offset-quantum-wells are on the left. Passive and modulation regions with the offset wells removed is shown on the right.

passive sections and the etching of holographically defined sampled gratings.

The transmitter's metal–organic chemical vapor deposition grown epitaxial structure (Fig. 3) is based on the DQW integration platform [6]. In this approach, a set of offset quantum-wells (photoluminescence $= 1550$ nm) located above the waveguide layer are used for the gain section of the SGDBR and the SOAs. A separate set of quantum-wells (photoluminescence $= 1480$ nm) are centered in the InGaAsP waveguide layer to aid the modulator efficiency. The implementation of the DQW integration platform provides a reduction in capacitance and thus an increase in bandwidth compared to bulk waveguide devices. This is due to the lower waveguide doping requirement in the DQW devices which increases the p-n junction depletion region.

III. Experiments

Following fabrication, the devices were thinned, cleaved, and mounted onto an aluminum nitride carrier for testing. All dc contacts were wirebonded to the carrier and contacted via a probe card. The modulator was directly probed with a ground-signal RF probe to prevent any parasitic effects from wirebonds.

Single-sided dc extinction for the 400-μm-long device was measured with one electrode held at a constant 0-V bias while the bias voltage across the other electrode was varied between

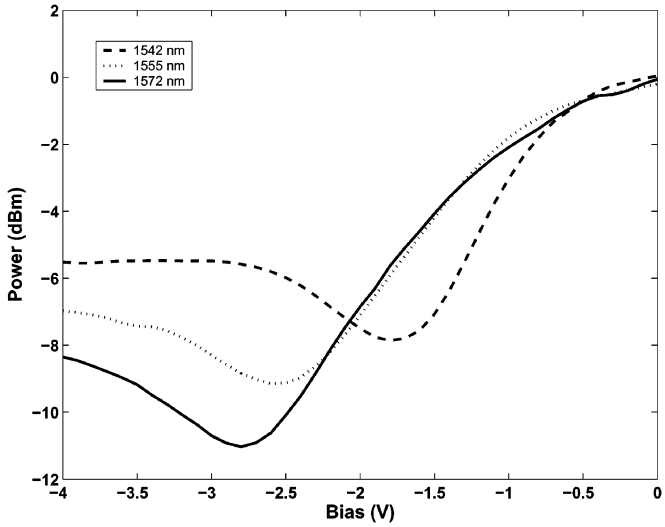

Fig. 4. DC extinction versus voltage for single-sided 400-μm-long devices. ($P_{\rm out} \simeq 1$ mW).

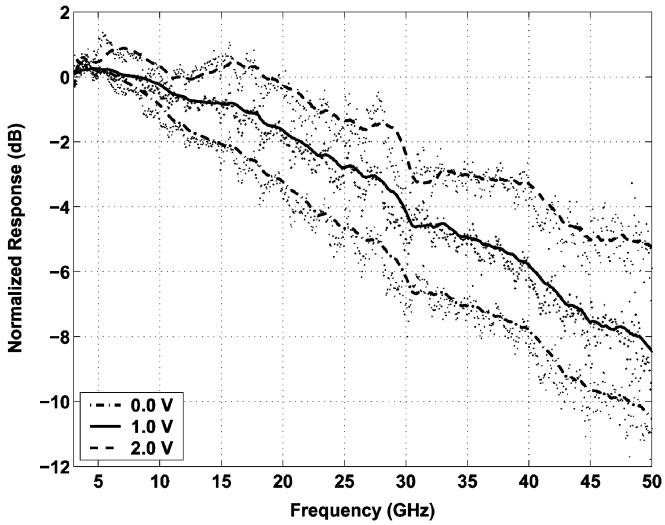

Fig. 5. Bandwidth of transmitter of different Mach–Zehnder reverse biases. ($I_{\rm gain} = 130$ mA; $I_{\rm SOA1} = I_{\rm SOA2} = 100$ mA; $I_{\rm phase} = 9.575$ mA).

-4 and 0 V. As shown in Fig. 4, the wavelength dependence of the device shows a V_π variation of $\sim$1 V across the wavelength range. The maximum dc extinction value increases with longer wavelengths where there is less absorption so there is a better optical power balance between the Mach–Zehnder arms. This power differential is not an issue when the device is operated in a series-push-pull fashion, since both arms have an identical dc reverse bias and the absorption is similar.

Bandwidth measurements have been taken for various modulator biases. A maximum bandwidth of 35 GHz was observed at -2-V dc bias, at which point the waveguide is fully depleted (Fig. 5).

A 40-Gb/s signal with 2.5 V_{p-p} from an SHF bit-error-rate tester (BERT) was used to drive the modulator. Eye diagrams with a $\sim$0.24-mW power swing demonstrated extinction ratio values of 7.9–9.0 dB across the 25-nm tuning range (Fig. 6). The modulator was biased at -1.5 V for 1556 and 1566 nm,

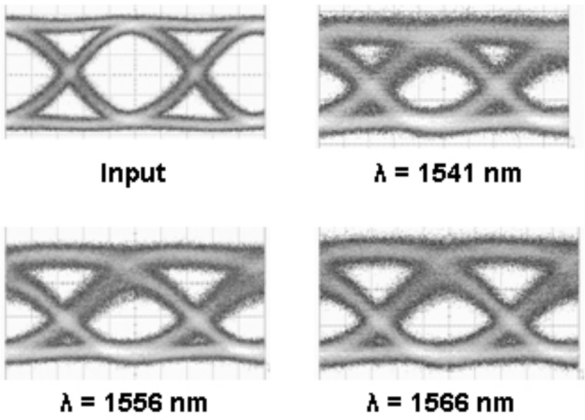

Fig. 6. Eyes at 40 Gb/s for $2^7 - 1$ PRBS and $V_{p-p} = 2.5$ V. ($\lambda = 1541$ nm, $V_{\mathrm{MZ1}} = V_{\mathrm{MZ2}} = -1$ V, $P_{\mathrm{out}} = 0.240$ mW. Extinction ratio $= 7.8$ dB;$\lambda = 1557$ nm, $V_{\mathrm{MZ1}} = V_{\mathrm{MZ2}} = -1.5$ V, $P_{\mathrm{out}} = 0.249$ mW. Extinction ratio $= 9.0$ dB; $\lambda = 1566$ nm, $V_{\mathrm{MZ1}} = V_{\mathrm{MZ2}} = -1.5$ V, $P_{\mathrm{out}} = 0.241$ mW. Extinction ratio $= 7.8$ dB).

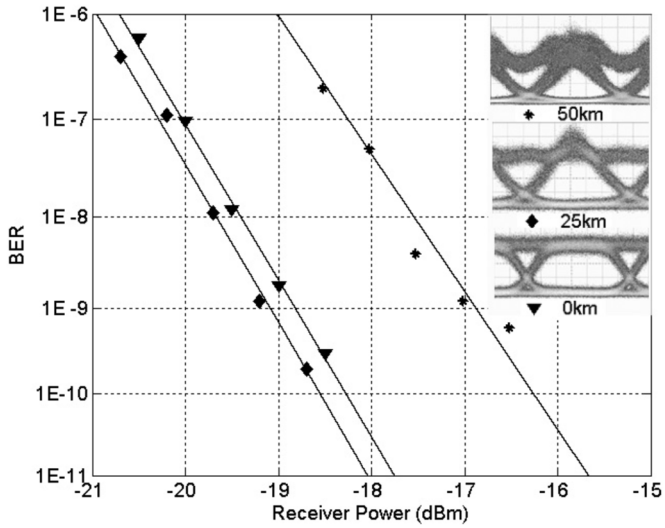

Fig. 7. BER versus receiver power at 10 Gb/s for a wavelength of 1541 nm. BER measurements were taken for transmission through 0, 25, and 50 km of Corning SMF-28 fiber. ($V_{p-p} = 1.87$ V; $V_{\mathrm{MZ1}} = V_{\mathrm{MZ2}} = -1$ V).

while -1 V was required at 1541 nm due to increased insertion losses.

BER testing at 10 Gb/s with a nonreturn-to-zero $2^{31} - 1$ pseudorandom bit sequence was done across the tuning range for both back-to-back and transmission through 25 and 50 km of Corning SMF-28 fiber. The modulator was biased at -1 V across each arm and driven with a 1.87 V_{p-p} electrical signal from a HP 70843B BERT. The optical signal from the device was amplified with a high power erbium-doped fiber amplifier followed by an optical filter, fiber for transmission, and an attenuator before being detected by an HP 83434A 10-Gb/s photoreceiver. Error-free operation (better than $1e - 9$ BER) and dynamic extinction ratios in excess of 10 dB were achieved across a wavelength range greater than 25 nm. Chirp values were calculated by fitting the data to the relationship between power penalty and distance described in [7]. Transmission power penalties corresponding to chirp values of -0.28, -0.46, and -0.96 were measured for wavelengths of 1568, 1556, and 1541 nm, respectively (Fig. 7).

IV. Conclusion

A widely tunable Mach–Zehnder transmitter has been fabricated on a DQW platform utilizing waveguide quantum wells for index modulation. The device demonstrates a bandwidth in excess of 35 GHz and at 40-Gb/s extinction ratios >7.8 dB are seen across the wavelength range of 1541–1566 nm. Error-free operation at 10 Gb/s has been demonstrated for up to 50 km of transmission through fiber and all wavelengths have negative chirp with a 1.87 V_{p-p} drive voltage.

References

[1] K. Tsuzuki, K. Sano, N. Kikuchi, N. Kashio, E. Yamada, Y. Shibata, T. Ishibashi, M. Takumitsu, and Y. Yasaka, "0.3 V_{pp} single-drive push-pull InP Mach–Zehnder modulator module for 43-Gbit/s systems," in *Optical Fiber Communication Conf. and Exposition and The National Fiber Optic Engineers Conf.*, Anaheim, CA, Mar. 2006, Paper OWC2.

[2] S. Akiyama, S. Hirose, T. Watanabe, M. Ueda, S. Sekiguchi, N. Morii, T. Yamamoto, A. Kuramata, and H. Soda, "Novel inp-based mach-zehnder modulator for 40 gb/s integrated lightwave source," in *IEEE 18th Int. Semiconductor Laser Conf.*, 2002, pp. 57–58.

[3] J. S. Barton, M. L. Masanovic, A. Tauke-Pedretti, E. J. Skogen, and L. A. Coldren, "Monolithically-integrated 40 gbit/s widely-tunable transmitter using series push-pull Mach-Zehnder modulator SOA and sampled-grating dbr laser," in *Optical Fiber Communication Conf. and Exposition and The National Fiber Optic Engineers Conf.*, Anaheim, CA, Mar. 2005, Paper OTuM3.

[4] W. Bardyszewski, D. Yevick, L. Yong, C. Rolland, and S. Bradshaw, "Theoretical and experimental analysis of mach-zehnder quantum-well modulators," *J. Appl. Phys.*, vol. 80, pp. 1136–41, Jul. 1996.

[5] R. G. Walker, "High-speed iii-v semiconductor intensity modulators," *IEEE J. Quantum Electron.*, vol. 27, no. 3, pp. 654–667, Mar. 1991.

[6] M. N. Sysak, J. W. Raring, D. J. Blumenthal, and L. A. Coldren, "A quantum well eam-sgdbr widely tunable transmitter fabricated in a novel dual-quantum-well integration platform," in *Device Research Conf. (DRC)*, University Park, PA, Jun. 2006, vol. IIA-2.

[7] G. P. Agrawal and 2002*, Fiber-Optic Communication Systems*, 3 ed. New York: Wiley.

Single-Chip 40Gb/s Widely-Tunable Transceivers with Integrated SG-DBR Laser, QW EAM, UTC Photodiode, and Low Confinement SOA

J. W. Raring[*], L.A. Johansson[†], E.J. Skogen[†], M.N. Sysak[†], H.N. Poulsen[†], S.P. DenBaars[*], and L.A. Coldren *[†]

[*]*Materials Engineering, University of California, Santa Barbara, CA 93106*
[†]*Electrical and Computer Engineering, University of California, Santa Barbara, CA 93106*
Phone: 805-893-7163, Fax: 805-893-4500, Email: jraring@engineering.ucsb.edu

Abstract

We present the first single-chip, widely-tunable 40Gb/s transceivers. The devices integrate sampled grating DBR lasers with electroabsorption modulators, low optical confinement semiconductor optical amplifiers, and uni-traveling carrier photodiodes.

I. Introduction

The generation, detection, modulation, amplification, and transport of light on a single chip allows for a new generation of high-functionality photonic integrated circuits (PICs) with reduced cost, size, and power dissipation. For these high-functionality PICs to replace discrete components in optical networks, high-yield fabrication methods must be developed to facilitate the optimization of the individual components contained on the chip. In this work we present 40Gb/s monolithic transceivers integrating widely-tunable sampled grating DBR (SG-DBR) lasers with quantum well electroabsorption modulators (QW-EAM), high and low optical confinement semiconductor optical amplifiers (SOA), and uni-traveling carrier (UTC) photodiodes on a single chip. These component structures represent the state of the art technologies for even discrete devices. The fabrication method couples a robust quantum well intermixing (QWI) technique with simple blanket MOCVD regrowth steps and avoids the difficulties associated with selective area growth or butt-joint regrowth [1]. The transmitters demonstrate over 30nm of tuning, low drive voltages (1.5-2.5V_{PtoP}), and low power penalty transmission through fiber at 40Gb/s [2]. The SOAs within the receivers provided up to 28dB of gain with saturation powers in the 18.5dBm range while the UTC photodiodes facilitated 40Gb/s operation under high photocurrent conditions. Chip-coupled receiver sensitivity better than –20dBm was demonstrated at 40Gb/s.

II. Fabrication

Device fabrication begins with the MOCVD growth of a centered multiple quantum well (c-MQW) base structure consisting of ten 6.5nm InGaAsP QWs and eleven 8.0nm InGaAsP barriers centered within a 1.3Q waveguide to yield a maximized optical confinement factor of 12.6%. Using the QWI method illustrated in Fig. 1a and detailed in [3], the as-grown c-MQW band-edge (λ_{PL}= 1540nm) was blue-shifted in the EAM (λ_{PL}= 1505nm) and passive regions (λ_{PL}= 1440nm). Following the QWI process, a blanket MOCVD growth was performed for the deposition of a low-confinement offset MQW (o-MQW) gain region. The o-MQW (λ_{PL}= 1550nm) contained 5 wells and was designed to have an optical confinement factor of ~1.4%. The

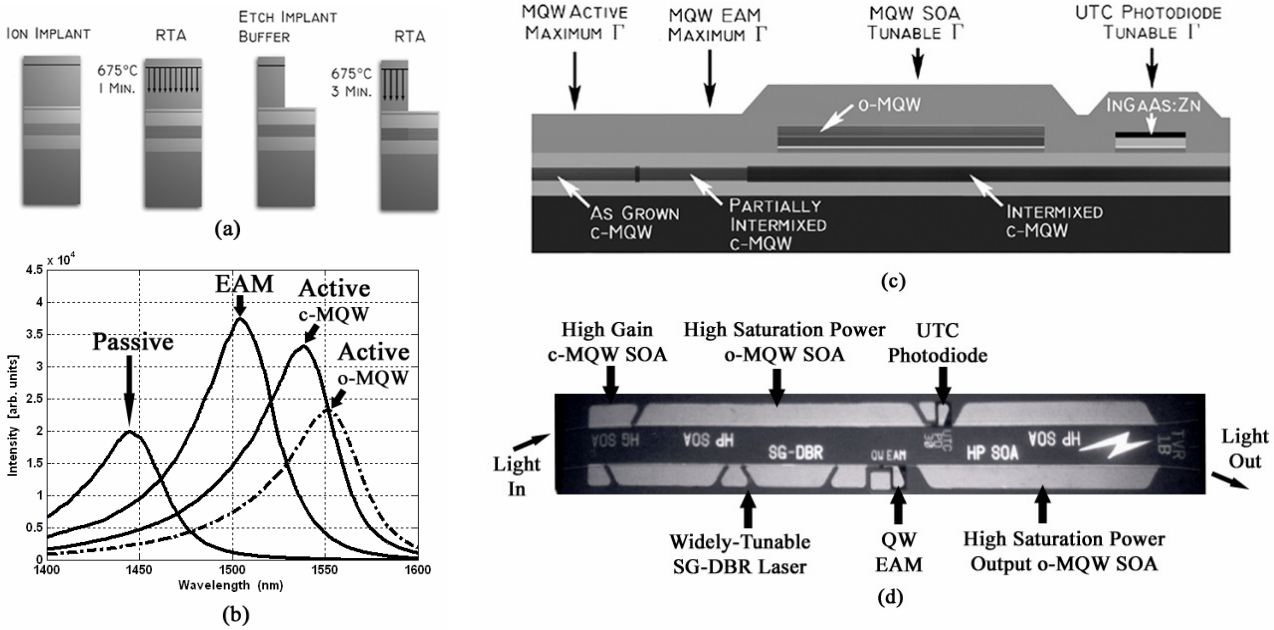

FIGURE 1. (a) QWI sequence used for controlled shifting of the c-MQW band-edge. (b) Photoluminescence of the as-grown c-MQW active, partially intermixed c-MQW EAM, severely intermixed c-MQW passive, and regrown o-MQW active regions. (c) Side view schematic of the high confinement c-MQW, low confinement o-MQW, and UTC photodiode regions. (d) Top-view SEM image of 0.5 by 3.5mm^2 transceiver device.

photoluminescence (PL) results from all four QW band-edges on the single-chip are shown in Fig. 1b. The o-MQW structure was defined in low confinement SOA regions with wet etching and a second blanket MOCVD regrowth was performed for the deposition of the UTC photodiode structure. The details of the growth sequence used for the o-MQW and UTC structures can be found in [4, 5]. Wet etching was used to define the UTC layer structure in the photodetector regions. A final MOCVD regrowth was performed for the upper InP:Zn cladding and InGaAs:Zn contact layers. Standard processing techniques were used to define surface ridge waveguide devices. A schematic side view illustrating the high confinement c-MQW regions, QW-EAM regions, low confinement o-MQW regions, and UTC photodiode regions on a single-chip is presented in Fig. 1c.

III. Transceiver Design

The single-chip transceiver devices were fabricated on the same wafer and employed a parallel ridge waveguide architecture with different transmitter and receiver designs. The transmitters consisted of a five section widely-tunable SG-DBR laser as described in [3] and a QW-EAM with a length of 125µm or 175µm. Select transmitters made use of an SOA positioned after the SG-DBR laser for increased output power. Two receiver designs were explored. Each design consisted of a dual section SOA and a UTC photodiode. The first design (#1) employed a 250µm high gain c-MQW front-end followed by a 1650µm high saturation power o-MQW gain section with a 30µm UTC photodiode. The second design (#2) consisted of a 400µm long high gain c-MQW front-end followed by a 1500µm long high saturation power o-MQW gain section and a 40µm UTC photodiode. A scanning electron micrograph (SEM) image of a transceiver with a footprint of only 0.5 by 3.5mm^2 is shown in Fig. 1d.

IV. Device Results

The SG-DBR lasers demonstrated threshold currents of 35mA, over 30nm of tuning, and output powers up to 35mW at a laser gain section current of 150mA. The EAMs demonstrated an optical 3dB bandwidth of 34 and 39GHz for 175µm and 125µm long devices, respectively. In Fig. 2a we present 40Gb/s broadband transmitter eye diagrams from a 175µm long EAM using a 2.5V_{PtoP} drive. The eye diagrams are open and demonstrate 10-12dB of signal extinction. The SOAs of receiver design #1 demonstrated a chip gain of over 22dB and a saturation output power of 18.6dBm while the SOAs of design #2 demonstrated over 28dB of gain and a saturation output power of 18.2dBm. In both cases the c-MQW high gain region was biased at 15kA/cm^2 and the o-MQW high saturation power section was biased at 6kA/cm^2. The internal quantum efficiency of the UTC photodiodes was limited to 30-35% due to a fabrication issue. Frequency response measurements of photodiodes terminated with a matched 50Ω resistor demonstrated less than 1dB of roll-off at the 20GHz of our testing capability with a 3V reverse bias and 20mA of average photocurrent. In Fig. 2b we present 40Gb/s eye diagrams taken from a receiver using design #2 positioned adjacent to the 40Gb/s transmitter of Fig. 2a. The open eye diagrams demonstrate output amplitudes up to 500mV.

Bit error rate (BER) testing was performed on transmitters and receivers at 40Gb/s using a non-return to zero format. A pseudo random bit sequence of 2^7-1 was used due to a noise floor in the bit-error rate test set-up at longer word lengths. The transmitters reported in [2] and fabricated on the same chip made use of a 125µm long EAM and exhibited only 0.2dB and 3.0dB of power penalty (1.5V_{PtoP}) for transmission through 2.3km and 5km of standard fiber, respectively. The 40Gb/s BER versus received power results for the two receiver designs are presented in Fig. 2d. Design #1 demonstrated error-free operation (1E-9) with a chip-coupled power of –16.8dBm and design #2 required only –20.3dBm for error-free operation.

V. Conclusions

We have demonstrated 40Gb/s widely-tunable transceivers consisting of SG-DBR lasers, QW-EAMs, high and low optical confinement SOAs, and UTC photodiodes. A high-flexibility integration scheme coupling a robust QWI technique with simple blanket MOCVD regrowth steps was used for device fabrication. The transmitters demonstrated low drive voltage 40Gb/s operation and low power penalty transmission through standard fiber. The two receiver designs exhibited –16.8dBm and –20.3dBm sensitivities at 40Gb/s. The SOAs within the receivers demonstrated up to 28dB of chip gain and saturation powers in the 18.5dBm range while the UTC photodiodes demonstrated 40Gb/s operation under high photocurrent conditions.

References

[1] J. Binsma, et al., IEICE Trans. Electron., vol. E80-C, pp. 675-681, 1997.
[2] J.W. Raring, et al, OFC. Opt Soc. America. Post-conference Technical Digest. PDP 26, 2006.
[3] E. Skogen, et al, IEEE J. Sel. Topics in Quantum Electron., vol. 9, pp. 1183-1190, 2003.
[4] J.W. Raring, et al,"IEE Electronics Letts. vol.41, issue 24 pp. 1345-1346 Nov. 2005.
[5] J.W. Raring, et al., IEEE Journal of Quantum Electronics, Vol. 42, No. 2, pp. 171-181, 2005.

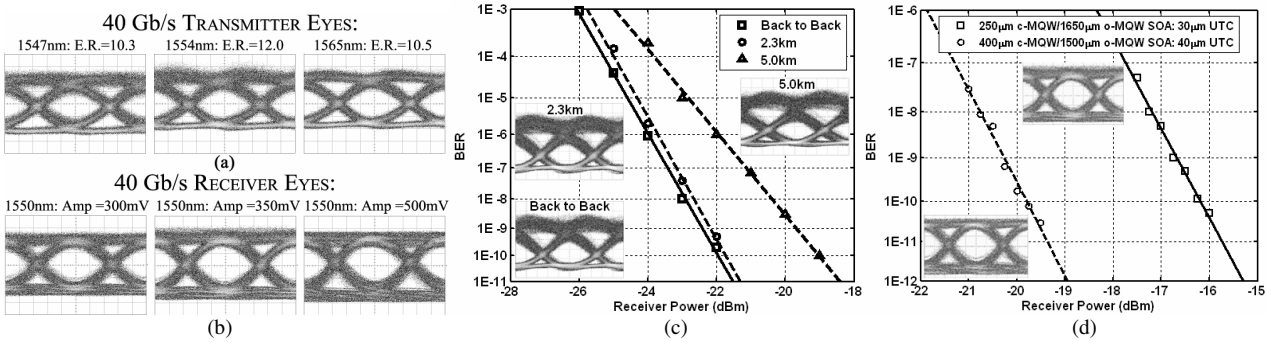

FIGURE 2. 40Gb/s eye diagrams from (a) transmitter and (b) receiver on a single 0.5mm by 3.5mm chip. (c) Bit error rate from a 125µm EAM at 40 Gb/s with a 1.5 V_{PtoP} drive and a wavelength of 1553nm. The back to back eye diagram along with the eye diagrams after transmission are shown as insets. (d) BER versus received power for the two dual section SOA/UTC photodiode receiver designs with inset eye diagrams.

Monolithically Integrated, Sampled Grating DBR Laser Transmitter with an Asymmetric Quantum Well Electroabsorption Modulator

Matthew N. Sysak[†], James W. Raring[*], Gordon P. Morrison[†], Daniel J. Blumenthal[†], Larry A Coldren[†*]

[*]*Materials Engineering, University of California, Santa Barbara, CA 93106*
[†]*Electrical and Computer Engineering, University of California, Santa Barbara, CA 93106*
Phone: 805-893-5828, Fax: 805-893-7990, Email: mnsysak@engineering.ucsb.edu

Abstract

We present the first widely-tunable transmitter that employs intra-step quantum wells for intensity modulation. Fiber coupled output power is >2dBm with tuning range >40nm. EAMs show modulation depths >20dB, slope efficiency >7dB/V, and 10GHz bandwidth.

I. Introduction

Monolithically integrated, widely tunable sampled grating DBR (SGDBR) laser transmitters with electroabsorption modulators (EAM)s are key components in next generation networks due to their compact size and their application in inventory reduction. The most common approach for fabrication of these devices is based on an offset quantum well (OQW) platform where a set of quantum wells above an optical waveguide is selectively removed to form passive/EAM regions and regions of optical gain (active). Recently, we have demonstrated a new dual quantum well (DQW) platform where a second set of square quantum wells (SQW)s is added to the waveguide layer of the OQW platform as shown in Fig 1a [1]. The additional waveguide SQWs significantly improve EAM performance over the OQW approach without additional processing or growth requirements.

In this work, we demonstrate for the first time, a novel SGDBR-SOA-EAM transmitter fabricated using the DQW platform that employs intra-step asymmetric waveguide quantum wells (IQW)s for intensity modulation. We show that the addition of IQWs does not affect the injection efficiency or material gain of the offset QWs used in the laser gain regions. Using photocurrent spectroscopy, we show that the presence of the potential discontinuity in the waveguide IQWs delays the exciton peak shift under applied bias as predicted in [2]. This delay in exciton shift has been used successfully to suppress the onset of EAM absorption and hence shift operating conditions to higher electric fields, where carrier screening effects are significantly reduced [3]. This work demonstrates that the DQW platform can employ exotic waveguide QW structures to taylor EAM properties, such as chirp and modulation efficiency, without degrading integrated laser performance and without additional growth requirements [4].

II. Transmitter Layout and Epitaxial Structure

The IQW tunable transmitter consists of a four section, sampled grating DBR laser, a 550 μm long SOA, and a 400 μm long EAM similar to that in [1]. Transmitters were thinned, anti-reflection coated, mounted on AlN carriers, and wirebonded for characterization. A low-K dielectric, photo-Bisbenzocyclobutene, is employed under EAM pads to reduce parasitic capacitance.

The waveguide layer in the DQW base structure contains 7x10 nm wide compressively strained IQWs and 6x5 nm wide tensile strained barriers. The IQW is divided into a deep 4 nm wide section, and a shallow 6 nm wide section, as shown in insets (i), (ii), and (iii) of Fig 2c. The band offsets to the deepest part of the IQWs are 100 meV and 125 meV, and the intra-step band offsets are 42 meV and 50 meV in the conduction and valence bands, respectively. The deep portion of the IQW is on the n- side of the waveguide PIN structure. The doping scheme in the waveguide is the same as in [1], with low n-type Si-doping ($5x10^{16}$ cm^{-3}) employed outside the wells and barriers. The photoluminescence (PL) peak of the IQW stack is 1465 nm. The remaining layers of the base structure, including the design of the offset QWs above the waveguide, are identical to that in [1].

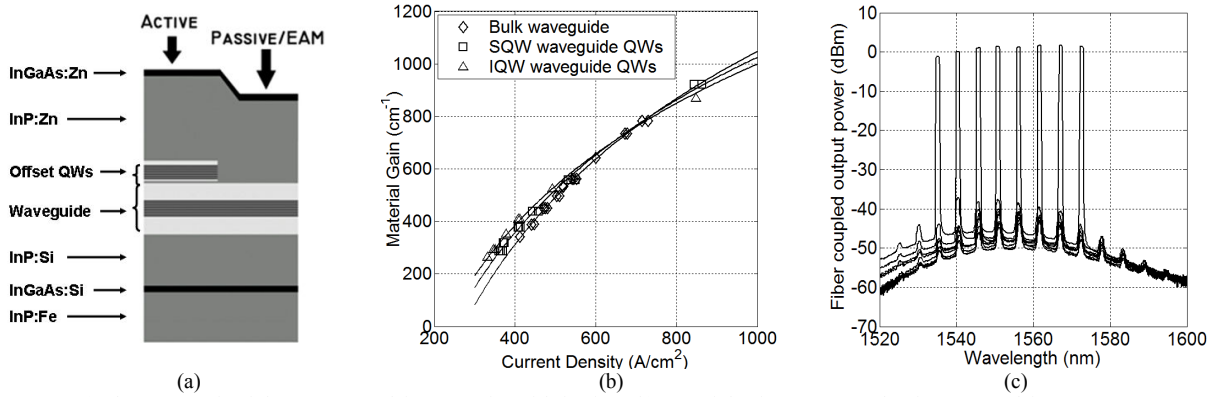

(a) (b) (c)

Figure 1. (a) The DQW epitaxial structure used for transmitter fabrication. (b) Material gain vs. current density extracted from BAL test structures. (c) Transmitter output spectra for various operating wavelengths with laser gain and SOA bias at 140 and 120 mA respectively.

III. Test Structures and Integrated Transmitter Results

To examine the impact that the waveguide IQWs have on optical gain regions, pulsed differential efficiency measurements were performed on a set of 50 μm wide Fabry-Perot broad area lasers (BAL) and 3 μm wide ridge lasers (RL) using the cleave back method. For comparison, an identical set of BALs and RLs employing either a bulk waveguide (PL = 1410 nm) or a set of SQWs in the waveguide (PL = 1480 nm) were fabricated and tested. From the threshold current and differential efficiency of the BALs, a two parameter fit material gain curve was generated for data from each of the three platforms. Results are shown in Fig 1b. The material gain parameter for the IQW, SQW, and bulk waveguide structures was 745, 764, and 826 cm^{-1}, and the transparency current density was 230, 270, and 246 A/cm^2. The injection efficiency extracted from the test RLs was 71%, 73 %, and 75% for IQW, SQW, and bulk waveguide designs respectively. The close agreement between the laser injection efficiency, material gain, and transparency current density results for devices fabricated from each structure indicates that arbitrary QW shapes could be used in the waveguide to taylor EAM performance without degrading laser characteristics.

The output spectra from the SGDBR-SOA-EAM transmitter is shown in Fig 1c. The SGDBR laser is tunable over greater than 40 nm ranging from 1535 to 1578 nm, and fiber coupled output power from the device was up to +2 dBm with gain section and output SOA biased to 140 and 120 mA respectively. On chip light vs. injected current (LI) was measured by reverse biasing the SOA positioned after the front mirror of the SGDBR laser. The threshold current at 1550 nm was 35 mA, which is in agreement with data from SGDBR lasers fabricated in the standard OQW platform, and greater than 12 mW of on-chip optical power was achieved with 100 mA gain bias. DC extinction characteristics of the 400 μm long integrated EAM are shown in Fig 2a. We observe > 7 dB/V slope efficiency along with modulation depths of > 20 dB over output wavelengths from 1535 to 1565 nm at -7V bias. Electrical to optical S_{21} measurements of the 50 Ω terminated EAM showed a 3dB bandwidth of 10 GHz.

Photocurrent spectroscopy measurements were performed on a set of test diode structures to compare the absorption coefficient of the EAM IQWs to a set of standard EAM SQWs. The experimental set-up and the diode dimensions are identical to that used in [5]. The SQWs waveguide region contained 7x10 nm wide compressively strained and with 6x5 nm wide tensile strained barriers. The PL peak of the SQWs was 1470 nm and the band offsets in the conduction and valence bands are the same as on deep side of the IQWs. Material absorption coefficient results from the spectroscopy measurements are shown in Fig. 2b and Fig. 2c respectively. Results for the SQW material absorption coefficient under applied bias shows a typical square QW exciton peak shift and corresponding decrease in exciton intensity as the wavefunctions polarize to opposite sides of the well. Simulated wavefunctions at (i) 0V, (ii) 1.5V, and (iii) 4V reverse bias are shown as insets in Fig. 2b to illustrate the polarization effect. For the IQWs, the absorption coefficient measurements show a high intensity, well resolved exciton peak that does not shift under applied bias. This confirms the predicted delay in exciton peak shift [2] that comes as a result of the intra-step barrier. Simulated wavefunctions for the IQW wells are shown in the insets of Fig 2c at (i) 0V (ii) 1.5V, and (iii) 4V applied reverse bias, where clear distortion of the heavy hole wavfunction is visible at 1.5V due to the intra-step barrier. This effect can be used to delay absorption in the EAMs, shifting operation to high biases and reducing the potential for carrier screening effects.

V. Conclusions

We have shown for the first time a monolithically integrated tunable transmitter that uses asymmetric IQWs in the EAMs for intensity modulation. The integrated SGDBR laser shows fiber coupled output powers up to +2 dBm and greater than 40 nm tuning between 1535 and 1578 nm. Integrated EAMs show modulation efficiency greater than 7dB/V, and modulation depths greater than 20 dB between 1535 and 1565 nm. The excellent agreement of the BAL gain data using active regions with various waveguide layers demonstrates the potential of the DQW platform to use arbitrarily shaped QWs for EAM modulation efficiency without degrading laser performance and without introducing additional growth complexity. Photocurrent spectroscopy has been used to measure the broadband absorption coefficient of the IQWs and we have observed a delay in the exciton peak shift under applied bias, which agrees with predicted performance.

References

[1] M. Sysak et al., Accepted for presentation *Device Research Conf.,* IIA-2, University Park, PA, June 2006.
[2] D-S, Shin et al., *J. App. Phys*., vol. 89, pp. 1515-1517, Jan. 2001.
[3] J.X. Chen et al., *IEEE Photon. Technol. Lett*. vol. 16, no. 2, pp. 440-443, Feb. 2004.
[4] W. Chen et al., *Semicond. Sci. Technol*., vol. 7, pp. 828-836, 1992.
[5] G.B. Morrison, et al.," *IEEE Photon. Technol. Lett*. vol. 17, no. 7, pp. 1414-1417, July 2005.

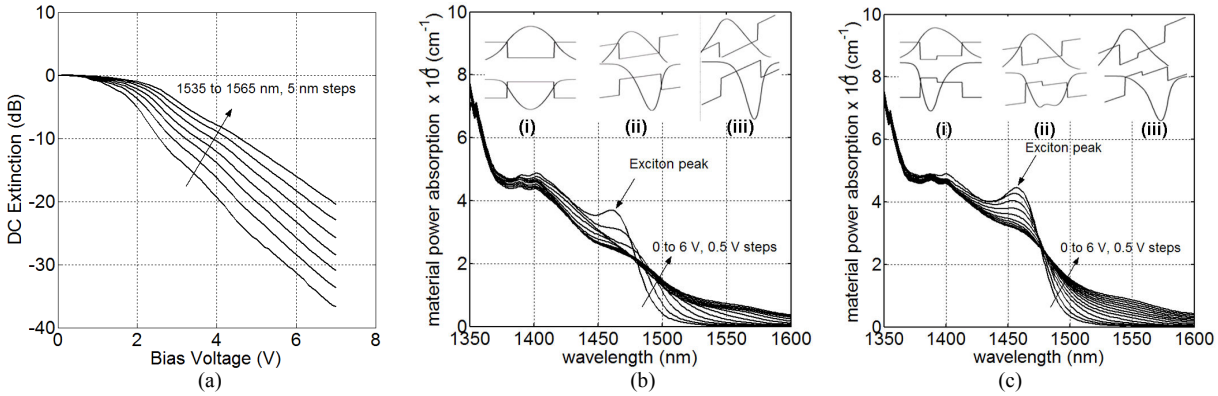

Figure 2. (a) DC extinction characteristics of integrated 400 μm long EAM. (b) Material absorption coefficient extracted from photocurrent spectroscopy for standard square QWs. (c) Material absorption coefficient extracted from photocurrent spectroscopy for IQWs.

I. Photonic IC Technology & Devices

C. Analog PICs and RF-Photonics

Baseband Optical Down-Sampling for High-Performance Analog Links

L.A. Johansson and L.A. Coldren
Department of Electrical and Computer Engineering, University of California, Santa Barbara, CA 93106.
Email: leif@ece.ucsb.edu

Abstract: A baseband optical down-sampling architecture is experimentally demonstrated where both inphase and quadrature channel are directly accessed using two integrated dual mode-locked lasers. A 2-dB conversion penalty is obtained for a 50Mbaud QPSK-modulated 2.5GHz RF signal.

OCIS codes: (070.1170) Analog optical signal processing; (140.4050) Mode-locked lasers

1. Introduction

The development of high-performance analog optical links will simplify the antenna RF front-end. Ideally, such optical link should have gain, low noise figure, dynamic range as good as state-of-the-art RF front-ends and be able to perform direct access to baseband signal. Link gain and low noise figure can be achieved using high performance laser sources and low V-pi optical modulators [1]. Achieving high dynamic range has proven more challenging, as most types of optical modulators have inherently a non-linear response and most efforts to linearize the modulator response have provided incremental improvements at best. Currently, a promising approach to achieve a high dynamic range is the implementation of post-detection digital signal processing (DSP) where the non-linear response of the modulator (and receiver) can be corrected for to the limit given by the knowledge of the modulator transfer function [2]. Due to the resolution / speed constrictions of A/D converters, the highest performance is obtained at low received frequencies. A second promising approach is to use optical phase modulation in combination with a tracking optical phase-lock loop receiver. The performance of this approach is limited by the amount of feedback gain available while maintaining a dynamically stable operation in the phase-locked receiver. This is in turn determined by the feedback phase lag such that the highest performance is again obtained at lower received frequencies.

High performance optical downconversion is a key function for high-performance antenna remoting applications, not only as a mean to overcome the limitations of electrical frequency downconversion, but also to make the analog optical link architectures above available at an extended frequency range. The challenge is to perform the optical downconversion in a manner that does not degrade link performance. Conventionally, an optical frequency-conversion link is realized by applying a secondary sinusoidal modulation to the optical carrier to downconvert the RF-modulation to an intermediate frequency [3]. Unfortunately, this leads to 6dB optical power penalty in a shot-noise limited optical link. This penalty can be reduced by using pulsed optical sampling downconversion for more efficient frequency conversion [4] and baseband downconversion to eliminate the frequency duality. This work demonstrates optical frequency down-conversion directly to baseband with low conversion penalty.

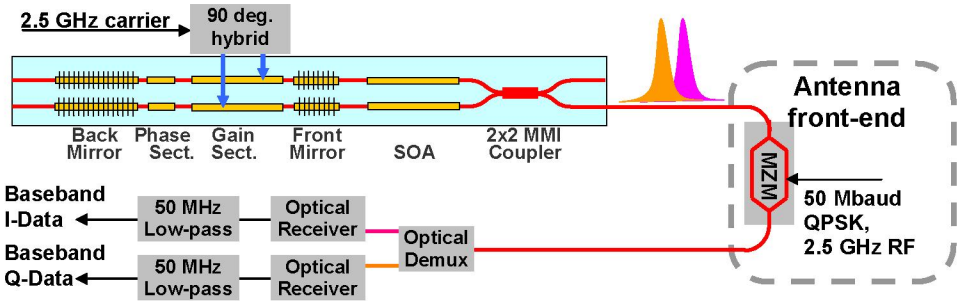

Fig. 1: Schematic of the optical down-sampling arrangement, including the dual mode-locked laser.

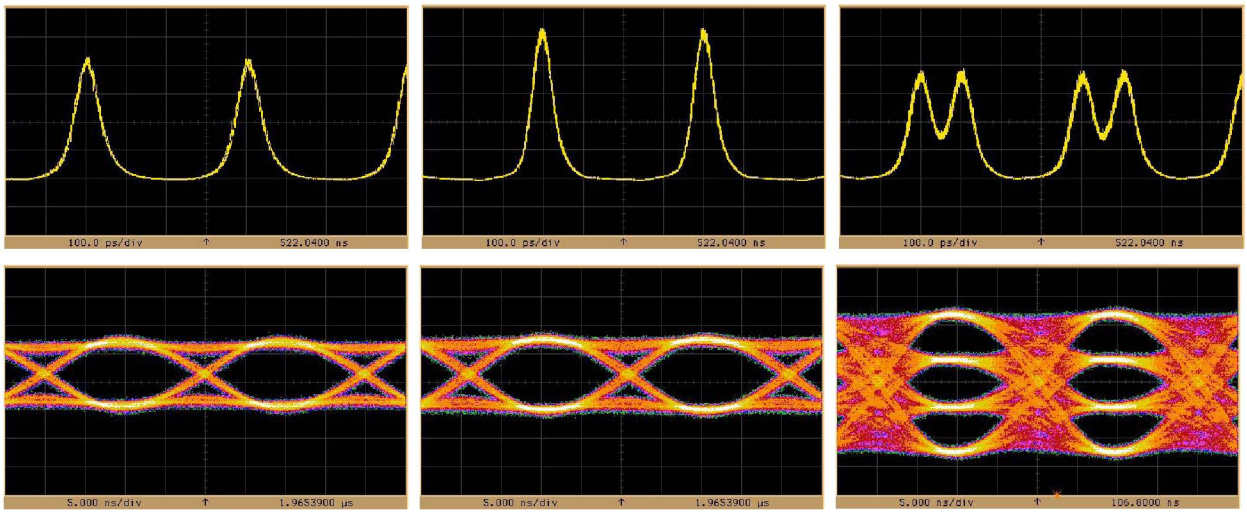

Fig. 2. *Top;* Generated pulsed waveforms from the two mode-locked lasers; I-channel, Q-channels and the combined pulse-train from left to right. Fig. 2. *Bottom* shows the corresponding demodulated baseband eye-diagrams for I-, Q- and combined channels. The lower right eye diagram has been rotated in phase to clearly show all four data levels.

2. Optical sampling downconversion scheme

For direct baseband downconversion, inphase and quadrature (I and Q) mixing is required to access the full vector information within the information band. In this work, this is being realized by supplying two sets of pulse-trains at the RF carrier frequency, 90 deg. shifted in phase. The two sets of pulses are supplied at different wavelengths and are being modulated by the input RF signal. A receiver demultiplexer can then separate the two downconverted signals and the I- and Q-channels are recovered separately. A schematic for the baseband down-sampling scheme is shown in Fig. 1 above, where a MZ modulator is modulating the two pulse-trains by the received RF signal to separately produce I- and Q- channel data. The use of two sets of optical pulse-trains at different wavelengths fits well into a local WDM network environment, where separate receivers can digitize the two waveforms and be further routed in digital form, if required.

In this work, the two pulse-trains were generated by using a single-chip source incorporating two widely-tunable Sampled-Grating DBR lasers [5] with an integrated 2x2 MMI coupler, produced by Agility Communications. The two lasers are being actively mode-locked at the carrier frequency using gain switching at 90 deg. relative phase offset. The resulting waveforms are shown top in Fig. 2 below, both separately demultiplexed (top left, top middle) and combined on the detector (top right). The generated optical pulses had between 15% and 20% duty cycle, corresponding to 60 ps to 80 ps FWHM at 2.5 GHz. Under gain-switched operation, the average optical power remained within 1 dB compared to CW operation using the same gain bias current.

By using a practical integrated dual semiconductor laser source, the demonstrated optical downconversion scheme can be applied in an antenna remoting configuration where direct data access is required. By replacing the need for post-detection frequency conversion and demodulation, this arrangement is particularly attractive at higher frequencies, where semiconductor laser sources have been used to demonstrate pulses up to 240 GHz repetition ratio [6]. To reach high performance in terms of link noise figure or available link signal-to-noise ratio, higher performance, low noise mode-locked lasers must be used [4].

3. Experiment

To demonstrate the baseband down-sampling approach, a simple test signal was used to drive a MZ modulator consisting of a 50Mbaud QPSK-modulated 2.5 GHz RF carrier. Selecting wavelength, either the I- or the Q-data stream could be directly accessed in the optical receiver, as shown in Fig. 2, bottom left and bottom middle. Correct operation could be verified by switching to exclusive I or Q modulation, where the second received wavelength remained unmodulated within the receiver passband. Combining both wavelengths on one receiver, a four-level demodulated eye could be generated when the I- and Q- phase has been rotated slightly to clearly show all four data levels.

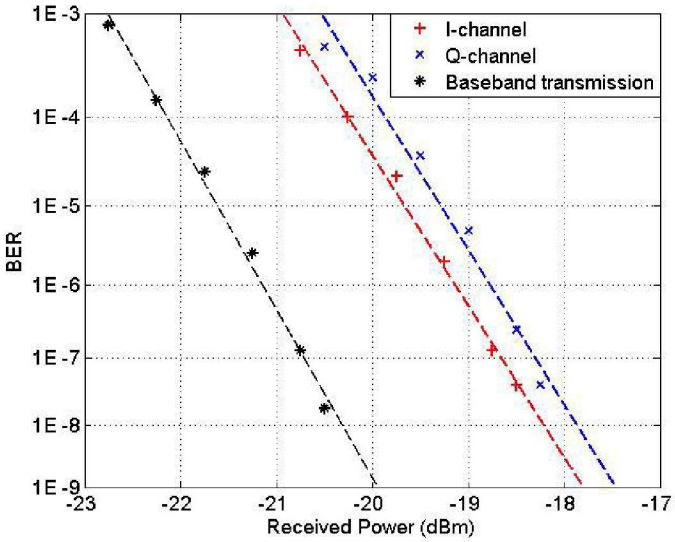

Fig. 3. Measured bit-error-rate as a function of received optical power for both baseband data modulation and downconverted I- and Q-channel data streams.

To evaluate the down-conversion penalty for the demonstrated approach, a 50 Mbps binary NRZ intensity modulated signal was generated and detected. The conversion penalty is then given by the required received power for a given bit error rate. Compared to baseband modulation, the downsampled signal require around 2 dB higher average optical power, lower than the theoretical limit given by sinusoidal carrier modulation. About 1-dB penalty can be attributed to the penalty predicted by the observed pulse-width, and the second 1-dB penalty is due to lower effective modulation index of the RF modulation, than that of the binary modulation that had 12dB extinction ratio. By improving pulse-width and modulation depth, a conversion penalty lower than 1-dB will be available using this technique.

4. Summary

In this paper we have demonstrated baseband optical down-sampling with low conversion penalty. In the demonstrated arrangement, an integrated dual mode-locked SG-DBR laser is used to produce two sets of pulse-trains for separate I- and Q-channel baseband access. Using a 50 Mbaud QPSK-modulated 2.5 GHz RF signal to characterize the sampling approach, a 2-dB power penalty is obtained compared to the baseband-modulated optical signal. With the current source, the downconversion scheme offers an alternative to electrical frequency conversion. However, using higher performance mode-locked lasers, the baseband optical downconversion scheme will play an important role in extending the frequency range of promising linear link technologies, such as the use of high resolution ADC's with digital signal processing, or the use of phase-lock loops in optical phase demodulators.

5. References

[1] W.K. Burns, M.M. Howerton, and R.P. Moeller, "Broad-band unamplified optical link with RF gain using a LiNbO3 modulator," IEEE Photonics Technology Letters, Volume 11, Issue 12, Pages: 1656-1658, Dec. 1999.

[2] J. C. Twichell and R. Helkey, "Phase-Encoded Optical Sampling for Analog-to-Digital Converters," IEEE Photonics Technology Letters, Volume 12, Issue. 9, Pages: 1239-1239, Sep. 2000

[3] P.D. Biernacki, L.T. Nichols, D.G. Enders, K.J. Williams and R.D. Esman, "A two-channel optical downconverter for phase detection," IEEE Transactions on Microwave Theory and Techniques, Volume 46, Issue 11, Part 1, Pages: 1784–1787, Nov. 1998.

[4] P.W. Juodawlkis, J.J. Hargreaves, R.D. Younger, G.W. Titi and J.C. Twichell, "Optical down-sampling of wide-band microwave signals" Journal of Lightwave Technology, Volume 21, Issue 12, Pages: 3116–3124, Dec. 2003.

[5] T. Liijeberg, R. Tohmon, E. Hall, P. Abraham, M. Focht, G.A. Fish, M.C. Larson and L.A. Coldren, "High-power, widely-tunable sampled grating DBR laser integrated with a semiconductor optical amplifier" IEEE 18th International Semiconductor Laser Conference, 2002. Pages: 45–46, 29 Sept.-3 Oct. 2002.

[6] T. Ohno, F. Nakajima, T. Furuta and H.Ito, "A 240-GHz active mode-locked laser diode for ultra-broadband fiber-radio transmission systems" OFC/NFOEC Optical Fiber Communication Conference, 2005. Technical Digest. Volume 6, Pages: 37-39, March 6-11, 2005

A High efficiency, Current Injection Based Quantum-Well Phase Modulator Monolithically Integrated with a Tunable Laser for Coherent Systems

Matthew N. Sysak, Leif A. Johansson, James W. Raring, Mark Rodwell, Larry A. Coldren, John Bowers
University of California Santa Barbara, Engineering II Santa Barbara, CA 93106
Tel: (805)893-8465, FAX: (805) 893-4500, email: mnsysak@engineering.ucsb.edu

Abstract: A monolithically integrated tunable laser and quantum-well phase modulator is demonstrated. Phase efficiency under forward bias is improved >20dB at low frequencies compared with reverse bias. Bandwidths >30 GHz are demonstrated in frequency modulation measurements.

OCIS codes: (230 4110) Modulators; (230 5590) Quantum Well Devices

This research was supported by DARPA under the PHOR-FRONT Program.

1. Introduction

Optical phase modulation continues to attract increased interest in optical communications systems. In digital systems, phase modulation offers increased receiver sensitivity, improved tolerance to fiber dispersion effects and constant envelope, which are attractive for WDM optically amplified links. Optical phase modulation is also well-positioned to generate very linear analog optical links. Linear optical intensity modulators have been difficult to realize because of the requirement to force a linear transfer function between the two hard limits of zero and full optical transmission. Optical phase modulation, meanwhile, does not have these limits. A linear phase modulator can be engineered by increasing the available output phase swing while keeping the modulation within the linear regime of the transfer function, in a manner that parallels the linearity of microwave amplifiers.

Semiconductor phase modulators based on the InGaAsP/InP materials system are particularly attractive since they can be integrated with other discrete components such as lasers for low packaging costs and coupling losses. For phase modulation these devices employ a variety of mechanisms including current injection based effects, such as the free carrier plasma effect, and field based effects such as the quantum confined stark effect (QCSE). Devices based on current injection in quantum wells are particularly attractive due to their large achievable change in refractive index. However, integrating quantum well based phase modulators with lasers has required advanced growth techniques [1], and results have been limited to single frequency DFBs. In this work, we demonstrate the first monolithically integrated sampled grating DBR laser tunable transmitter/phase modulator with index shifts up to $\Delta n = 0.019$ by applying current injection into quantum wells. Compared to current injection into a bulk waveguide, quantum wells have been shown to provide superior phase modulation efficiency [2]. The device is fabricated on a modified offset quantum well platform and requires only a single blanket InP regrowth step [3]. We observe improvements up to 20 dB for phase modulation efficiency at low frequency for current injection conditions compared with reverse bias conditions employing the QCSE

To overcome the sinusoidal response of a standard optical phase demodulator, we have proposed the use of an optical phase-lock loop (OPLL) to form a linear phase demodulator [4]. In its electrical counterpart, a voltage controlled oscillator is normally used to track the incoming phase with zero steady state error. A frequency modulated laser can take this function, in essence being a current controlled oscillator (CCO). However, in practice, a laser CCO will not simultaneously meet the twin requirements of high modulation bandwidth and low laser phase noise of the most high-performance optical phase-lock loops. It has previously been shown that a phase modulator operating beyond its traditional 3-dB bandwidth produces frequency modulation [5]. Along with the demonstration of a tunable phase modulator transmitter, we also show for the first time that the current injection based quantum well phase modulators can generate frequency modulation with a response up to 35 GHz, and that these devices are suitable for integration as a CCO in an optical phase-lock loop.

2. Epitaxial Structure and device layout

The phase modulator is fabricated as part of an integrated Mach-Zehnder interferometer in combination with a tunable sampled grating DBR (SGDBR) laser source using a modified offset quantum well based integration platform [3]. The mach-zehnder design was selected for ease of characterization, since in this configuration, changes in phase are translated into an amplitude response which can be easily measured using an optical power meter. A diagram of the epitaxial layers for device fabrication is shown in Fig. 1.

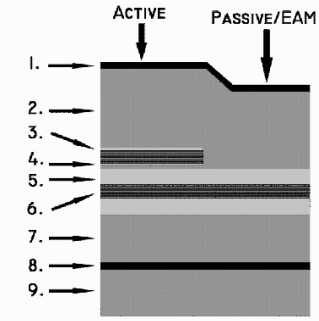

Region	Description
1	p-contact
2	p-cladding
3	Offset QWs
4	Stop Etch
5	Waveguide
6	Centered QWs
7	n-Buffer
8	n-contact
9	Fe-substrate

Fig 1. Epitaxial layer structure for the modified offset quantum well phase modulator/SGDBR integration platform

Laser and propagation/phase modulator regions are separated by the selective removal of the offset quantum well stack that is used for gain in the optical amplifiers and the laser. A simple,blanket p-type InP regrowth follows the selective removal of the offset wells, after which exposed waveguides are patterned and etched. Phase modulator regions are formed by evaporating a Ti/Pt/Au contact on the top of the exposed ridges and electrically isolating devices using a proton implant. In the center of the waveguide, a quantum well superlattice is designed to have a photoluminescence of 1460 nm and consists of 8x10 nm compressively strained wells and 7x5 nm tensile strained barriers. The optical waveguide regions surrounding the wells have a photoluminescence peak at 1350 nm. Integrated devices were thinned, cleaved, anti-reflection coated, mounted on AlN carriers, and wirebonded.

3. Results

The refractive index shifts, along with 50 Ω terminated small signal frequency response curves were generated for the integrated Mach-Zehnder/SGDBR laser transmitter. The index shift was measured by monitoring the DC extinction characteristics of the Mach-Zehnder when a 300 um long electrode in one of the arms is forward biased and the laser wavelength is tuned to 1550 nm. Results are shown in Fig. 2 and Fig. 3.

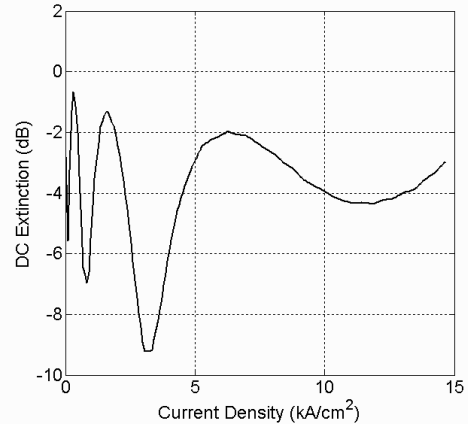

Fig 2. DC Extinction characteristics of integrated tunable SGDBR laser and Mach-Zehnder modulator at 1550 nm.

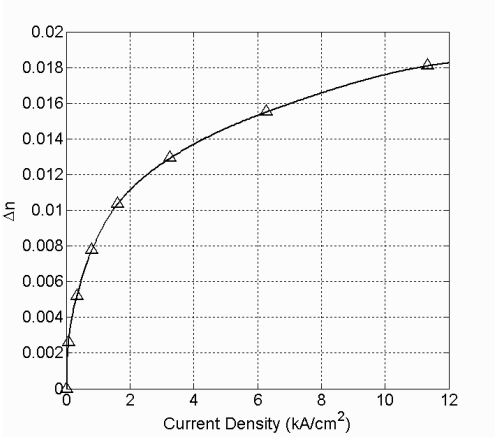

Fig 3. Experimental index shift for current injection based phase modulator. A trend line has been added to guide the eye.

In the frequency response measurements, the forward or reverse DC bias conditions are set through a bias-T that is linked to a current/voltage source. The small signal is applied through a 50 Ω terminated ground signal probe.

Under forward bias operation, the DC bias point is set to 10 mA. Under reverse bias, the applied voltage is -2V. Results are shown in Fig. 4.

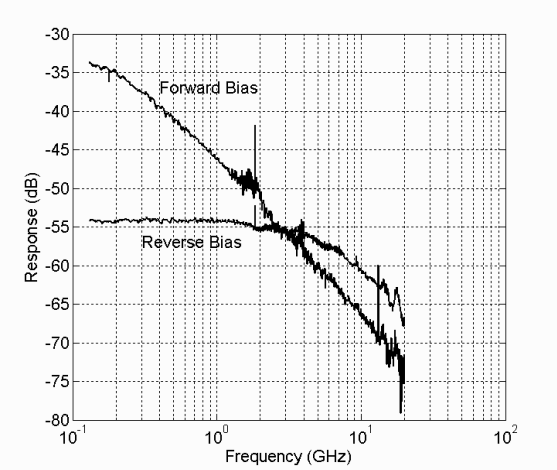

Fig 4. Small signal amplitude response for the Mach Zehnder under forward and reverse bias conditions.

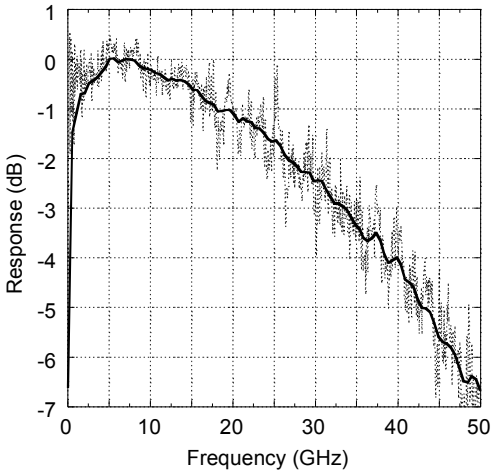

Fig 5. Small signal response of the CCO phase modulator with optical frequency discriminator

The un-normalized frequency response measurements of these devices show up to 20 dB improvement in phase efficiency using current injection at low frequencies when compared with the reverse bias quantum confined stark effect approach. It should be noted that under forward bias conditions, the RF matching is poor due to the small device impedance (~10 Ω) and improving this would lead to even greater efficiency.

Finally, we have used this device under forward bias conditions in combination with an optical filter for frequency discrimination as in [1], and measured the resulting FM response. This is of great relevance for applications in an optical phase-lock loop, where any roll-off in the FM frequency response will add a loop phase lag, reducing the stability of the phase-lock loop. For a phase modulator with a pure 1/f-type phase response, we would expect that the corresponding FM response is flat. This is also what we observe in the experimental results that are shown in Fig. 5. Greater than 35 GHz bandwidth is obtained, which makes this device an excellent candidate for optical phase-lock loop applications with loop bandwidths up to and exceeding 10 GHz.

4. Conclusions

We have demonstrated a monolithically integrated quantum well phase modulator in a Mach-Zehnder configuration with a widely tunable Sampled Grating DBR laser. The phase efficiency under both forward and reverse bias conditions has been investigated and we have shown up to 20 dB improvement in phase response for forward biased current injection conditions at low frequency. We have also used this device to generate optical frequency modulation and observe a 3-dB bandwidth in excess of 35 GHz.

5. References

[1] T. Tanbun-Ek, P.F. Sciortino, Jr, A.M. Sergent, K.W. Wecht, P. Wisk, Y.K. Chen, C. G. Bethea, S.K. Sputz, "DFB Lasers Intergated with Mach-Zehnder Optical Modulator Fabricated by Selective Area Growth MOVPE Technique" IEEE Photon. Tech. Lett., vol. 7, no. 9, pp. 1019-1021, 1995.

[2] J.I Shim, M. Yamaguchi, P. Delansay, M. Kitamaru, "Refractive Index and Loss Changes Produced by Current Injection in InGaAs(P)-InGaAsP Multiple Quantum –Well (MQW) Waveguides" IEEE J. Select. Topics in Quantum Electron., vol. 1, no. 2, pp. 408-414, June 1995.

[3] M.N Sysak, J.S. Barton, J.W. Raring, M. Dummer, A. Tauke-Pedretti, D.J. Blumenthal and L.A. Coldren. "10 Gb/s Photocurrent Driven, Widely Tunable Electroabsorption Based Wavelength Converter*" presented at Optical Fiber Communications Conference,* Anaheim, CA 2005. OtuM4

[4] Hsu-Feng Chou, A. Ramaswamy, D. Zibar, L.A. Johansson, J.E. Bowers, M. Rodwell and L..A. Coldren, "SFDR Improvement of a Coherent Receiver Using Feedback," Submitted to COTA 2006.

[5] L.A. Johansson, J.S. Barton, L.A. Coldren. And G.A. Fish, "High-Speed Optical Frequency Modulation in a Monolithically Integrated Widely-Tunable Laser - Phase Modulator," in *Optical Fiber Communication Conference on CD-ROM (Optical Society of America, Washington, DC, 2004),* FL2

SFDR Improvement of a Coherent Receiver Using Feedback

Hsu-Feng Chou, Anand Ramaswamy, Darko Zibar, Leif A. Johansson, John E. Bowers, Mark Rodwell, and Larry Coldren
Department of Electrical and Computer Engineering, University of California, Santa Barbara, CA 93106, USA
Hsu-Feng.Chou@ieee.org

Abstract: A novel coherent optical receiver is proposed and experimentally demonstrated by using a feedback technique capable of reducing the nonlinear distortion in a traditional receiver while retaining the signal to noise ratio. Up to 15 dB of SFDR improvement is obtained.

OCIS codes: (060.1660) Coherent communications; (120.5060) Phase modulation

1. Introduction

The nonlinear intensity response of optical modulators has been a major limiting factor of intensity modulated analog optical links [1]. In general, the modulation depth has to be restrained and the bias point needs to be properly set in order to achieve higher linearity [2]. System parameters such as noise figure and link gain can be degraded by these requirements. In contrast, optical phase modulators have excellent linearity over a wide modulation range. The modulation depth is not limited by the optical power as in intensity modulation but only by the total modulation capability of the phase modulator. However, the challenge of linearity in a phase-modulated link is shifted to the receiver side. The traditional interferometer-based phase demodulator has a sinusoidal response that limits the spur free dynamic range (SFDR) [3]. To overcome this limitation, a novel feedback technique is proposed in this paper to increase the linearity of an analog optical link. In the proposed approach, the demodulated signal is fed back to the input of the coherent receiver through a local phase modulator, which compensates the phase difference between the signal and the local optical waves. As a result, the phase difference seen by the phase demodulator is reduced and falls in the linear region of the response curve. As a result of the feedback architecture, the signal to noise ratio (SNR) in the receiver remains unchanged, despite the reduced net depth of the detected phase difference. For successful operation, the delay of the feedback must be short compared to the speed of the incoming signal in order to stay in phase. We present experimental verification of this novel approach using discrete components. In practice, an integrated implementation is necessary to achieve the short feedback delays necessary for proper operation at gigahertz frequencies. We successfully demonstrate the increased linearity without penalty in SNR, resulting in an overall SFDR improvement of 14.9 dB. The results are also in line with what is predicted from a time-domain analysis that addresses theoretical predictions and imperfect realizations [4].

2. Experiment and results

The experimental setup is shown in Fig. 1 where the transmitted signals are 160 kHz and 180 kHz. These

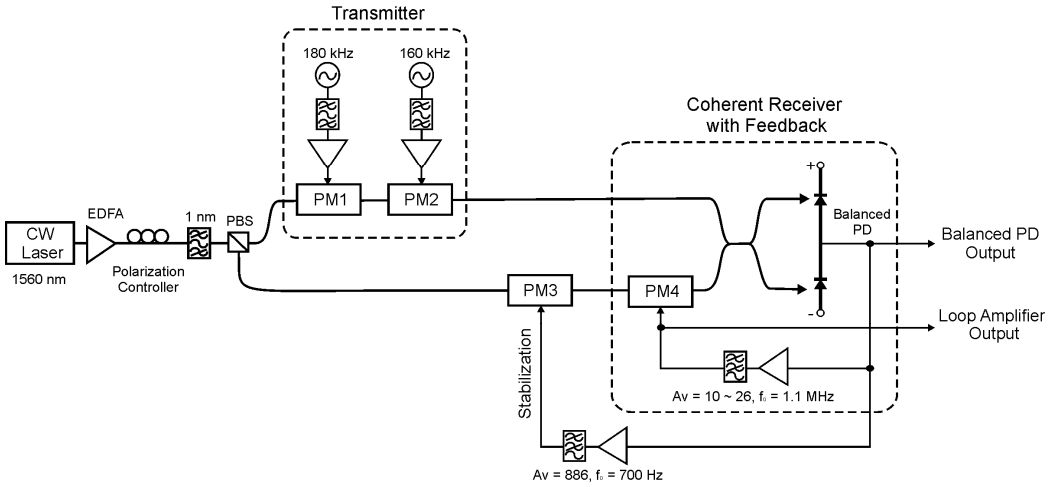

Figure 1 Experimental setup of the optical coherent receiver with feedback technique. PM#: phase modulator, A_v: voltage gain, f_o: 3-dB frequency, PBS: polarization beam splitter.

frequencies are limited by the delays due to the fiber patch cords of the optical components. An external-cavity tunable laser is used as the CW laser source at 1560 nm whose output is amplified by a high-power EDFA. The interferometer-based optical link is constructed with polarization maintaining fibers and components for better stability. The power ratio between the two branches can be adjusted by a polarization controller through polarization dependent splitting of the polarization beam splitter (PBS). The transmitter is composed of two optical phase modulators, PM1 and PM2, used to apply phase modulations at different frequencies. This arrangement decouples the driving electronics at respective tones. The V_π of the phase modulators is around 4.4 V.

On the other arm of the interferometer are the two phase modulators on the receiver side. PM3 is used to compensate environmentally induced slow phase drifts between the two branches and stabilizes the interferometer to the quadrature point. Up to 6π rad of differential phase drift can be compensated. PM4 is the local phase modulator used to apply the feedback signal for compensating the phase difference. The voltage gain is adjustable with a 3-dB bandwidth of 1.1 MHz, set by a first-order RC filter. The two interferometer branches are connected to a polarization maintaining coupler and eventually to a balanced photodetector, as in a traditional phase demodulator.

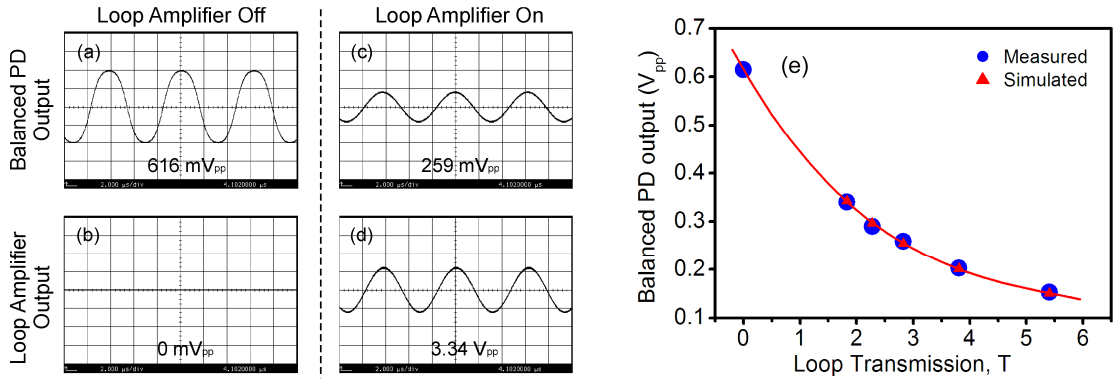

Figure 2 Scope traces in one-tone measurement. The modulation depth is π rad peak-to-peak at 160 kHz. (a) and (b): loop amplifiers off; (c) and (d): loop amplifiers on with loop transmission of 2.8; (e) balanced photodetector output as a function of loop transmission

First, a one-tone measurement is conducted at 160 kHz to demonstrate the successful operation of phase-tracking. The optical power in each interferometer branch before the coupler is 10 mW. The transmitter modulation depth is π rad. As shown in Fig. 2(a), with the loop amplifiers turned off, which corresponds to a traditional phase demodulator, the balanced photodetector output is distorted due to the nonlinear response. However, when the loop amplifiers are turned on, Fig. 2(c) shows that the voltage swing as well as distortion of the balanced photodetector output is reduced. The loop amplifier output that drives PM4 (Fig. 2(d)) is an amplified replica of the balanced photodetector output. Fig. 2(e) shows that when the loop transmission, T, which represents the closed-loop phase gain, is increased, the balanced photodetector output reduces. This would in turn lead to better linearity. Excellent matching with the time-domain numerical simulation [4] is obtained.

More detailed linearity measurements can be obtained by two-tone (160 kHz and 180 kHz) measurements. The (third-order) intermodulation is measured at 140 kHz. The signals are measured after an amplifier with a DC voltage gain of 11.2 and a 3-dB bandwidth of 1.1 MHz. Fig. 3(a) shows the results *without* using the feedback technique (i.e. a traditional phase demodulator). Due to the nonlinear response of the receiver, the output power of the fundamental tone starts to saturate at 17 dBm of output power. The noise level is measured to be -111.9 dBm/Hz with no input signal to PM1 and PM2 but everything else remains active. The SFDR can thus be obtained as 88.6 $dB \cdot Hz^{2/3}$.

Next, the feedback loop is closed by sending the demodulated signal to PM4. The amplifier voltage gain is adjusted to 23.9 which results in a loop transmission of 6.5. From Fig. 3(b), it is clear that no saturation in the output power of the fundamental tone is observed because of the reduced phase difference due to feedback. Therefore, the intermodulation level is reduced as a result of the reduced swing at the phase demodulator. The resulting SFDR is 103.5 $dB \cdot Hz^{2/3}$, corresponding to an improvement of 14.9 dB over the traditional receiver.

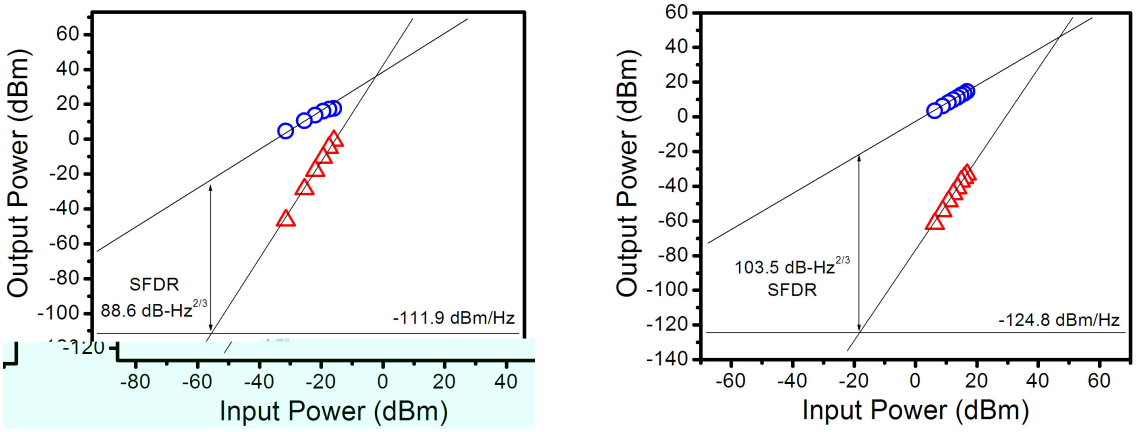

Figure 3 Two-tone SFDR measurements (a) without feedback (traditional phase demodulator); (b) with feedback. The vertical and the horizontal scales of the two plots are exactly the same but shifted for clearer comparison. Circle: signal, triangle: intermodulation.

It is observed from Fig. 3(a) and (b) that the SNR of the two cases are almost identical but the intermodulation level is suppressed by the feedback technique, verifying that the proposed approach can increase linearity without any penalty in SNR. The experimentally observed noise floor of -124.8 dBm/Hz with feedback is 6.4 dB higher than the theoretical shot-noise limited value of -131.2 dBm/Hz. The most likely cause is the finite noise figure of the loop amplifiers. The intermodulation level can be further suppressed by increasing the loop transmission (loop gain). However, it is limited in practice by the loop delay (~ 5 meters) imposed by the fiber patch cords and electronic phase delays. When the loop transmission increases beyond 6.5 in the current setup, oscillations around 8.5 MHz occur. The excessive noise and, in particular, limited loop transmission constrained the experimentally achievable SFDR. Therefore, integration of the local phase modulator, the balanced photodetector, and the loop electronics should improve the performance and is under intensive investigation.

3. Conclusion

A novel coherent optical receiver with feedback is proposed and demonstrated experimentally with up to 15 dB of SFDR improvement compared to the traditional approach. The feedback technique effectively reduces the signal swing at the phase demodulator and achieves a higher level of linearity. The SNR is preserved by this feedback technique. The currently realized SFDR of 103.5 $dB \cdot Hz^{2/3}$ is limited by the excessive noise of the loop amplifiers and the delay due to the fiber patch cords of the optical components. Improved performance at higher operating speeds is promising by using advanced integration technologies.

4. Acknowledgment

This research was supported by DARPA under the PHOR-FRONT Program.

5. References

[1] C.H. Cox III, E.I. Ackerman, G.E. Betts, J.L. Prince, “Limits on the Performance of RF-Over-Fiber Links and Their Impact on Device Design,” IEEE Transactions on Microwave Theory and Techniques, Volume 54, Issue 2, Part 2, pp: 906-920, Feb. 2006.

[2] Bin Liu, Jongin Shim, Yi-Jen Chiu, Adrian Keating, Joachim Piprek, and John E. Bowers, “Analog Characterization of Low-Voltage MQW Traveling-Wave Electroabsorption Modulators”, Journal of Lightwave Technology, Volume 21, Issue 12, pp: 3011-3019, December 2003.

[3] R.F. Kalman, J.C. Fan, L.G. Kazovsky, “Dynamic range of coherent analog fiber-optic links,” Journal of Lightwave Technology, Volume 12, Issue 7, pp: 1263-1277, July 1994.

[4] D. Zibar, L. A. Johansson, H.-F. Chou, A. Ramaswamy, and J. E. Bowers, “Time-Domain Analysis of a Novel Phase-Locked Optical Demodulator”, submitted to Coherent Optical Technologies and Applications (COTA) 2006

Integrated Adaptively Predistorted Analog Optical Transmitter

L. A. Johansson[1], Y. A. Akulova[2], P. C. Koh[2], L. A. Coldren[3]
1: ECE Department, University of California, Santa Barbara. leif@ece.ucsb.edu
2: JDSU, 3: University of California, Santa Barbara and JDSU

Abstract *An integrated photonic transmitter circuit incorporating an adaptive optical predistortion circuit is demonstrated. Simultaneous distortion cancellation of an electroabsorption modulator and driver amplifier allows improvement in dynamic range while using an efficient but nonlinear driver.*

Introduction

Several linearization schemes have been deployed to improve the linearity of optical transmitters. Perhaps the commercially most successful is using a predistortion circuit where improvements in performance can be achieved using an inexpensive power efficient electronic circuit [1]. This approach is typically not adaptive with changing operating conditions and require that the response of the transmitter stays constant. It is therefore not suitable for integration with a widely tunable transmitter and a modulator that has wavelength-dependent response.

An alternative is using feed-forward linearization where the modulated signal is tapped off and compared to the input to form a correcting signal to be added to the output [2]. In this way any variations of the response are automatically corrected. However, the added signal must be separated in wavelength to avoid coherence effects, and is therefore not compatible with a WDM environment.

In this work, a predistortion circuit is constructed by measuring the nonlinearities of a first optical modulator to provide the predistorted input to a second modulator. This approach combines dynamic extraction of non-linear response and WDM compatibility. Past demonstrations of this approach has typically been limited by the need to use two separate transmitters with slightly different response [3]. Here, the two modulators are integrated closely on a single chip, sharing a single optical source. Any variations in chip temperature, input power or wavelength now affects both modulators equally and can be dynamically compensated for.

Experimental arrangement

Figure 1 shows a schematic of the demonstrated predistortion arrangement. The input signal is split in a 2:1 ratio, where the lesser part is used to drive the predistortion link. The output of the link is then subtracted from the remainder of the input signal to form the predistorted input to the second transmitter. A driver amplifier and an optical attenuator are included in the link to ensure that the input power to the two transmitters stays equal for optimum distortion cancellation.

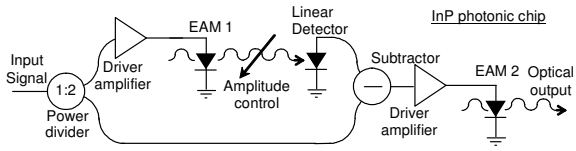

Fig. 1. Operational schematic of broadband linearization scheme.

If the response of the two driver amplifiers is the same, any non-linear response of these are also cancelled in this configuration. In this manner more non-linear, but lower power driver amplifiers can be used. This is a significant advantage, as typical linear amplifiers can easily consume many Watts of supplied power.

Optical device

In this work, all photonic components of the linearized transmitter are integrated on one single InP chip, including the optical source, splitter, modulators, optical attenuator and detector. The integration is achieved using an offset quantum-well material structure where passive sections are defined by selective removal of the quantum wells. The device is based around a widely tunable SGDBR laser – SOA with more than 40 nm tuning range [4]. This type of device with a single EA modulator has previously been shown to generate a 126 $dBHz^{4/5}$ SFDR [5].

Figure 2 shows a schematic of the integrated photonic circuit. The power from the source is split into two Franz-Keldysh modulators located in close proximity on the chip. The optical 3dB-bandwidth of the modulator is 8 GHz. A second reversed biased section acts as an optical attenuator and the detector then completes the on-chip optical link in one of the two waveguide paths. The second waveguide forms the optical output.

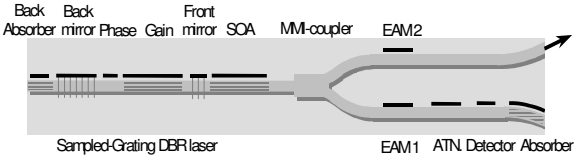

Fig. 2. Schematic of integrated photonic circuit.

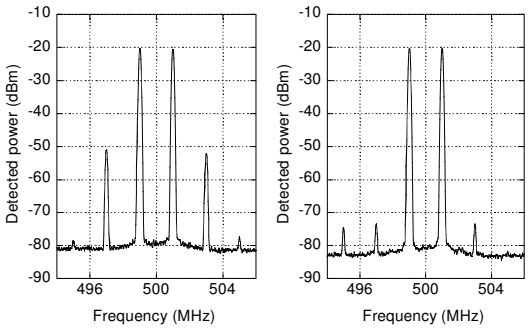

Fig. 3: RF spectra around 500MHz for transmitter with and without predistortion.

Experimental results

The spurious-free dynamic range (SFDR) of the EA modulator without any predistortion or driver amplifier is measured at 98 $dBHz^{2/3}$, when biased at maximum slope. This is about 7 dB lower than devices incorporating a single EA modulator [5], which can be attributed to the lower transmitted power of this particular device. Adding a driver amplifier with low power consumption (~800mW) and low third order intercept point (+15 dBm), the overall link gain is improved at the expense of a penalty in SFDR, now 93 $dBHz^{2/3}$. The left plot of Fig. 3 shows the captured RF spectrum around 500 MHz, where third order intermodulation terms can be clearly observed.

Activating the on-chip predistortion link to compensate for non-linearities, the third-order intermodulation terms can be reduced. The right plot of Fig. 3 shows the captured spectrum where the amplitude and phase response of the predistortion circuit has been carefully matched. More than 20 dB suppression of third order intermodulation terms is observed. This corresponds to a very closely matched phase and amplitude in the summation of signal and predistortion link output. To generate 20 dB of intermodulation suppression, the power must be matched within 0.3dB. The measured SFDR at 500 MHz is compared to the uncompensated case in Fig.4 where a fifth-order intermodulation-limited SFDR of 110 $dBHz^{4/5}$ is obtained, more than compensating for the nonlinearities of the driver amplifier.

To investigate the bandwidth of the predistortion circuit, the center frequency was shifted while keeping all adjustments in the predistortion part constant. The results are shown in Fig. 5 where the dynamic range in a more realistic 1 MHz bandwidth is plotted as a function of frequency offset. 10 MHz frequency offset corresponds to only a 2 dB penalty in SFDR, while the added distortion of the driver amplifier is compensated for within a 50 MHz single-sided bandwidth. This fractional bandwidth can be improved by using more uniform response RF components or an equalizing circuit.

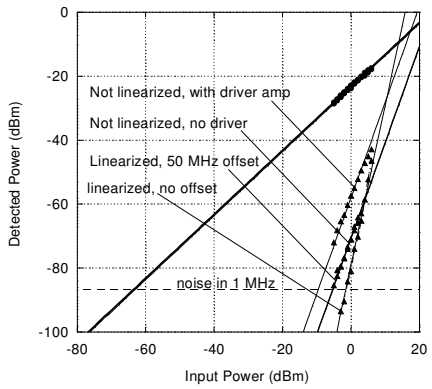

Fig.4: SFDR of the predistorted transmitter with and without 50 MHz frequency offset from setting, and not predistorted with and without driver. The input power has been adjusted to facilitate comparison.

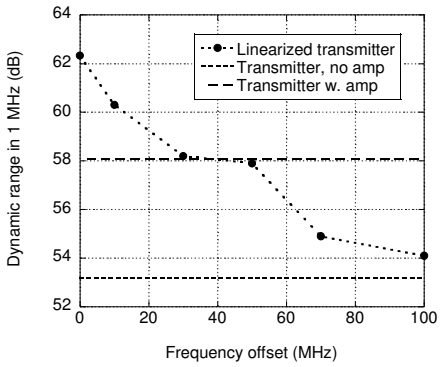

Fig. 5: Measured dynamic range in 1 MHz of the linearized transmitter as a function of shift in operating frequency.

For automatic linearization over the entire tuning range, automatic predistortion gain control will need to be implemented to compensate for the variations in EA slope sensitivity with wavelength.

Summary

We have demonstrated a novel widely-tunable optical transmitter device with an integrated adaptive predistortion circuit based on extraction of nonlinearities using an on-chip optical link. The circuit has not only been showed to compensate for modulator nonlinearities, but also for driver distortion, allowing the use of more power-efficient driver amplifiers. The predistorter compensates for driver amplifier nonlinearities at a 20% fractional bandwidth.

References

1 G.C. Wilson, *et al, J.Lightwave Tech.*, **15** (1997), p. 1652
2 T. Ismail *et al, Proc. MWP 2004*, p. 229
3 J. Yu, *et al, Photon. Tech. Lett.,* **10** (1998), p. 433
4 Y.A. Akulova *et al*, *J.S.T. Quantum Elec.* **8** (2002), p.1349
5 L.A. Johansson *et al, J.Lightwave Tech.* **21** (2003) p.2268

This work was sponsored by the DARPA/MTO CSWDM program under grant no. MDA972-02-3-0006.

Characterization of Third Order Distortion in InGaAsP Optical Phase Modulator Monolithically Integrated with Balanced UTC Photodetector

Matthew N. Sysak[†], Leif A. Johansson[†], Jonathan Klamkin*, Larry A. Coldren, John E. Bowers[†]

[†]*Electrical and Computer Engineering, University of California, Santa Barbara, CA 93106*

[*]*Materials Engineering, University of California, Santa Barbara, CA 93106*

Phone: 805-893-5828, Fax: 805-893-7990, Email: mnsysak@engineering.ucsb.edu

This material is based upon work supported by the DARPA PHOR-FRONT program under United States Air Force contract number FA8750-05-C-0265.

Abstract

We demonstrate a novel, dynamic characterization technique for measuring third order distortion products in an InGaAsP phase modulator. The phase modulator exhibits an output phase IP3 of 4.4π.

I. Introduction

Optical phase modulators are well positioned for use in both next generation analog and digital transmission systems. For digital communications, phase modulation allows greater transmission distances due to larger tolerance to dispersion effects, and wide wavelength transparency due to a broad operating envelope. In analog links, phase modulators are promising to overcome the response of standard amplitude modulators by permitting modulation depths beyond the standard zero and full rail.

Traditionally, measurements of the efficiency and distortion in optical phase modulators has relied on DC characterization techniques such as Mach-Zehnder interferometers and Fabry-Perot resonators [1,2]. However, under large signal conditions these techniques are inherently limited by the nonlinearities generated in the phase to amplitude conversion process. Furthermore, because of the added nonlinearities in the phase detection process, it has been difficult to demonstrate a dynamic measurement of third order distortion at frequencies other than DC.

In this work we propose and demonstrate for the first time, a large signal, dynamic two-tone measurement technique for examining the third order distortion in an optical phase modulator without significant added nonlinearity from the phase recovery process. We use this technique to characterize a forward biased, InGaAsP quantum well (QW) phase modulator that is part of a monolithically integrated InGaAsP/InP photonic receiver chip. Experimental results show that the phase modulator can generate a phase swing of 4.4π before the magnitude of the third order distortion and fundamental response become equivalent.

II. Experiment

The experimental set up used to characterize the distortion products in the InGaAsP phase modulator is shown in Fig 1. An optical transmitter consisting of a single frequency laser source at an operating wavelength of 1545 nm, an EDFA, and a 1 nm FWHM optical bandpass filter is split into two optical paths in a Mach-Zehnder interferometer (MZI) configuration. In one of the arms of the MZI an external $LiNbO_3$ modulator is combined with the 500 μm long InGaAsP test phase modulator that is part of the photonic receiver chip. The photonic chip consists of two parallel optical waveguides, a 2x2 multi-mode interference (MMI) combiner, and a set of 100 μm long uni-travelling carrier photodetectors (UTC-PDs) similar to that in [3] in a balanced configuration. The 2x2 MMI and the balanced photodetectors convert the phase modulation produced by the $LiNbO_3$ and InGaAsP modulators to an amplitude response which can be examined in an electrical spectrum analyzer (ESA).

A set of electrical signal generators are used to create two electrical tones at 249.57 and 249.67 MHz. These two tones are combined using 2:1 combiner, then split into two separate pathways using a 1:2 splitter. One of the outputs from the 1:2 splitter is routed to the $LiNbO_3$ modulator, while the second output is routed to the InGaAsP modulator. A set of attenuators are used to control the amount of electrical power delivered to either the $LiNbO_3$ or InGaAsP phase modulator. External bias tees are used to set the bias conditions on both modulators. The center frequency between the two tones from the signal synthesizers is chosen

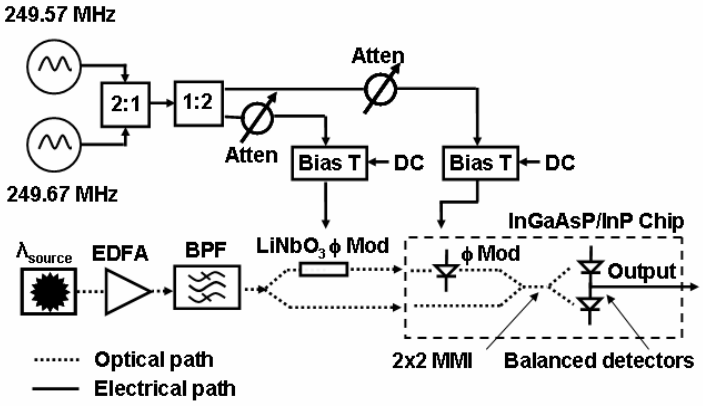

Fig 1. Experimetal set-up for dynamic two tone characterization of third order distortion products in the InGaAsP phase modulator. The optical and electrical paths are indicated by dashed and solid lines respectively.

so that the physical path length difference from the 1:2 electrical splitter to either the InGaAsP or $LiNbO_3$ modulator corresponds to a phase delay of π radians.

Device characterization requires two experiments. The first set of experiments is used to extract the fundamental response of the phase modulator, while a second set of experiments is used to characterize the distortion terms. In the first experiment only the electrical signal used to drive the InGaAsP phase modulator shown in Fig. 1 is enabled. The power out of the electrical signal generators is varied from -19 to -14 dBm, and the phase response of the device is characterized by examining the fundamental and third order distortion peaks generated during the phase to amplitude conversion process in the UTC-PDs. A sample ESA output spectrum from the balanced detector is shown in Fig 2 and labeled "uncompensated response".

In the second experiment, the electrical signals used to drive both the InGaAsP and $LiNbO_3$ modulators are enabled. Since these drive signals are delayed by π radians relative to one another, the phase response of the $LiNbO_3$ modulator compensates the response of the InGaAsP phase modulator. Assuming that the majority of the third order distortion is produced in the semiconductor modulator [4], the phase compensation affects mostly the fundamental response of the InGaAsP device while leaving the distortion products relatively unchanged. The reduction of the fundamental response allows the phase to amplitude conversion process in the UTC-PDs to remain within the linear regime of the Mach-Zehnder, and preserves the phase distortion produced in the InGaAsP modulator without adding nonlinearities from the detection process. A sample spectrum of the electrical response from the balanced detector with both modulators operating is shown in Fig 2 where the peak amplitude modulation is -58 dBm. The response is labeled "compensated response."

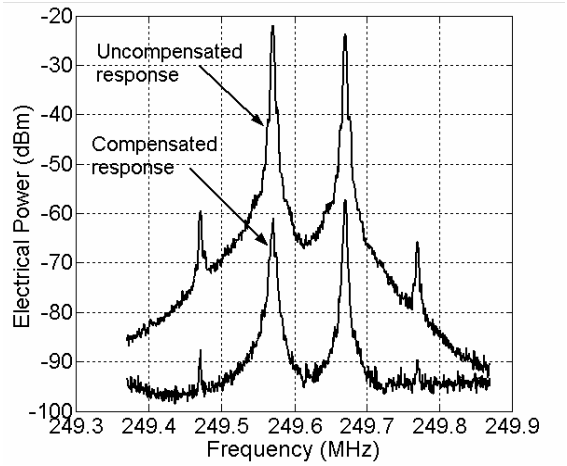

Fig 2. Compensated and uncompensated balanced detector response. Electrical drive power is -15 dBm and -10 dBm to the InGaAsP and $LiNbO_3$ modulators respectively

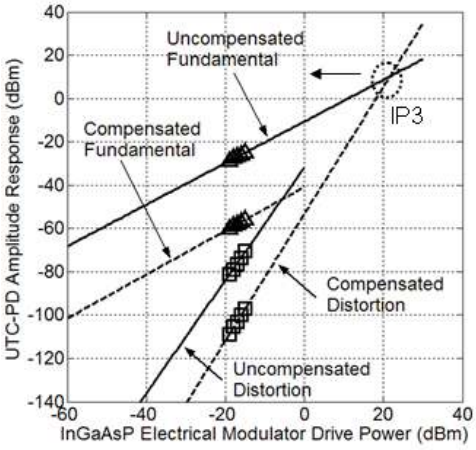

Fig 3. Fundamental and third order distortion in the amplitude response of the UTC-PDs for both compensated and uncompensated experiments.

III. Results

The response of the fundamental and third order tones from the balanced photodetector as a function of applied power to the InGaAsP phase modulator in both the compensated and uncompensated experimental cases are shown in Fig 3. As expected, the addition of the $LiNbO_3$ phase modulator (compensated fundamental and distortion curves) reduces the fundamental response of the InGaAsP modulator and enables the response of the balanced detector to operate under small signal conditions where the phase recovery process is linear. To extract the output phase response of the InGaAsP modulator where the third order intermodulation products have equal power to the fundamental tones (IP3), the amplitude response from the UTC-PDs must be converted to a phase modulation. Since the fundamental response in the uncompensated experiments represents the fundamental response of the InGaAsP modulator for the given range of input powers, and since the third order distortion generated by the InGaAsP modulator is represented by the distortion in the compensated measurements, the IP3 intercept point is taken as the intercept between these two data sets. From Fig 3, the output IP3 of the forward biased phase modulator is +10 dBm, which translates into a balanced photodetector current of 14.1 mA assuming a 50 Ω internal load in the ESA. Given that the average output photocurrent from the UTC-PDs for a π phase shift is 1.6 mA (3.2 mA pp), the output phase IP3 is 4.4π, calculated based on the ratio of the balanced photodetector current at the IP3 point to the current for a π phase shift.

IV. Conclusions

We have proposed and demonstrated for the first time a novel technique for measuring the dynamic distortion in optical phase modulators. Using this approach, we have characterized a forward biased InGaAsP phase modulator monolithically integrated with a set of UTC-PDs. The output phase IP3 of the forward biased InGaAsP phase modulator was measured to be 4.4π.

References

[1] H. Mosheni et. al., "Highly linear and efficienct GaInAsP-InP phase modulators," *Laser and Electro-Optics (CLEO)*, vol. 1, 2004.

[2] M.N. Sysak et. al., "A High efficiency, Current Injection Based Quantum-Well Phase Modulator Monolithically Integrated with a Tunable Laser for Coherent Systems," Coh. Opt. Tech. and Appl. (COTA) 2006, CFC6.

[3] J.W. Raring et. al., "Design and demonstration of novel QW intermixing scheme for the integration of UTC-type photodiodes with QW-based components," IEEE JQE, vol. 42, no. 2, pp. 171-181, Feb 2006.

[4] H.F. Chou et. al., "SFDR Improvement of a Coherent Receiver using Feedback," Coh. Opt. Tech. and Appl. (COTA) 2006, CFA3.

Monolithically Integrated Balanced Uni-Traveling-Carrier Photodiode with Tunable MMI Coupler for Microwave Photonic Circuits

Jonathan Klamkin, Leif A. Johansson, Anand Ramaswamy, Hsu-Feng Chou, Matthew N. Sysak, James W. Raring, Navin Parthasarathy, Steven P. DenBaars, John E. Bowers, Larry A. Coldren
Materials Department and Electrical and Computer Engineering Department
University of California, Santa Barbara, CA 93106 USA
Email: klamkin@engineering.ucsb.edu
Telephone: (805) 893-2875, Fax: (805) 893-4500

***Abstract*—A monolithically integrated balanced uni-traveling-carrier photodiode (UTC-PD) with a tunable 2x2 multimode interference (MMI) coupler has been fabricated and tested. Two waveguide UTC-PDs are electrically isolated using high-energy Helium implantation, and then connected in series using a monolithic metal interconnect. On chip metal-insulator-semiconductor (MIS) capacitors provide some DC decoupling. The tunable MMI coupler allows for tuning of the power balance in the PDs. Output saturation currents greater than 40 mA at 1 GHz are demonstrated for a single 10 μm x 150 μm UTC-PD. The third order intermodulation distortion (IMD3) is also measured and exhibits an output intercept point (OIP3) of 43 dBm at 20 mA and 34 dBm at 40 mA for this same UTC-PD. In the balanced configuration, the OIP3 values are therefore 49 dBm and 40 dBm. The balanced UTC-PD is also highly symmetric; the common mode rejection ratio (CMRR) was measured to be around 40 dB.**

Keywords-balanced photodiode (BPD), common mode rejection ratio (CMRR), fiber-optic link, linearity, saturation current, third order intermodulation distortion (IMD3), third order output intercept point (OIP3), uni-traveling-carrier photodiode (UTC-PD).

I. INTRODUCTION

Phase modulated coherent fiber-optic links have the potential for greatly enhanced spur free dynamic range (SFDR) [1]. The backbone of a coherent link is the coherent optical receiver used to demodulate the phase of the received signal. A coherent receiver consists of a coupler for mixing the incoming signal with a local oscillator (LO) signal, and a balanced photodiode (BPD) for detecting the phase difference between the two waves. BPDs are employed because of their ability to suppress laser relative intensity noise (RIN) [2]. Some of the desired attributes for a coherent receiver are high power, high linearity, and large CMRR. A pin BPD has been reported with more than 20 dB CMRR [3]. UTC-PDs are attractive for BPDs because of their high saturation current capabilities made possible by reduced space charge effects [4]. Recently an advanced device architecture has been developed allowing for the monolithic integration of waveguide UTC-PDs with other optical components [5]. A monolithically integrated coherent receiver is advantageous because the optical power coupled to the PDs can be maximized. In this work, we have fabricated and tested a monolithically integrated BPD consisting of two series connected UTC-PDs,

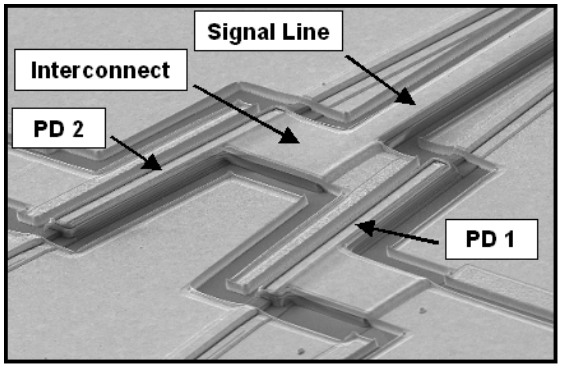

(a)

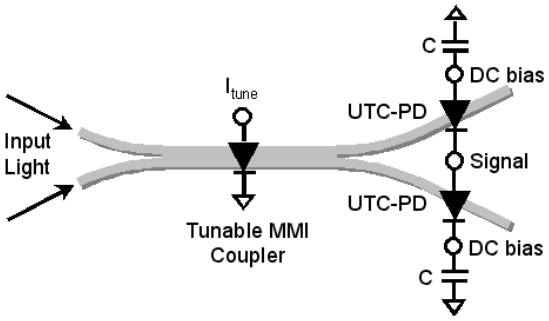

(b)

Fig. 1. (a) SEM image of UTC-PD pair connected in series and (b) schematic of balanced UTC-PD with integrated tunable MMI coupler.

a tunable 2x2 MMI coupler, and DC decoupling capacitors. With a single regrowth process, several optical components have been monolithically integrated to form a highly functional microwave photonic circuit. The UTC-PDs exhibit both high saturation current and high linearity. The MMI can be fine tuned to a 50:50 splitting ratio allowing for accurate control of the power balance in the PDs. The BPD is also highly symmetric lending to a large CMRR.

II. Device Design and Fabrication

The device structure is grown on a semi-insulating InP substrate by MOCVD. The optical waveguide consists of unintentionally doped (UID) InGaAsP QWs and barriers sandwiched between two InGaAsP waveguide layers. The bandgap wavelength of the QWs is significantly detuned from the input wavelength in order to minimize optical losses in the passive sections of the device. The UTC-PD structure is grown above the optical waveguide. This consists of a highly n-doped InP layer, followed by a UID InP collection layer, some band smoothing layers, and a highly p-doped InGaAs absorbing layer. Photodetection regions are formed by selectively removing these UTC-PD layers. The highly n-doped InP layer ensures that the electric field drops only across the collection layer in the photodetection regions. After formation of these regions, a blanket InP cladding regrowth is performed. Following regrowth, ridges and mesas are etched. Topside n- and p-contacts are then deposited and annealed. Benzocyclobutene (BCB) dielectric is used for reducing parasitic pad capacitance. The UTC-PDs are electrically isolated with a series of high energy Helium implants ranging in energy from 40 keV to 1.325 MeV. This provides a sheet resistance of 5.28 MΩ/square on the n-side and 2.46 MΩ/square on the p-side of the diodes as determined by transmission line model (TLM) measurements. A SEM and schematic of the balanced UTC-PD are shown in Fig. 1. The PDs are connected in series with a monolithic metal interconnect. This electrical isolation and series connection technique has been used in previous work for the fabrication of tunable bipolar cascade lasers and photonic integrated circuits (PICs) [6]. The MIS capacitors are fabricated by sandwiching a thin layer of dielectric between the p-metal and a buried n-contact layer. The capacitance is around 30 pF but can be varied simply by adjusting the dielectric thickness.

The 2x2 MMI coupler is a general interference type MMI [7]. It is 8 μm wide and 336 μm long. For tuning, current is injected uniformly across the width and into a region 70 μm long in the center of the MMI. In a MMI, the input field is reproduced in single or multiple images at periodic intervals. By modifying the refractive index around a selected area within one interval of the MMI, new phase relations between self-images are produced in the next interval resulting in a modified output image [8]. Therefore locally injecting current to change the refractive index can be used to tune the splitting ratio of the MMI.

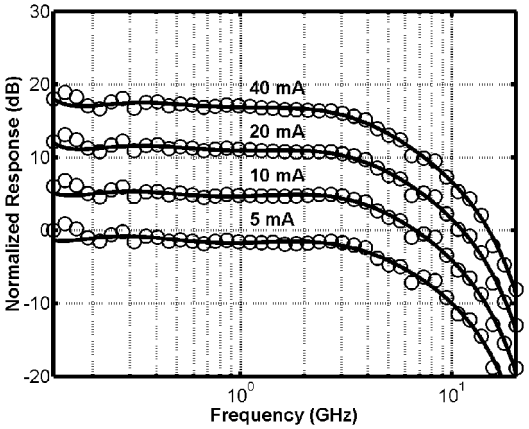

Fig. 2. Normalized response of a 10 μm x 150 μm UTC-PD at varying photocurrent levels. The bias is –5 V.

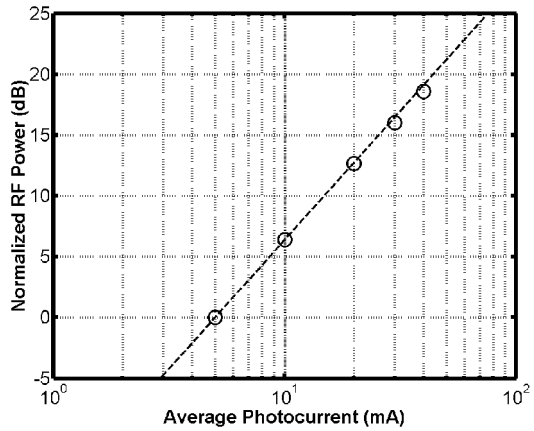

Fig. 3. Normalized RF power as a function of average photocurrent at 1 GHz for a single 10 μm x 150 μm UTC-PD. The bias is –5 V.

III. Results

To characterize the saturation current and linearity of the UTC-PDs, they were measured discretely. The optical-to-electrical frequency response was measured using a lightwave component analyzer. Fig. 2 shows the normalized response for up to 40 mA of average DC photocurrent for a single 10 μm x 150 μm UTC-PD. Fig. 3 shows the normalized RF power as a function of average DC photocurrent. The saturation current is greater than 40 mA at a bias of –5 V. The IMD3 was measured using a two-tone setup similar to that in [9]. Two DFB lasers were externally modulated to generate two tones, and the signals were combined in a 3 dB coupler.

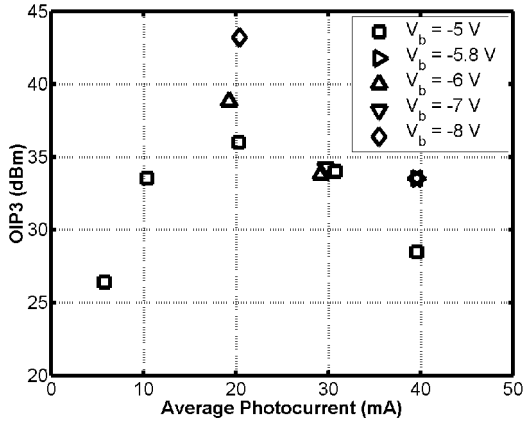

Fig. 4. OIP3 as a function of average photocurrent for varying biases. This is for a single 10 μm x 150 μm UTC-PD.

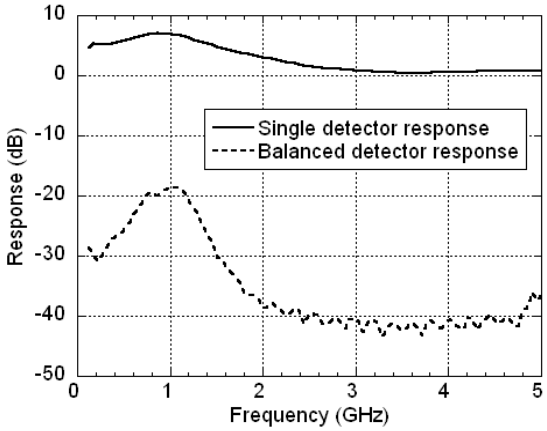

Fig. 6. Frequency response measurement with optical input to single PD and with balanced optical input.

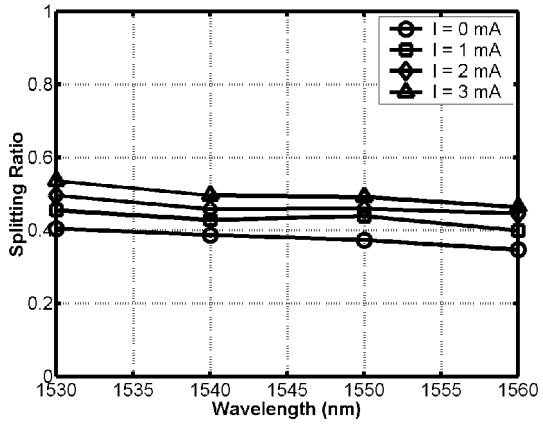

Fig. 5. Tunable MMI coupler splitting ratio as a function of wavelength for several current injection levels.

An EDFA was used to vary the optical power input to the UTC-PD. Fig. 4 shows a plot of the extracted OIP3 as a function of average DC photocurrent for several biases. For a fixed photocurrent level, say 20 mA, increasing the reverse bias enhances the OIP3 by reducing space charge effects in the PD [10]. The OIP3 at 20 mA and a bias of –8 V was 43 dBm and at 40 mA and a bias of –5.8 V was 34 dBm. This corresponds to 49 dBm and 40 dBm in the balanced configuration. To the best of our knowledge, these are some of the highest OIP3 values reported for a waveguide PD.

To characterize the tunability of the MMIs, the splitting ratio was measured over a wide wavelength range for varying levels of injected current. Fig. 5 shows that with just a few milliamps of injected current, the splitting ratio can be adjusted in order to balance the power in the output arms of the MMI. This indicates that only slight changes in refractive index are necessary for tuning the splitting ratio. If higher refractive index changes and thus higher levels of injected current were necessary, the device performance could degrade [8]. The CMRR was measured by comparing the measured electrical response with light input to one UTC-PD to that with light input to both UTC-PDs with a balance of optical power. To do this, the tunable MMI coupler was used to achieve a maximum power imbalance and then an optimized power balance. Fig. 6 shows the corresponding measured frequency responses. The CMRR is 40 dB for frequencies above 2 GHz.

IV. Conclusions

We have fabricated and characterized a waveguide balanced UTC-PD where adjacent UTC-PDs are electrically isolated using high energy Helium implants and series connected with a metal interconnect. The BPD has been monolithically integrated with a tunable 2x2 MMI coupler using a simple single regrowth fabrication process. By injecting current into a section of the MMI to locally change the refractive index, the splitting ratio can be tuned to balance the power in the PDs. A single UTC-PD has a saturation current greater than 40 mA and OIP3 values of 43 dBm and 34 dBm at DC photocurrent levels of 20 mA and 40 mA respectively. These correspond to 49 dBm and 40 dBm for the balanced configuration. The splitting ratio of the MMI coupler can be tuned with just a few milliamps of injected current. The BPD has a CMRR of 40 dB as measured by comparing the electrical response with light input to a single PD to that with a balanced optical input. This BPD can be

used for enhancing the performance of coherent fiber-optic links as well as other microwave photonic links.

V. REFERENCES

[1] H. Chou, A. Ramaswamy, D. Zibar, L. A. Johansson, J. E. Bowers, M. Rodwell, L. Coldren, "SFDR Improvement of a Coherent Receiver Using Feedback," *Coherent Optical Technologies and Applications (COTA) Conference*, 2006.

[2] F. Xia, S. Datta, S. R. Forrest, "A Monolithically Integrated Optical Heterodyne Receiver," *IEEE Photon. Technol. Lett.* vol. 17, pp. 1716-1718, Aug. 2005.

[3] A. Beling, H.G. Back, D. Schmidt, G.G. Mekonnen, M. Rohde, L. Molle, H. Ehlers, A. Umbach, "High-speed balanced photodetector module with 20 dB broadband common-mode rejection ratio," *Optical Fiber Communications Conference (OFC), 2003.*

[4] T. Ishibashi, T. Furuta, H. Fushimi, S. Kodama, H. Ito, T. Nagatsuma, N. Shimizu, Y. Miyamoto, "InP/InGaAs Uni-Traveling-Carrier Photodiodes," *IEICE Trans. Electron.,* vol. E83-C, pp. 938-949, June 2000.

[5] J.W. Raring, E.J. Skogen, C.S. Wang, J.S. Barton, G.B. Morrison, S. Demiguel, S.P. DenBaars, L.A. Coldren, "Design and Demonstration of Novel QW Intermixing Scheme for the Integration of UTC-Type Photodiodes with QW-Based Components," *IEEE J. Quantum Electron.,* vol. 42, pp. 171-181, Feb. 2006.

[6] J. Klamkin, J. M. Hutchinson, J. T. Getty, L. A. Johansson, E. J. Skogen, L. A. Coldren, "High Efficiency Widely Tunable SGDBR Lasers for Improved Direct Modulation Performance," *IEEE J. Sel. Topics Quantum Electron.*, vol. 11, pp. 931-938, Sep./Oct. 2005.

[7] L. B. Soldano, E. C. M. Pennings, "Optical Multi-Mode Interference Devices Based on Self-Imaging: Principles and Application," *IEEE J. Lightwave Technol.*, vol. 13, pp. 615-627, Apr. 1995.

[8] J. Leuthold, C. H. Joyner, "Multimode Interference Couplers with Tunable Power Splitting Ratios," *IEEE J. Lightwave Technol.*, vol. 19, pp. 700-707, May 2001.

[9] T. Ohno, H. Fukano, Y. Muramoto, T. Ishibashi, T. Yoshimatsu, Y. Doi, "Measurement of Intermodulation Distortion in a Unitraveling-Carrier Refracting-Facet Photodiode and a p-i-n Refracting-Facet Photodiode," *IEEE Photon. Technol. Lett.*, vol. 14, pp. 375-377, Mar. 2002.

[10] K. J. Williams, R. D. Esman, "Design Considerations for High-Current Photodetectors," *IEEE J. Lightwave Technol.*, vol. 17, pp. 1443-1454, Aug. 1999.

II. Photonic IC Wavelength Converters

A. Photo-Current Driven Wavelength-Converters

Field modulated wavelength converters

Jonathon S. Barton, Matthew N. Sysak, Anna Tauke-Pedretti, Matthew Dummer, James Raring, Leif A. Johansson, Milan L. Mašanović, Daniel J. Blumenthal, Larry A. Coldren

Materials and Electrical and Computer Engineering Depts., University of California, Santa Barbara, 93106
jsbarton@engineering.ucsb.edu

ABSTRACT

We demonstrate 10Gbit/s operation of two different types of monolithic photocurrent driven wavelength converters (PD-WC). These photonic integrated circuits use a Semiconductor Optical Amplifier (SOA)-PIN photodetector receiver to drive an Electro-absorption (EA), or Mach-Zehnder (MZ) modulator that is integrated with a SGDBR tunable laser. We demonstrate improvements in optical bandwidth, insertion losses, device gain, and modulation efficiency.

Keywords: Wavelength conversion, high-speed modulators, optically controlled gate, tunable laser, semiconductor optical amplifier, Electro-absorption modulator, Mach-Zehnder modulator.

I. INTRODUCTION

Networking and infrastructure providers see great value in continuing to pursue technology that can lower costs yet provide increased flexibility and manageability of network capacity. Next generation networks using wavelength division multiplexing will benefit from highly functional large-scale Photonic Integrated Circuits (PICs). These new wavelength transparent networks will require important functions such as wavelength provisioning, add-drop multiplexing and packet switching that will need fast and dynamic wavelength conversion to eliminate wavelength blocking and wavelength management issues for high traffic networks. Traditionally, wavelength conversion is performed using a wavelength interchanging cross connect (WIXC) with conventional transponders and optical/electrical/optical (OEO) conversion. This approach does allow for clock recovery and 3R regeneration of the signal at the node. Unfortunately, these OEO devices consume increasingly large amounts of power at high bit rates, have a large footprint, and due to the electronics involved, lack bit-rate transparency[1-3]. Dynamic widely-tunable solutions that can cut power consumption, size, weight and ultimately costs are seen as essential, in not only terrestrial networks but increasingly avionic and ship based communication systems.

A number of different wavelength converter approaches have been explored. Typical approaches use either semiconductor optical amplifiers (SOAs) or Electro-absorption (EA) modulators with cross-gain modulation (XGM)[4], Four-Wave Mixing (FWM)[5], Difference Frequency Generation(DFG)[6], Nonlinear Optical Loop Mirror (NOLM)[7], SAGNAC[8], Michelson interferometer[9], delayed interference[10], Photocurrent Assisted Wavelength (PAW) conversion [11], and cross-phase modulation in fiber[12] and All Optical SOA Indium Phosphide (InP) based Mach-Zehnder structures [13,14]. Arrays of devices have been demonstrated in both in-plane and vertically illuminated[15] configurations. Also, tunable laser integrated devices have been demonstrated such as a wavelength selectable laser with all-optical wavelength converter[16]. Additionally, All Optical Label Swapping (AOLS) has been demonstrated with 40 Gbit/s RZ packets and 10Gbit/s labels using a Sampled Grating Distributed Bragg Reflector (SGDBR) laser integrated differential driven active Mach-Zehnder all-optical wavelength converter[17]. Another approach takes advantage of gain suppression by direct injection into either Super Structure Grating Distributed Bragg Reflector (SSGDBR)[18] or Grating Coupled Sampled Reflector (GCSR)[19] lasers.

The key issues that impact the performance of the wavelength converter include: insertion losses/coupling losses, wavelength dependence of output power, extinction ratio, input and output optical, input power dynamic range, power dissipation particularly with arrays, optical filtering of the input wavelength, bandwidth limitations such as carrier

Optoelectronic Integrated Circuits VIII, edited by Louay A. Eldada, El-Hang Lee,
Proc. of SPIE Vol. 6124, 612417, (2006) · 0277-786X/06/$15 · doi: 10.1117/12.656011

lifetime, cascadability, and chirp. Effective design needs to attempt to achieve adequate performance of all these metrics simultaneously.

II. PHOTOCURRENT DRIVEN WAVELENGTH CONVERSION

In this paper we present our latest results from a class of widely-tunable photocurrent driven wavelength converters (PD-WC). These devices operate by the generation of photocurrent in a detector, which changes the electric field across the depletion region in a reverse biased modulator. With this approach, switching speeds are not limited by carrier modulation effects such as carrier lifetime, and there is the potential for very high modulation bandwidths without requiring optical filtering of the input signal at the output. Very high optical bandwidths have been demonstrated with a similar optical gating approach using an integrated traveling wave Electro-absorption modulator (EAM) and high-speed detector[20]. In this manuscript, we demonstrate some of the first tunable laser integrated photocurrent driven 10Gbit/s capable devices based on both EAM and MZM devices. The structures benefit from a simple process and chip-to-chip optical gain (10dB), as well as operate at high data rates (10Gbit/s) with high extinction ratios (>10dB). These integrated devices make use of an optically pre-amplified receiver to eliminate the need for electrical amplification in the device. Additionally, they have the potential of exhibiting less dissipated power than conventional SOA based all-optical WC devices. PD-WCs are also inherently filterless due to spatial separation of the input and output ridge. In practice, stray light often can be coupled at the output through the substrate of photonic integrated circuits. With proper design with separation and curving of the waveguides, we achieve very high suppression of the input signal at the output (>40dB).

Monolithically integrated widely-tunable 2.5Gbit/s wavelength conversion has been previously demonstrated using an offset-QW integration platform with the direct modulation of SGDBR[21] and Bipolar Cascade SGDBR (BC-SGDBR) lasers[22] as well as externally modulated EA[23] and MZ[24] modulators integrated with a SGDBR laser, Semiconductor Optical Amplifiers (SOA), and a photodetector. Recently, 10Gbit/s operation has been demonstrated using a hybrid traveling wave series push-pull (SPP) MZM and amplified photodetector [25]. In this work, we aim to demonstrate fully integrated functionality, as well as reduce the high input power requirements and provide device gain. By using a more optimized SOA receiver design, input power requirements have been reduced considerably – down to approximately -10dBm. Improvements have also been made by modifying the integration platform growth structure. In the next section we examine the epitaxial structure in more detail.

III. MATERIAL STRUCTURE

Monolithic wavelength converters have been fabricated using a number of different integration platforms such as offset QW, quantum well intermixing, and butt joint regrowth techniques. A detailed discussion of these techniques is outlined elsewhere[26]. This manuscript will show some our latest results using a dual QW epitaxial structure which provides higher efficiency, higher bandwidth modulators and detectors, and potentially lower device insertion losses, when compared with the traditional offset quantum well (OQW) approach. This is achieved without modifying the simple fabrication sequence associated with the OQW platform or adding any regrowth steps [26-27].

It is well known that by implementing QWs in a modulator structure, one can improve the efficiency of modulation at lower DC biases on the modulator. The challenge is to simultaneously achieve low propagation losses and wavelength independence. We can take advantage of this added performance by using a dual QW structure in which offset gain QWs are used in the SOA and gain section of a SGDBR tunable laser, and wide and shallow centered QWs are used for the modulation and tuning regions. This approach improves the modulation efficiency considerably without increasing the propagation losses, or excessively restricting the wide wavelength range.

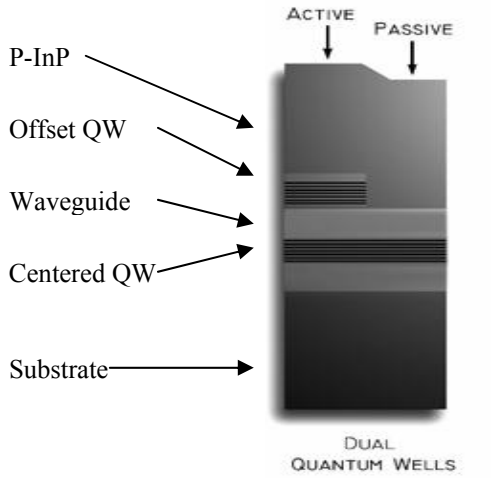

Layer	Doping	Thickness
P+InGaAs	1e19 cm^{-3} Zn	100nm
p- InP	1e18 cm^{-3} Zn	2µm
Offset QW	UID	106.5nm
Waveguide 1.3Q	5e16 cm^{-3} Zn	126nm
Centered MQW	UID	93nm
Waveguide 1.3Q	5e16 cm^{-3} Zn	126nm
InP Buffer	1e18 cm^{-3} Zn	1.8µm
N InGaAs	1e18 cm^{-3} Zn	100nm
InP buffer	1e18 cm^{-3} Zn	0.5µm
Substrate	Fe Semi-insulating	100µm

Fig.1 Dual Quantum Well growth structure

The base structure seen in fig. 1, is almost identical to the offset QW structure[24], except for a multi-quantum well region centered in the optical waveguide layer. The centered QW stack contains 7 x 9nm compressively strained (0.33 %) wells and 6 x 5nm tensile strained (0.075 %) barriers and has a photoluminescence peak at 1480 nm. With the proper design of the CQW stack, it is possible to achieve low propagation loss ($6cm^{-1}$), high injection efficiency (69%), high modulation efficiency and broad optical modulation bandwidths. Due to the reduced doping (5e16 cm^{-3} Si) in the waveguide region of the dual QW base structure, there is a significant bandwidth increase in comparison with OQW Franz Keldysh devices[26]. In addition, by utilizing shallow QW for the CQW stack, devices can operate under high waveguide optical power levels (>30 mW) without degradation of optical bandwidth. In the next two sections we will examine in more detail results from both fully integrated EAM and MZM based PD-WCs.

IV. ELECTROABSORPTION BASED DEVICES

Electro Absorption Modulator (EAM) based PD-WCs utilize two parallel waveguide ridges, one functioning as a receiver and the other functioning as a transmitter. The receiver consists of an SOA for amplification of the input signal and a photodiode for signal detection. The transmitter ridge consists of a widely-tunable SGDBR laser, output SOA and an EAM. The EAM and photodetector are interconnected such that the generated photocurrent in the detector drops across a termination load, resulting in a voltage swing across the EAM. For optimum performance, the SGDBR should provide wide tunability and high output power, the EAM should provide sufficient bandwidth for the desired data rate and high extinction efficiency, and the SOA/photodetector receiver needs to provide sufficient bandwidth and linear output power versus input power over the range required to drive the EAM. In other work, regrowth schemes are being explored for the separate optimization of the individual components[26]. Previously, 2.5Gbit/s operation had been demonstrated with an offset QW EAM based PD-WC[24], however more recent work using this very low capacitance dual QW structure enables 10Gbit/s non return to zero (NRZ) operation as illustrated in the next section.

1.1. Monolithic Dual QW EAM Based 10 Gb/s Wavelength Converter

In recent progress we have demonstrated the first 10Gbit/s NRZ monolithic widely-tunable EAM based PD-WC. Scanning electron micrographs showing the device layout are shown in fig. 2.

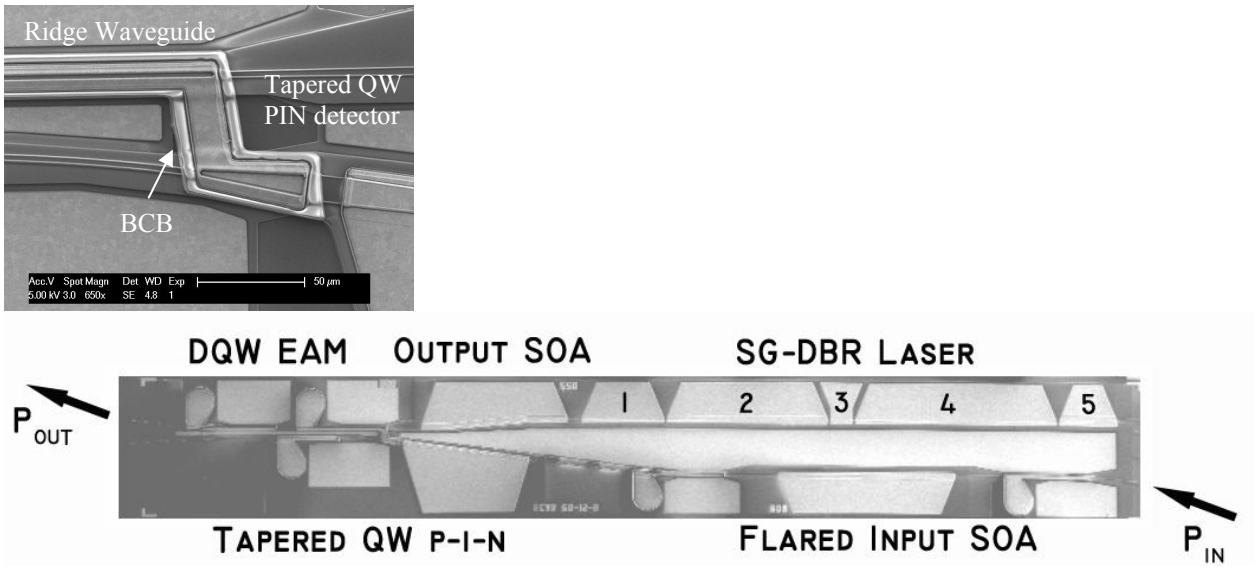

Fig. 2 Top view SEM of EAM based PD-WC device fabricated using the dual QW platform

For the EA modulator based devices, the input signal is fed into a passive curved waveguide as shown to the right of fig 2. It is amplified by two SOAs. The first SOA is 600 μm long and has a ridge width of 3.0 μm. The function of this SOA is to amplify the input signal from the fiber coupled level to just below the 1-dB gain compression for an optical amplifier of that particular ridge width. The second SOA is 400 μm long and has a flared waveguide ridge that is designed to maintain the overall photon density while the optical mode is expanded and the overall power level is increased. The second SOA is exponentially flared from 3.0 μm to 12 μm. The transmitter portion of the PD-WC is comprised of a four section SGDBR followed by a 550 μm long SOA for output amplification, and a shallow QW EAM electrode. The waveguide quantum well stack consists of seven 90 Å compressively strained wells and six 50 Å tensile strained barriers. The SEM inset in Fig. 2 shows the device electrode between the tapered QW detector and EAM ridge. Photo-bis-benzocyclobutene (BCB) low K dielectric is used under the high-speed modulator and detector electrodes to reduce the parasitic pad capacitances.. Additional optional passive section electrodes were integrated for power monitoring and diagnostics on both the input and output waveguides.

The SGDBR laser consists of a front mirror(1), gain(2), phase(3), rear mirror(4), and backside absorber(5), as depicted in fig. 2. Typical SGDBR wavelength spectra are shown for such a device in fig. 3a. The phase and mirror sections function to tune the wavelength of the laser over greater than 40 nm. The laser design is similar to that described previously[24]. Figure 3b shows the light/current/voltage characteristics for an untuned SGDBR laser with typical threshold currents close to 39mA.

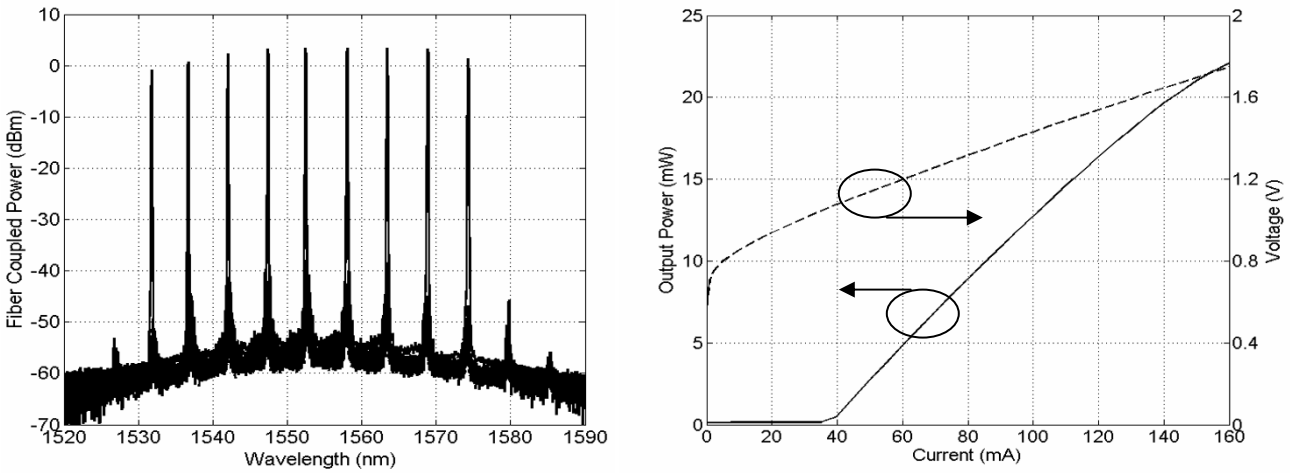

Fig. 3.(a) Tuning spectra and (b) light/voltage characteristics versus current for SGDBR fabricated on dual QW platform at 1555nm at 18 ^{0}C

One can see from fig. 4a that the wavelength shift possible under forward bias in the Sampled Grating (SG) Mirror sections using the dual QW structure is slightly improved with respect to a similar bulk waveguide SG mirror. With optimum MQW design, large refractive index changes are possible within the constraints of excessive optical losses[28]. As can be seen in Fig. 4b, the propagation losses through the device are increasingly wavelength dependent for long wavelength QW photoluminescence compositions. As mentioned before, the material used to fabricate the wavelength converter has a shallow QW PL peak centered at 1480nm. This corresponds to optical losses varying from approximately 15cm^{-1} at the lower limit of the C-Band to as low as 6cm^{-1} at 1565nm.

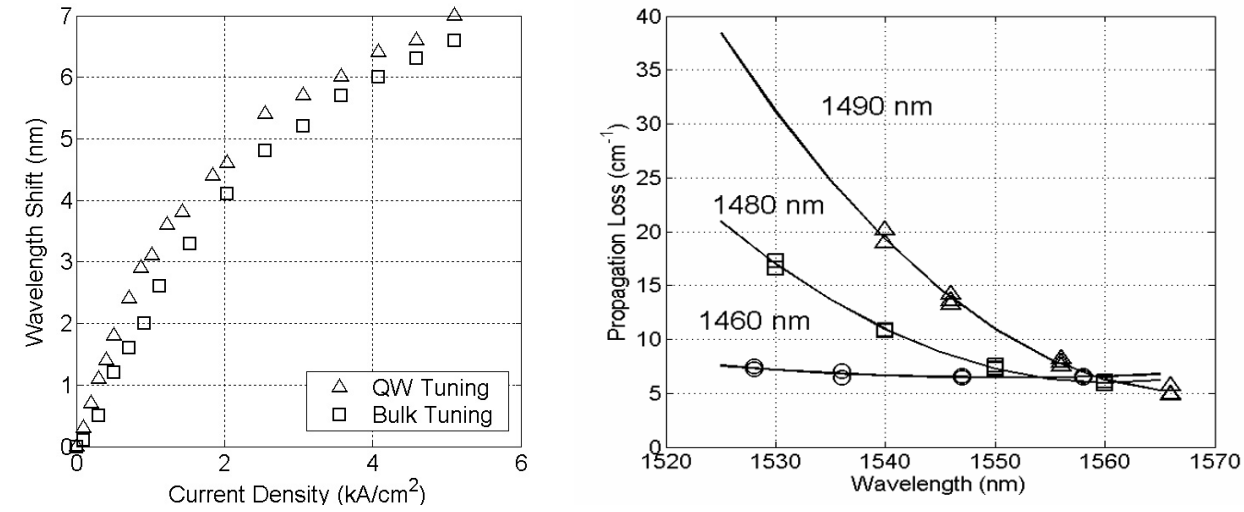

Fig. 4(a) Wavelength shift as a function of current density in the Sampled Grating mirror sections (b) Propagation loss versus operating wavelength for three different waveguide MQW designs employed in the dual QW platform[26]

Modulator efficiency is another important parameter that we wish to optimize. As can be seen in fig. 5a, the slope efficiency as a function of reverse bias can provide as high as two times the efficiency as a bulk InGaAsP Franz-Keldysh waveguide device based on the offset QW platform over the full wavelength range of operation. Since the efficiency improves with reverse bias, previous Franz-Keldysh based devices incurred large insertion losses in order to achieve sufficient extinction ratios and acceptable bit error rate (BER) performance. With the dual QW platform, much lower reverse biases can be used (2.5V-3.5V) for optimal efficiency which benefits from lower power dissipation and higher device gain due to the much lower insertion losses. As can be seen in fig. 5b, increased modulator length is advantageous for wavelength converter efficiency.

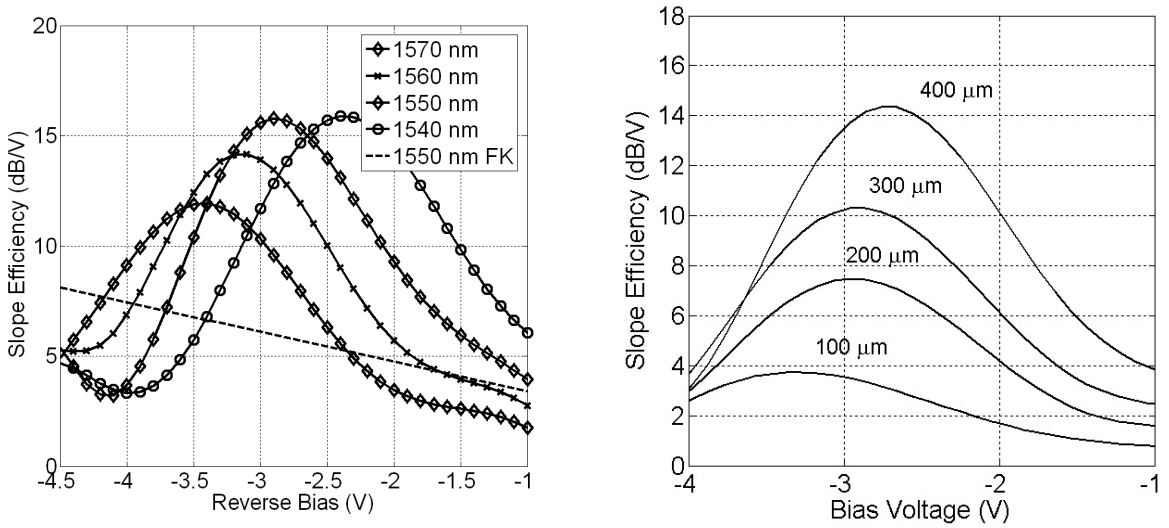

Fig. 5(a) Slope efficiency as a function of DC bias for different wavelengths using material with a shallow QW PL of 1480nm. Modulator is 400μm long. FK designates Franz-Keldysh offset QW structure (b) Slope efficiency as a function of DC bias for different electrode lengths at 1560nm

Key performance characteristics from wavelength converters with different EAM/detector schemes were measured to determine the optimum device layout for the EA based dual quantum well wavelength converters. The extinction ratio and output power versus reverse bias for wavelength converters comprised of a 50μm long tapered detector (as previously described) interconnected to a 200μm, 300μm, and 400μm long EAM are shown in fig. 6a and fig. 6b, respectively, at 10Gbit/s with a 50ohm termination. Wavelength conversion was performed between 1548 nm and 1550 nm and the input power level is –5 dBm. Input amplifier bias currents are set to maintain a current density of 6 kA/cm2 and the transmitter gain section is biased at 120 mA. The output transmitter SOA is biased at 75 mA.

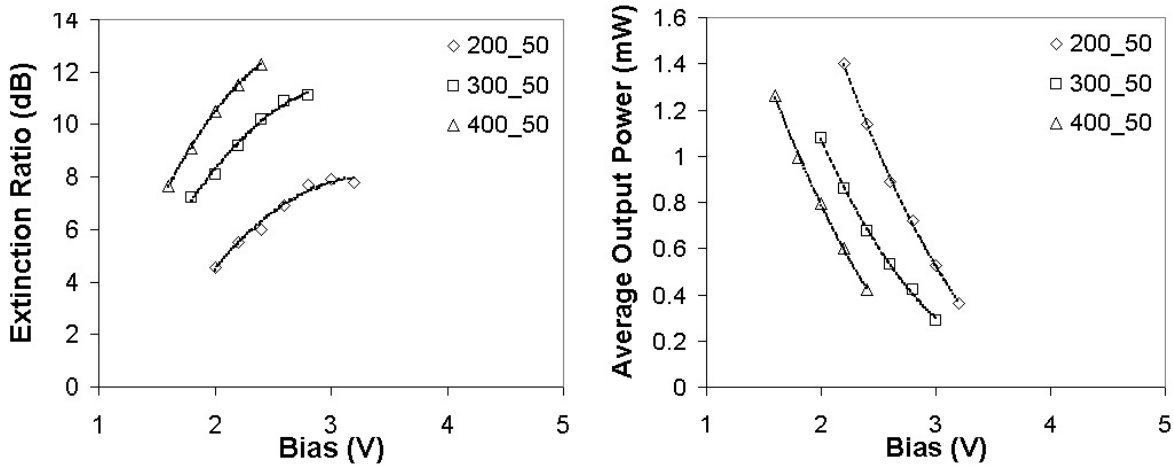

Fig. 6(a) Extinction Ratio (dB) vs. DC bias. (b) Average output power vs DC bias.
Wavelength converter 200μm long EAM- 50μm det / 300μm long EAM/50μm det / 400μm long EAM-50μm det. (centered and lined up?)

In Fig. 6, it can be seen that by increasing the length of the modulator, a higher extinction ratio and higher output power is possible with lower modulator bias.

The facet to facet device gain was measured for a device with a 300μm and 400μm long EAM electrode as can be seen

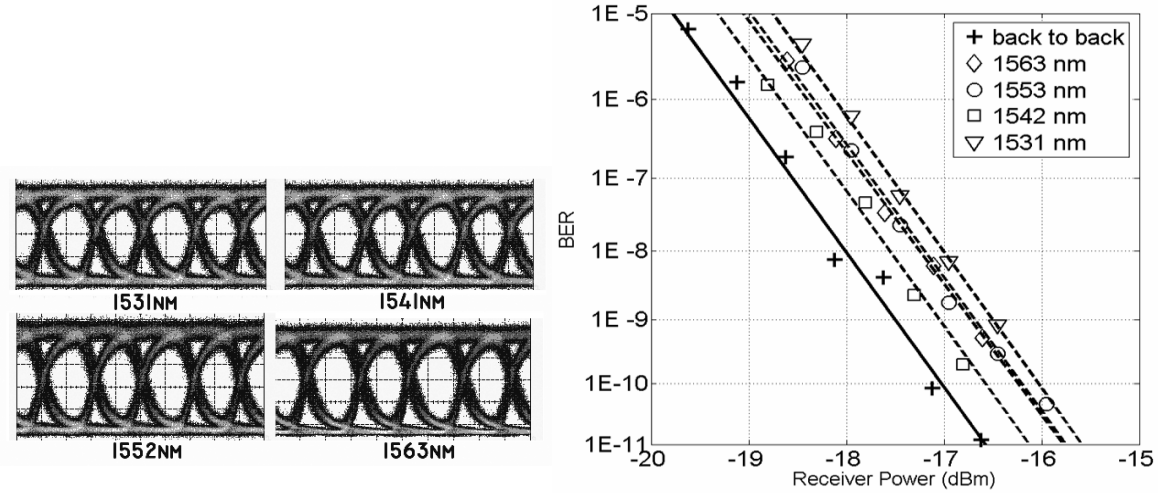

Fig. 8 (a) 10 Gb/s wavelength conversion eye diagrams for device with 400μm long EAM and 50μm long detector (b) BER measurements for received power for an input wavelength of 1548nm and various output wavelengths with a pattern length of 2^{31}-1

in fig. 8. 5-9dB of gain is demonstrated over the whole C-Band with an input power of -5dBm and over 10dB extinction ratio.

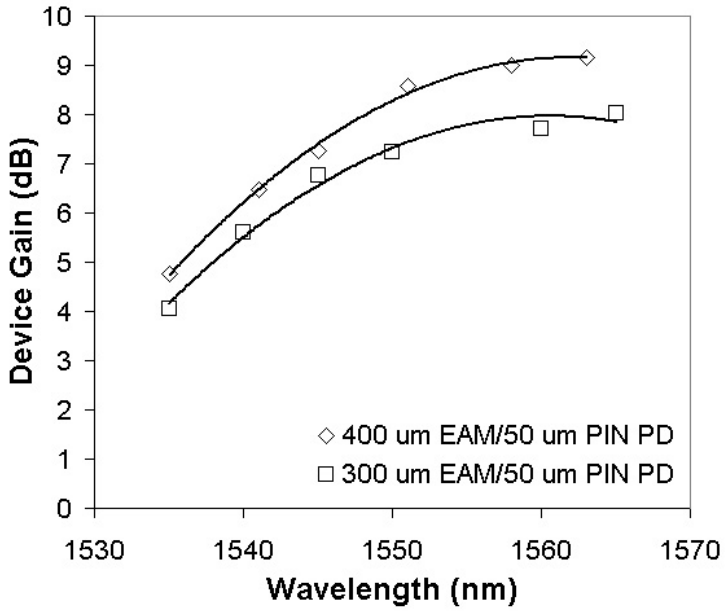

Fig. 8. Facet-to-facet device gain through device as a function of wavelength for input power of -5dBm. Coupling losses are 4.2dB for input and output lensed fiber.

Over the wavelength range, the SOA gain varies with a peak at 1550nm. Bias conditions were selected to achieve over 10dB extinction ratio at the output. As the 400μm long EAM based wavelength converter had sufficient optical bandwidth to operate at 10Gbit/s, it was chosen to perform bit error rate (BER) measurements. 10Gbit/s eye diagrams and BER measurements are given for an input wavelength of 1548nm to output wavelengths at 1531nm, 1541nm, 1552nm, and 1563nm using a pattern length of 2^{31}-1 Pseudo Random Bit Stream (PRBS). As can be seen in Fig. 7, all eye diagrams are open and clear. Greater than 10 dB of signal extinction was achieved at all wavelengths when biasing the EAM/photodetector in the 1.7-2.5V range. Less than 1-dB of power penalty can be seen over an operating

wavelength range of 32 nm. The reverse bias range and coupled-chip power used in this measurement was 1.7-2.5V and under -10 dBm, respectively. These results demonstrate the viability of single-chip wavelength conversion using the widely-tunable EAM PD-WC scheme.

VI. MACH-ZEHDNER BASED DEVICES

Two types of Mach-Zehnder based photocurrent-driven wavelength converters have been demonstrated recently using an OQW integration platform. The first configuration used photocurrent generated in a passive region photodiode to drive an integrated SOA-SGDBR transmitter with a single MZ lumped electrode[23]. Although appealing due to its polarization insensitivity, the device did not use any optical amplification leading to fairly high input power requirements. Without traveling wave electrodes, the optical bandwidth of the device is limited. More recently a hybrid integrated device using traveling wave series push pull (SPP) Mach-Zehnder modulator electrodes has demonstrated 10Gbit NRZ wavelength converter operation over a wide wavelength range with low power penalties[25]. This work used a SOA-PIN receiver to drive a 400μm long modulator[29]. A monolithic version of this device is shown in fig. 9. The total footprint of the chip is less than 1mm x 3.8mm. As this device is fabricated on a Fe-doped semi-insulating substrate, GeAuNiAu separate n-contacts are required in the laser, modulator, SOA and detector regions.

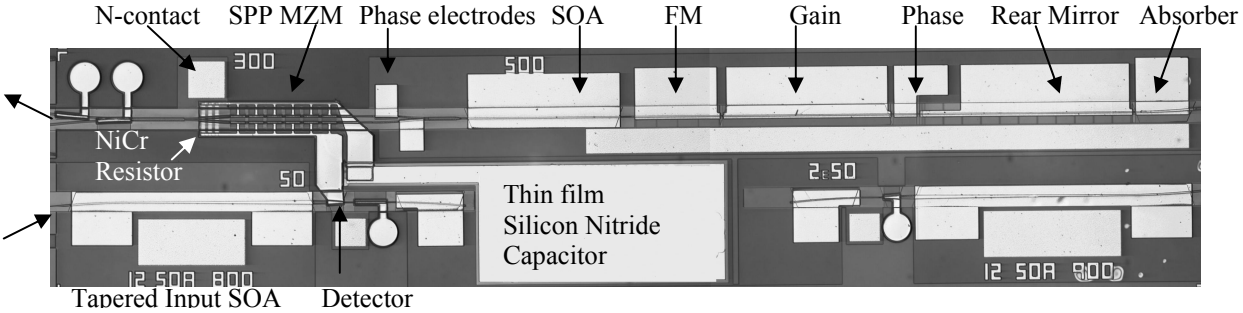

Fig. 9 Top view SEM of monolithic Series Push-Pull MZ based PD-WC device fabricated using the dual QW platform.

The input signal is fed into an 800 μm long tapered SOA from 3 μm to 9 μm which is detected in a 50 μm long shallow quantum well based tapered detector (from 9μm to 6μm). This photocurrent is used to drive a series push-pull (SPP) modulator on the transmitter side[30]. The device uses a SGDBR laser transmitter similar to as described earlier for the EAM based device followed by a 500 μm long SOA. The light is split into a Mach-Zehnder structure with 75 μm long phase electrodes on either branch to control the off state of the modulator. The series push-pull electrode structure uses eight T electrodes that are 50 μm long spaced by 10 μm for a total contact length of 400 μm long.

The electrical bias configuration is more complicated than that for the EAM case shown previously as shown in Fig. 10a. In the EAM case, there was a single DC bias on both the detector and modulator. This is ideal from a bias complexity perspective, however is not optimum from a bandwidth and insertion loss perspective. In the MZ case, we have integrated a thin film silicon nitride capacitor so that the detector can be biased relatively high (-4.5V) to maximize the bandwidth of the device, and a fairly low bias on the modulator electrodes (-1V) to achieve low insertion losses for the device and high efficiency. If both MZM electrodes are biased with the same value, one can also remove the DC component of the power dissipated across the integrated 50 ohm NiCr load resistor that is found at the end of the electrode. Each DC bias has a RF blocking inductor connection.

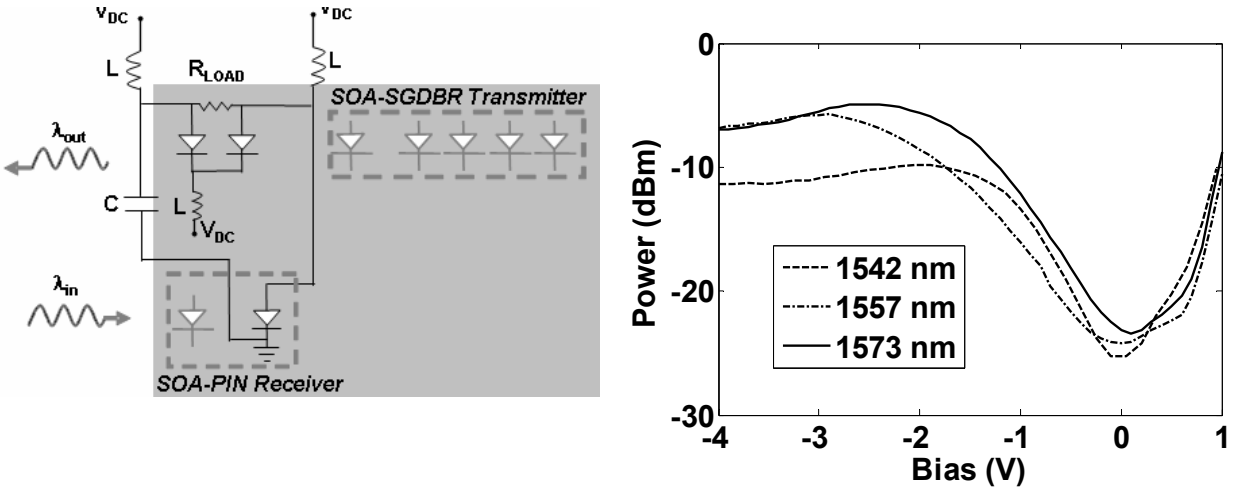

Fig. 10(a) Series Push-pull (SPP) MZ photocurrent-driven wavelength converter bias configuration (b) DC extinction curves for 300um long Dual QW MZ modulator as a function of wavelength.

Similar to the EAM case, the MZ device has high efficiency. DC extinction measurements are shown in fig. 10b for a transmitter with the following biases: I_{gain} = 100mA, I_{soa} = 100mA, P_{out} = 0.5mW.

Chirp is another important parameter for the wavelength converter. At high bit rates the dispersion in optical fibers will reduce the reach that is possible for a sub-optimal chirp parameter. A standard SOA based All-optical Mach-Zehnder interferometer uses mostly cross-phase modulation in one branch of the modulator to produce negative chirp in the non-inverting operation and positive chirp in the inverting operation. A tunable photocurrent-driven wavelength converter using a single-side drive Mach-Zehnder modulator will provide negative chirp with inverting operation and positive chirp with non-inverting operation[23]. The series push-pull configuration Mach-Zehnder modulator enables tailorable chirp, which can be achieved in both non-inverting and inverting operation. It is important to optimize the chirp parameter and extinction ratio simultaneously in order to maximize the transmission distance. Both branches of the Mach-Zehnder were biased to -1V with proper biasing of the phase electrode to achieve >10dB extinction ratio at the output. The power penalty was measured for 25km and 50km of Corning SMF-28 fiber using a 10Gbit/s 2^{31}-1 PRBS as can be seen in fig. 11.

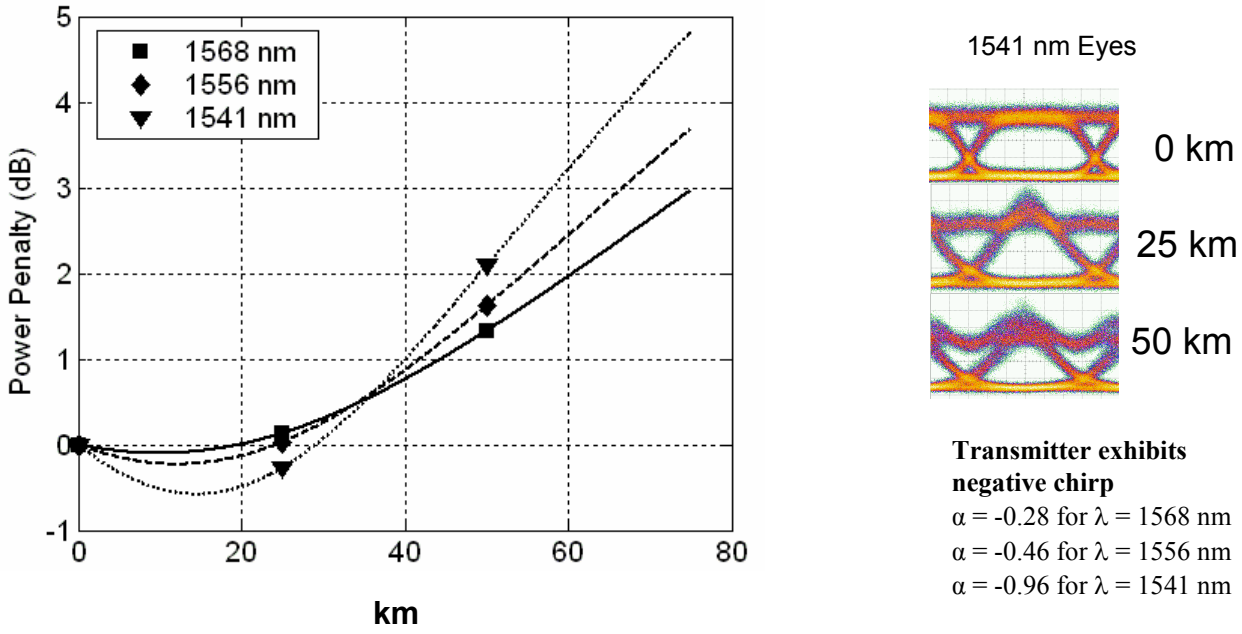

Fig. 11 Power penalty vs transmission distance for different output wavelengths biased with -1V on each MZ electrode. 1.87 Vpp input signal was applied to transmitter at different wavelengths for a 400μm long SPP MZM modulator.

Large signal chirp parameters were extracted for the different wavelengths as shown in Fig. 11.

VII. CONCLUSION

We have demonstrated high-speed wavelength conversion for two different photocurrent driven wavelength converter (PD-_WC) configurations. Both utilize a dual QW base structure that benefits from lower capacitance and improved efficiency. Both structures demonstrate the potential for wavelength conversion at 10Gbit/s with low power penalties(<2dB) over a wide wavelength range(30nm). With SOA design optimization, devices have been fabricated that have a net optical facet-to-facet gain (>5dB over whole wavelength range) and work well with very low input power requirements (<-10dBm).

PD-WC based on EAM technology have been fabricated and tested with both offset QW and dual QW integration platforms. With the introduction of the QW stack in the center of the waveguide, it has been shown that an improvement in the bandwidth efficiency product is possible for the EAMs while maintaining high injection efficiency and low propagation losses in the laser section. We have demonstrated wavelength conversion over 32 nm at 10 Gb/s with 10 dB optical extinction and less than 1dB power penalty with a PRBS of 2^{31}-1. Optimal wavelength conversion was obtained with -10dBm input power. This is a significant improvement over previously reported results for EA modulator based widely tunable wavelength converters.

The use of high-gain, high saturation power receivers coupled with high bandwidth efficient modulators have been shown to allow the realization of viable wavelength conversion at high bit rates. Series push-pull MZ PD-WCs have demonstrated error-free wavelength conversion over 37nm with <1dB power penalty, and low input power (1.3mW).

VIII. ACKNOWLEDGMENTS

This work was supported by Intel Corporation grant # TXA001630000, and DARPA MTO – CS-WDM grant #N66001-02-C-8026. We acknowledge Agility Communications for the regrowth of the MZM devices, and deposition of antireflection coatings.

IX. REFERENCES

1. Yoo S.J.B., "Wavelength Conversion Technologies for WDM Network Applications", IEEE J. Lightwave Technology, 14, 944-966 (1996).
2. Stubkjaer KE, Kloch A, Bukhave Hansen P, Poulsen HN, Wolfson D, Stockholm Jepsen K, Clausen AT, Limal E, Buxens A. "Wavelength converter technology." *IEICE Transactions on Electronics, vol.E82-C, no.2, Feb. 1999, pp.338-48. Publisher: Inst. Electron. Inf. & Commun. Eng, Japan.*
3. Yates Jennifer M., Michael P Rumsewicz, Jonathan P.R. Lacey, "Wavelength converters in dynamically reconfigurable WDM networks" IEEE Communications Surveys Second Quarter 1999.
4. Nesset D, Kelly T, Marcenac D. All-optical wavelength conversion using SOA nonlinearities. *IEEE Communications Magazine, vol.36, no.12, Dec. 1998, pp.56-61.*
5. Geraghty David F., Robert B. Lee, Marc Verdiell, Mehrdad Ziari, Atul Mathur, and Kerry J. Vahala,"Wavelength Conversion for WDM Communication Systems Using Four-Wave Mixing in Semiconductor Optical Amplifiers", IEEE Journal of Selected Topics in Quantum Electronics, Vol. 3, No. 5, Oct. 1997
6. C. Q. Xu, H. Okayama, and M. Kawahara, "1.5 pin band efficient broadband wavelength conversion by difference frequency generation in a periodically domain-inverted LiNbOs channel waveguide," *Appl. Phy. Lett,* vol. 63, p. 3559, 1993.
7. Cao, X.D. Jiang, M. Dasika, P. Islam, M.N. Evans, A.F. Hawk, R.M. Nolan, D.A. Pastel, D.A. Weidman, D.L. Moodie, D.G., "All-optical 40 GHz demultiplexing in a NOLM with sub-pJ switching energy" 1997. CLEO '97., Vol. 11, pp. 446-447, 18-23 May 1997.
8. Suzuki Y, Ito T, Shibata Y. "Monolithically integrated wavelength converter: Sagnac interferometer integrated with parallel-amplifier structure (SIPAS) and its application." 2002 LEOS Summer Topical Meetings IEEE.2002, ppWB2-12.
9. Wolfson D, Fjelde T, Kloch A, Janz C, Poingt F, Pommereau F, Guillemot I, Gaborit F, Renaud M. Detailed experimental investigation of all-active dual-order mode Mach-Zehnder wavelength converter. Electronics Letters, vol.36, no.15, 20 July 2000, pp.1296-7.
10. Leuthold J., C.H. Joyner, B. Mikkelsen, G. Raybon, J.L.Pleumeekers, B.I. Miller, K. Dreyer and C.A. Burrus 100Gbit/s all-optical wavelength conversion with integrated SOA delayed-interference configuration, Elect. Letts. Vol. 33, pp. 2137 (1997).
11. Hsu-Feng Chou, Yi-Jen Chiu, Adrian Keating, John E. Bowers, and Daniel J. Blumenthal, "Photocurrent-Assisted Wavelength (PAW) Conversion With Electrical Monitoring Capability Using a Traveling-Wave Electroabsorption Modulator", IEEE. Photonics Technology Letters, Vol. 16, No. 2, February 2004.
12. Olsson B-E, Ohlen P, Rau L, Blumenthal DJ. A simple and robust 40-Gb/s wavelength converter using fiber cross-phase modulation and optical filtering. IEEE Photonics Technology Letters, vol.12, no.7, July 2000, pp.846-8.
13. Wolfson D, Hansen PB, Kloch A, Fjelde T, Janz C, Coquelin A, Guillemot I, Garorit F, Poingt F, Renaud M. All-optical 2R regeneration at 40 Gbit/s in an SOA-based Mach-Zehnder interferometer. *OFC/IOOC'99. Optical Fiber Communication Conference and the International Conference on Integrated Optics and Optical Fiber Communications (Cat. No.99CH36322). IEEE. Part Suppl., 1999, pp.PD36/1-3 Suppl.. Piscataway, NJ, USA.*
14. Spiekman LH, Koren U, Chien MD, Miller BI, Wiesenfeld JM, Perino JS. All-optical Mach-Zehnder wavelength converter with monolithically integrated DFB probe source. *IEEE Photonics Technology Letters, vol.9, no.10, Oct. 1997, pp.1349-51.*
15. Demir HV, Sabnis VA, Jun-Fei Zheng, Fidaner O, Harris JS Jr, Miller DAB. "Scalable wavelength-converting crossbar switches." *IEEE Photonics Technology Letters, vol.16, no.10, Oct. 2004, pp.2305-7. IEEE.*
16. Broeke RG, Smit MK. "A wavelength converter with integrated tunable laser." *Integrated Photonics Research (Trends in Optics and Photonics Series Vol.91). Optical Soc. of America. 2003, pp.15-17. Washington, DC.*

17. Lal V, Masanovic M, Wolfson D, Fish G, Coldren C, Blumenthal DJ. "Monolithic widely tunable optical packet forwarding chip in InP for all-optical label switching with 40 Gbps payloads and 10 Gbps labels." 31st European Conference on Optical Communication. IEE. Part vol.6, 2005, pp.25-6 vol.6.
18. Yasaka H, Sanjoh H, Ishii H, Yoshikuni Y, Oe K. Finely tunable wavelength conversion of high bit-rate signals by using a superstructure-grating distributed Bragg reflector laser. *Journal of Lightwave Technology, vol.15, no.2, Feb. 1997, pp.334-41. IEEE.*
19. Lavrova OA, Rau L, Blumenthal DJ. "10-Gb/s agile wavelength conversion with nanosecond tuning times using a multisection widely tunable laser." *Journal of Lightwave Technology, vol.20, no.4, April 2002, pp.712-17 .IEEE.*
20. Kodama S, Yoshimatsu T, Ito H. 320 Gbit/s error-free demultiplexing using ultrafast optical gate monolithically integrating a photodiode and electroabsorption modulator. Electronics Letters, vol.39, no.17, 21 Aug. 2003, pp.1269-70. IEE.
21. Hutchinson J.M., J. Zheng, J.S. Barton, J.A. Henness, M.L. Mašanovic, M.N. Sysak, L.A. Johansson, D.J. Blumenthal, L.A. Coldren, H.V.Demir, V.A. Sabnis, O. Fidaner, J.S. Harris, and D.A.B. Miller, "Indium Phosphide-Based Optoelectronic Wavelength Conversion for High-Speed Optical networks"
22. Klamkin J., L. A. Johansson, J. T. Getty, J. M. Hutchinson, E. J. Skogen and L. A. Coldren, "Photocurrent Driven Widely-Tunable Wavelength Converter based on a Directly Modulated Bipolar Cascade SGDBR Laser ", LEOS 2004.
23. Barton J.S., Masanovic ML, Sysak MN, Hutchinson JM, Skogen EJ, Blumenthal DJ, Coldren LA. 2.5-Gb/s error-free wavelength conversion using a monolithically integrated widely tunable SGDBR-SOA-MZ transmitter and integrated photodetector. *IEEE Photon Tech. Letts, vol.16, no.6, June 2004, pp1531-3.*
24. Sysak MN, Barton JS, Johansson LA, Raring JW, Skogen EJ, M. L. Mašanović, Blumenthal DJ, Coldren LA. "Single-chip wavelength conversion using a photocurrent-driven EAM integrated with a widely tunable sampled-grating DBR laser." *IEEE Photonics Technology Letters, vol.16, no.9, Sept. 2004, pp.2093-5.*
25. Barton, J.S., A. Tauke-Pedretti, M. Dummer, M.N. Sysak, M.L. Mašanović, J.W. Raring, E.J. Skogen, and L.A. Coldren, "10Gbit/s Wavelength Conversion Using a Widely-Tunable Series Push-Pull Photocurrent-Driven Transmitter," IEEE Photon. Technol. Lett., vol. 17, pp. 1902-1904, 2005.
26. James W. Raring, Matthew N. Sysak, Anna Tauke-Pedretti, Mathew Dummer, Erik J. Skogen, Jonathon S. Barton, S. P. DenBaars, and Larry A. Coldren, "Advanced Integration Schemes for High-Functionality/High-Performance Photonic Integrated Circuits" SPIE Photonics West, 2006.
27. Barton J.S., A. Tauke-Pedretti, M. Dummer, E. J. Skogen, J. Raring, M. N. Sysak, L. A. Johansson, M. L. Masanovic, L. A. Coldren, "Widely-tunable photocurrent-driven wavelength converters", 5729-23, SPIE Photonics West, 2005.
28. Bennett, B., R. Soref, and J. DelAlamo, "Carrier-induced change in refractive index of InP, GaAs, and InGaAsP," IEEE Journal of Quantum Electronics, vol.26, pp. 113-122, Jan 1990.
29. Tauke-Pedretti, Anna, M. M. Dummer, J. S. Barton, M.N. Sysak, J. Raring, and L.A.Coldren," Integrated Photoreceivers with High Saturation Power, High Gain and >20GHz Bandwidth", Submitted to Photonics Tech. Letts. Sept 2004.
30. Tauke-Pedretti, Matthew N. Sysak, Jonathon S. Barton, James W. Raring, Matthew Dummer and Larry A. Coldren, "Monolithic Dual-Quantum-Well 10Gb/s Mach-Zehnder Transmitter"LEOS 2005 conference proc..

10 Gb/s Monolithically Integrated, Photocurrent Driven Wavelength Converter with Widely Tunable SGDBR Laser and Optical Receiver

Matthew N. Sysak, James W. Raring, Jonathon S. Barton, Matthew Dummer, Anna Tauke-Pedretti, Henrik N. Poulsen, Daniel J. Blumenthal, Larry A. Coldren
University of California Santa Barbara, Engineering II Santa Barbara, CA 93106
Tel: (805)893-8465, FAX: (805) 893-4500, email: mnsysak@engineering.ucsb.edu

Abstract: A monolithically integrated photocurrent driven wavelength converter is fabricated and characterized. Bit-Error-Rate measurements at 10Gb/s show 1dB power penalties over 32nm with extinction ratios between 8.5-9.5dB. Input power is -11dBm and conversion efficiency is +13dB.

OCIS codes: (250.5300) Photonic Integrated Circuits; (250.3140) Integrated Optoelectronic Circuits

1. Introduction

Photonic integrated circuits are key components in future all optical networks for increased functionality and lower packaging costs along with dynamic wavelength management. The development of a device that is capable of wavelength conversion and switching at high speeds without filtering to separate input and output signals, and without the cumbersome electronics associated with traditional OEO repeaters, has received significant attention [1]. To further reduce packaging costs and optical loss in such a device, a wavelength converter that is compatible with a monolithically integrated widely tunable laser source is a very attractive solution.

For very high speed filterless operation, wavelength converters based on photocurrent driven technology have been shown to support data rates up to 500 Gb/s [2]. In this device an input optical signal is detected in a photodetector and the generated photocurrent changes the voltage characteristics across a load resistor. This changes the transmission of a reverse biased Electroabsorption Modulator (EAM) and completes the wavelength conversion process. Several fully monolithic devices that utilize this technology have been demonstrated with a tunable laser source and optical amplifiers using the offset quantum well InGaAsP/InP integration platform, but bit rates were limited to 2.5 Gb/s and high input powers were required [3,4]. In this work, we demonstrate the first fully monolithically integrated widely tunable wavelength converter operating at 10 Gb/s with no filtering requirements and extremely low input average waveguide power requirements (-11 dBm).

2. Device Layout and Epitaxial Structure

The architecture of the monolithically integrated wavelength converter consists of two parallel ridges interconnected by a very short (35 μm) single gold trace. The transmitter ridge contains a four section widely tunable sampled grating DBR laser, a 600-μm-long SOA, followed by a 400 μm EAM. A receiver ridge contains an optical pre-amplifier and photodetector similar to that used in [5]. The preamplifier is divided into a straight waveguide section that is designed for high efficiency and is 600 μm long, followed by a high power section that has an exponentially flared ridge width up to 12 μm and is 400 μm long. The photodetector contains laser offset quantum wells (OQW) that is reverse biased and is 50 μm long. The photodetector ridge waveguide is tapered from the final width of the amplifier (12 μm) down to 3 μm in order to accommodate high optical power levels in the receiver. The device uses a single applied bias for both photodetector and EAM with a single 50-Ω load applied after a bias-T. A device schematic from a Scanning Electron Micrograph (SEM) along with an equivalent circuit is shown in fig. 1. As a result of the physical separation between the input and output waveguides, the Input Signal Suppression Ratio (ISSR) is larger than 50 dB.

The epitaxial layer structure uses a Dual Quantum Well (Dual QW) integration platform similar to the offset quantum well (OQW) platform that has been used extensively for advanced PICs. The OQW stack provides gain in the laser and amplifiers (Photoluminescence (PL) = 1550 nm) and is located above the optical waveguiding layer. The second separate set of quantum wells (PL = 1480 nm), centered in the InGaAsP waveguide (PL = 1300 nm),

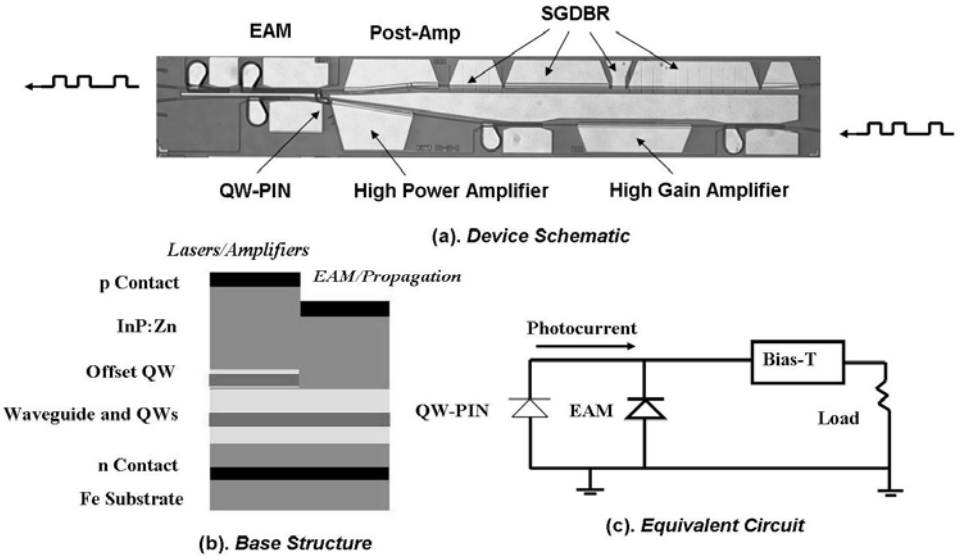

Fig 1. (a) SEM of wavelength converter. (b) Outline of Base structure for fabrication. (c) Wavelength converter equivalent circuit

provides broadband modulation efficiency when reverse biased in the EAM. The centered QW stack contains 7 x 90 A compressively strained wells and 6 x 50 A tensile strained barriers. The layer stack is shown in Fig. 1.

3. Results

Device optical to optical S_{21} bandwidth measurements, EAM DC extinction characteristics, optical receiver characteristics, and Bit Error Rate (BER) measurements have been performed for a device that uses an external 50 Ω load. DC extinction characteristics are shown in fig.2. Measurements for the 400 μm long EAM show greater than 20 dB extinction over 30 nm with less than –4V bias. Receivers were characterized by fiber coupling DC light into pre-amplifiers. The input on-chip power levels were measured by reverse biasing the high gain receiver SOA. Both receiver SOAs were then forward biased and the output power levels measured in the QW-PIN. Results are presented in fig. 2 where devices show a 3-dB compression of +16 dBm. SOA bias current density was 6 kA/cm^2.

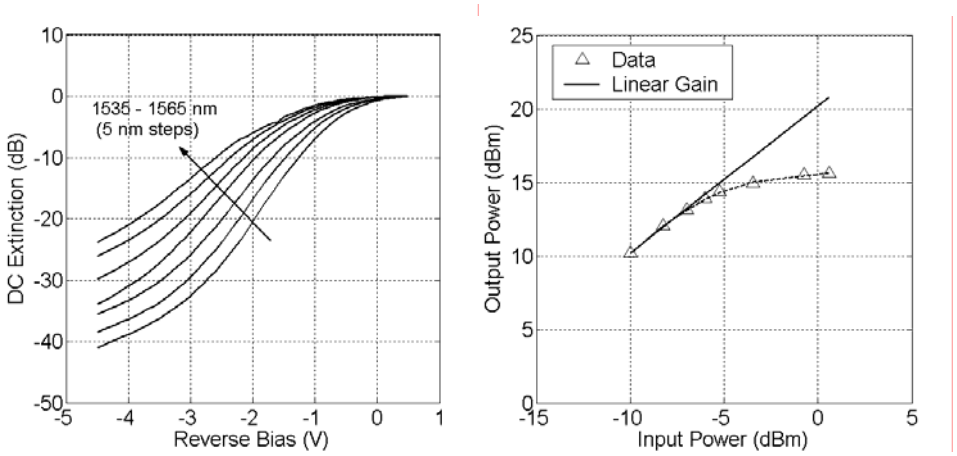

Fig. 2. DC extinction characteristics for Dual QW EAM (left) and SOA PIN receiver characteristics (right). Receiver input wavelength is 1548.1 nm. Input power levels are quoted as on-chip power levels and bias current is 6 kA/cm^2 for both receiver amplifiers. The reverse bias on the detector is -2.5 V.

BER measurements at a wavelength of 1548.1 nm using a non-return-to-zero (NRZ) $2^{31} – 1$ pseudorandom bit stream were performed at 10 Gb/s with an Agilent 83433A transmitter and bit error rate tester. The transmitter had an extinction ratio of 14 dB. The optical test signal was routed to an EDFA followed by an optical filter, then

through a polarization controller and was coupled to the device using a lensed fiber. In this experiment, -5.5 dBm of optical fiber power corresponding to -11 dBm of waveguide power was required. After wavelength conversion, the output signal from the device was routed to a variable attenuator, then to a photodetector and back to the Bit-Error Rate tester. Error-free operation at a BER of 10^{-9} has been demonstrated with a power penalty of less than 1-dB over a bandwidth of 32 nm. Eye diagrams are shown in fig. 3 for transmitter (bottom left) and wavelength converted data (top right). Results for Extinction Ratio, output power, and BER curves for a variety of output wavelengths are shown in fig 3.

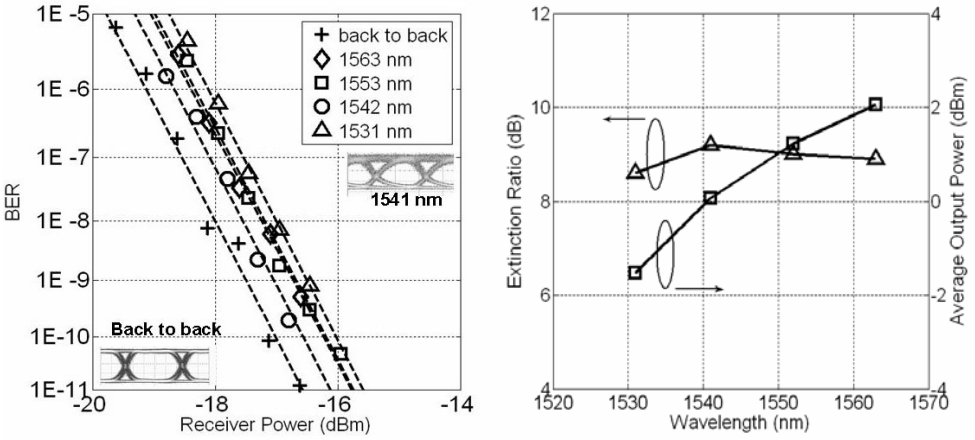

Fig. 3. Extinction Ratio and average output power accounting for 4.5 dB coupling loss (left) and 10 Gb/s BER curves for 50 Ω terminated EAM based wavelength converter (right). Input wavelength is 1548.1 nm with waveguide power of -11 dBm.

4. Conclusions

We have demonstrated the first filterless wavelength converter with an integrated tunable laser source operating at 10 Gb/s with compatibility over a wide tuning range (32 nm) with large extinction ratios (> 8.5 dB). The device showed less than 1-dB power penalty for wavelength conversion and required less than -5.5 dBm of input fiber power and -11 dBm of waveguide power. Overall facet to facet conversion efficiency ranged from +9 to +13 dB neglecting fiber coupling loss.

5. References

[1] J. Leuthold, P. Besse, E. Gamper, M.Dulk, S. Fisher, G. Guekos and H. Melchior, "All-Optical Mach-Zehnder Interferometer Wavelength Converters and switches with Integrated Data and Control signal separation schemes," *IEEE J. Lightwave Tech.*, vol.17, pp.1056-66, Jun. 1999.

[2] S. Kodama, T. Yoshimatsu, and H. Ito, "500 gbit/s optical gate monolithically integrating photodiode and electroabsorption modulator," *Electronics Letters*, vol. 40, pp. 555–6, Apr 2004.

[3] M.N Sysak, J.S. Barton, L.A. Johansson, J.W. Raring, E.J. Skogen, M.L. Masanovic, D.J. Blumenthal and L.A. Coldren. "Single-Chip Wavelength Conversion Using a Photocurrent-Driven EAM Integrated With a Widely Tunable Sampled-Grating DBR Laser" *IEEE Photon.Technol. Lett*., vol. 16, pp.2093-2095, Sept. 2004.

[4] J.S. Barton, E.J. Skogen, M.L. Masanovic, M.N. Sysak, D.J. Blumenthal and L.A. Coldren. "2.5 Gbit/s error-free wavelength conversion using a monolithically-integrated widely-tunable SGDBR-SOA-MZ transmitter and integrated photodetector" *IEEE Photon.Technol. Lett*., vol. 16, pp.1531-1533, June 2004.

[5] A. Tauke-Pedretti, M. Dummer, J.S. Barton, M.N. Sysak, J.W. Raring and L.A. Coldren "High Saturation Power and High Gain Integrated Receivers," *IEEE Photonics Technology Letters*, vol. 17, no. 10, pp. 2167-9, Oct. 2005.

Single-chip, widely-tunable 10 Gbit/s photocurrent-driven wavelength converter incorporating a monolithically integrated laser transmitter and optical receiver

M.N. Sysak, J.W. Raring, J.S. Barton, M. Dummer, A. Tauke-Pedretti, H.N. Poulsen, D.J. Blumenthal and L.A. Coldren

A single-chip photocurrent-driven wavelength converter operating at 10 Gbit/s is presented. The device consists of a monolithically integrated widely tunable transmitter and an optical receiver. The transmitter consists of a sampled grating DBR laser, electroabsorption modulator and semiconductor optical amplifier (SOA). The optical receiver includes a quantum-well *pin* photodetector and a set of two SOA preamplifiers. Bit error rate measurements at 10 Gbit/s with a $2^{31}-1$ PRBS showed less than 1 dB of power penalty for conversion between 1550 nm and output wavelengths ranging from 1531 to 1563 nm.

Introduction: Dynamic wavelength switching in next generation optical networks will require improvements in traditional optical to electrical to optical (OEO) wavelength conversion techniques to achieve efficient wavelength routing [1]. From an integrated device perspective there have been several proposed solutions to this issue that utilise a variety of mechanisms. These include cross-gain, cross-phase and cross-absorption modulation along with an assortment of interferometric techniques [2, 3]. However, it has been challenging to demonstrate a device with a small form factor that does not require optical output signal filtering, operates at high bitrates, and is compatible with an on-chip laser source for efficient optical coupling between discrete components. For high bitrate applications where optical filtering is problematic, a particularly attractive solution is a single-chip photocurrent-driven-based device.

The electroabsorption modulator (EAM)-based photocurrent-driven approach relies on generation of a photocurrent from a detector that changes the voltage across an EAM, through a load resistor. This voltage modulates the transmission characteristics of the EAM, which is connected to a laser source operating at a different wavelength from the input. Using this technique, monolithically integrated photodetector and modulator devices without integrated lasers or amplifiers have been shown to be compatible with up to 500 Gbit/s [4]. Fully integrated wavelength converters have been demonstrated with tunable laser sources and amplifiers, but performance was limited to 2.5 Gbit/s as a result of low-efficiency Franz-Keldysh bulk waveguide EAMs and/or limited saturation output power in integrated optical amplifiers [5, 6]. In this Letter, the first 10 Gbit/s single-chip photocurrent-driven wavelength converter is demonstrated with bit error rate (BER) power penalties of less than 1 dB over a wide range of output wavelengths (32 nm). The fibre-coupled waveguide input power was −11 dBm, which, to the best of our knowledge, is the lowest reported for an integrated photocurrent-driven device.

Experiment: The wavelength converter consists of receiver and transmitter regions that are fabricated on neighbouring, parallel waveguides, as shown in Fig. 1. This configuration allows for complete separation of the optical input and output signals, eliminating the possibility of crosstalk and hence the need for optical filtering at the device output that is required by many other types of wavelength converters with on-chip sources. The receiver and transmitter waveguides are connected with a short (35 µm) Ti/Pt/Au metal interconnect to allow the generated photocurrent to be routed between the two sections. The receiver contains a set of two optical amplifiers that are operated in their linear regime, followed by a QW-*pin* photodetector. The first amplifier is 600 µm long and has a waveguide width of 3 µm. This SOA is used to boost the fibre-coupled input power level to just below the 1 dB gain compression point for a given operating current density. The second amplifier is 400 µm long and has an exponentially flared waveguide width (3–12 µm) to expand the cross-section of the optical mode. This geometry enhances the 1 dB output power compression of the SOA, while still allowing for gain at the expense of additional applied current [7]. The QW-*pin* photodetector is 50 µm long and is simply a reverse-biased region containing the offset quantum well (OQW) stack that is used for gain in the laser and amplifiers. The photodetector ridge width is linearly tapered down from 12 to 3 µm for low capacitance and increased saturation power. The transmitter section consists of a five-section widely tunable sampled grating distributed Bragg reflector (SGDBR) laser [8], a 550 µm optical amplifier and a 400 µm-long QW EAM. The EAM and the QW-*pin* photodetector share a common electrical reverse bias that is applied through a 50 µm pitch ground-signal probe in combination with an external bias tee that includes the 50 Ω load resistor. Low-*k* dielectric, photo-bis-benzocylcobutene (BCB), is incorporated in the QW-*pin*, EAM and the metal interconnect to minimise any parasitic capacitance from bondpads and metal electrodes.

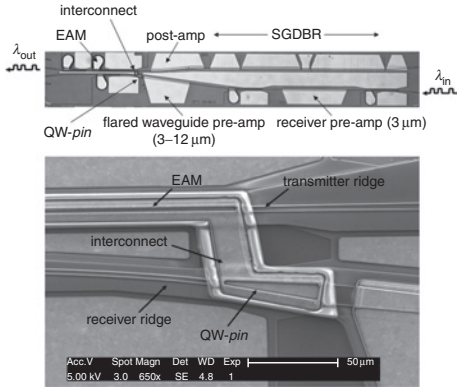

Fig. 1 *Scanning electron micrograph (SEM) images*

SEM images of monolithically integrated, small form factor (3.0 × 0.5 mm) wavelength converter (top)
SEM image of EAM/QW-*pin* interconnect (bottom)

The wavelength converter is fabricated in the InGaAsP/InP material system using exposed ridge waveguides on a dual quantum well (DQW) integration platform. This integration platform is very similar to the more common OQW platform that has previously been used for SGDBR-based photonic integrated circuits (PICs) [7]. Compared to the OQW approach, the DQW platform includes an additional set of quantum wells that are inserted into the optical waveguide region to enhance the modulation efficiency of the integrated EAMs. These waveguide quantum wells have a photoluminescence peak of 1480 nm and consist of 7 × 9.0 nm wells and 6 × 5.0 nm barriers. This platform is attractive since it uses all the processing techniques developed for the OQW PICs and requires only a single blanket *p*-InP overgrowth to fill in the gratings on the tunable laser. A diagram of the DQW integration platform with a detail of the individual layers is shown in Fig. 2.

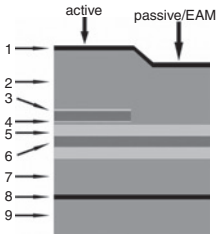

region	description
1	*p*-contact
2	*p*-cladding
3	offset QWs
4	stop etch
5	waveguide
6	centred QWs
7	*n*-buffer
8	*n*-contact
9	Fe-substrate

Fig. 2 *Layer structure of DQW InGaAsP/InP integration platform*

Offset quantum wells are used for optical gain in amplifiers and gain section of laser. Waveguide quantum wells provide modulation efficiency for integrated EAMs

Results: Devices were antireflection (AR) coated and mounted on copper blocks for testing. The temperature in all the following experiments was maintained at 15°C. Optical to optical S_{21} response measurements of a 50 Ω terminated wavelength converter showed a 3 dB frequency roll-off of 7 GHz. Bias conditions in the frequency response measurement were −2.5 V over both EAM and QW-*pin* and the wavelength converter was operated with an input of 1548 nm and an output of 1565 nm. Characterisation of the discrete 400 µm EAM DC extinction for wavelengths between 1531 and 1563 nm showed greater than 20 dB total extinction with less than −4 V bias and slope

efficiencies greater than 10 dB/V. The optical receiver, including both SOA preamplifiers and the QW-*pin* photodetector, was characterised and showed a collective output power 1 dB compression of +15 dBm along with 20 dB of gain at an applied current density of 6 kA/cm^2. The photodetector reverse bias was −2.5 V.

For the BER measurements, a non-return-to-zero (NRZ) $2^{31}-1$ pseudorandom bit stream at 10 Gbit/s from a BER tester transmitter (Agilent 83433A) was input into an EDFA followed by an optical filter and polarisation controller, then transmitted to the device using a lensed fibre. The wavelength converted signal was routed to a variable attenuator, followed by a photodetector and finally back to the bit-error-rate tester. The input optical fibre power level was −5.5 dBm, corresponding to −11 dBm of coupled waveguide power, and the input extinction ratio was 14 dB. The SGDBR gain and transmitter post-amplifier are biased at 130 and 120 mA, respectively, and the receiver preamplifiers are biased for a current density of 6 kA/cm^2.

Error-free operation (BER of 10^{-9}) is demonstrated (Fig. 3) with less than 1 dB power penalty for wavelength conversion between a fixed input wavelength of 1548 nm and a range of output wavelengths from 1531 to 1563 nm. The converted output extinction ratio varied between 8.7 and 9.2 dB and the average output powers, with fibre coupling losses removed, ranged between −1.8 and +2 dBm.

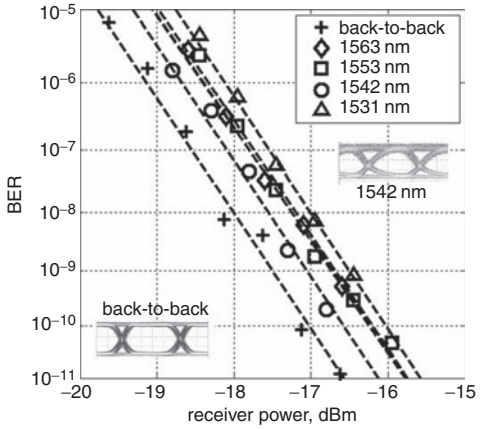

Fig. 3 *BER measurements at 10 Gbit/s for wavelength conversion between fixed input (1548 nm) to variable output (1531–1563 nm)*

Applied wavelength converter bias levels were −1.4, −2.0, −2.9 and −3.1 V for wavelengths of 1531, 1542, 1553 and 1563 nm, respectively. Optical eyes shown for back-to-back and wavelength converted (1542 nm) signals

Conclusions: We have demonstrated the first photocurrent-driven wavelength converter with a monolithically integrated tunable laser and optical receiver operating at 10 Gbit/s with BER power penalties of 1 dB over a wide output tuning range (32 nm). Input powers were kept at −5.5 dBm in the fibre and −11 dBm in the waveguide, which is to the best of our knowledge the lowest reported for this type of device.

28 February 2006
Electronics Letters online no: 20060621
doi: 10.1049/el:20060621

M.N. Sysak, J.S. Barton, M. Dummer, A. Tauke-Pedretti, H.N. Poulsen, D.J. Blumenthal and L.A. Coldren (*Electrical and Computer Engineering Department, University of California, Santa Barbara, CA 93106, USA*)

E-mail: mnsysak@engineering.ucsb.ed

J.W. Raring (*Materials Department, University of California, Santa Barbara, CA 93106, USA*)

References

1 Yoo, S.J.B.: 'Wavelength conversion technologies for WDM network applications', *J. Lightwave Technol.*, 1996, **14**, pp. 955–966
2 Lal, V., *et al.*: 'Quantum-well-intermixing monolithically integrated widely tunable all-optical wavelength converter operating at 10 Gbps', *IEEE Photonics Technol. Lett.*, 2005, **17**, pp. 1689–1691
3 Bernasconi, P., *et al.*: 'Monolithically integrated 40 Gbps wavelength converter with multi-frequency laser'. Proc. Optical Fiber Communications Conf. (OFC), 2004, Paper PDP16
4 Kodama, S., Yoshimatsu, T., and Ito, H.: '500 Gbit/s optical gate monolithically integrated photodiode and electroabsorption modulator', *Electron. Lett.*, 2004, **40**, pp. 555–556
5 Sysak, M., *et al.*: 'Single-chip wavelength conversion using a photocurrent driven EAM integrated with a widely tunable sampled grating DBR laser', *IEEE Photonics Technol. Lett.*, 2004, **16**, pp. 2093–2095
6 Raring, J.W., *et al.*: 'Quantum well intermixing for monolithic integration: a demonstration of widely tunable 10 Gb/s transmitters and wavelength converters'. Integrated Photonics Research Conf., San Francisco, CA, USA, 2004, Paper IWC3
7 Tauke-Pederetti, A., *et al.*: 'High saturation power and high gain integrated receivers', *IEEE Photonics Technol. Lett.*, 2005, **17**, (10), pp. 2167–2169
8 Akulova, Y.A., *et al.*: 'Monolithically integrated tunable transmitters'. Proc. IPRA, San Diego, CA, USA, April 2005, Paper IWF4

Widely Tunable Single-Chip Transceiver for 10 Gb/s Wavelength Conversion

Matthew M. Dummer, Matthew N. Sysak, James W. Raring, Anna Tauke-Pedretti, and Larry A. Coldren

University of California, Department of Electrical Engineering, Santa Barbara, CA 93106
Phone: 805-893-7163 Fax: 805-893-4500 Email: dummer@engr.ucsb.edu

Wavelength conversion is an essential function in wavelength-division-multiplexing (WDM) optical networks, as it enables better utilization of bandwidth and reduces blocking probabilities. This work presents, for the first time, a fully integrated transceiver solution to wavelength conversion in which all microwave signals are confined on a single InP chip. This device architecture, referred to as a photocurrent-driven wavelength converter (PD-WC), is particularly attractive due to the potential for low power dissipation, high bandwidth, data regeneration, and no optical output filtering requirement unlike many all-optical implementations [1]. The PD-WC approach consists of an interconnected receiver and transmitter such that photocurrent from an optically pre-amplified receiver is used to drive a modulator, which functions to translate the signal onto any output wavelength within the range of a widely tunable laser. Previous widely-tunable PD-WC demonstrations have required high speed probes, bias-T's, and in some cases complex bias circuitry [1]. In this work, a termination resistor and DC-blocking capacitor are integrated with an electro-absorption modulator (EAM) based PD-WC such that only DC biases are necessary for device operation and no microwave signal must travel off the chip. This widely-tunable device demonstrates error free 10 Gb/s conversion and utilizes both a simple, single-regrowth fabrication and a simple bias configuration.

The PD-WC is essentially a monolithically integrated transceiver within a compact footprint of 3.1 by 0.5 mm. The transmitter ridge consists of a widely tunable sampled grating (SG) DBR laser followed by semiconductor optical amplifier (SOA) and a 400 μm long EAM. The receiver ridge consists of two SOAs followed by a p-i-n quantum well photodetector (QW-PD). The ridge width of the second SOA is flared (3 to 9 μm) to achieve a 3-dB saturation power greater than 15 dBm. The QW-PD is 20 μm long with a tapered ridge (9 to 7 μm) to prevent saturation at the front end while minimizing the total capacitance [2]. Benzo-cyclobutene (BCB), a low-k dielectric, is defined underneath the QW-PD and EAM electrodes for reduced parasitic capacitance and a 75 μm long microstrip line above the BCB connects the QW-PD to the EAM electrode in a traveling wave configuration. The EAM is terminated with a 35 Ω NiCr resistor followed by a large (~30 pF) on-chip parallel-plate capacitor in series, providing an RF path to ground. An additional chip capacitor is added in parallel on the submount to provide a low impedance ground path for frequencies less than 500 MHz.

The device was fabricated on a dual quantum well (DQW) base structure with a semi-insulating Fe-doped InP substrate. The DQW consists of a set of 7 offset quantum wells (λ_{PL}=1542 nm) above the waveguide layer, for gain in laser and amplifier regions, and 8 shallow quantum wells (λ_{PL}=1455 nm) centered in the waveguide for modulation efficiency. The offset wells were selectively etched from all passive and modulation regions before the p-type InP cladding was grown.

Wavelength conversion experiments at 10 Gb/s in the non-return to zero (NRZ) format demonstrated open eye diagrams with output extinction ratios ranging from 8.0 to 6.6 dB for output wavelengths from 1527-1553 nm. Bit error rate measurements achieved 10 Gb/s error free wavelength conversion over the same 25 nm output wavelength tuning range. In this tuning range, the power penalty of wavelength conversion ranged from 1.5 -2.5 dB compared to back to back transmission. The input power for these measurements was -4.5 dBm neglecting coupling losses. DC characterization experiments showed the receiver SOA gain to be greater than 18 dB and QW-PD output to be linear up to 25 mA of photocurrent. The EAM demonstrated peak DC extinction slope efficiencies from 10 to 20 dB/V for wavelengths from 1527 to 1553 nm.

This work was supported by DARPA MTO-LASOR Grant W911NF-04-9-0001.

[1] J. Barton, et al., SPIE Photonics West, 5729, pp. 177-191, March 2005
[2] A. Tauke-Pedretti, et al., IEEE Photonics Tech. Lett. , Vol. 17, No. 10, October 2005

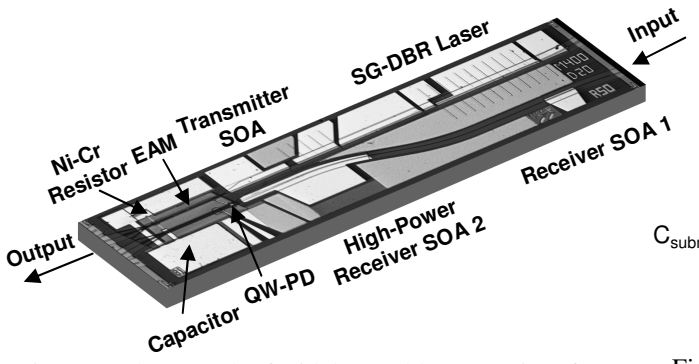

Figure 1: Photograph of widely tunable transceiver for wavelength conversion. Device dimensions are 3.1 mm by 0.5 mm.

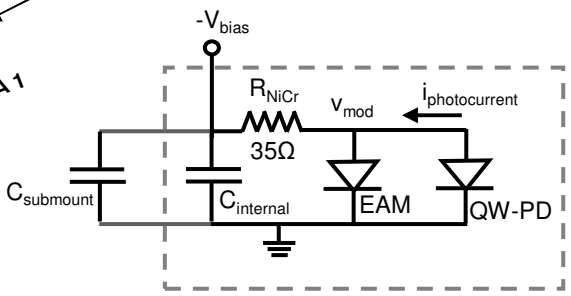

Figure 2: Circuit diagram of QW-PD and EAM with on-chip termination and single DC bias configuration with no bias-Ts.

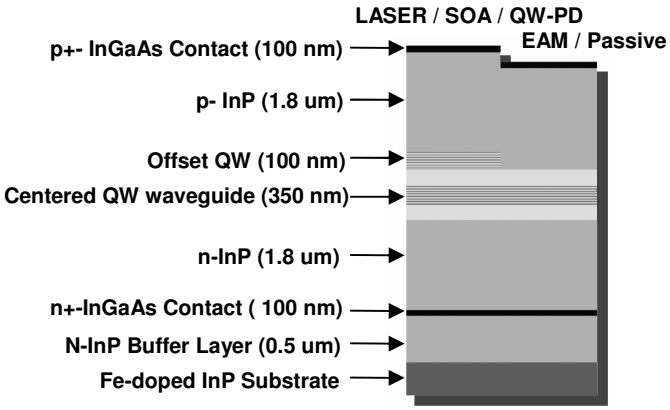

Figure 3: Diagram of epitaxial layer structure for dual quantum well integration platform.

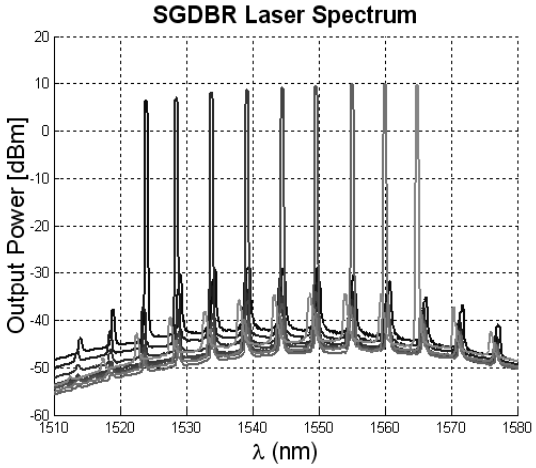

Figure 4: Tuning spectrum and fiber-coupled output power of SG-DBR laser with output SOA.

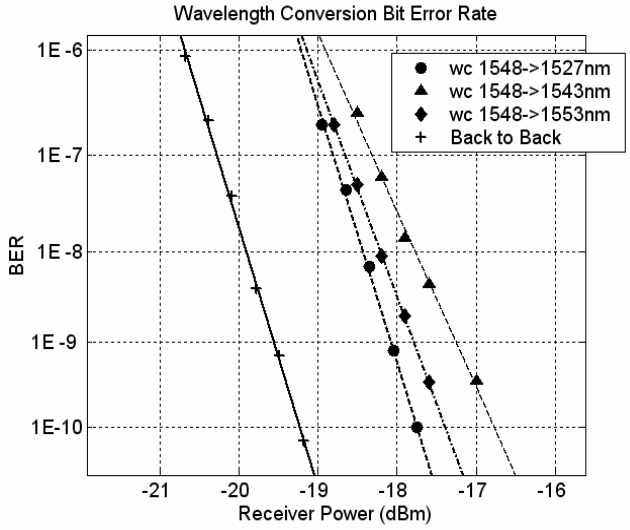

Figure 5: Wavelength converter bit error rate at 10 Gb/s demonstrating error free operation with less than 2.5 dB power penalty compared with back-to-back transmission over 25 nm output tuning range.

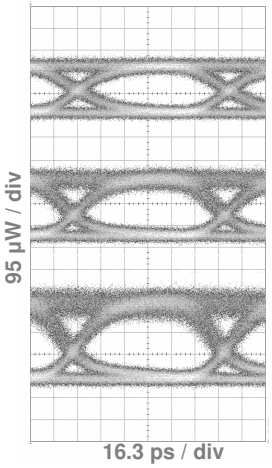

λ_{out} = 1527nm
E.R.= 8.07dB
P_{out} = -7 dBm
V_{bias}= -2.2 V

λ_{out} = 1543nm
E.R.= 7.41dB
P_{out} = -6.2 dBm
V_{bias}= -2.9 V

λ_{out} = 1553nm
E.R.= 6.63dB
P_{out} = -5.0 dBm
V_{bias}= -3.2 V

Figure 6: Wavelength converted output eye diagrams corresponding to BER measurements in Figure 5. Average output power (P_{out}), extinction ratio (E.R.) and EAM/ QW-PD operating bias (V_{bias}) are listed.

Optical 2R and 3R Signal Regeneration in Combination with Dynamic Wavelength Switching Using a Monolithically Integrated, Widely Tunable Photocurrent Driven Wavelength Converter

(Invited)

Matthew N. Sysak (1), James W. Raring (2), Leif Johansson (1), Henrik N. Poulsen (1), Jonathon S. Barton (1), Daniel J. Blumenthal (1), Larry A. Coldren (1,2)
1: University of California Santa Barbara, ECE Department, Santa Barbara, CA 93106
mnsysak@engineering.ucsb.edu
2: University of California Santa Barbara, Materials Department

Abstract *Optical 2R and 3R signal regeneration along with dynamic wavelength switching is demonstrated for the first time using a monolithically integrated, widely tunable photocurrent driven wavelength converter.*

I. Introduction

Wavelength conversion in combination with optical regeneration, including signal retiming, signal reshaping and signal reamplification, is viewed as a key functionality for improving blocking probabilities and signal quality in next generation optical networks. To perform this function, several devices have been proposed and demonstrated [1,2]. However, prior to this work, regenerators with high levels of integrated functionality, including on-chip tunable laser sources, have not been demonstrated. Here we present wavelength switching and signal regeneration using a single-chip widely tunable, photocurrent driven wavelength converter (PD-WC) [3]. The small form factor highly integrated chip enables reduced packaging complexity and costs along with reduced optical loss between discrete components.

In Section II, we examine the wavelength switching, signal extinction ratio regeneration, and signal reamplification (2R) properties of the device using a degraded non-return to zero (NRZ) input signal. For conversion from 1548 nm to 1545 nm we observe regeneration with an increased extinction ratio from 4 dB to greater than 12 dB, facet to facet gain of up to 12 dB (excluding coupling losses), and a 3.5 dB negative power-penalty in Bit Error Rate (BER) experiments at 2.5 Gb/s.

In Section III, we examine the wavelength switching, signal reshaping, signal reamplification, and signal retiming (3R) properties of the PD-WC using a 10 Gb/s return to zero (RZ) input signal . Error-free wavelength switching is demonstrated with a 1-dB power penalty from 1548 nm to 1545 nm using an ideal input signal. For a degraded input with timing distortion and a 4 dB extinction, wavelength converted signal regeneration shows a negative 2.8-dB power penalty through the device, with facet to facet gain (excluding coupling losses) of +6.4 dB. Measurements of the peak to peak jitter before and after the device show a reduction from 35 ps to 17 ps using input signals with added 10 MHz sinusoidal frequency modulation.

II. 2R regeneration and wavelength switching

II(a). 2R PD-WC device arrangement

The single chip EAM-based photocurrent driven wavelength converter is fabricated in the InGaAsP/InP materials system using a dual quantum well (DQW) integration platform [4].

The wavelength converter is arranged in a parallel ridge architecture as shown in Fig. 1. Light at wavelength λ_{in} enters the device receiver section and is amplified by a set of two linear SOAs. The first SOA is 600 μm long and has a ridge width of 3 μm. The second SOA is 400 μm long and has an exponentially flared ridge width (3 μm to 12 μm) to increase the saturation power characteristics [5]. The amplified signal is fed to a tapered 50 μm long QW-PIN photodetector. Total receiver optical gain at 1548 nm is 21 dB including the quantum efficiency of the

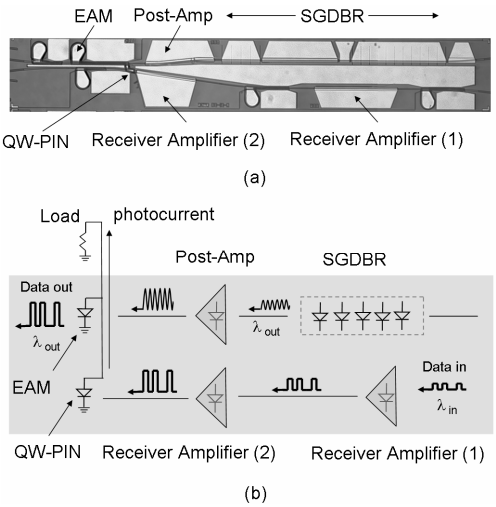

Fig 1. (a) Scanning electron mocrograph of single chip, widely tuneable wavelength converter (b) Functional diagram of integrated components in wavelength converter for 2R regeneration experiments

QW-PIN photodetector. The photocurrent from the receiver is routed to a 400 μm long EAM that shares an optical waveguide with the SGDBR laser and shares a circuit node with an external bias tee and a 50 Ω load resistor. As the photocurrent drops across the load resistor, the EAM potential is altered changing its transmission characteristics. Since the EAM is positioned after the SGDBR laser, it functions to transfer the input signal onto the output of the tuneable laser (λ_{out}), resulting in wavelength conversion. The DC voltage for both QW-PIN and EAM is applied through the external bias tee. Overall device optical 3-dB bandwidth is 6 GHz.

II(b). 2R regeneration experiments

Device re-amplification and reshaping (extinction ratio regeneration) properties were examined by degrading the input signal power and extinction ratio (ER) to the wavelength converter, and measuring the resulting converted signal power and ER. The experimental set-up is identical to that found in [3]. Measurements of the converted signals were performed by examining waveforms on an oscilloscope. To confirm the regenerating properties of the wavelength converter, Bit Error Rate (BER) measurements were performed with non-return to zero (NRZ) signals at 2.5 Gb/s using a 2^{31}-1 pseudo random bit stream (PRBS). Input signal optical signal to noise ratios (OSNR) were greater than 20 dB in all experiments. Receiver SOAs were biased at 6.6 kA/cm^2, and SGDBR gain and SOA post amp were biased at 130 mA and 100 mA respectively.

II(c). 2R regeneration results

The wavelength converted output (1545 nm) ER as a function of applied reverse bias is shown in Fig. 2 for input signal (1548 nm) extinction ratios of 4 dB and 10 dB. At both input conditions, the average on-chip

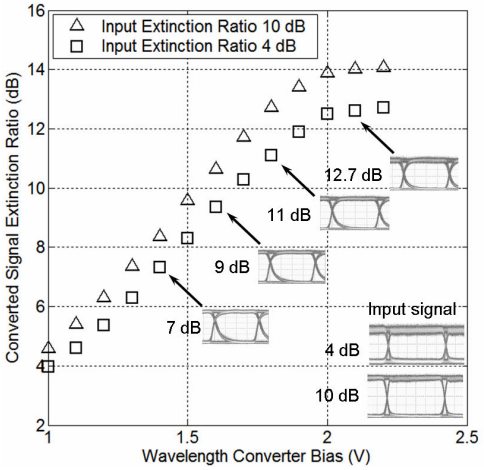

Fig 2. Wavelength converted (1548 to 1545 nm) signal extinction ratio characteristics and eye diagrams as a function of device bias conditions. Input eye diagrams are also included.

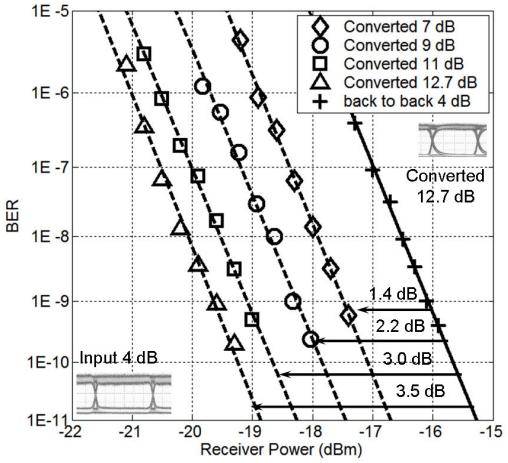

Fig 3. Wavelength converted (1548 to 1545 nm) BER measurement results. Input extinction ratio is 4 dB, output ER are indicated alng wih power penalties. Eye diagrams are for converted (2.1 V, 12.7 dB) and back to back (4 dB) signals.

receiver power was -7 dBm. The wavelength converted signals show ER of greater than 12 dB for the 4 dB ER input case and 14 dB for the 10 dB ER input case with a reverse bias of -2.1 V. Converted eye diagrams and input eye diagrams are also shown in Fig. 2.

Wavelength converted and back to back BER measurements for the 4-dB ER input signal case are shown in Fig 3. The output signal conditions are matched with the eye diagrams that are embedded in Fig. 2. As the reverse bias is increased, the wavelength converted signal ER improves, leading to improved receiver sensitivity and negative power penalties. At a bias of 2.1 V the converted signal extinction ratio improvement from 4 to 12.7 dB leads to a negative 3.5 dB power penalty.

The re-amplification characteristics for the device are measured as facet to facet gain, where

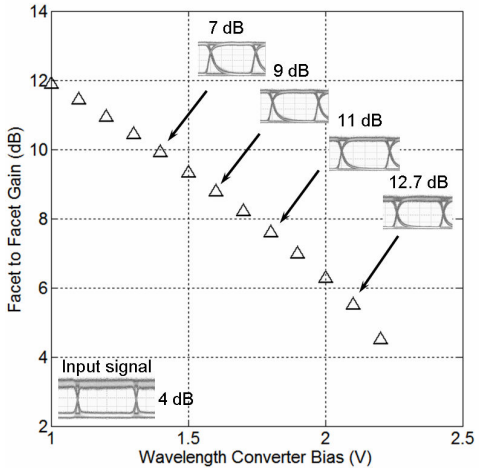

Fig 4. Wavelength converted (1548 nm to 1545 nm) facet to facet gain with fiber coupling loss removed. Input extinction ratio is 4 dB. Eye diagrams are shown for wavelength converted and input signals. Extinction ratios in eye diargams are indicated.

input and output fiber coupling losses (4.2 dB) are removed. Results are shown in Fig. 4 for a range of reverse bias conditions for the 4 dB ER input signal. As seen in the figure, between 4 dB and 12 dB of gain can be achieved depending on the applied bias conditions.

III. 3R regeneration and wavelength switching

III(a). 3R PD-WC device arrangement

For 3R regeneration experiments, the PD-WC chip described in Section I(a) is combined with an external electrical clock recovery circuit, and a second EAM (EAM 2) that spatially follows the EAM (EAM 1) connected to the QW-PIN photodetector. A functional schematic of the wavelength conversion and 3R signal regeneration process in the device, including eye diagrams, is shown in Fig. 5. For clock recovery, the photocurrent generated in the QW-PIN is used to drive an electrical PLL-clock circuit (Fig. 5). The effective 50 Ω impedance of the clock recovery circuit is used as a resistive termination. The recovered 10 GHz clock signal from the PLL is then amplified and fed to EAM 2. The single frequency sine wave controls the transmission properties of EAM 2 and gates the band-limited (3-dB optical bandwidth ~ 6 GHz) wavelength converter signal produced by the combination of EAM 1 and the QW-PIN. This approach has been shown to reduce noise and jitter [6]. Electrical delay lines are used to phase match the clock and data signals and DC bias tees are used to apply a reverse bias to the wavelength converter and to EAM 2.

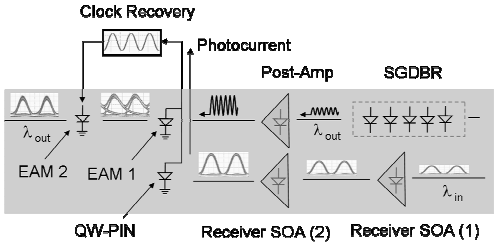

Fig. 5. Functional overview of monolithically integrated PD-WC and data/clock recoverv circuitrv.

III(b). 3R regeneration experiments

Device wavelength switching, and signal regeneration properties have been examined using a return to zero (RZ) 10 Gb/s pseudo random bit stream (PRBS) with a 2^{31}-1 word length. For wavelength switching with an ideal input, a signal with an extinction ratio (ER) of 15 dB at 1548 nm was fed to the wavelength converter. The converted signal ER and output power were measured using waveforms on an oscilloscope. Bit error rate (BER) measurements were performed using the set-up shown in Fig 6.

For regenerative wavelength switching of signals with eye shape distortion, measurements of

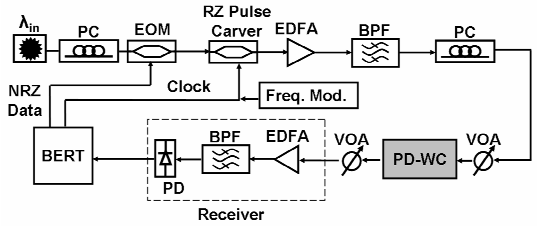

Fig 6. Experimental set up for measuring RZ signal regeneration and wavelength switching with the PD-WC.

the BER, wavelength converted ER, and output power were been performed. To degrade the signal ER and eye-shape, the polarization of the laser transmitter is rotated before entering the electro-optic modulator (EOM) in Fig. 6. The ER of the degraded input was 4 dB and the pulse width was broadened.

Jitter experiments were performed by adding a 10 MHz sinusoidal frequency modulation to the data signal from the BERT tester before being fed to the EOM. Input optical signal to noise ratios (OSNR) were greater than 25 dB in all experiments.

Receiver SOAs were biased at 6.6 kA/cm^2, and SGDBR gain section and SOA post amp were biased at 130 mA and 100 mA respectively. The amplified peak to peak 10 GHz clock tone used to drive EAM 2 was 3 V measured before the device. The wavelength converter EAM and QW-PIN (EAM 1) was biased at -2.2 V and EAM 2 was biased at -1.5 V.

III(c). 3R regeneration results

BER measurements results for wavelength conversion and signal regeneration are shown in Fig 7. Using an ideal input signal at 1548 nm with average on-chip input power of -7 dBm, BER measurements show a 1-dB power penalty for conversion to 1545 nm. Fiber coupled wavelength converted average output power was -8.2 dBm into a lensed fiber and ER was 13 dB. Measured fiber coupling loss was 4.2 dB giving an overall facet to

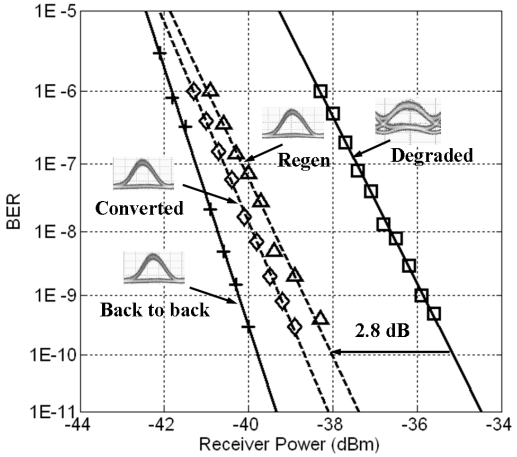

Fig 7. BER measurement results for wavelength conversion between 1548 nm and 1545 nm uisng an ideal input signal with 15 dB ER and degraded input (4 dB ER).

facet conversion gain of +7.2 dB.

For the degraded input signal, back to back BER curves and regenerated BER curves in addition to eye diagrams are shown in Fig 7. Degraded signal input extinction ratio is 4 dB at 1548 nm, and average input power to the wavelength converter was -7 dBm. After conversion the output ER at 1545 nm was 11 dB. BER measurements of the regenerated input signal show a negative 2.8 dB power penalty compared with back to back. The converted average output power was -9 dBm which gives a facet to facet conversion gain of +6.4 dB.

Device input and wavelength converted eye diagrams and their corresponding values of peak to peak jitter are shown in Fig 8. Wavelength conversion through the device provides a reduction in the input jitter by 7 ps, 12 ps and 18 ps for input jitter levels of 15 ps, 25 ps and 35 ps respectively.

Input Eyes

Jitter In (ps)	Jitter Out (ps)
15	8
25	13
35	17

Converted Eyes

Fig 8. Input and wavelength converted eye diagrams with various amounts of added peak to peak jitter. Wavelength conversion is from 1548 to 1545 nm.

IV. Summary

We have demonstrated wavelength switching in combination with both 2R and 3R regeneration using a monolithically integrated widely tunable PD-WC.

In 2R regeneration experiments with NRZ data, signal extinction ratios are improved from 4 dB to greater than 12 dB with facet to facet gain ranging from 4 dB to 12 dB. BER measurements show negative power penalties of up to 3.5 dB when the converted signal extinction ratio is regenerated from 4 dB to 12.7 dB.

In 3R regeneration experiments with RZ data, facet to facet gain for conversion of degraded input signals is +6.4 dB, and a negative power penalty of 2.8 dB is observed in BER measurements. Jitter experiments show a reduction from 35 ps to 17 ps through the PD-WC.

V. References

1 O.Leclerc et al, J. Lightwave Technol. v. 21 (2003), 2179-2190.

2 T.Otani et al, J. Lightwave Technol. v. 20 (2002), 195-200.

3 M.N. Sysak et al, Proc. IPRA (2006), ITuC5.

4 M.N. Sysak et al, Proc. DRC (2006), II. A-2.

5 A. Tauke-Pedretti et al, IEEE Photon. Technol. Lett., v. 17, n. 7, (2005), 2167-2169.

6 H.F. Chou et al, Optics Express, v. 13, n. 7, (2005), 2742-2746.

Extinction ratio regeneration, signal re-amplification (2R), and broadband wavelength switching using a monolithically integrated photocurrent driven wavelength converter

Matthew N. Sysak, James W. Raring, Jonathon S. Barton, Henrik N. Poulsen, Daniel J. Blumenthal and Larry A. Coldren

Department of Electrical and Computer Engineering, University of California, Santa Barbara, CA 93106
Department of Materials, University of California, Santa Barbara, CA 93106
mnsysak@engineering.ucsb.edu

Abstract: Detailed wavelength conversion, extinction ratio regeneration, and signal re-amplification experiments are performed using a monolithically integrated, widely tunable photocurrent driven wavelength converter. A -3.5 dB power penalty is observed in bit error rate measurements at 2.5 Gb/s when the extinction ratio of an incoming signal is regenerated from 4 dB to 11 dB, and the input signal wavelength is switched from 1548 nm to an output wavelength range between 1533 nm and 1553 nm. When the input signal extinction ratio is regenerated from 4 to 11 dB, the wavelength converter provides facet to facet conversion gain of 5 dB, 7.7 dB, and 7.6 dB for conversion from 1548 nm to output wavelengths of 1533, 1545 nm, and 1553 nm.

OCIS codes: (250.5300) Photonic Integrated Circuits; (130.3120) Integrated Optics Devices

References and links

1. M. Webster, A. Wonfor, R. V. Penty, and I. H. White, "All-optical 2R regeneration and wavelength conversion at 10 Gb/s in an integrated semiconductor optical amplifier/distributed feedback laser," Proc. European Conf. on Opt. Comm. (ECOC) **4**, 578-579 (2001).
2. D. C. Kim, M. Y. Jeon, Y. A. Leem, E. D. Shim, D. S. Yee, and K. H. Park, "Extinction ratio improvement and negative BER penalty for 2R regeneration in Mach-Zehnder wavelength converter," Proc. European Conf. on Opt. Comm. (ECOC) **3**, 749-750 (2005).
3. P. S. Cho, D. Mahgerefteh, and J. Coldhar, "All-optical 2R regeneration and wavelength conversion at 20 Gb/s using an electroabsorption modulator," IEEE Photon. Technol. Lett. **11**, 1662-1664 (1999).
4. S. B. Yoo, "Wavelength conversion technologies for WDM network applications," J. Lightwave Technol. **14**, 955-966 (1996).
5. M. N. Sysak, J. W. Raring, J. S. Barton, M. Dummer, D. J. Blumenthal, and L. A. Coldren, "A single regrowth integration platform for photonic circuits iincorporating tunable SGDBR lasers and quantum well EAMs," IEEE Photon. Technol. Lett. **18**, 1630-1632 (2006).
6. M. N. Sysak, J. W. Raring, J. S. Barton, M. Dummer, A. Tauke-Pedretti, H. N. Poulsen, D. J. Blumenthal, and L. A. Coldren, "Single-chip, widely-tunable 10 Gbps photocurrent-driven wavelength converter incorporating a monolithically integrated laser transmitter and optical receiver," IEE Electronics Lett. **42**, 657-658 (2006).
7. A. Tauke-Pederetti, M. Dummer, J. Barton, M. Sysak, J. Raring, L. A. Coldren, "High saturation power and high gain integrated receivers," IEEE Photon. Technol. Lett. **17**, 2167-2169 (2005).

I. Introduction

Optical signal regeneration, including signal reshaping and re-amplification (2R) and optical wavelength conversion are critical functionalities for increasing transmission distances and reducing blocking probabilities in next generation networks. To perform this function, several devices using a variety of approaches have been proposed and demonstrated. For

#73744 - $15.00 USD Received 7 August 2006; revised 11 September 2006; accepted 11 September 2006

simultaneous regeneration and wavelength conversion, these include optically injected lasers, semiconductor optical amplifier Mach Zehnders, electroabsorption modulators (EAM), and a variety of discrete component optoelectronic approaches [1-3]. Although significant progress has been made in operating speed and regeneration efficiency using these techniques, the majority of currently available wavelength converters that are compatible with regeneration suffer from a variety of drawbacks. These drawbacks include large chirp, high losses between discrete components, high power dissipation, limited dynamic wavelength conversion between identical wavelengths, and additional external optical filtering requirements for separating input and output wavelength converted signals [4].

In contrast to these techniques, recently we have demonstrated a photocurrent driven wavelength converter (PD-WC) that is fully transparent to a range of input and output wavelengths. The PD-WC does not require optical filtering to separate input and output signals and incorporates an on-chip tunable laser source to limit optical losses between discrete components. The device is fabricated using a simple dual quantum well (DQW) integration platform [5] where active regions used for optical gain, passive regions for waveguide routing, and EAM regions are defined using a selective etch technique to remove a set of quantum wells located above the optical waveguide layer. Completion of PD-WC fabrication requires only a single blanket InP regrowth.

In this work we show signal regeneration in combination with broadband wavelength switching using the PD-WC. Signal regeneration is performed through extinction ratio (ER) regeneration and signal reamplification (2R). Using a degraded input signal with a 4 dB ER at a wavelength of 1548 nm, conversion through the PD-WC to wavelengths between 1533 nm and 1553 nm shows extinction ratio improvements from 4 dB to 11 dB, facet to facet device gain of up to 7.7 dB, and a negative power penalty of 3 dB at a bit rate of 2.5 Gb/s.

2. PD-WC wavelength switching and signal regeneration mechanism

The photocurrent driven wavelength converter (PD-WC) consists of a monolithically integrated pre-amplified receiver and externally modulated widely tunable sampled grating DBR (SGDBR) based transmitter [6]. A scanning electron micrograph (SEM) of the device is

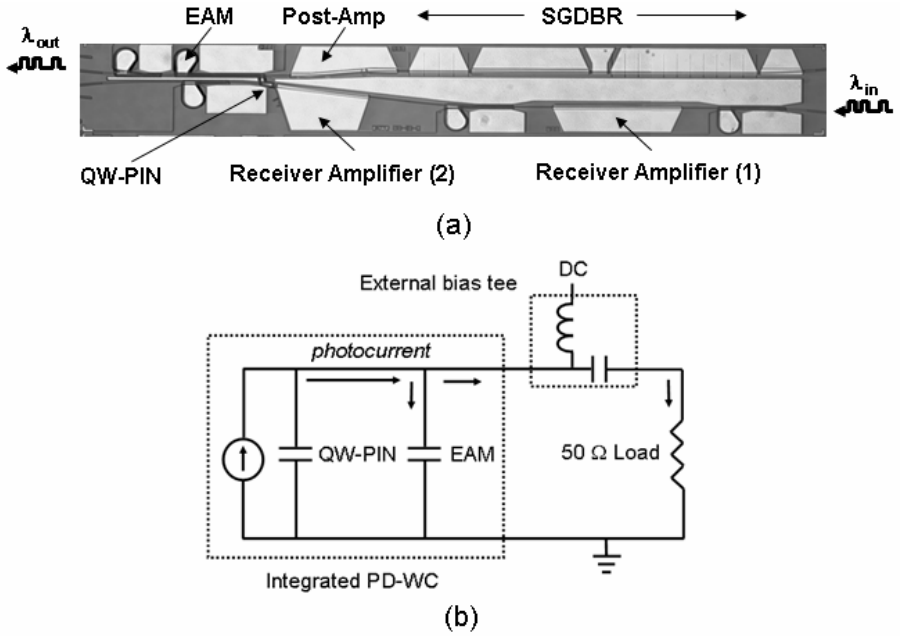

Fig 1. (a) SEM image of monolithically integrated photocurrent driven wavelength converter. (b) Equivalent circuit diagram for switching elements in the PD-WC showing the QW-PIN and EAM. Arrows indicate photocurrent from the QW-PIN photodetector.

#73744 - $15.00 USD Received 7 August 2006; revised 11 September 2006; accepted 11 September 2006

shown in Fig. 1(a). Light enters the receiver on λ_{in} and is amplified by a set of two integrated semiconductor optical amplifiers (SOAs). The first SOA is 600 μm long and boosts the optical input power level to just below the 1-dB output power gain compression for a 3 μm wide amplifier. A second 400 μm long SOA with a flared waveguide geometry (3-12 μm) is then used to further boost the optical power before the input signal enters a quantum well (QW)-PIN photodetector [7]. The photocurrent from the receiver is routed over a short 35 μm long metal interconnect to a 400 μm long EAM that shares an optical waveguide with the SGDBR laser and shares a circuit node with an external bias tee and a 50 Ω load resistor. As the photocurrent drops across the load resistor, the EAM potential is changed, resulting in a modulation of its transmission characteristics. Since the EAM shares an optical waveguide with SGDBR laser, when the transmission characteristics are modified, the photocurrent signal from the QW-PIN is transcribed onto the output of the tunable laser operating at λ_{out}, completing the wavelength conversion process. The DC voltage for both QW-PIN and EAM is applied through the external bias tee. The integrated receiver, including the quantum efficiency of the QW-PIN photodetector, has a gain of between 20 and 21 dB with an applied current density of 6 kA/cm^2. The terminated S_{21} optical to optical bandwidth of the device is 7 GHz.

Extinction ratio regeneration in the PD-WC can be understood by examining a small signal equivalent circuit diagram of the active components in the wavelength switching process ([1(b)]. The components consist of a current source, representing the photocurrent in the receiver, two capacitors representing the QW-PIN and EAM, an inductor and capacitor for the external bias tee, and a load resistor. For an input signal that has a degraded extinction ratio, the inductive nature of the bias tee routes very low frequency components (DC offsets) through the inductor to the DC voltage source. Assuming an ideal source, the low frequency components are compensated by additional current, allowing the voltage at the QW-PIN/EAM circuit node to remain fixed. Since the voltage at this node is used to set the off state of the transmitter EAM (and hence the PD-WC), the off state at the output of the PD-WC can be set independently of the DC level at the input. For higher frequency components, the majority of the photocurrent generated in the receiver is routed to the load resistor, where it creates a voltage swing across the capacitor associated with the EAM. As long as the combination of the off state set by the voltage source and the high frequency voltage swing over the EAM is sufficient to generate an output extinction that is larger than that of the input, the PD-WC can provide signal regeneration.

For regeneration at data rates beyond the RC limited bandwidth of the device (7 GHz), the frequency dependent impedance of the PD-WC becomes important. At these high bit rates, although the optical power generated by the integrated receiver SOAs does not change, a reduction in the voltage drop over the EAM occurs due to the lowering of the effective impedance associated with the equivalent circuit shown in Fig. 1(b). The reduction in drive voltage lowers the output extinction of the wavelength converted signals, reducing the ability of the device to perform re-conditioning. As such, scaling the bandwidth and efficiency of the integrated photodetector and modulator is a key improvement in next generation designs of the PD-WC.

3. Regeneration experiments

Device re-amplification and extinction ratio regeneration characteristics were examined by degrading the input signal power and ER to the wavelength converter and measuring the resulting converted signal power and ER. The experimental set-up is identical to that found in [6]. Bit error rate (BER) measurements were performed for both degraded input signals and regenerated, wavelength converted signals. The BER experiments used a non-return to zero (NRZ) signal at 2.5 Gb/s with a 2^{31}-1 pseudo random bit stream (PRBS). Input signal optical signal to noise ratios (OSNR) were greater than 20 dB in all experiments. Receiver

#73744 - $15.00 USD Received 7 August 2006; revised 11 September 2006; accepted 11 September 2006

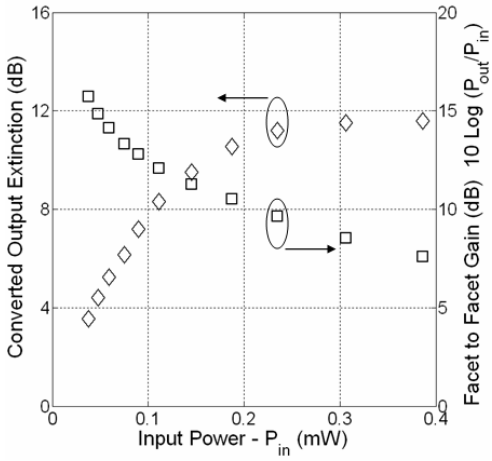

Fig 2. PD-WC converted extinction ratio and facet to facet gain at 2.5 Gb/s as a function of input power. The input and output signals are at 1548 nm and 1550 nm respectively. QW-PIN/EAM bias is -2.0V.

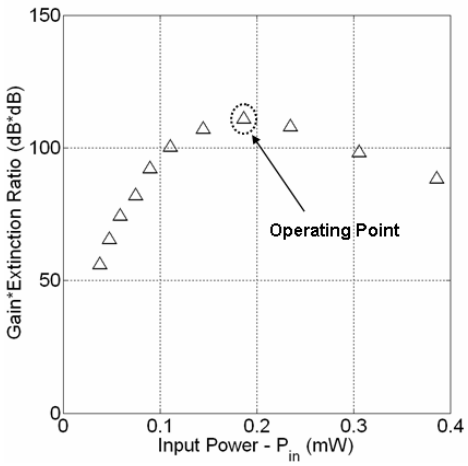

Fig 3. Product of the PD-WC gain and output extinction ratio as a function of input power. Input and output wavelengths are the same as in Fig. 4 as well as bias conditions. Optimal input power level is indicated.

SOAs were biased at 6 kA/cm^2, and SGDBR gain and SOA post amp were biased at 130 mA and 100 mA respectively.

For regeneration and re-amplification it is desirable to obtain the highest possible extinction ratio and the largest possible conversion gain from the PD-WC for a given input signal. To select the optimal input conditions to the device, an experiment was performed where an optical signal at 1548 nm with 10 dB extinction was fed to the PD-WC receiver at various power levels. The converted extinction out of the wavelength converter operating at 1550 nm was measured on an oscilloscope and the facet to facet gain from the device was calculated based on the fiber coupled input and output power, assuming 4.2 dB coupling loss. In these experiments the QW-PIN/EAM circuit node was biased at -2.0V. Results of the conversion gain and the output extinction from the PD-WC are shown in Fig. 2 and show that as the receiver power increases, the extinction from the device increases while the facet to facet gain decreases. To optimize the trade off between these two quantities the product of the

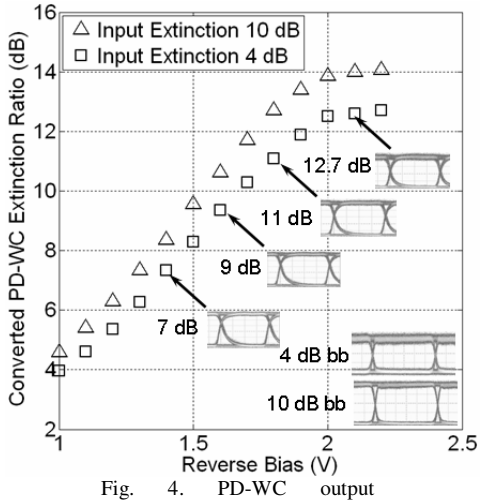

Fig. 4. PD-WC output extinction ratio for input signals with 4 dB ER or 10 dB ER. Back to back eye diagrams and converted etye diagrams are included. Input and output wavelengths are 1548 and 1545 nm respectively.

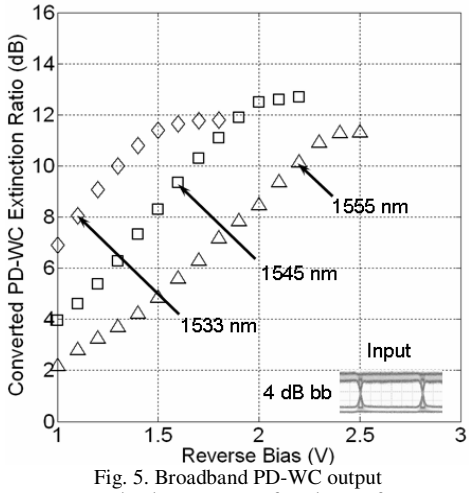

Fig. 5. Broadband PD-WC output extinction as a function of applied bias using a degraded 4 dB ER input signal. Output conversion is shown for operating wavelengths of 1533nm (diamonds), 1545 nm (squares), and 1555 nm (triangles).

#73744 - $15.00 USD Received 7 August 2006; revised 11 September 2006; accepted 11 September 2006

conversion gain and output extinction ratio as a function of input power is shown in Fig 3. From this figure, the input power that maximizes both gain and extinction simultaneously is approximately 0.19 mW (-7.2 dBm).

With the optimized input power level of -7.2 dBm, the regeneration properties of the PD-WC were further characterized using input signals at 1548 nm with extinction ratios of 4 dB and 10 dB. The output extinction ratio as a function of applied bias for these two input conditions is shown in Fig. 4. For wavelength conversion from 1548 nm to 1545 nm the PD-WC can regenerate the 4 dB extinction input signal to greater than 12 dB. Embedded eye diagrams for back to back (bb) conditions and wavelength converted signals with extinction ratios of 7 dB, 9 dB, 11 dB, and 12.7 dB are also included in the figure. The back to back eye diagrams were taken directly out of the transmitter used as an input to the wavelength converter for each input case. For broadband wavelength conversion and regeneration, the output extinction ratio generated by the PD-WC with the 4 dB ER input case is shown in Fig. 5. For output operating wavelengths that range from 1533 to 1553 nm, the converted extinction ratio from the wavelength converter can be regenerated to 11 dB depending on the applied bias to the device.

BER measurements were performed for signal regeneration and wavelength conversion from 1548 nm to a variety of output wavelengths using the 4-dB ER input signal. For conversion from 1548 nm to 1545 nm with applied reverse biases of 1.4V, 1.6V, 1.8V, and 2.1 V, results of the BER as a function of receiver power are shown in Fig. 6. As the reverse bias is increased, the wavelength converted signal ER improves as shown in Fig. 4, leading to improved receiver sensitivity and negative power penalties. At a bias of 2.1 V the converted signal extinction ratio improvement from 4 to 12.7 dB leads to a negative 3.5 dB power penalty.

For broadband wavelength conversion and regeneration, BER measurements were performed where the reverse bias applied to the PD-WC was selected based on data in Fig. 5 to achieve an 11 dB converted ER for each output operating wavelength. For output wavelengths of 1533 nm, 1545 nm, and 1553 nm, the applied bias conditions to achieve this extinction were 1.4V, 1.7V and 2.3V respectively. Results of the BER experiments are shown in Fig 7. For all output operating wavelengths, the 4-dB extinction ratio can be regenerated to 11 dB which leads to improved receiver sensitivity and negative 3-dB power penalty.

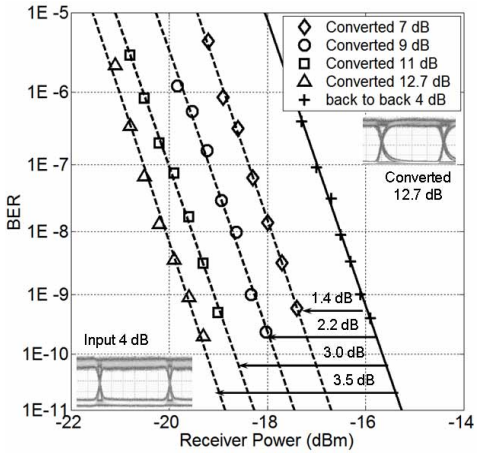

Fig. 6. Wavelength converted (1548 to 1545 nm) BER measurement results for a degraded input signal with 4 dB ER. Converted ER is indicated along with power penalties. Eye diagrams are for converted (2.1 V, 12.7 dB ER) and back to back signals.

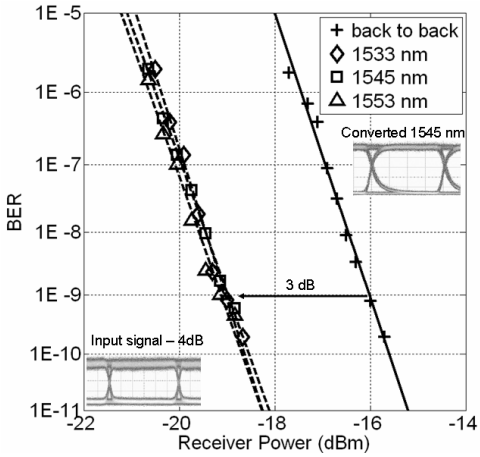

Fig. 7. Broadband wavelength converted BER measurement for degraded input signal with 4 dB ER. For each output wavelength the bias of the PD-WC is set to achieve an output ER of 11 dB. Eye diagrams are for input signal and converted output at 1545 nm.

#73744 - $15.00 USD Received 7 August 2006; revised 11 September 2006; accepted 11 September 2006

Broadband re-amplification characteristics of the PD-WC as a function of applied reverse bias are shown in Fig. 8 using the 4 dB ER input signal. The conversion gain is shown as facet to facet gain where the input and output fiber coupling losses (4.2 dB) have been removed. For output wavelengths ranging from 1533 nm to 1553 nm, the PD-WC conversion gain varies from 2 dB to 15 dB depending on the applied bias conditions. For a fixed output wavelength of 1545 nm, the conversion gain for the applied bias levels used to generate the data in Fig. 6 were 10 dB, 8.7 dB, 7.8 dB, and 5.5 dB. Eye diagrams from the PD-WC at each of these reverse biases have been included. For the conditions indicated to achieve an 11 dB output ER over a range of output wavelengths of 1533 nm, 1545 nm and 1553 nm, the conversion gain is 5 dB, 7.7 dB, and 7.6 dB.

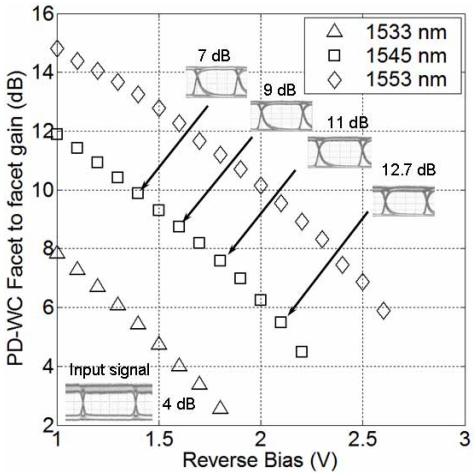

Fig. 8. Broadband PD-WC re-amplification characteristics. Eye diagrams included are for back to back (4 dB ER) and converted eye diagrams for the bias conditions indicated in Fig 6.

4. Conclusion and future work

Signal regeneration in combination with broadband wavelength switching using a monolithically integrated photocurrent driven wavelength converter. Signal regeneration is performed through extinction ratio regeneration and signal reamplification. Using a degraded input signal with a 4 dB ER at a wavelength of 1548 nm, conversion to output wavelengths of 1533 nm, 1545 nm, and 1553 nm shows a regenerated extinction of 11 dB, and conversion gain of 5 dB, 7.7 dB, and 7.6 dB. BER measurements for conversion to each of these wavelengths with an output ER of 11 dB shows a negative 3 dB power penalty. Future improvements in the device include scaling both the bandwidth and efficiency of the integrated photodetector and modulator for regeneration at higher bit rates.

Acknowledgments

This work was funded by DARPA/MTO under CS-WDM Grant No. N66001-02-C-8026. The authors would like to thank Agility Corp. (JDS Uniphase) for AR coatings.

Broadband return-to-zero wavelength conversion and signal regeneration using a monolithically integrated, photocurrent-driven wavelength converter

M.N. Sysak, L.A. Johansson, J.W. Raring,
H.N. Poulsen, D.J. Blumenthal and L.A. Coldren

Broadband wavelength switching and signal regeneration experiments with 10 Gbit/s return-to-zero signals using a photocurrent-driven wavelength converter (PD-WC) are presented. For wavelength switching using an ideal input signal to the PD-WC, the device generates up to +3.7 dB facet to facet gain and shows < 1 dB power penalty in bit error rate measurements. For wavelength switching with a degraded input signal, the PD-WC shows extinction ratio regeneration from 5 to > 11 dB, jitter reduction from 35 to 17 ps, significant eyeshape regeneration, and a −2.8 dB power penalty.

Introduction: Dynamic wavelength switching and signal regeneration are critical functions to enhance the performance of next generation networks. Of particular importance is a monolithically integrated device that can perform these functions, including signal reamplification, reshaping, retiming (3R) and wavelength conversion with a small form factor. Such a device has the potential for low packaging costs and low coupling losses between discrete components.

Several approaches have been explored for simultaneous wavelength switching and signal regeneration. These include interferometric optical amplifiers, nonlinear fibres, and a variety of electroabsorption modulator (EAM) approaches [1–3]. However, these approaches generally have high loss between components, high power dissipation, or need optical filtering to separate input and regenerated signals. Recently we have demonstrated a small form factor monolithically integrated PD-WC [4]. The high degree of integration allows for low coupling losses, and the separation of input and output signals enables full wavelength transparency without output signal filtering. In this Letter we present optical wavelength switching and 3R regeneration using the PD-WC. The device employs a tandem modulator clock recovery technique [5] to regenerate the degraded optical signals.

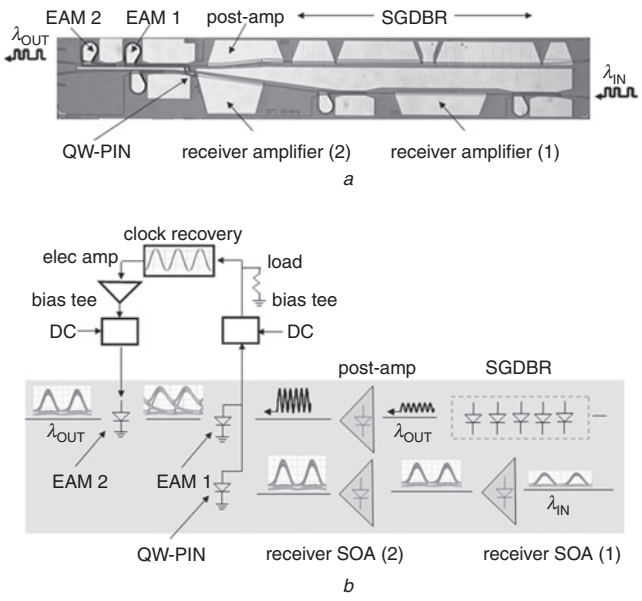

Fig. 1 *SEM image of monolithically integrated (3.0 × 0.5 mm) PD-WC, and functional schematic, eye diagrams at various locations in wavelength converter, and clock recovery apparatus used for signal regeneration*

a SEM image
b Functional schematic, eye diagrams, clock recovery apparatus

The PD-WC consists of an optically preamplified receiver and a widely tunable transmitter fabricated in a parallel waveguide arrangement as shown in Fig. 1*a*. The receiver contains two SOAs followed by a quantum well (QW)-PIN photodetector and provides 20 dB gain for transverse electric (TE) polarised input signals. The compressively strained quantum wells used for gain throughout the device make it polarisation sensitive, with preference for TE polarised signals. The transmitter consists of a sampled grating DBR (SGDBR) laser, an SOA post-amplifier, a 400 µm-long EAM (EAM-1), and an additional 200 µm-long EAM (EAM-2). EAM-1 and the QW-PIN share a common reverse bias applied through a bias tee and a ground-signal probe. An external 50 Ω load resistor is used on the RF side of the bias tee for bandwidth. A 35 µm-long Ti/Pt/Au metal trace connects the QW-PIN photodetector and EAM-1.

For wavelength switching, photocurrent from the receiver is routed over the metal interconnect and used to change the voltage across EAM-1 via the load resistor. The voltage change modulates the transmission characteristics of this EAM which inscribes the input signal onto the output wavelength of the SGDBR. The DC bias applied to EAM-1 and the RF swing from the QW-PIN set the zero level and the gate opening (EAM-1) at the output from the tunable transmitter. For signal reshaping and retiming, the device uses a second EAM (EAM-2) that spatially follows EAM-1 on the transmitter waveguide. The generated photocurrent used to drive EAM-1 is used to trigger an external clock recovery circuit. The clock source is then electrically amplified and fed back to EAM-2 which acts as a pulse carver, gating the shape of the optical signal from EAM-1. Variable delay elements are used to phase match the recovered clock to the data. A functional schematic of the wavelength conversion and clock recovery along with eye diagrams at various points in the device are shown in Fig. 1*b*.

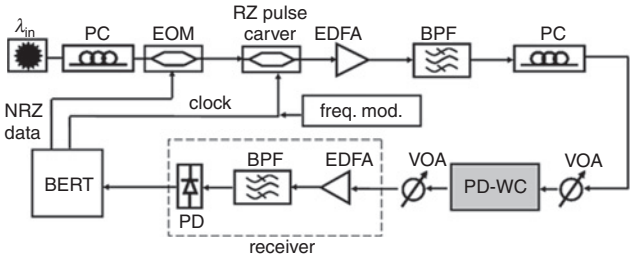

Fig. 2 *Experimental setup for regeneration and wavelength switching experiments using PD-WC*

NRZ data converted to RZ data using carving Mach-Zehnder modulator over-driven by clock source from BERT. Frequency modulation introduced onto carving modulator using swept frequency source

Experiment: Wavelength switching and signal regeneration were performed using the experimental setup shown in Fig. 2. A non-return-to-zero (NRZ) $2^{31}-1$ word length pseudorandom bit stream (PRBS) at 10 Gbit/s was generated from a bit error rate tester (BERT) at 1548 nm. To form the RZ data, the NRZ signal is gated using an external carving Mach-Zehnder modulator that is over-driven by the NRZ clock source from the BERT such that it switches from off- to on-state in a single bit period. The RZ optical data signal is then amplified with an EDFA and filtered with a 0.35 nm filter before being coupled to the device using a lensed fibre. After regeneration and wavelength conversion, the output from the device is coupled to another lensed fibre and routed to an optical receiver before either being fed back to the BERT, or to a digital component analyser (DCA). Measurements of the wavelength converted eye diagrams and the converted optical power, ER, and jitter were performed using the DCA. Jitter was added to the input optical signal fed to the PD-WC by introducing a 10 MHz sinusoidal frequency modulation onto the electrical signal driving the carving modulator.

Results: Measurements of the frequency response of the wavelength converting portion of the regenerator (QW-PIN and EAM-1) with a 50 Ω termination showed an optical to optical 3 dB bandwidth of between 6 to 7 GHz. The slightly band-limited characteristics are attractive since the converted pulse becomes spread out in time before entering the carver. This allows more margin for the gating function of EAM-2 to carve out the inside of the converted signal.

For wavelength switching, a 15 dB ER input signal at 1548 nm with −7 dBm fibre coupled on-chip power was fed to the PD-WC. The receiver amplifiers were biased to 6 kA/cm^2, the transmitter SGDBR gain was biased to 130 mA and the transmitter post-amplifier was biased to 100 mA. The applied bias on EAM-1 and the QW-PIN photodetector was −2.0, −2.6 and −3.0 V for output wavelengths of 1541, 1553 and 1563 nm, respectively. The bias on the carving EAM

was −1.5 V. The amplified clock signal fed back to the carving EAM was 3 V*pp*, and was measured after the bias tee before entering the device. For switching from 1548 to 1541, 1553 and 1563 nm, BER measurements are shown in Fig. 3 and show a 1 dB power penalty for converted signals. The converted extinction ratios were 11.3, 11.2 and 11.4 dB, and output power levels were −8.2, −8 and −7.5 dBm for each of the indicated output wavelengths. After measuring and accounting for the 4.2 dB fibre coupling loss, the facet to facet gain of the device at each of these wavelengths is +3, +3.2 and +3.7 dB.

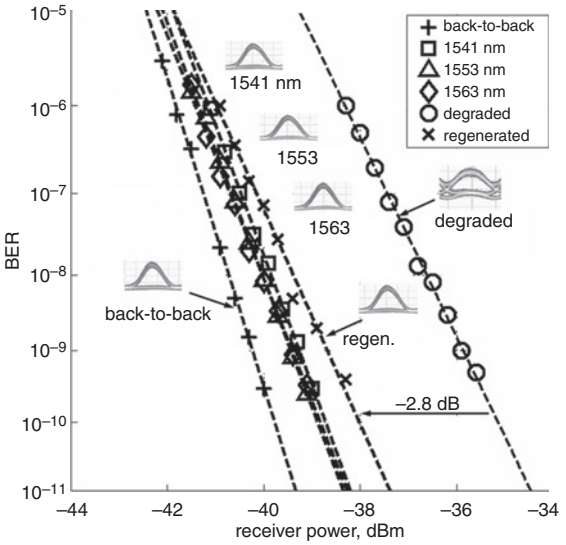

Fig. 3 *BER measurements at 10 Gbit/s for wavelength switching using ideal input signal and signal regeneration with degraded input*

Receiver amplifier biased to 6 kA/cm^2; transmitter laser gain and post-amp SOA biased to 130 and 100 mA, respectively, in all experiments

To demonstrate ER regeneration and eye diagram reshaping, the input to the PD-WC was degraded by rotating the polariser before the carving Mach-Zehnder modulator in Fig. 2. An eye diagram of the degraded input signal at 1548 nm is shown in Fig. 3. The degraded input signal ER was 5 dB, the optical signal-to-noise ratio was 25 dB, and the on-chip input power to the receiver was −7 dBm. Bias conditions in the PD-WC were identical to that used for wavelength switching experiments with an output of 1541 nm. After wavelength conversion to 1545 nm and signal regeneration, the output signal extinction was improved to 11 dB, the fibre coupled output power was −9 dBm, and the output OSNR was 45 dB. BER measurements were performed and we observe a −2.8 dB power penalty between the BER curves for the degraded and regenerated signals.

Jitter reduction experiments were performed by examining input and converted waveforms after adding various amounts of 10 MHz sinusoidal frequency modulation onto the MZ-pulse carving modulator in Fig. 2. Input and output wavelengths were 1548 and 1541 nm, respectively. Converted eye diagrams and measurements of the peak-to-peak jitter are summarised in Fig. 4. Bias conditions on the PD-WC are identical to that used for conversion to 1541 nm, except that the wavelength converter (EAM-1 and QW-PIN) bias is set to −2.3 V. For input peak-to-peak jitter of 35, 25 and 15 ps, conversion through the device reduced the jitter to 17, 13 and 8 ps, respectively.

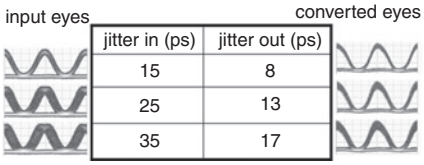

Fig. 4 *Wavelength switched input and output eye diagrams with added jitter at input of device*

Jitter added as a 10 MHz frequency modulation onto Mach-Zehnder pulse carving modulator outlined in Fig. 2

Conclusion: We have demonstrated a monolithically integrated wavelength converter capable of broadband wavelength switching, facet to facet reamplification, signal reshaping, and signal retiming. For wavelength switching using ideal input signals, the PD-WC provides signal reamplification up to +3.7 dB. For degraded input signals, the PD-WC shows reshaping of the converted signal eye diagrams and extinction ratio improvements from 5 to >11 dB. Jitter measurements show jitter reduction from 35 to 18, 25 to 13 and 15 to 8 ps for wavelength switching though the device with added 10 MHz frequency modulation onto the input. BER measurements show −2.8 dB power penalty for degraded waveform signals after regeneration through the PD-WC.

17 August 2006
Electronics Letters online no: 20062415
doi: 10.1049/el:20062415

M.N. Sysak, L.A. Johansson, H.N. Poulsen, D.J. Blumenthal and L.A. Coldren (*Electrical and Computer Engineering Department, University of California, Santa Barbara, CA 93106, USA*)

E-mail: mnsysak@engineering.ucsb.edu

J.W. Raring (*Materials Department, University of California, Santa Barbara, CA 93106, USA*)

References

1 Schubert, C., *et al.*: '160 Gbit/s wavelength converter with 3R regenerating capability', *Electron. Lett.*, 2002, **38**, (16), pp. 903–904
2 Leuthold, J., *et al.*: 'Novel 3R regenerator based on semiconductor optical amplifier delayed-interference configuration', *IEEE Photonics Technol. Lett.*, 2001, **13**, (8), pp. 860–862
3 Hu, Z., *et al.*: 'Optical clock recovery circuits using travelling-wave electroabsorption modulator based ring oscillators for 3R regeneration', *IEEE J. Sel. Top. Quantum Electron.*, 2005, **11**, (2), pp. 329–337
4 Sysak, M.N., *et al.*: 'Single-chip, widely-tunable 10 Gbit/s photocurrent-driven wavelength converter incorporating a monolithically integrated laser transmitter and optical receiver', *Electron. Lett.*, 2006, **42**, (11), pp. 657–658
5 Chou, H.F., and Bowers, J.E.: 'Simplified optoelectronic 3R regenerator using nonlinear electro-optical transformation in an electroabsorption modulator', *Opt. Express*, 2005, **13**, (7), pp. 2742–2746

II. Photonic IC Wavelength Converters

B. “All-Optical” Wavelength-Converters and Buffers @ 40Gb/s

Performance Optimization of an InP-Based Widely Tunable All-Optical Wavelength Converter Operating at 40 Gb/s

Vikrant Lal, *Student Member, IEEE*, Milan L. Mašanović, *Member, IEEE*, Joseph A. Summers, *Student Member, IEEE*, Larry A. Coldren, *Fellow, IEEE*, and Daniel J. Blumenthal, *Fellow, IEEE*

***Abstract*—We report on the design and performance optimization of a quantum-well active region-based semiconductor optical amplifier Mach–Zehnder interferometer wavelength converter monolithically integrated with a widely tunable sampled-grating distributed Bragg reflector laser, operating differentially at 40 Gb/s. The device is fabricated using an offset quantum-well platform, requiring a single regrowth. We show error-free operation, with a less than 3-dB power penalty at the optimal differential delay, and open eyes across a 25-nm output tuning range.**

***Index Terms*—Mach–Zehnder interferometer (MZI), photonic integrated circuit, semiconductor optical amplifier (SOA), wavelength conversion, wavelength-division multiplexing.**

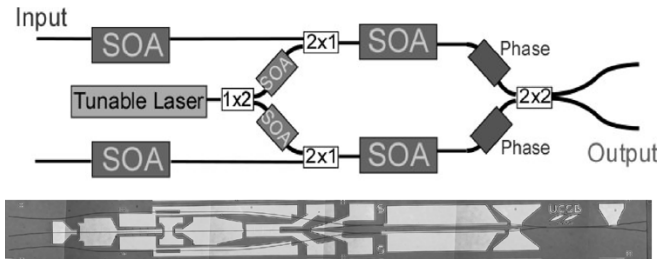

Fig. 1. Schematic of the device design showing the different components and a microscope image of the fabricated device.

I. Introduction

ULTRAHIGH capacity optical data routing systems are expected to form the backbone of future networks. The realization of such systems though, depends on significant reductions in power, footprint, and cost requirements. One key function in such systems will be all-optical wavelength conversion, due to the potential advantages it can offer such as increased connection flexibility, network capacity, ease of network management, and potential reduction in optical buffering requirements [1].

Monolithic integration of high-speed all-optical wavelength converters is a very important step toward meeting the cost requirements. Semiconductor optical amplifier (SOA)-Mach–Zehnder interferometer (SOA-MZI)-based integrated wavelength converters are a good candidate for systems operating at 40 Gb/s due to the ultrafast carrier-depletion-induced refractive index changes in an SOA. The maximum speed of the SOA-MZI converters is limited primarily by the carrier recovery lifetime in the SOAs. An attractive approach that has been previously demonstrated to overcome the SOA carrier recovery limitation, and is used in this letter, is a differential scheme in which the fast carrier-depletion in one arm is used to switch the MZI on, while the same fast carrier-depletion is used, after a suitable delay, in the other arm to turn it back off [2]–[5]. An optimized delay is crucial for the chip performance, and a detailed study on its influence of the converter performance, to the best of our knowledge, has not been published before.

In this letter, for our delay study, we used a differential 40-Gb/s widely tunable all-optical wavelength converter (TAO-WC) with on-board widely tunable sampled-grating distributed Bragg reflector (SG-DBR) laser fabricated in the offset quantum-well (OQW) platform [6]. The device schematic is shown in Fig. 1, along with a microscope image of the fabricated device. The dimensions of the fabricated device are 0.5×4.8 mm^2. The OQW integration platform offers a robust and simple high yield approach for high density integration of active–passive components on chip. The on-chip tunable laser source greatly simplifies the operation of the device and allows us to select the desired output wavelength from the converter in a fast and power efficient manner. We have previously demonstrated the operation of wavelength converters in the OQW platform operating at 10-Gb/s nonreturn-to-zero (NRZ) [6], [7]. The OQW platform offers an excellent approach for fabricating complex quantum-well-based low-power consumption photonic integrated circuits. One potential limitation of this platform is the low confinement factor that results due to the position of the quantum wells on top and not in the center of the waveguide [7].

For 40-Gb/s operation reported in this letter, the devices are redesigned to have shorter preamplifier SOAs (600 μm long) to reduce saturation and pattern-dependent effects while still providing adequate gain for the input signal. Also, for use in an external differential-delay-based configuration, two input waveguides are needed, which are then bent in opposite directions to allow easy coupling of two fibers to the input facet. We study the effect of the differential delay on the performance of the device and show that selection of the optimal delay is very important for this class of devices. The optimal delay value depends

Manuscript received July 15, 2005; revised November 23, 2005. This work was supported by the Defense Advanced Research Projects Agency (DARPA)/MTO DOD-N program under the LASOR Project Award W911NF-04-9-0001.

The authors are with the Electrical and Computer Engineering Department, University of California at Santa Barbara, Santa Barbara, CA 93106 USA (e-mail: lal@ece.ucsb.edu).

Digital Object Identifier 10.1109/LPT.2005.864000

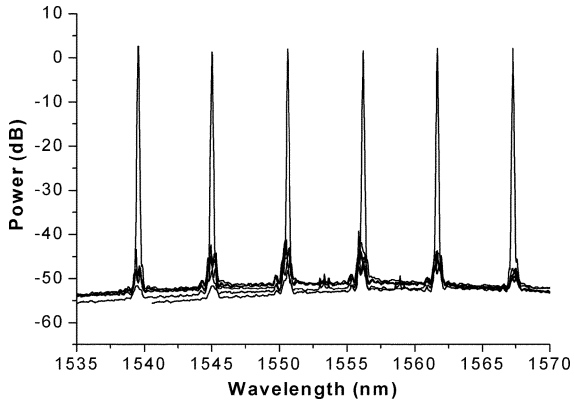

Fig. 2. Output tuning spectrum showing a few representative output wavelengths.

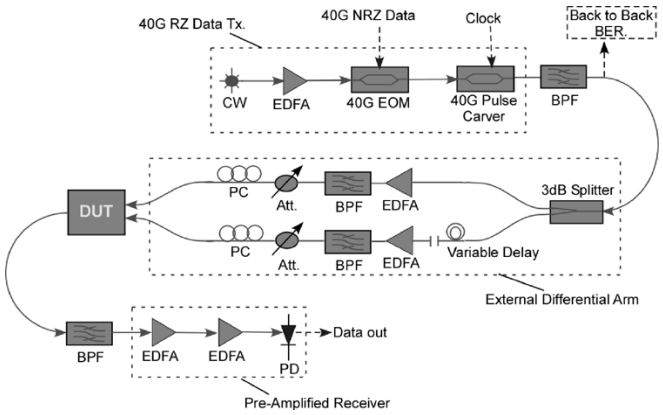

Fig. 3. A 40-Gb/s wavelength conversion experimental setup.

on the input pulsewidth and needs to be determined before the delay can be integrated on-chip.

We also demonstrate that error-free operation can be achieved at 40-Gb/s return-to-zero (RZ) with a less than 3-dB power penalty at the optimal delay value. The devices show clearly open eyes across an output wavelength tuning range of 25 nm, which is limited by the available erbium-doped fiber amplifier (EDFA) gain bandwidth in the receiver.

II. Device Design and Operation

The device consists of a widely tunable SG-DBR laser monolithically integrated with an SOA-MZI [7]. The on-chip tunable laser source greatly increases the functionality and efficiency of the device and simplifies the operation by providing a stable continuous-wave (CW) signal, and maintaining a fixed CW polarization state. Fig. 2 shows overlaid spectra from the SG-DBR laser at a few representative wavelengths. The laser itself can be continuously tuned over this entire range. The SOA-MZI has 1-mm-long SOAs in each branch. The SOA dimensions were chosen based on our previous experiments [7] to get a large phase swing in the MZI and fast SOA operation.

We characterize the effect of varying the differential delay on the performance of the device, and find that selection of a large enough delay is critical to the performance of the device. The optimal delay value is determined primarily by the input pulsewidth and needs to be optimized before the delay can be integrated on-chip. Fig. 3 shows the experimental setup for 40-Gb/s wavelength conversion using an external differential arm. The input signal is obtained by first modulating a CW source with 40-Gb/s NRZ data, generated using an SHF 40-Gb/s bit-error-rate tester (BERT). This signal is then converted to RZ format using a pulse carver to shape the pulses. The measurements in this letter are performed using pseudorandom binary sequence (PRBS) $2^{31}-1$ data. The resulting signal in our setup has a pulsewidth of 11 ps. The input signal is split into two paths, which are delayed with respect to each other; this delay can be controlled in order to control the output pulsewidth from the TAO-WC. The two versions of the input data are amplified using EDFAs and filtered using 2-nm filters to remove ASE and then coupled into the device by using two lensed fibers mounted on piezo-controlled translation stages, to couple to the two input arms of the MZI. The typical coupling loss for our setup is 4 dB. The input signal is amplified by using SOAs to get the desired signal power into the SOA-MZI. These preamplifier SOAs are among the critical components in these devices. The slow gain recovery in the preamplifiers leads to pattern dependence that can severely hamper the device performance. It is, therefore, very important to minimize the pattern dependence introduced by the preamplifier SOAs. Our current device design has 600-μm-long preamplifiers; the length was chosen to minimize patterning due to saturation effects, while still getting sufficient output power to drive the MZI. Further optimization of the preamplifier design for integrated high-speed tunable wavelength converters is a current topic of our research. The operating point of the wavelength converter is optimized by selecting the relative delay and gain of the arms. With proper selection of the relative gain and delay between the arms to balance the phase change, we use the fast carrier depletion process to turn the MZI ON and OFF [3]. The output signal of the device is filtered using a 1.2-nm-wide filter to remove the input signal wavelength and then sent through a preamplified receiver, as shown in Fig. 3, to a 50-GHz photodetector. The BER measurements are performed using an SHF 40-GHz BERT.

III. Device Performance

The delay between the pulses greatly influences the performance of the wavelength converter. Enough delay is needed to allow the MZI to achieve enough differential phase swing in the switching window. If the delay is too small, then the phase swing in the switching window is low and the output signal power is reduced, leading to excessive power penalty. It is expected that to allow for maximum phase swing, the differential delay should be similar to the input pulsewidth. A longer delay will not cause a larger eye-opening but will increase the output pulsewidth, and hence power, also leading to an increased penalty. The differential delay was varied from 6.67 to 13.33 ps, and BER measurements were performed. Fig. 4(a) shows the BER curves obtained at different delay values. We see that as the delay is reduced below 10 ps, the BER curve tends to move away from the back-to-back. This can also be seen in Fig. 4(b), which shows the power penalty obtained at different differential delay. It can be seen that a delay of around 12 ps is optimal. As expected, the required differential delay correlates very well with our input pulsewidth of around 11 ps. A greater delay does

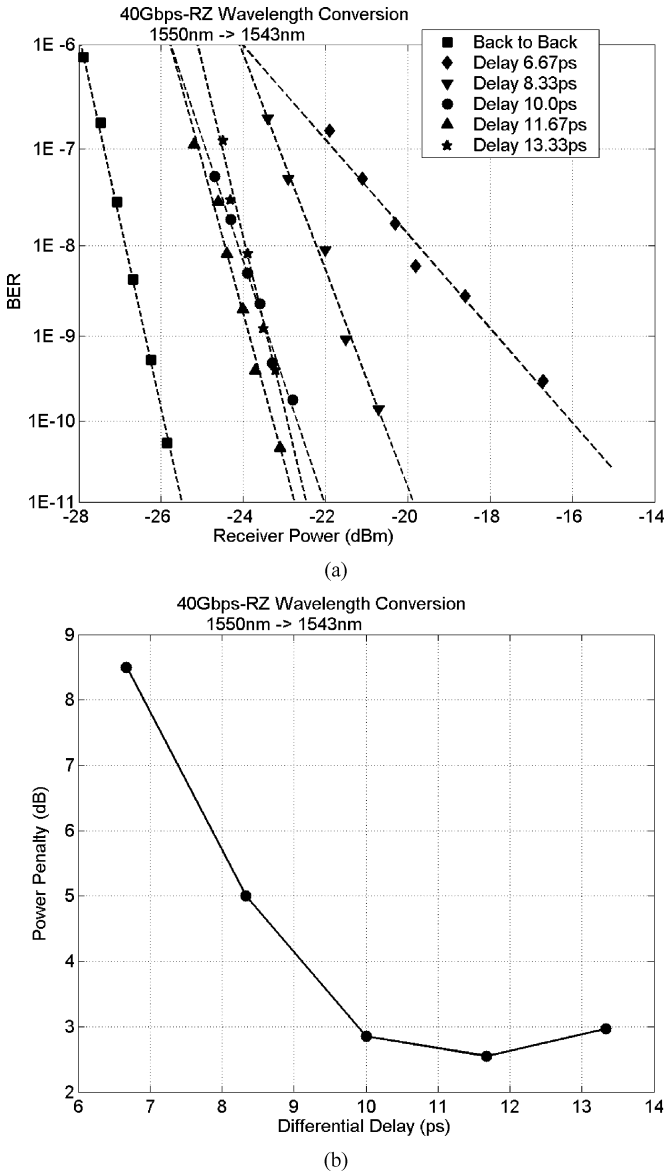

Fig. 4. (a) BER plots at 40-Gb/s operation for different differential delay. (b) Power penalty versus differential delay.

not cause any degradation, but as we move toward integrating the delay on-chip, we need to select the smallest possible delay to minimize the chip area and passive loss.

We also measured the performance of the device for different output wavelengths at 40-Gb/s data rates. The input power level required for our device was around 5 dBm in each input fiber and the output power was around -10 dBm in the output fiber. The OSNR of the output signal for a 1-nm optical bandwidth was 29 dB. The preamplifier SOAs were biased at around 80 mA to reduce the pattern effects and the MZI-SOAs were biased at 300 mA. We were able to operate the device from 1540 to 1565 nm, and obtain clear open eyes with an extinction ratio greater than 9 dB. Fig. 5 shows the output eye diagrams for a set of output wavelengths. The input wavelength was fixed at 1550 nm. The EDFAs and thin film filters in our device testing setup limited us to wavelengths below 1565 nm, even though the device itself can tune to wavelengths longer than 1565 nm.

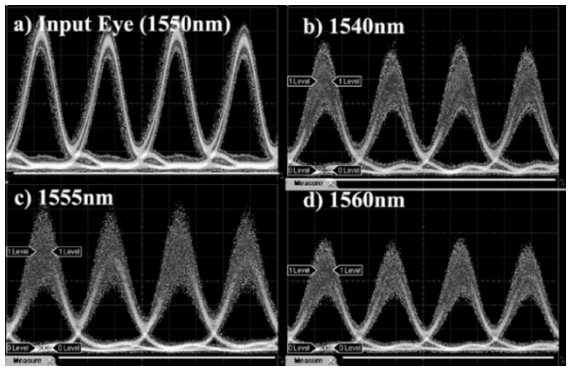

Fig. 5. A 40-Gb/s wavelength converter operation. (a) Input eye 1550 nm. (b)-(d) Converted eyes at different output wavelengths.

IV. Conclusion

In this letter, we demonstrated the 40-Gb/s operation of a monolithically integrated widely TAO-WC realized in an OQW platform. We characterized the effect of the differential delay and showed a power penalty, at $1E-9$ error rate, of less than 3 dB at the optimal delay. Error-free wavelength conversion was performed at 40-Gb/s RZ with an output extinction ratio $>$ 9 dB across a 25-nm output tuning.

The OQW platform allowed robust integration of active–passive components on-chip. This demonstration of high-speed wavelength conversion using OQW active-region-based devices and the characterization of the effect of the differential delay opens the way toward realizing more complex devices, both in terms of the integration process, and function. The next generation of these devices is currently being fabricated with the optimal delay integrated on-chip to realize a monolithic implementation.

References

[1] S. L. Danielsen, P. B. Hansen, and K. E. Stubkjaer, "Wavelength conversion in optical packet switching," *J. Lightw. Technol.*, vol. 16, no. 12, pp. 2095–2108, Dec. 1998.

[2] C. Joergensen, S. L. Danielsen, M. Vaa, B. Mikkelsen, K. E. Stubkjaer, P. Doussiere, F. Pommerau, L. Goldstein, and M. Goix, "40 Gbit/s alloptical wavelength conversion by semiconductor optical amplifiers," *Electron. Lett.*, vol. 32, pp. 367–368, 1996.

[3] B. Mikkelsen, K. S. Jepsen, M. Vaa, H. N. Poulsen, K. E. Stubkjaer, R. Hess, M. Duelk, W. Vogt, E. Gamper, E. Gini, P. A. Besse, H. Melchior, S. Bouchoule, and F. Devaux, "All-optical wavelength converter scheme for high speed RZ signal formats," *Electron. Lett.*, vol. 33, pp. 2137–2139, 1997.

[4] M. L. Nielsen, M. Nord, M. N. Petersen, B. Dagens, A. Labrousse, R. Brenot, B. Martin, S. Squedin, and M. Renaud, "40 Gbit/s standard mode wavelength conversion in all-active MZI with very fast response," *Electron. Lett.*, vol. 39, pp. 385–386, 2003.

[5] J. Leuthold, B. Mikkelsen, G. Raybon, C. H. Joyner, J. L. Pleumeekers, B. I. Miller, K. Dreyer, and C. A. Burrus, "All-optical wavelength conversion up to 100 Gbit/s with SOA delayed-interference configuration," in *26th Eur. Conf. Optical Communication*, vol. 3, 2000, pp. 119–20.

[6] M. L. Mašanović, V. Lal, J. A. Summers, J. S. Barton, E. J. Skogen, L. A. Coldren, and D. J. Blumenthal, "Design and performance of a monolithically-integrated widely-tunable all-optical wavelength converter with independent phase control," *IEEE Photon. Technol. Lett.*, vol. 16, no. 10, pp. 2299–2301, Oct. 2004.

[7] M. L. Mašanović, V. Lal, J. A. Summers, J. Barton, E. Skogen, L. Rau, L. Coldren, and D. Blumenthal, "Widely tunable monolithically integrated all-optical wavelength converters in InP," *J. Lightw. Technol.*, vol. 23, no. 3, pp. 1350–1362, Mar. 2005.

Demonstration of 40 Gbit/s optical packet synchronisation using fibre Bragg gratings and fast-tunable wavelength converters

C.-H. Chen, D. Wolfson, L.A. Johansson, D.J. Blumenthal and L.A. Coldren

A method of all-optical synchronisation is proposed and demonstrated at 40 Gbit/s. Based on pre-programmable fibre Bragg grating array and fast-switched widely-tunable wavelength converters, negligible power penalty is achieved up to 1 μs delay as well as 100% layer 2 throughput.

Introduction: All-optical packet switching networks [1] are becoming the solution of fast-growing telecommunication with the advantages of scalability and efficiency by reducing O/E/O conversion and higher available data rate beyond current electronic routing technologies. To ease the design of the key component, the optical packet switch, the incoming packets need to be aligned to a common time reference to eliminate the delay variations introduced by factors such as different routes in networks, fibre chromatic dispersion and thermal expansion in the links. The start of the arriving packet can be determined by a packet delineation function beforehand. Once the packet delineation has been carried out, the synchroniser can be configured by an electronic signal corresponding to the time difference between the arriving packet and the reference clock. In this Letter, a method of optical packet synchronisation based on fibre Bragg gratings (FBGs) combined with tunable wavelength converters (TWCs) [2–4] is proposed and demonstrated.

The configuration is shown in Fig. 1. A series of FBGs with different centre wavelengths are deployed along the fibre to form a wavelength-dependent delay line. The header part of the incoming packet is removed before the optical synchroniser. During synchronisation the payload is converted by a rapidly-tunable WC to one of the FBG centre wavelengths according to the required delay value. The outgoing delayed payload is then forwarded to the next switching stage where it is converted to a desired wavelength by the second TWC. Here we use an InP-based Mach-Zehnder interferometric wavelength converter monolithically integrated with a fast tunable SGDBR as characterised in [4, 5]. It has an output switching window of 6 ps, extinction ratio >9 dB, less than 4 dB power penalty at 10^{-9} BER and low pattern dependence across a 25 nm tuning range operating at 40 Gbit/s using RZ signals, which demonstrate its feasibility for this application.

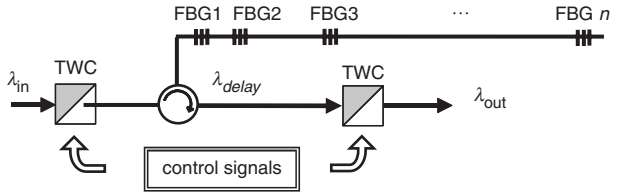

Fig. 1 *Schematic structure of optical packet synchroniser*

The proposed method benefits from low insertion loss and a long available maximum delay up to several microseconds because of the nature of optical fibre. It furthermore decreases the required number of spools for different delay values to potentially one. Also with the fast-switching widely-tunable wavelength converter, rapidly selectable [6] discrete delay values and a large number of channels are attainable. For the 200 GHz channel spacing used in this work, more than 20 channels in the C-band and more than 60 channels in C + L-band are achievable depending on the tuning range of the wavelength converter. Moreover by using interleavers, or 100 GHz channel spacing, the number of channels can be doubled. Note that it is not necessary that the channels are on the ITU grid since they are internal channels.

Experiments: For initial demonstration of functional feasibility at 40 Gbit/s, a configuration of four FBGs with 100 GHz reflection bandwidth and 200 GHz channel spacing serially connected to a three-port circulator was established. The fibre lengths between adjacent FBGs were designed with an exponential increment. Dispersion compensation fibre (DCF) of 345 m is added before FBG4 to compensate the non-negligible fibre dispersion. The delay of each FBG channel and its centre wavelength is listed in Table 1. Preliminary characterisation has also been reported in [7].

Table 1: Experiment results

	FBG1	FBG2	FBG3	FBG4
Centre λ	1553.55 nm	1550.22 nm	1551.91 nm	1558.88 nm
Time delay results				
Time delay to FBG1	0	0.029 μs	1.06 μs	10.47 μs
Fibre length to FBG1	0	2.9 m	106 m	1047 m
Short pulse input measurement				
Input T_{FWHM}	6.55 ps	6.02 ps	6.56 ps	8.07 ps
Output T_{FWHM}	10.25 ps	9.90 ps	10.17 ps	10.82 ps
Pulse spreading	3.7 ps	3.88 ps	3.61 ps	2.75 ps

The insertion loss can ultimately be reduced to the fibre transmission loss (< 0.2 dB/km) and the FBG reflectivity; with current bandwidth and channel spacing the crosstalk is below −25 dB which gives negligible passband loss. It enables realisation of large numbers of different delay values and thus resolution. The raised-cosine FBG weighting function provides a Gaussian-like reflected pulse with no apparent sidelobes in the time domain. The pulse spreading is measured to be less than 4 ps for the four channels. It is shown that the broadening effect in the first three FBGs is dominated by the filtering effect while in the case of FBG4 with long fibre it is dominated by the fibre dispersion due to non-perfect compensation. For a 6 ps pulse generated by the TWC [4], the delayed pulse was demonstrated to remain well within the 40 Gbit/s bit slot.

Bit error rate and layer 2 results: The bit error rate for the PRBS 40 Gbit/s RZ operation is measured with an SHF 50 Gbit/s BERT. Four sets of curves corresponding to four FBG channels and their back-to-back signals are shown in Fig. 2. Negligible power penalty is measured for the first three channels with a fibre distance up to 100 m (round trip 200 m). No obvious signal degradation is observed for FBG1, 2 and 3. However for FBG4 with longer fibre length a power penalty of less than 2 dB is measured. It is believed that this penalty can be eliminated if more careful dispersion management is used.

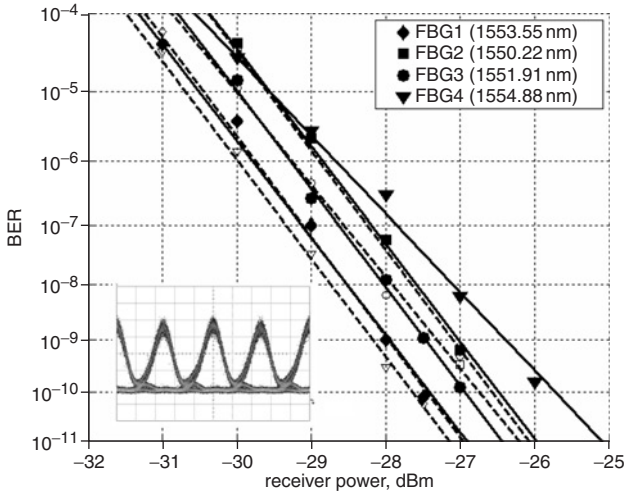

Fig. 2 *Bit error rate measurement for four FBGs*

Back-to-back signals (dashed lines) and FBG signals (solid lines) shown
Inset: Eye diagram for back-to-back signal at 1553.55 nm

To further understand the packet level recovery behaviour, a layer 2 measurement, which was defined in [8], is presented. The layer 2 measurement here is defined as capturing the payload stream and calculating how many payloads are captured. The received optical payload stream was stored in the BERT internal RAM, and then transferred to a personal computer for analysing by software. By calculating how many payloads are correctly captured, the payload recovery curves can be generated. The payload stream with 8 ns payload length and 100 ns guard band is uniquely identified by a 64-bit field as used in [8]. As shown in Fig. 3, 100% payload recovery

is possible for all four channels with proper optical power. It is noticeable that about 3 dB negative penalty at 90% recovery rate was measured. One possible cause of negative penalty is the spectral filtering effect for the reflection band of the FBGs. By looking at the BER curves in Fig. 2, owing to the slope difference between the back-to-back and FBG signal, it has a crossover at high bit error rate values for each channel as can be seen by extrapolating the curves. Also, according to previous experience it is inferred that the noise statistic has been changed for high error-rate range, thus different error-rate behaviour.

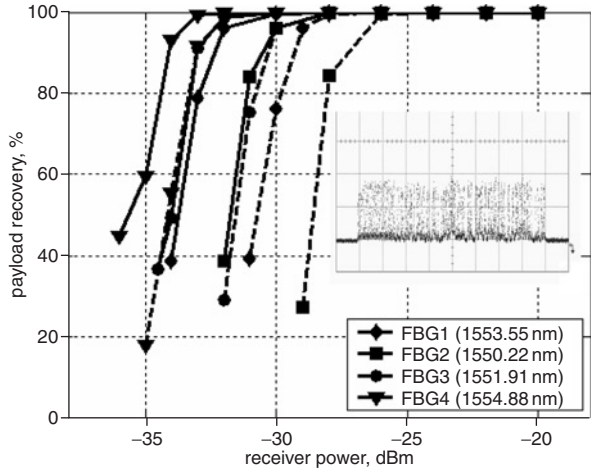

Fig. 3 *Layer 2 payload recovery measurements*

Recovery curves of back-to-back (dashed lines) and four FBG channels (solid lines) shown
Inset: Packet stream used in layer 2 measurements

Conclusion: An optical packet synchroniser with a large number of rapidly selectable discrete delay values, low insertion loss and long available maximum delay is established by the proposed method of using FBG array and fast-tunable wavelength converters. 40 Gbit/s RZ negligible power penalty up to 1 μs and <2 dB power penalty for more than 10 μs was obtained. Also, layer 2 packet recovery measurements show that 100% payload recovery is possible.

14 January 2006
Electronics Letters online no: 20060132
doi: 10.1049/el:20060132

C.-H. Chen, L.A. Johansson, D.J. Blumenthal and L.A. Coldren (*Department of Electrical and Computer Engineering, University of California at Santa Barbara, Santa Barbara, CA, USA*)

D. Wolfson (*IPITEK, Carlsbad, CA, USA*)

E-mail: janet@ece.ucsb.edu

References

1 Blumenthal, D.J., Bowers, J.E., Rau, L., Chou, H.-F., Rangarajan, S., Wang, W., and Poulsen, K.N.: 'Optical signal processing for optical packet switching networks', *IEEE Commun. Mag.*, 2003, **41**, (2), pp. 523–529
2 Sysak, M.N., Barton, J.S., Johansson, L.A., Raring, J.W., Skogen, E.J., Mašanović, M.L., Blumenthal, D.J., and Coldren, L.A.: 'Single-chip wavelength conversion using a photocurrent-driven EAM integrated with a widely tunable sampled-grating DBR laser', *IEEE Photonics Technol. Lett.*, 2004, **16**, (9), pp. 2093–2095
3 Mašanović, M.L., Lal, V., Summers, J.A., Barton, J.S., Skogen, E.J., Coldren, L.A., and Blumenthal, D.J.: 'Design and performance of a monolithically-integrated widely-tunable all-optical wavelength converter with independent phase control', *IEEE Photonics Technol. Lett.*, 2004, **16**, (10), pp. 2299–2301
4 Lal, V., Mašanović, M.L., Summers, J.A., Coldren, L.A., and Blumenthal, D.J.: '40 Gbps operation of an offset quantum well active region based widely-tunable all-optical wavelength converter'. Optical Fiber Communication Conf., Anaheim, CA, USA, 2005
5 Lal, V., Mašanović, M.L., Wolfson, D., Poulsen, H.N., Fish, G., Coldren, C., and Blumenthal, D.J.: 'Monolithic widely tunable optical packet forwarding chip in InP for all-optical label switching with 40 Gbps payloads and 10 Gbps labels'. ECOC'05, PDP, 2005, pp. 25–26
6 Simsarian, J.E., Bhardwaj, A., Gripp, J., Sherman, K., Su, Y., Webb, C., Zhang, L., and Zirngibl, M.: 'Fast switching characteristics of a widely tunable laser transmitter', *IEEE Photonics Technol. Lett.*, 2003, **15**, (8)
7 Chen, C.-H., Johansson, L.A., Lal, V., Mašanović, M.L., Blumenthal, D.J., and Coldren, L.A.: 'Programmable optical buffering using fiber Bragg gratings combined with a widely-tunable wavelength converter'. Optical Fiber Communication Conf., Anaheim, CA, USA, 2005
8 Wolfson, D., Lal, V., Mašanović, M., Poulsen, H.N., Coldren, C., Epps, G., Civello, D., Donner, P., and Blumenthal, D.J.: 'All-optical asynchronous variable-length optically labeled 40 Gbps packet switch'. ECOC'05, PDP, 2005

III. MBE Technology & Devices

A. GaAs-based Vertical-Cavity Lasers and Technology

Accurate carbon doping system for low-voltage and low-loss VCSELs

Y.-C. Chang, C. S. Wang, J. H. English, and L.A. Coldren
ECE and materials departments, University of California, Santa Barbara

As the performance of microprocessors keeps increasing, new interconnect architecture with higher bandwidth capacity will be required. Optical interconnects can meet this demand and vertical cavity surface emitting lasers (VCSEL) are ideal for optical interconnects because they have small footprint, can be easily made into arrays, and have higher bandwidth at lower power. However, existing VCSELs do not have the efficiency and necessary bandwidth when formed with small dimensions. The drive voltages need to be reduced without adding undue optical losses. Here we report a new wide-range carbon doping system that incorporates a temperature-controlled CBr_4 source, a variable leak valve to control the doping level, and run/vent valve switches. Low voltage, small diameter 980 nm VCSELs have been grown by molecular beam epitaxy using the improved carbon doping system. The VCSELs have three InGaAs/GaAs quantum wells and a tapered oxide aperture in the cavity. The top mirror is a 30 period carbon-doped distributed Bragg reflector (DBR) and the bottom mirror consists of a 4 period section silicon-doped DBR on top of a 3/4 wavelength n-contact layer, followed by 14 periods of undoped DBR. Because carriers have to propagate through the DBRs, these AlGaAs/GaAs interfaces have to be bandgap-engineered with special grading and doping schemes to eliminate the hetero-barriers, especially for the p-type DBRs because of the low mobility of holes. This imposes stringent requirements on the accuracy of doping in the 10^{17}~10^{18} cm^{-3} range typically used in p DBRs. On the other hand, very high doping in the 10^{20} cm^{-3} range is needed for the contact layer. The temperature of CBr_4 in our system is controlled by a custom-designed system using thermoelectric coolers (TEC). When the p-DBRs were grown, the CBr_4 temperature was kept at -25 °C for better control of the doping levels. The p-contact layer was then grown at -10 °C to reach 10^{20} cm^{-3} doping. With this TEC controlled approach, accurate doping and wide doping ranges can be realized simultaneously. The VCSELs grown with this carbon doping system have very low threshold voltage of 1.55 V, only 300 mV above the lower limit defined by the quasi-Fermi level separation. These devices show constant differential efficiencies of 75 % from 10 μm to 1 μm aperture diameter devices, which indicates tapered oxide aperture can effectively eliminate the optical diffraction loss [1]. With low voltage, hence low electrical dissipation, and high differential efficiency, wall-plug efficiencies are maximized. The wall-plug efficiency for 1 μm diameter devices is 33 % and maximum 40 % is achieved in 3.5 μm devices. The highest bandwidth achieved is 16 GHz for 2.5 μm aperture devices.

[1] E. R. Hegblom et al., IEEE J. Select. Topics Quantum Electron., vol 5, pp 553-560, 1999.

Quantum Dot Spontaneous Emission Lifetime Modification in Optical Microcavities using Oxide Apertured Micropillars

N. G. Stoltz, M. Rakher, S. Strauf, D. Bouwmeester, P. M. Petroff, and L. A. Coldren.
University of California, Santa Barbara, CA 93106.

ABSTRACT

An oxide aperture is used to confine optical modes in a micropillar structure. This method overcomes the limitations due to sidewall scattering loss typical in semiconductor etched micropillars. High cavity quality factors (Q) up to 48 000 are determined by external Fabry-Perot cavity scanning measurements, a significantly higher value than prior work in III-V etched micropillars. Measured Q values and estimated mode volumes correspond to a maximum Purcell factor figure of merit value of 72. A Purcell Factor of 2.5 is experimentally observed from a single quantum dot emitter coupled to a high Q cavity mode.

Keywords: Micropillars, Microcavities, Quantum Dots, Purcell Effect, Quantum Dot-Microcavity Coupling, Time Correlated Photon Counting.

1. INTRODUCTION

Optical microcavities combined with active emitters provide a great opportunity to study the light-matter interaction at a fundamental level. To produce a high quality microcavity it is necessary to confine light to precise resonance frequencies with little or no optical loss [1]. The measure of this optical confinement is referred to as the cavity quality factor (Q). In order to increase the coupling between an emitter and mode in a cavity it is also important to reduce the effective optical mode volume (V_{eff}). When an optical emitter is both spatially and spectrally coupled to a high quality microcavity, the Purcell Effect is observed [2]. The Purcell Effect is experimentally observed through the modification of active emitter spontaneous emission lifetimes. In the weak coupling regime, the spontaneous emission lifetime of an emitter coupled to a microcavity is decreased by the Purcell Factor [2]. The Purcell Factor is proportional to the ratio of Q/V_{eff} and includes factors accounting for both spatial and spectral detuning of the emitter with respect to the cavity. Potential applications include solid state quantum electrodynamics (CQED) experiments, modification of single emitter lifetimes, and single photon emitters and detectors for quantum cryptography [1, 2].

1.1 III-V Semiconductor Microcavity Architectures

Several solid-state microcavity architectures including microdisks [3, 4], photonic crystals [5, 6, 7], and micropillars [8, 9] have shown CQED effects in III-V micropillars using self-assembled quantum dots (QD's) as active emitters. The Purcell Effect has been experimentally observed in each of these microcavity architectures. Microdisks have shown coupled QD lifetimes of 370 ps corresponding to a Purcell Factor of 3.5 [3]. Photonic crystals and micropillars have both shown QD lifetimes of 200 ps corresponding to a Purcell Factor of 5 [6, 8]. In addition all three architectures have exhibited the transition from the weak to strong coupling regime [4, 7, and 9].

Among these architectures, micropillars couple light normal to the semiconductor in a single lobed Gaussian pattern that is easily fiber coupled [10]. This high photon collection efficiency makes micropillars a better alternative for device applications. However, micropillars exhibit higher V_{eff} ($\sim 5\ (\lambda/n)^3$) and lower Q's (~2000-10 000) when compared with photonic crystals [1, 9]. These V_{eff} can be reduced by decreasing pillar diameter, but scattering losses due to sidewall roughness have been shown to limit achievable Q values [1, 11].

1.2 Oxide Aperture Micropillars

An alternative approach using oxide apertured micropillars to reduce V_{eff} while maintaining high Q values has been previously shown [12]. Oxidized micropillars have been used for vertical cavity laser (VCL) applications to produce low threshold laser devices that are fabricated into inexpensive arrays for optical data networks [13]. By confining the

Laser Beam Control and Applications, edited by Alexis V. Kudryashov, Alan H. Paxton, Vladimir S. Ilchenko, Adolf Giesen, Detlef Nickel, Steven J. Davis, Michael C. Heaven, J. Thomas Schriempf,
Proc. of SPIE Vol. 6101, 61010W, (2006) · 0277-786X/06/$15 · doi: 10.1117/12.669580

optical mode with a laterally oxidized aperture layer these structures simultaneously provide optical mode and electrical current confinement while eliminating the scattering loss due to sidewall roughness inherent to etched pillar structures.

This method has been applied to the field of QD-microcavity coupling with limited success due to very low Q's (<1000) as well as high V_{eff} (~35 $(\lambda/n)^3$) when compared with conventional micropillars [14, 15]. Oxidized micropillars have shown QD lifetimes of 900 ns corresponding to a Purcell factor of 2 [14]. If these values are improved, the advantages in ease of fabrication will make oxide apertured micropillars very attractive for coupled QD-microcavity device applications.

2. SAMPLE DESIGN AND FABRICATION

Micropillar samples investigated in this study were grown by molecular beam epitaxy on a semi-insulating GaAs (100) substrate with a 0.1 μm buffer layer. There are four independent sections in the structure: the bottom mirror, the active region, the aperture region, and the top mirror as shown schematically in Fig. 1(a). Mirrors consist of alternating one quarter optical thickness distributed Bragg reflector (DBR) layers of GaAs and $Al_{0.9}Ga_{0.1}As$. 32 pairs of $Al_{0.9}Ga_{0.1}As$/GaAs layers with thicknesses of 79.8/68.4 nm respectively form the bottom DBR mirror, while the top DBR mirror is made of 23 pairs. The active region is one optical wavelength in thickness, with two 135.4 nm layers of GaAs embedding a centered InGaAs/GaAs QD layer. QD's self-assemble during epitaxy operating in the Stranski-Krastanov growth mode. InGaAs islands are partially covered with GaAs and annealed before completely capped with GaAs. This procedure blue shifts the QD's emission wavelengths toward the spectral region where Si-based detectors are more efficient [16]. The thickness of the aperture region is three quarters optical wavelength and consists of a pure AlAs layer sandwiched by $Al_{0.89}Ga_{0.11}As$ and $Al_{0.75}Ga_{0.25}As$ in order to produce the desired oxide aperture qualities. It is designed to give a change in effective index, Δneff = 0.08, between the fully oxidized and unoxidized regions of the micropillar in addition to a linear oxide taper with a length of 1.1 μm after an approximate 10 μm oxidation.

A scanning electron microscopy (SEM) image of a fabricated oxide apertured microcavity is shown in Fig. 1(b), while Fig. 1(c) shows a cross-sectional SEM image of an oxidized mesa calibration sample with mirror, active, and aperture regions corresponding to Fig. 1(a). Samples are fabricated by optical lithography and reactive ion etch (RIE) in Cl_2 plasma penetrating approximately 5 mirror periods into the bottom DBR. Micropillars are fabricated in large arrays with diameters varying from 21-25 μm. The wet lateral oxidation is performed at 430˚C in order to oxidize the aperture region by converting AlAs into Al_xO_y.

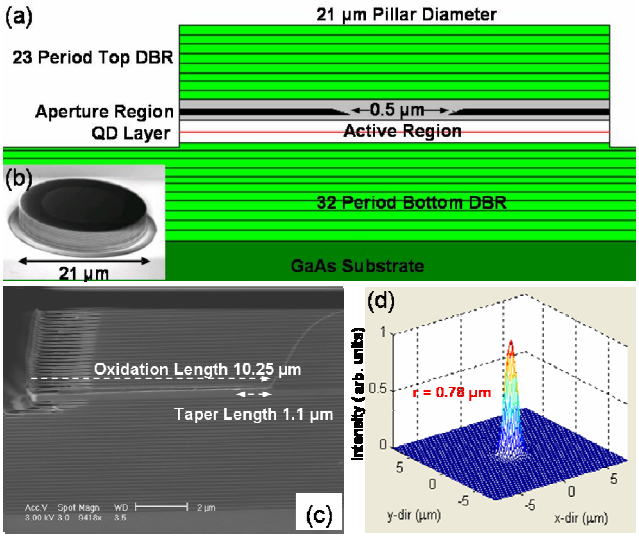

Figure 1 (a) Schematic and layer structure for the oxide apertured micropillars in this study. (b) SEM image of a fully processed 21 μm micropillar. (c) SEM cross-section image of an oxidized mesa calibration showing actual layer structure depicted in (a). (d) The theoretical fundamental mode profile for the 21 μm micropillar modeled in this study with a Gaussian mode radius of 0.78 μm.

3. EXPERIMENTAL SETUP

Micro-photoluminescence (μ-PL) measurements are performed using a He-flow cryostat (4-300K). QD's are excited non-resonantly by a continuous wave 780 nm laser diode focused to a spot size of 2.5 μm using a microscope objective with numerical aperture of 0.55. μ-PL emission is collected through the same objective and recorded with a 1.25 m spectrometer equipped with a charge-coupled device with 30 μeV spectral resolution at 900 nm.

A scanning Fabry-Perot cavity along with a single photon counting avalanche photodiode detector and an integrated counting unit are used to experimentally determine linewidths beyond the resolution of the spectrometer.

Lifetime traces of single QDs are taken by time-correlated photon counting (TCPC) using a Ti:Sa laser operated at 780 nm with a repetition rate of 82Mhz for excitation and a single photon counting avalanche diode for detection. Second order coherence functions are measured by passing the signal through two single photon counting avalanche photodiodes in a Hanbury-Brown and Twiss setup. Measuring the difference in arrival time between photons at each of the two detectors provides a measure of the second order correlation function [17].

Table I.

21μm Pillar Fundamental Mode	
Modeling Parameters	
n_{core}	3.12
Δn	0.081
Core Width (μm)	0.5
Taper Length (μm)	1.1

Simulation Results	
L_{eff} (μm)	1.39
α_{rad} (cm^{-1})	1.66e-3
α_{scat} (cm^{-1})	1.66
α_{m} (cm^{-1})	13.86
Γg_{th} (cm^{-1})	14.69
λ (nm)	914.36
Q_{cold}	14 480
$V_{eff}[(\lambda/\mathrm{n})]^{-3}$	51
Γ	3.65e-3

Experimental Results	
λ (nm)	914.11
$Q_{\exp}$	48 000
F_p	72
$\Gamma g_{\exp}$ (cm^{-1})	10.44

Table I. Simulation parameters, theoretical results, and experimental values are given for the fundamental mode of the 21 μm diameter micropillar in this study.

4. MODELING THE CAVITY

A two-dimensional model of the cavity has been developed based on the experimentally determined values for the oxide aperture taper length and core width from SEM images (Fig. 1) along with the one-dimensional reflectivity spectrum of the unprocessed sample. This produces a two-dimensional index profile determined by the effective index (n_{eff}) in the growth direction for the unoxidized and oxidized layer stack. The Δn_{eff} between the unoxidized and oxidized regions is evaluated by replacing the AlAs and $Al_{0.89}G\ a_{0.11}As$ with Al_xO_y (n=1.5). It has been demonstrated [18] that the linear oxide taper shown in Fig. 1(c) corresponds to a parabolic index grade over the length of the taper.

We used this model to solve for the eigenmodes of the two-dimensional scalar wave equation using a finite difference technique with a non-uniform mesh [19]. The solution for the fundamental mode of a 21μm pillar (with parameters given in Table 1) is shown in Fig. 1(d) and has a Gaussian mode radius of approximately 0.78 μm. Scattering and radiation losses are determined by propagating a scalar field around the unfolded cavity until the field no longer changes shape. This procedure is analogous to the classic work of Fox and Li [20].

Mirror, scattering, and radiation losses determine the empty or cold cavity linewidth of the apertured micropillar. Assuming that undoped AlGaAs regions have no internal optical loss at 4K, the only optical loss mechanisms in the cavity are due to mirror loss (α_m), radiation loss (α_{rad}), and aperture scattering losses (α_{scat}) [19]. Furthermore, α_{rad} and α_{scat} are very small for the fundamental mode, 1.66e-3 and 1.66 cm^{-1} respectively. This leaves photon escape through the top DBR mirror as the dominating loss mechanism in the cavity; here α_m is calculated as 13.86 cm^{-1}. Cold cavity (Q_{cold}) values are determined by these cavity losses according to $\frac{\omega}{Q_{cold}} = \frac{1}{\tau_p} = v_g \Gamma g_{th} = v_g (\alpha_{scat} + \alpha_{rad} + \alpha_m)$ [19]. Here τ_p is cavity lifetime, v_g is group velocity, ω is frequency, Γ is the confinement factor, and g_{th} is the threshold material gain. The estimated Q_{cold} for a 21 μm micropillar is 14 480. Other theoretical values for various parameters are given in Table 1 for a 21μm micropillar.

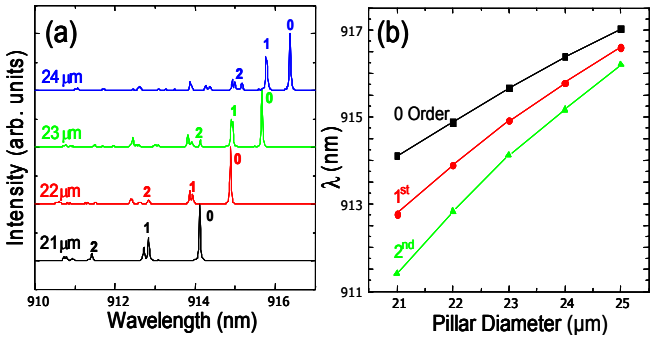

Figure 2 (a) Normalized optical mode spectra for 21-25 um micropillars measured by μ-PL at 4 K are shown. Fundamental, first, and second order modes are labeled by numbers 0, 1, and 2 respectively. (b) Mode position in nm is shown as a function of pillar diameter for fundamental, first, and second order modes.

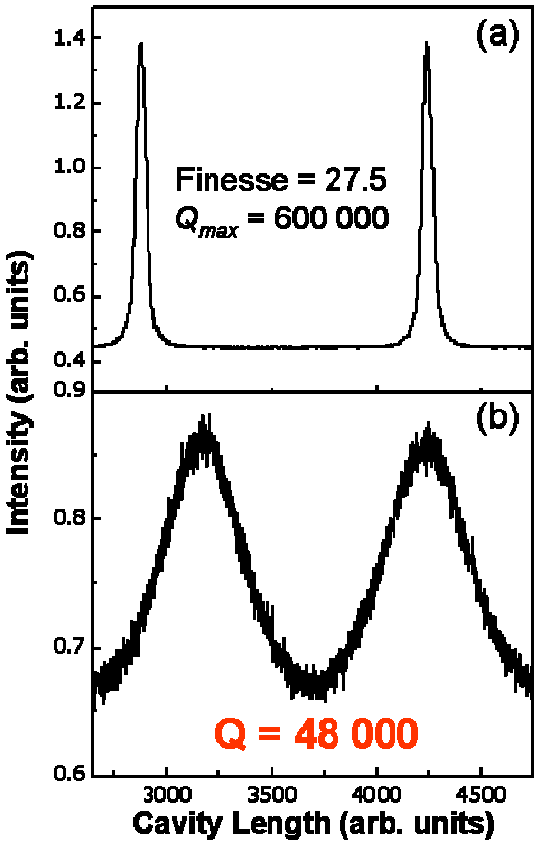

Figure 3 (a) Transmission through a Fabry-Perot cavity as a function of cavity length for a reference laser. Using the given free spectral range of the measurement cavity, the reference laser has Q > 600000 giving a maximum measurable Q. (b) The Fabry-Perot measurement of the fundamental mode linewidth of a 21 μm micropillar cavity. The measured linewidth corresponds to Q > 48000. This measurement was done at 50 μW pump power at 4 K.

5. EXPERIMENTAL MODE SPECTRA

Experimental mode spectra for 21-25μm diameter pillars are shown in Fig. 2(a). Mode orders 0, 1, and 2 are labeled in Fig. 2(a). The lifting of higher order mode degeneracy is due to asymmetry in the fabrication process. μ-PL data shows cavity modes with lower fundamental energies as well as increasing mode spacing as pillar diameter decreases. This effect is shown in Figure 2(b) for varying pillar diameters. In addition, intensity decreases are observed for higher order modes due to increased scattering losses, an intentional effect produced by the oxide aperture and the larger effective radii of multi-lobed higher order modes.

A Fabry-Perot scanning cavity is used to determine experimental Q values. First a reference laser is used to calibrate the maximum measurable Q for the Fabry-Perot cavity as 600 000, shown in Fig. 3(a). The fundamental cavity mode is then directed through a 1 nm bandpass filter into the detector for sample measurement. Experimental quality factor (Q_{exp}) is determined to be approximately 48 000 for a 21 μm pillar as shown in Fig. 3(b). This value is larger than the theoretical cold cavity value due to linewidth narrowing caused by modal gain from the QD active region. The gain in the QD active region (g_{exp}) is determined by the relationship between Q_{cold} and Q_{exp} values according to

$$\frac{\omega}{Q_{\exp}} = \frac{\omega}{Q_{cold}} - v_g \Gamma g_{\exp}$$ [19]. Estimated gain values are shown in Table I.

Q values show little change with increasing pump power and no laser threshold behavior is observed up to 50 μW pump power. This indicates that material gain in the QD layer saturates before the threshold condition is achieved. Estimated values show that g_{exp} in the QD active region saturates at approximately 10.44 cm^{-1}, corresponding to approximately 2864 cm^{-1} material gain from the active region. This is a reasonable value for the single QD layer in this cavity design [21].

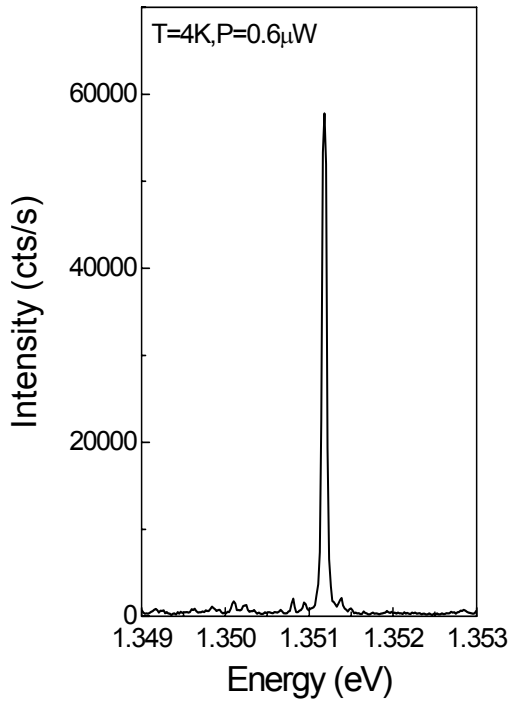

Figure 4. Optical spectra of device G7 taken at low pump powers of 600 nW at 4K. The spectra shows sharp resolution limited transition lines.

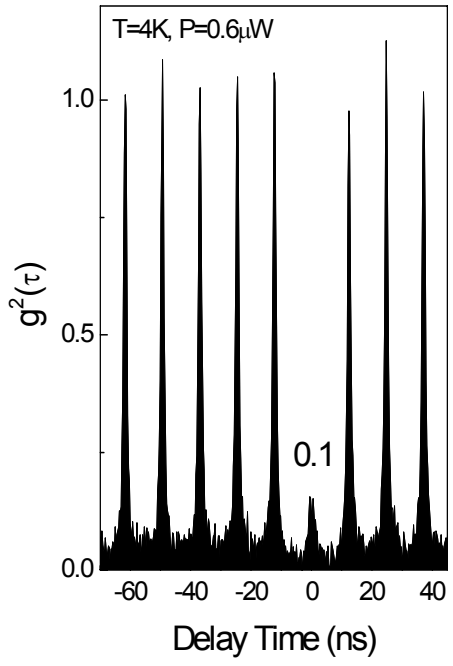

Figure 5. Second order coherence as a function of delay time for device G7 showing pronounced photon antibunching. The zero delay time peak area is ~10 % with respect to the sidepeak areas. This is indicative of a single photon emitter.

6. EXPERIMENTAL OBSERVATION OF THE PURCELL EFFECT

The Purcell factor determines the figure of merit for a coupled QD-microcavity in the weak coupling regime. Using theoretical V_{eff} and experimental Q_{exp} values it is possible to estimate the maximum achievable F_p according to $F_p = \frac{3}{4\pi^2}\frac{Q\left(\lambda/n_{eff}\right)^3}{V_{eff}}$ [22]. Experimentally observed values are decreased due to spectral and spatial detuning. Estimating the Purcell factor with experimental linewidths gives a maximum value of 72.

The experimental spectra for a QD coupled to a fundamental cavity mode for 21 μm oxidized micropillar device G7 is shown in Fig. 4. This device exhibits sharp resolution limited modes at approximately 1.351 eV under low excitation powers of 0.6 μW. The second order coherence function shows that this spectrum is due to single QD emission as shown in Fig. 5. Multiple non-interacting QD emitters show a zero delay time peak ≥ 0.5, while single QD emitters show a zero delay time peak ≤ 0.5. Here the zero delay time peak is approximately 10% with respect to the sidepeaks. This corresponds to a 10 times decrease in multiphoton emission events if compared to an attenuated laser (Poissonian) light source and is indicative of a single photon source.

TCPC lifetime traces of this device are shown in Fig. 5. QD spontaneous emission lifetimes of 440 ps are observed. A reference QD lifetime from a sample without a cavity exhibits spontaneous emission lifetimes of 1100 ps. This corresponds to a Purcell factor of approximately 2.5 when compared to the reference QD. Maximum achievable Purcell effects are limited due to the random spatial position of the QDs with respect to the cavity mode.

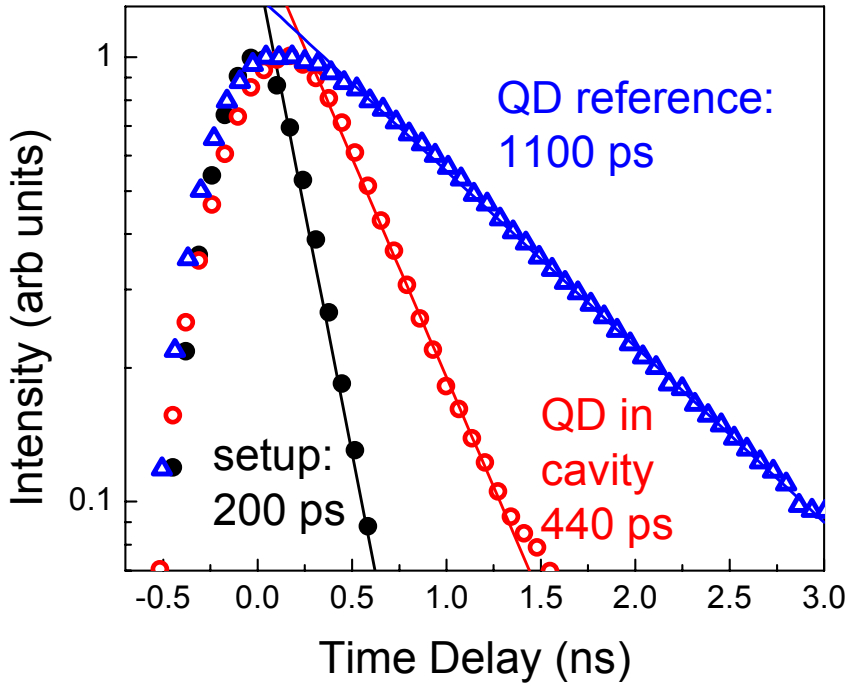

Figure 6. Lifetime traces of single QDs taken by time-correlated photon counting (TCPC) using a Ti:Sa laser operated at 780 nm with a repetition rate of 82Mhz for excitation and a single photon counting avalanche diode for detection. Data have been taken for a reference sample without a cavity (open blue triangles) and for a typical single QD spectrally tuned into resonance with a micropillar cavity mode (open red circles). The black circles are the system response for a short laser pulse illustrating the timing resolution of the setup of 200 ps.

7. CONCLUSIONS

Oxidized micropillars have a promising outlook for QD-microcavity coupling due to high Q values. Further improvement for these devices could be achieved by reducing V_{eff}. Although oxide aperture micropillars reduce two dimensional mode areas while maintaining high Q values, V_{eff} remains relatively high. This is due to the large effective cavity length (L_{eff}) in the growth direction of this structure, approximately 1.39 μm. Improvement lies in reducing this L_{eff} value, potentially by replacing AlGaAs/GaAs DBR mirrors with Al_xO_y/GaAs DBR mirrors having reduced mirror penetration depths.

The observed Purcell factor of 2.5 is smaller that the theoretical maximum value of 72. This is due to spatial detuning of the QD emitter with respect to the cavity mode. Micropillars are fabricated on a random array of quantum dots. When the QD emitter is not spatially aligned to an electric field maximum of the cavity mode a corresponding decrease in the Purcell Effect occurs. This spatial detuning may potentially be overcome by developing active positioning schemes that fabricate pillars around known QD candidates.

Experimental data shows very high Q (48 000) optical microcavities using an oxide apertured micropillar architecture. Devices exhibit controlled mode positions and sizes down to core widths of approximately 0.5 μm. Unlike etched air interface micropillars, which can be difficult to fabricate with acceptable loss values at smaller diameters, apertured micropillars accomplish this in a controllable and repeatable fashion. Cavities exhibit low loss values resulting from gain related linewidth narrowing effects due to stimulated emission from the QD active region. Apertured micropillars show promise for QD-microcavity coupling applications due to these high experimental Q values producing a maximum Purcell factor of 72. A Purcell Factor of approximately 2.5 is experimentally observed in a single QD emitter coupled to a cavity mode.

REFERENCES

[1] J. M. Gerard, in *Single Quantum Dots: Fundamentals, Applications, and New Concepts*, edited by P. Michler (Springer, Berlin, 2003), Vol. **90**, Chap. 4, p.269-314.

[2] K. J. Vahala, Nature **424**, 839 (2003).

[3] A. Kiraz, P. Michler, C. Becher, B. Gayral, A. Imamoglu, L. Zhang, W. V. Schoenfeld, and P. M. Petroff, Appl. Phys. Lett. **78**, 3932 (2001).

[4] E. Peter, P. Senellart, D. Martou, A. Lemaitre, J. Bloch, J. Hours, and J. M. Gerrard, in preparation (available at http://xxx.lanl.gov/abs/quant-ph/0411076).

[5] T. D. Happ, I. I. Tartakovski, V. D. Kulakovskii, J. –P. Reithmaier, M. Kamp, and A. Forchel, Phys. Rev. B **66**, 041303 (2002).

[6] A. Badolato, K. Hennessy, M. Atature, J. Dreiser, E. Hu, P. M. Petroff, and A. Imamoglue, Science **308**, 1158 (2005).

[7] T. Yoshie, A. Scherer, J. Hendrickson, G. Khitrova, H. M. Gibbs, G. Rupper, C. Ell, O. B. Shchekin, and D. G. Deppe, Nature **432**, 200 (2004).

[8] J. Vuckovic, D. Fattal, C. Santori, G. S. Solomon, and Y. Yamamoto, Appl. Phys. Lett. **82**, 3596 (2003).

[9] J. P. Reithmaier, G. Sek, A. Loffler, C. Hormann, S. Kuhn, S. Reitzenstein, L. V. Keldysh, V. D. Kulakovski, T. L. Reinecke, and A. Forchel, Nature **432**, 197 (2004).

[10] M. Pelton, J. Vukovic, G. S. Solomon, A. Scherer, and Y. Yamamoto, IEEE J. Quantum Electron. **38**, 170 (2002).

[11] T. Rivera, J. –P. Debray, J. M. Gerard, B. Legrand, L. Manin-Ferlazzo, and J. L. Oudar, Appl. Phys. Lett. **74**, 911 (1999).

[12] N. G. Stoltz, M. Rakher, S. Strauf, A. Badolato, D. Lofgreen, P. M. Petroff, L. A. Coldren, and D. Bouwmeester, Appl. Phys. Lett. **87**, 031105 (2005).

[13] L. A. Coldren, H. Temkin, and C. W. Wilmsen, *Vertical-Cavity Surface-Emitting Laser*, **First** edition (Cambridge University Press, Cambridge, UK, 1999), Vol. **1**, Chap. 1, p.1.

[14] L. A. Graham, D. L. Huffaker, and D. G. Deppe, Appl. Phys. Lett. **74**, 2408 (1999).

[15] D. G. Deppe, L. A. Graham, and D. L. Huffaker, IEEE J. Quantum Electron. **35**, 1502 (1999).

[16] P. M. Petroff, A. Lorke, and A. Imamoglu, Physics Today **54**, 46 (2001).

[17] B. D. Gerardot, S. Strauf, M. J. A. de Dood, A. M. Bychkov, A. Badolato, K. Hennessy, E. L. Hu, D. Bouwmeester, and P. M. Petroff, Phys. Rev. Lett. **95**, 137403 (2005).

[18] E. R. Hegblom, N. M. Margalit, A. Fiore, and L. A. Coldren, IEEE J. Sel. Top. Quantum Electron. **5**, 553 (1999).

[19] Larry A. Coldren and Scott W. Corzine, in *Diode Lasers and Photonic Integrated Circuits*, **First** edition, edited by Kai Chang (John Wiley & Sons, INC., New York, 1995), Vol. **1**, Ch. 16 Apps. 4,16, pp. 188,226,444,563-567.

[20] A. G. Fox and T. Li, Bell Sys. Tech. J. **40**, 453 (1961).

[21] S. Schneider, P. Borri, W. Langbein, U. Woggon, R. L. Sellin, D. Ouyang, and D. Bimberg, IEEE J. Quantum Electron. **40**, 1423 (2004).

[22] E. M. Purcell, Phys. Rev. **69**, 681 (1946).

High-efficiency, high-speed VCSELs with deep oxidation layers

Y.C. Chang, C.S. Wang, L.A. Johansson and L.A. Coldren

A novel method to reduce the parasitics of vertical-cavity surface-emitting lasers (VCSELs) using deep oxidation layers is proposed. Using this method, high-efficiency, high-speed 980 nm, tapered-aperture VCSELs with a −3 dB frequency of 17.9 GHz, the highest bandwidth without using proton implantation, are demonstrated.

Introduction: High-efficiency, high-speed VCSELs are in high demand for optical interconnects because they have small footprints, dissipate less power, can be easily fabricated into arrays, and are cost effective. The bandwidth of a VCSEL is determined by the intrinsic laser properties as well as the extrinsic parasitics. Various methods have been proposed to lower the parasitics so that the modulation bandwidth can reach the laser intrinsic limit [1–4]. Proton implantation is widely used to kill the parasitic capacitance associated with the thin oxide aperture capacitance and junction capacitance. The highest two VCSEL modulation bandwidths reported are 21.5 [4] and 20 GHz [5] and they were both proton-implanted. Proton implantation significantly complicates the fabrication since very thick mask is needed to block the high energy protons, e.g. 6 μm-thick photoresist is needed to block 300 keV protons which penetrate ~2.5 μm in $Al_{0.5}Ga_{0.5}As$ [6]. In this Letter, we propose a new method to reduce the parasitic capacitance using deep oxidation layers. By increasing the aluminium fraction of the first several *p*-distributed Bragg reflectors (DBRs), deep oxidation layers can be formed simultaneously with the oxide aperture. These deep oxidation layers increase the equivalent capacitor thickness, thus reducing the capacitance. This method is simple and the fabrication remains unchanged. Using this method, we demonstrate high-efficiency, high-speed 980 nm VCSELs with differential efficiency up to 68%, peak wall-plug efficiency of 37%, and modulation bandwidth of 17.9 GHz.

Device structure and fabrication: Fig. 1 shows the schematic cross-section of the VCSEL. The sample was grown on a semi-insulating GaAs (100) substrate by molecular beam epitaxy. The bottom mirror consists of a 14-period undoped GaAs/AlAs DBR, followed by a five-quarter wavelength thick silicon-doped *n*-contact layer, and a 4-period *n*-type $GaAs/Al_{0.9}Ga_{0.1}As$ DBR. The highly-doped *n*-contact layer is placed four periods away from the cavity to lower the optical loss as well as to reduce the effective cavity length for high speed consideration. The active region has three InGaAs/GaAs quantum wells embedded in a $Al_{0.3}Ga_{0.7}As$ separate confinement heterostructure layer. The oxide aperture consists of 100 Å AlAs followed by 1430 Å $Al_{0.82}Ga_{0.18}As$ in order to form a tapered tip. The lens-like effect of this tapered aperture decreases optical losses for increased efficiency [7]. The top mirror consists of a 30-period carbon-doped GaAs/AlGaAs DBR, followed by a highly-doped *p*-contact layer. The aluminium fraction of the first two periods of the DBRs is increased from 85 to 93% in order to form the deep oxidation layers. This also increases the refractive index contrast, and, consequently, reduces the mode volume.

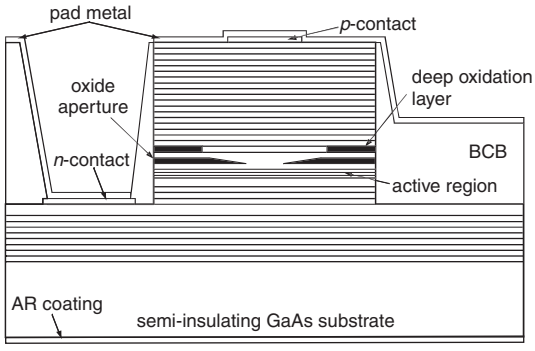

Fig. 1 *Schematic cross-section of VCSEL*

The fabrication began by etching cylindrical mesas ranging from 20.5 to 30 μm in diameter down to the *n*-contact layer using reactive ion etch. The oxide apertures were then formed by wet oxidation, resulting in a ~8 μm oxidation depth with a 4.5 μm taper length from either side. The two deep oxidation layers above the oxide aperture were formed simultaneously as shown in the SEM in Fig. 2. The two $Al_{0.93}Ga_{0.07}As$ layers oxidised 4.2 μm in depth, 3 μm deeper than the rest of the $Al_{0.85}Ga_{0.15}As$ layers. Ti/Pt/Au and AuGe/Ni/Au were evaporated for *p*- and *n*-contacts, respectively. Benzocyclobutene (BCB) was applied, patterned to open windows, and fully cured. The BCB was used for planarisation, passivation, and capacitance reduction purposes. Ti/Au was then deposited on top of BCB as pad metal. Finally, an antireflection coating was deposited to reduce backside reflection.

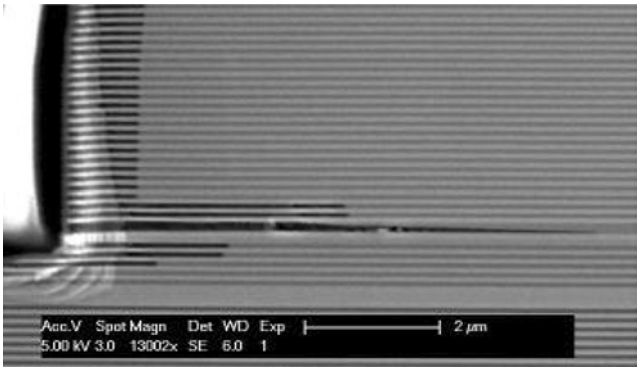

Fig. 2 *Cross-section SEM of VCSEL*

Results: Fig. 3 shows the voltage and output power against current (*L-I-V*) curves for a 4 μm diameter device which has the highest bandwidth. The device has a differential efficiency of 68% and a low threshold current of 0.18 mA. This low threshold current indicates that incorporating deep oxidation layers does not add extra scattering loss and degrade the device performance. This is because the optical modes are mainly confined by the tapered oxide aperture and do not see the oxidation layers. The threshold voltage is 1.53 V, only 270 meV larger than quasi-Fermi level separation. This indicates our bandgap engineering scheme effectively eliminates the hetero-barriers at the DBR interfaces. The series resistance is ~240 Ω, resulting from the insufficient doping levels of the DBRs near the active region. The peak wall-plug efficiency is 37% at a current of 1 mA and the maximum output power is 5.7 mW at a bias current of 9.5 mA.

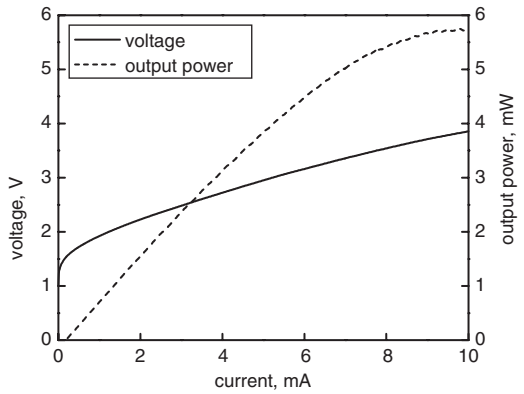

Fig. 3 *L-I-V curves for 4 μm diameter device at 20°C*

Small-signal modulation responses were measured on-wafer using an RF probe and a calibrated vector network analyser. Output power was collected using a 50 μm multimode fibre and a high-speed photodetector. The frequency responses for the 4 μm diameter device under different bias currents are shown in Fig. 4. The maximum electrical –3 dB frequency is 17.9 GHz at a bias current of 4.75 mA, corresponding to only 10 mW of power dissipation. This is the highest bandwidth for a VCSEL without using proton implantation. Although the bandwidth is still limited by the parasitics, it is mainly due to the relatively high series resistance and can be reduced by increasing the doping.

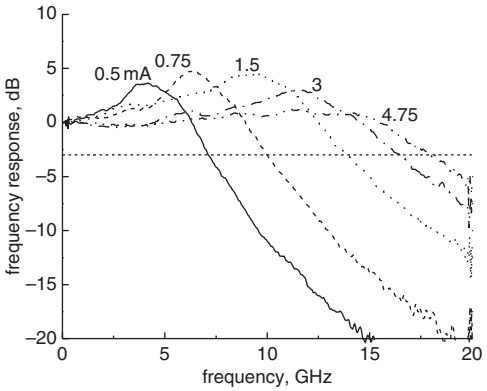

Fig. 4 *Small-signal modulation responses for 4 μm diameter device under different bias currents at 20°C*

Conclusion: A novel method using deep oxidation layers to reduce the parasitics of a VCSEL is proposed. By incorporating the deep oxidation layers into our devices, we demonstrated high-efficiency, high-speed 980 nm VCSELs with bandwidth 17.9 GHz.

14 August 2006
Electronics Letters online no: 20062538
doi: 10.1049/el:20062538

Y.C. Chang, C.S. Wang, L.A. Johansson and L.A. Coldren (*Department of Electrical and Computer Engineering, University of California, Santa Barbara, CA 93106-9560, USA*)

E-mail: yuchia@engineering.ucsb.edu

References

1 Peters, M.G., Thibeault, B.J., Young, D.B., Scott, J.W., Peters, F.H., Gossard, A.G., and Coldren, L.A.: 'Band-gap engineered digital alloy interfaces for lower resistance vertical-cavity surface-emitting lasers', *Appl. Phys. Lett.*, 1993, **63**, pp. 3411–3413

2 Lear, K.L., Hou, H.Q., Banas, J.J., Hammons, B.E., Furioli, J., and Osinski, M.: 'Vertical cavity lasers on p-doped substrates', *Electron. Lett.*, 1997, **33**, pp. 783–784

3 Al-Omari, A.N., and Lear, K.L.: 'Polyimide-planarized vertical-cavity surface-emitting lasers with 17.0-GHz bandwidth', *IEEE Photonics Technol. Lett.*, 2004, **16**, pp. 969–971

4 Lear, K.L., Hietala, V.M., Hou, H.Q., Banas, J., Hammons, B.E., Zolper, J., and Kilcoyne, S.P.: 'Small and large signal modulation of 850 nm oxide-confined vertical-cavity surface-emitting lasers', *Advances in Vertical Cavity Surface Emitting Lasers in Trends in Optics and Photonics Series*, 1997, **7**, pp. 69–74

5 Suzuki, N., Hatakeyama, H., Fukatsu, K., Anan, T., Yashiki, K., and Tsuji, M.: '25-Gbps operation of 1.1-μm-range InGaAs VCSELs for high-speed optical interconnections'. Optical Fiber Communications Conf., Tech. Dig., 2006, paper no. OFA4

6 Wilmsen, C.W., Temkin, H., and Coldren, L.A.: 'Vertical-cavity surface-emitting lasers: design, fabrication, characterization, and applications' (Cambridge University Press, 1999), Chap. 5

7 Hegblom, E.R., Babic, D.I., Thibeault, B.J., and Coldren, L.A.: 'Scattering losses from dielectric apertures in vertical cavity lasers', *IEEE J. Sel. Top. Quantum Electron.*, 1997, **3**, pp. 379–389

III. MBE Technology & Devices

B. InP-based Vertical-Cavity Lasers and Technology

Optically pumped Silicon laser based on evanescent coupling of Si micro-disk to III-V DBR stack

Subal Sahni and Eli Yablonovitch
Department of Electrical Engineering, University of California, Los Angeles, California, 90095
subal@ee.ucla.edu

David Buell and Larry Coldren
Department of Electrical and Computer Engineering, University of California, Santa Barbara, California, 93106

Abstract: A Si laser with a Si micro-disk evanescently coupled to a III-V gain medium is proposed. The III-V also functions as a DBR at the gain wavelength to minimize the perturbation of the cavity mode.

OCIS codes: (130.0130) Integrated optics; (140.5960) Semiconductor lasers; (250.5300) Photonic integrated circuits

Fabrication of lasers in Silicon has been a long-standing goal in the field of opto-electronics. In the last couple of years Raman amplification has emerged as a leading solution to this problem [1,2]. Another approach is to heterogeneously integrate Si with III-V compounds primarily through wafer bonding. A novel evanescent Si laser based on such integration was recently demonstrated by Park et. al. [3].

Here we propose a similar evanescent laser, where a Si micro-disk is coupled to a III-V structure [Fig 1(a)]. The III-V material, which can be optically or electrically pumped, amplifies only the light in the evanescent tail of the cavity mode [Fig 1(b)]. If the loss in the micro-disk is low enough, this small amount of gain will be enough to offset the losses in the Si cavity and achieve lasing. Since Si micro-disks with quality factors approaching 10^6 can be fabricated [4], the amount of gain needed from the III-V can be reduced to < 1dB/cm. This lowering of required gain serves two purposes: firstly, the lower gain drastically reduces the laser threshold carrier density, thereby significantly reducing the pump powers needed by the laser. Secondly, the III-V stack can be moved farther from the Silicon micro-disk because lasing can be achieved with a smaller overlap between the modal field and the gain medium. The increased distance between the Si and the III-V minimizes the effect of the gain medium on the micro-disk mode and helps maintain its high Q. Therefore the lasing mode is essentially a mode of the Si disk with the III-V appearing only as a perturbation. It must be mentioned that in these respects our design differs significantly from the work presented in ref [3], wherein a linear rib waveguide is used as the cavity and the overall laser mode is a 'supermode' of the III-V and the Si with a considerable fraction of the power being confined in the III-V.

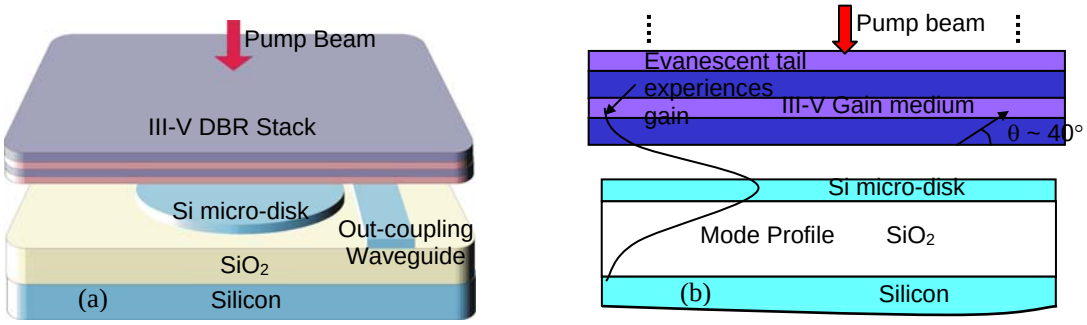

Fig. 1. (a) Schematic of a Si micro-disk coupled to III-V gain medium. The pump beam (@1.31 μm in our experiments) enters from the top of the stack. The laser light is out-coupled through the waveguide, which is also used for Q measurements. (b) Cross-sectional schematic of the device. θ represents the angle at which the evanescent light enters the III-V. The separation between the Si and the III-V stack is of the order of a few 100 nm.

Another crucial feature of our device is the use of a novel DBR structure as the gain medium. While the layers closest to the Si cavity provide gain at a specific wavelength λ_g, the remaining layers of the III-V stack are designed to *reflect* the evanescent portion of the Si mode at λ_g. This further helps limit the overlap between the evanescent tail and the III-V to an amount that is just sufficient to initiate lasing. More importantly it prevents the Si mode from leaking into the bulk InP substrate. In order to construct a Bragg mirror at 1.55 μm, an Antimonide based alloy combination was chosen. Unlike the conventional InGaAsP material system, AlAsSb and GaAsSb have a high

enough index contrast (~0.4) to construct an efficient DBR. The exact thicknesses of the layers in the stack are calculated from the vertical component (k_V) of the propagation constant of the evanescent field inside each layer. k_V is simply given by the expression $(k_g^2 - k_{Si}^2)^{1/2}$, where $k_g = 2\pi n_g$ is the total wave-vector of the light in the III-V layer and k_{Si} is the effective propagation constant of the mode in the Si micro-disk (n_g is the refractive index of each layer). For our Si disks, k_V @1.55 μm is ~7.5 and ~10.2 μm^{-1} for the alternating layers, yielding corresponding thicknesses of ~210 nm and ~154 nm [Fig 2]. The gain layers ($Al_{0.01}Ga_{0.99}As_{0.51}Sb_{0.49}$), which have a band-gap of 0.8eV (1.55 μm), are also designed to contribute to the DBR action even though their refractive indices are highly dispersive at the gain wavelength. From the effective masses of the carriers in the gain medium, we estimate that carrier densities of the order of $10^{19}/cm^3$ will yield a gain coefficient in excess of 300dB/cm. All the alloys used are lattice matched to InP and the whole structure shown in Fig 2 has been fabricated using MBE.

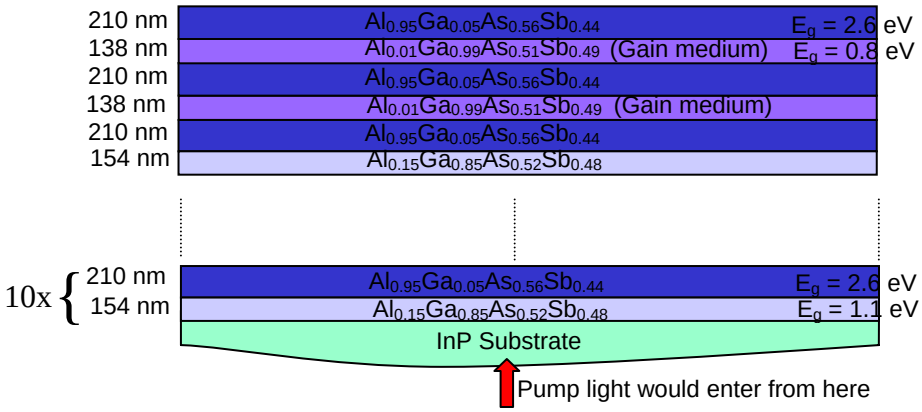

Fig. 2. Structure of the III-V DBR stack. The composition of the gain alloy is chosen so as to have a band-gap of 0.8eV (1.55 μm). The 0.01 Al content in the gain layer improves its stability in air. There are only two layers of the gain medium since the Si modal field is not expected to penetrate very deep into the DBR stack. The topmost layer in the above structure ($Al_{0.95}Ga_{0.05}As_{0.56}Sb_{0.44}$) would be closest to the Si disk in the laser. The gain medium is not grown as the last layer in order to avoid excess surface recombination-induced decrease in carrier lifetime. As indicated, the pump beam for the laser would enter from the bottom InP substrate. A pump at 1310nm (0.95eV) would be absorbed only by the gain layer.

Our initial experiments on this laser structure are being carried out using pulsed optical pumping at 1310nm. The focused pump light enters the DBR from the back [Fig 1(a)] and is absorbed only by the gain medium. 10 μm radius disks, which exhibit Q values of ~10,000 (measured through coupling to an adjacent waveguide), are being used in the setup. Even for these mediocre quality factors, with strong enough pump powers, lasing can be expected from chips in which the separation between the III-V stack and the disk surface is as high as 300nms. SiO_2 spacer layers on the Si maintain the appropriate distance between the DBR and the Si. In our initial experiments the III-V is placed on the spacers without bonding to get preliminary measurements.

In conclusion, a micro-disk based Si evanescent laser has been proposed where the lasing mode is almost entirely in the Si. The device can be expected to exhibit lasing at medium pump powers (~100mW) in spite of mediocre Q factors. The DBR and micro-disks have been fabricated and initial results on light output are expected soon.

References

[1] O. Boyraz, and B. Jalali, "Demonstration of a Silicon Raman laser", Optics Express **12**, 5269-5273 (2004).
[2] H. Rong, R. Jones, A. Liu, O. Cohen, D. Hak, A. Fang and M. Paniccia, "A continuous-wave Raman Silicon laser," Nature **433**, 725-728 (2005).
[3] Hyundai Park, Alexander W. Fang, Satoshi Kodama, and John E. Bowers, "Hybrid Silicon evanescent laser fabricated with a Silicon waveguide and III-V offset quantum wells", Optics Express **13**, 9460-9464 (2005).
[4] Matthew Borselli, Kartik Srinivasan, Paul E. Barclay and Oskar Painter, "Rayleigh scattering, mode coupling, and optical loss in silicon microdisks", Applied Physics Letters **85** (17), 3693-3695 (2004).

Optical Design of InAlGaAs Low-Loss Tunnel-Junction Apertures for Long-Wavelength Vertical-Cavity Lasers

D. Feezell, D. A. Buell, D. Lofgreen, M. Mehta, and L. A. Coldren, *Fellow, IEEE*

***Abstract*—We report on the optical design of thin selectively etched InAlGaAs tunnel-junction apertures for the realization of optically efficient long-wavelength vertical-cavity surface-emitting lasers (VCSELs). These apertures were designed to introduce minimal optical loss to the structure, facilitate single-mode operation, and yield optical mode diameters that better match the injected current density profile. We then demonstrate InP-based VCSELs emitting at 1304 nm utilizing these low-loss InAlGaAs apertures, resulting in optically efficient low-loss devices with differential quantum efficiencies of up to 60%.**

***Index Terms*—Aperture, InAlGaAs, InP-based, long wavelength, semiconductor laser processing, semiconductor lasers, tunnel junction, vertical-cavity surface-emitting lasers (VCSELs).**

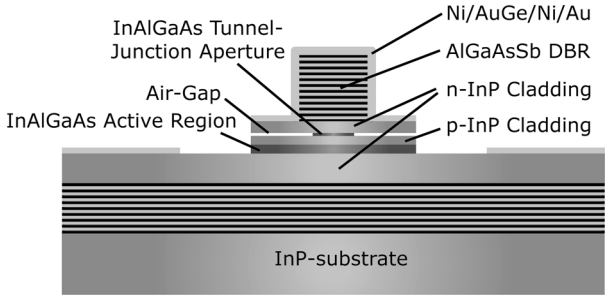

Fig. 1. Schematic of bottom-emitting all-epitaxial VCSEL structure with undercut thin tunnel-junction aperture.

I. Introduction

LONG-wavelength vertical-cavity surface-emitting lasers (VCSELs) emitting in the 1300–1600-nm wavelength range are attractive light sources for short to midrange optical fiber communications. These devices target low-loss and low-dispersion windows in standard optical fibers and are expected to provide a low-cost alternative to the existing edge-emitting infrastructure. With low power consumption, on-wafer testing, simple packaging, and high fiber-coupling efficiency, VCSELs are ideal transmitters for metro, local area, and storage area networks.

Recently, many promising long-wavelength VCSEL results have been demonstrated [1]–[5]. However, it is still desirable to continually demonstrate devices with significantly reduced optical loss. More optically efficient structures with low internal loss will facilitate reduced threshold currents and enable higher differential quantum efficiencies. These are desirable characteristics for achieving improved modulation performance with lower required drive currents.

Previously, our group has reported InP-based devices operating in the 1300–1600-nm wavelength region [6], [7]. These devices utilized well-established InAlGaAs active region technology and AlGaAsSb distributed Bragg reflectors (DBRs). This combination facilitates monolithic all-epitaxial InP-based devices spanning the entire long-wavelength telecommunications band. With this platform, we have recently demonstrated devices with efficient modulation characteristics and high differential quantum efficiencies [8]. The high differential quantum efficiencies observed resulted from the implementation of thin selectively etched tunnel-junction apertures for low-loss optical guiding [9]. In this work, we describe the optical design of these thin selectively etched tunnel-junction apertures. First, the free carrier absorption (FCA) loss from the highly doped tunnel-junction layer is minimized. Then, using a two-dimensional model of the optical cavity, thin selectively etched tunnel-junction apertures are designed to provide effective guiding of the fundamental lateral mode with low scattering loss. We then fabricate and characterize optically efficient single-mode 1304-nm InP-based VCSELs utilizing these apertures, with devices demonstrating high differential quantum efficiencies of greater than 60%, optical efficiencies up to 80%, and single-mode continuous-wave operation up to 90 °C.

The bottom-emitting device structure is shown in Fig. 1 for reference and is the same as previously reported [7]. A $1/2-\lambda$ InAlGaAs multiple-quantum-well active region is clad on both sides by InP layers. Intracavity contacts are made to these InP layers, allowing for the AlGaAsSb DBRs to remain undoped. Embedded within the upper InP cladding layer is a 35-nm n^{++}-InAlGaAs–p^{++}-InAlGaAs tunnel-junction layer that is selectively etched to form a thin air-gap aperture for electrical and optical confinement. Details regarding the fabrication of these devices have been previously reported [7]–[9].

Manuscript received February 14, 2006; revised March 2, 2006. This work was supported in part by the National Science Foundation.

D. Feezell and L. A. Coldren are with the Department of Electrical and Computer Engineering and the Department of Materials, University of California, Santa Barbara, CA 93106 USA (e-mail: feezell@engineering.ucsb.edu).

D. A. Buell is with CNRS-CRHEA, 06560 Valbonne, France.

D. Lofgreen is with Raytheon Vision Systems, Goleta, CA 93117 USA.

M. Mehta is with the University of New Mexico, Albuquerque, NM 87131 USA.

Digital Object Identifier 10.1109/JQE.2006.874007

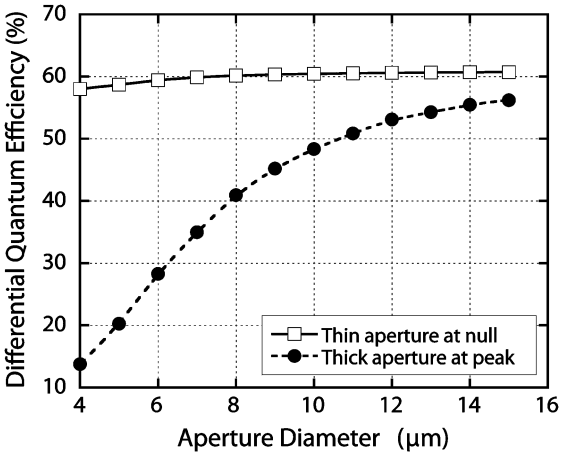

Fig. 2. Simulated differential efficiencies for an active region apertured device and a tunnel-junction apertured device, demonstrating the scaling benefits provided by thin apertures.

II. Motivation for Thin Tunnel-Junction Apertures

Despite the promising results previously obtained by our group, these devices employed a rather inefficient aperturing scheme [6], [10]. A thick (200 nm) undercut active region aperture, inherently placed at standing wave peak, was employed for optical confinement. The strong guiding effect of this thick aperture introduced a significant amount of scattering loss to the devices. In fact, up to 60% of the total internal loss in these devices was due to aperture scattering of the mode. As a result, these devices only achieved differential quantum efficiencies of 23%. Additionally, these devices suffered from increased sidewall recombination at the thick exposed etched active region [10]. The implementation of thin tunnel-junction apertures alleviates these problems by providing low-loss optical confinement, avoiding exposed active region sidewalls, and generating an injected current density profile that better matches the shape of the optical mode.

An additional benefit provided by thin low-loss apertures is the ability to scale the aperture diameters to smaller dimensions without introducing increased scattering loss. As an example, Fig. 2 shows a simulation of predicted differential efficiencies for the previously reported devices with a thick active region aperture and the thin tunnel-junction apertured devices of this work. These differential efficiencies are estimated from the calculated loss in the devices (i.e., aperture scattering loss and FCA loss). The loss calculation will be explained in subsequent sections. Fig. 2 is intended to demonstrate the trend between scaling to smaller dimensions for both aperturing schemes. It is clear that the thin tunnel-junction aperturing scheme maintains a more constant differential quantum efficiency value down to smaller aperture dimensions. This is an important benefit for realizing higher differential quantum efficiency devices with lower threshold currents.

III. Tunnel-Junction Aperture Optical Design

With the goal of limiting optical loss in the structure, reduction of the FCA loss introduced by the tunnel junction layer is of prime importance. The placement of the tunnel junction relative to the optical standing wave in the cavity and its thickness are critical design issues due to the high doping (N_A = 1e20 cm^{-3}, N_D = 3e19 cm^{-3}) required in the tunnel junction layer to achieve efficient quantum tunneling. The tunnel junction aperture layer should be designed to minimize the single-pass optical loss. For a tunnel junction with a thickness $L = L_n + L_p$, where L_n and L_p are the thicknesses of the n and p sides of the junction, respectively, the single-pass optical loss is calculated by $1 - e^{-\alpha_i L \Gamma_{\rm enh}}$. Here, α_i is the internal optical loss from FCA and $\Gamma_{\rm enh}$ is the standing-wave enhancement factor [11]. In order to minimize the single-pass optical loss from a highly doped layer, such as the tunnel junction, $\Gamma_{\rm enh}$ and L must be minimized. The standing wave enhancement factor can be minimized to some extent by selectively placing the highly doped tunnel-junction layer at an optical standing wave null in the cavity, as shown in Fig. 3. This reduces the overlap between the highly doped tunnel-junction layer and regions of high electric field. To illustrate the importance of the standing-wave enhancement factor on optical loss, the FCA loss introduced by the tunnel junction as a function of its relative position to the optical standing-wave null was calculated and is shown in Fig. 4. For variations from the null in the range of tens of nanometers, we observe an order of magnitude increase in FCA loss.

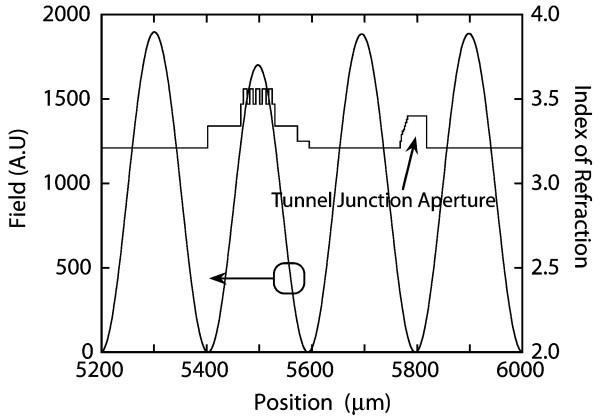

Fig. 3. Electric field and index profile in the cavity of the structure, showing the placement of the tunnel junction aperture layer at an optical standing wave null for the minimization of the standing-wave enhancement factor.

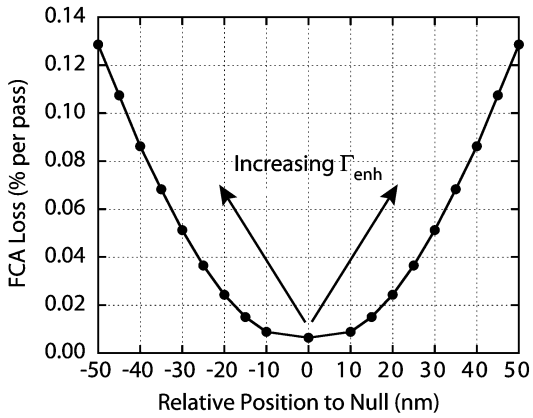

Fig. 4. Simulated FCA loss from the tunnel-junction layer as a function of variation from its placement at an optical standing-wave null.

Another method to further limit the FCA loss from the tunnel-junction layer is to reduce its thickness. This also relaxes epi-

taxial growth tolerances. However, due to restrictions on doping levels and quantum tunneling probability, there are practical minimum allowable values for the junction thicknesses, L_n and L_p. These values can be calculated via the WKB method reported by Mars, *et al.* [12]. For the InAlGaAs tunnel junctions in this work, these values were determined to be in the range of 10–20 nm. Specifically, for the reported devices, $L_n = 20$ nm and $L_p = 15$ nm.

The figure of merit employed for the optical design of the etched aperture is the effective index perturbation to the optical mode, $\Delta n_{\text{eff}} = n_{\text{eff}}^{\text{core}} - n_{\text{eff}}^{\text{undercut}}$, where $n_{\text{eff}}^{\text{core}}$ and $n_{\text{eff}}^{\text{undercut}}$ are the effective indexes in the growth direction of the core and undercut regions of the aperture, respectively. This treatment yields a two-dimensional index profile that provides a simple optical model of the aperture. For a given physical aperture diameter, the index perturbation determines the important optical properties of the aperture, specifically the effective optical mode diameter and the aperture scattering loss. Constraints on these parameters predominately determine the allowed index perturbation introduced by the aperture. If the index perturbation is too small, the optical mode diameter may be significantly larger than the injected current density profile, leading to increased absorption loss in the unpumped areas of the quantum wells. Conversely, if the index perturbation is too large, the optical mode may experience significantly increased scattering loss. Therefore, as described below, an index perturbation is chosen that provides effective guiding with minimal scattering loss.

To determine the waveguide eigenmodes, and thus the effective optical mode diameter, the two-dimensional scalar wave equation was solved on this index profile using a finite difference technique with a nonuniform mesh [13]–[15]. The calculated effective optical mode diameters (determined at the $1/e^2$ point of the normalized mode amplitude) for the fundamental lateral mode versus the physical aperture diameter, are shown in Fig. 5(a) for various values of Δn_{eff}. For high differential quantum efficiencies and reduced threshold currents, increased overlap between the optical mode and the current density profile is desired. Since current spreading is minimal in the p-InP beneath the tunnel junction aperture, the current density profile is primarily determined by the physical aperture diameter. Therefore, for optimal modal gain, the effective optical mode diameter should be similar to the physical aperture diameter. Effective optical mode diameters larger than the physical aperture diameter will lead to increased absorption loss from overlap of the optical mode tails with unpumped regions of the quantum wells. For mechanically stable single-mode devices, aperture diameters in the range of 6–8 μm are desired. From Fig. 5(a), it is determined that a Δn_{eff} in the range of 0.005 to 0.01 is required to satisfy the above guiding condition.

The optical scattering loss associated with the aperture was then examined by propagating the optical mode through an unfolded cavity. The procedure implemented is similar to that described by Fox and Li [13]–[15]. As the field is propagated, a position-dependent phase shift, a position-dependent gain, and an absorption are applied to the mode. The phase shift, described by $\phi(x, y) = k_0 \Delta n_{\text{eff}}(x, y) L_{\text{cav}}$, where k_0 is the free space wave vector and L_{cav} is the effective cavity length, is what approximates the effect of the aperture in the model. The phase,

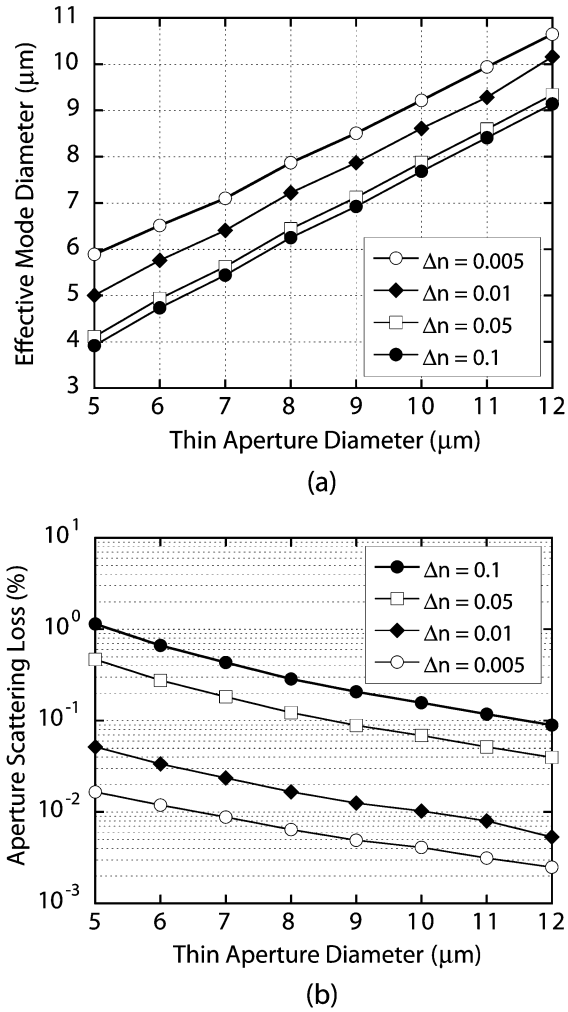

Fig. 5. (a) Calculated effective optical mode diameter for the fundamental mode versus physical aperture diameter for various aperture strengths. (b) Calculated aperture scattering loss versus physical aperture diameter for various aperture strengths.

gain, and absorption values are continually adjusted until there is only a phase shift associated with a pass through the cavity. At this point, the mode of the system and the gain are known. The scattering loss is then determined from the modal gain. Fig. 5(b) shows the calculated aperture scattering loss versus physical aperture diameter for various values of Δn_{eff}. From the figure, the values of Δn_{eff} needed to achieve the required effective optical mode diameters determined above (i.e., —$\Delta n_{\text{eff}} \approx 0.005$ to 0.01) produce apertures that contribute very little scattering loss to the structure. This result is in stark contrast to our previously reported thick etched active region apertures placed at an optical standing wave peak ($\Delta n_{\text{eff}} = 0.10$) and represents over an order of magnitude reduction in optical loss [10].

Although it is possible to further limit optical scattering loss from the aperture by reducing Δn_{eff} below 0.005, quantum tunneling probability requires a tunnel-junction thickness on the order of 35 nm, which already introduces a Δn_{eff} of nearly 0.005. Additionally, the restrictions stated above regarding the effective optical mode diameter do not allow for such low values of Δn_{eff}, and by the analysis above, it was determined that a selectively etched aperture with $\Delta n_{\text{eff}} = 0.01$ effectively guides

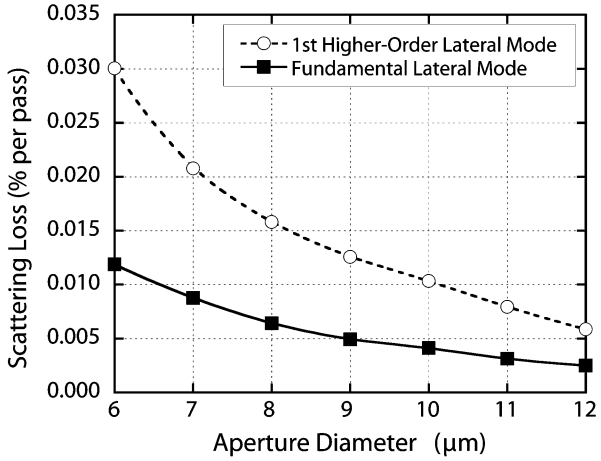

Fig. 6. Calculated aperture scattering loss ($\Delta n_{\text{eff}} = 0.005$) per pass for the fundamental lateral mode and the next higher order lateral mode as a function of aperture diameter, demonstrating the increased scattering loss experienced by higher order modes.

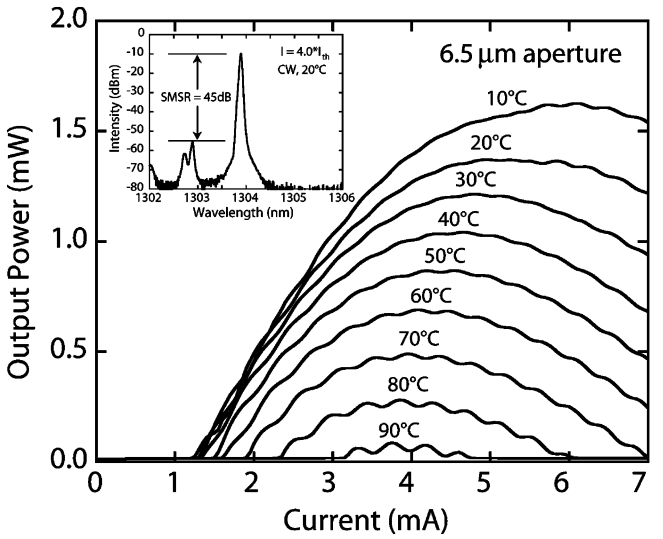

Fig. 7. Continuous-wave light versus current curves for various stage temperatures, showing high room-temperature differential quantum efficiency of 60%. The inset shows the lasing spectrum, demonstrating single-mode behavior with a 45-dB SMSR.

the optical mode while still introducing very little scattering loss. $\Delta n_{\text{eff}} = 0.005$ was not chosen in order to avoid operating near the limit of the optical mode becoming larger than the current density profile. Since the 35-nm n^{++}-InAlGaAs–p^{++}-InAlGaAs tunnel junction did not quite achieve the necessary $\Delta n_{\text{eff}} = 0.01$, a section of etchable lowly doped and compositionally graded InAlGaAs was placed adjacent to the tunnel junction layer to increase Δn_{eff} to the desired value of 0.01. This grade is shown near the tunnel junction aperture in Fig. 3.

Finally, to achieve single-mode operation, an effective aperture design should suppress higher order lateral modes from lasing. As discussed above, the effective optical mode diameter of the fundamental mode was designed to closely mimic the current density profile, ensuring this mode reaches lasing at the lowest possible threshold. Moreover, due to the shapes of the higher order modes, they typically experience increased scattering loss from the aperture, thus further increasing their lasing thresholds. A comparison between the calculated scattering loss experienced by the fundamental lateral mode and the first higher order lateral mode for an aperture with $\Delta n_{\text{eff}} = 0.005$ is shown in Fig. 6. For aperture diameters in the range of 6–8 μm, we observe an increase in scattering loss of several times for the next higher order mode. This additional loss further ensures single-mode lasing operation of the fundamental mode at these aperture dimensions.

IV. Results and Discussion

A VCSEL structure with the designed low-loss tunnel-junction aperture ($\Delta n_{\text{eff}} = 0.01$) was then grown by molecular beam epitaxy in a single growth step [16]. Devices were then fabricated and characterized. Fig. 7 shows the continuous-wave light versus current characteristics for a device with a 6.5-μm aperture diameter. This device achieved a high continuous-wave differential quantum efficiency of 60% at room-temperature and operated up to 90 °C, the highest reported temperature operation for a VCSEL with Sb-based DBRs. The lasing spectrum is also inset in Fig. 7 and demonstrates strong single-mode behavior with a side-mode suppression ratio (SMSR) of 45 dB. These results, particularly the high differential quantum efficiency, clearly indicate the effectiveness of the optical design of the low-loss aperture and represent a significant improvement over the previously reported work. As a result of the differential quantum efficiency values observed, the optical efficiency of these devices was also quite high. The optical efficiency η_0 is calculated by $\eta_0 = \eta_d/\eta_i$, where η_d is the differential quantum efficiency and η_i is the injection efficiency as determined from edge-emitting lasers with the same active region structure [11]. Conceptually, η_0 is the percentage of photons generated in the active region that leave the optical cavity through the desired DBR mirror and are collected as useful output. Since the injection efficiency was determined to be 75% by the method referenced above, the optical efficiency is therefore calculated to be 80%.

As evidenced by the high differential quantum efficiencies these devices achieved, the internal optical loss was very low. This was largely a result of the design and implementation of the thin tunnel-junction aperture. However, several other factors contributed to the performance. The DBRs were undoped to limit optical loss and very smooth, with the entire epitaxial structure displaying an RMS roughness of only 3.1 Å. Furthermore, the implementation of tunnel junctions limited the incorporation of highly absorbing p-type material.

The known contributions to optical loss in the devices from FCA and aperture scattering were estimated. The FCA loss for each section of the device was determined by overlapping the optical mode with the doping profile in the structure and the aperture scattering loss was calculated by the method described above. The results of these calculations are shown in Table I. The total calculated internal loss in the structure due to FCA and aperture scattering is shown to be $\approx$0.16% per pass ($\approx$5 cm^{-1}). We believe this to be a significantly low number for a long-wavelength VCSEL. Although the FCA loss reported here and the FCA loss reported in our previous devices is similar, the

TABLE I
CALCULATED LOSS CONTRIBUTIONS FROM VARIOUS SOURCES IN THE DEVICE

Loss Source	Loss (% per pass)
Aperture Scattering	0.0287
Tunnel Junction (FCA)	0.0234
p-InP Cladding (FCA)	0.0743
n-InP Cladding (FCA)	0.0350
Active Region (FCA)	0.0005
Total Calculated Internal Loss	**0.1619**

aperture scattering loss has been reduced by approximately one order of magnitude in this work.

The internal loss can also be experimentally obtained to verify our calculated estimations. By the method described by Coldren and Corzine, the measured VCSEL differential quantum efficiency, the calculated VCSEL mirror loss, and the injection efficiency obtained from InAlGaAs edge-emitting lasers are utilized to obtain the internal loss [11]. This method yields an experimental internal loss value of $\approx 6\ \mathrm{cm}^{-1}$, just slightly higher than the calculated estimate. The small discrepancy in the experimentally obtained value from the calculated value is explained by the presence of unaccounted for loss, such as macroscopic defect sites and surface roughness.

V. SUMMARY AND CONCLUSIONS

In conclusion, we have designed thin selectively etched tunnel-junction apertures for more efficient optical confinement in InP-based long-wavelength VCSELs. These apertures were designed to provide effective guiding of the optical mode, while introducing minimal optical loss to the structure. We have then grown, fabricated, and characterized VCSELs utilizing these low-loss air-gap apertures. The resulting optically efficient devices yielded low internal loss estimates, demonstrated differential quantum efficiencies of 60%, and achieved single-mode operation up to 90 °C.

REFERENCES

[1] N. Nishiyama, C. Caneau, S. Tsuda, G. Guryanov, M. Hu, R. Bhat, and C. Zah, "10-Gb/s error-free transmission under optical reflection using isolator-free 1.3-μm InP-based vertical-cavity surface-emitting lasers," *IEEE Photon. Technol. Lett.*, vol. 17, no. 8, pp. 1605–1607, Aug. 2005.

[2] J. Chang, C. L. Shieh, X. Huang, G. Liu, M. V. R. Murty, C. C. Lin, and D. X. Xu, "Efficient CW lasing and high-speed modulation of 1.3 μm AlGaInAs VCSELs with good high temperature lasing performance," *IEEE Photon. Technol. Lett.*, vol. 17, no. 1, pp. 7–9, Jan. 2005.

[3] M. Ortsiefer, K. Windhorn, G. Bohm, J. Rosskopf, R. Shau, E. Ronneberg, W. Hofman, and M. Amann, "2.5-mW single-mode operation of 1.55-μm buried tunnel junction VCSELs," *IEEE Photon. Technol. Lett.*, vol. 17, no. 8, pp. 1596–1598, Aug. 2005.

[4] V. Iakovlev, G. Suruceneau, A. Caliman, A. Mereuta, C. Berseth, A. Syrbu, A. Rudra, and E. Kapon, "High-performance single-mode VCSELs in the 1310-nm waveband," *IEEE Photon. Technol. Lett.*, vol. 17, no. 5, pp. 947–949, Jan. 2005.

[5] V. Jayaraman, M. Mehta, A. W. Jackson, S. Wu, Y. Okuno, J. Piprek, and J. E. Bowers, "High-Power 1320-nm wafer-bonded VCSELs with tunnel junctions," *IEEE Photon. Technol. Lett.*, vol. 15, no. 11, pp. 1495–1497, Nov. 2004.

[6] S. Nakagawa, E. Hall, G. Almuneau, J. K. Kim, D. A. Buell, H. Kroemer, and L. A. Coldren, "88 °C, continuous-wave operation of apertured, intracavity contacted, 1.55 μm vertical-cavity surface-emitting lasers," *Appl. Phys. Lett.*, vol. 78, pp. 1337–1339, 2001.

[7] D. Feezell, D. A. Buell, and L. A. Coldren, "Continuous wave operation of all-epitaxial InP-based 1.3 μm VCSELs with 57% differential quantum efficiency," *Electron. Lett.*, vol. 41, no. 14, pp. 803–804, Jul. 2005.

[8] D. Feezell, L. A. Johansson, D. A. Buell, and L. A. Coldren, "Efficient modulation of InP-based 1.3 μm VCSELs with AsSb-based DBRs," *IEEE Photon. Technol. Lett.*, vol. 17, no. 11, pp. 2253–2255, Nov. 2005.

[9] D. Feezell, D. A. Buell, and L. A. Coldren, "InP-based 1.3–1.6 μm VCSELs with selectively etched tunnel-junction apertures on a wavelength flexible platform," *IEEE Photon. Technol. Lett.*, vol. 17, no. 10, pp. 2017–2019, Oct. 2005.

[10] S. Nakagawa, "InP-Lattice-Matched, Long-Wavelength Vertical-Cavity Surface-Emitting Lasers for Optical Fiber Communications," Ph.D. dissertation, Dept. Elect. and Comp. Eng., University of California Santa Barbara, Santa Barbara, CA, 2001.

[11] L. A. Coldren and S. W. Corzine, *Diode Lasers and Photonic Integrated Circuits*. New York: Wiley, 1995.

[12] D. E. Mars, Y. L. Chang, M. H. Leary, S. D. Roh, and D. R. Chamberlin, "Low-resistance tunnel junctions on GaAs substrates using GaInNAs," *Appl. Phys. Lett.*, vol. 84, pp. 2560–2562, 2004.

[13] A. G. Fox and T. Li, "Resonant modes in a maser interferometer," *Bell Syst. Tech. J.*, vol. 40, pp. 453–488, 1961.

[14] E. R. Hegblom, D. I. Babic, B. J. Thibeault, and L. A. Coldren, "Scattering losses from dielectric apertures in vertical-cavity lasers," *IEEE J. Sel. Top. Quantum Electron.*, vol. 3, no. 2, pp. 379–386, Apr. 1997.

[15] D. Lofgreen, "Investigation of selective quantum well intermixing in vertical cavity lasers," Ph.D. dissertation, Dept. Elect. Comp. Eng., Univ. California, Santa Barbara, 2004.

[16] D. A. Buell, D. Feezell, and L. A. Coldren, "Molecular beam epitaxy of AlGaAsSb-based long-wavelength vertical-cavity lasers," *J. Vac. Sci. Technol. B*, to be published.

Daniel F. Feezell received the B.S. degree in electrical engineering from the University of California, Irvine, in 2000. He then joined Prof. L. Coldren's group at the University of California, Santa Barbara, where he received the M.S. and Ph.D. degrees in 2001 and 2005, respectively.

He is currently working on design, fabrication, and characterization of novel GaN-based light-emitting devices as a Postdoctoral Researcher under Prof. S. Nakamura at the University of California, Santa Barbara.

David A. Buell received the Ph.D. degree in materials from the University of California, Santa Barbara (UCSB), in 2005 for his work on InP-based vertical cavity lasers.

He is a Researcher in molecular beam epitaxy of III–V and II–IV semiconductors with a focus on optoelectronics and optical phenomena, UCSB. He is currently researching ZnO at CNRS-CRHEA, Valbonne, France, as a Chateaubriand Fellow.

Dan Lofgreen received the B.S. degrees in both electrical and computer engineering from Iowa State University, Ames, in 1997. He then joined Prof. L. Coldren's group at the University of California, Santa Barbara, where he received the M.S. and Ph.D. degrees in 1999 and 2004, respectively.

He is currently working on design, growth, and characterization of HgCdTe-based infrared detectors at Raytheon Vision Systems, Goleta, CA.

Manish Mehta received the Ph.D. degree in electrical engineering from the University of California, Santa Barbara, in February 2006.

He is currently working on the development of midinfrared semiconductor lasers as a Postdoctoral Researcher under Dr. D. Huffaker at the University of New Mexico, Albuquerque.

Larry A. Coldren (S'67–M'72–SM'77–F'82) received the Ph.D. degree in electrical engineering from Stanford University, Stanford, CA, in 1972.

After 13 years in the research area at Bell Laboratories, he was appointed Professor of Electrical and Computer Engineering at the University of California at Santa Barbara (UCSB) campus in 1984. In 1986, he assumed a joint appointment with Materials and ECE, and in 2000 the Fred Kavli Chair in Optoelectronics and Sensors. He is also Chairman and Chief Technology Officer of Agility Communications, Inc. At UCSB, his efforts have included work on novel guided-wave and vertical-cavity modulators and lasers as well as the underlying materials growth and fabrication technology. He is now investigating the integration of various optoelectronic devices, including optical amplifiers and modulators, tunable lasers, wavelength-converters, and surface-emitting lasers. He has authored or coauthored over 500 papers, five book chapters, one textbook, and has been issued 32 patents.

Prof. Coldren is a Fellow of the Optical Society of America (OSA) and a past Vice-President of IEEE Laser and Electro-Optics Society (LEOS), the recipient of the 2004 John Tyndall Award, and a member of the National Academy of Engineering.

Molecular beam epitaxy of InP-based alloys for long-wavelength vertical cavity lasers

David A. Buell[a)]
Department of Materials, University of California, Santa Barbara, California 93106

Daniel Feezell
Department of Electrical and Computer Engineering, University of California, Santa Barbara, California 93106

Bjørn-Ove Finland[b)]
Department of Electrical and Computer Engineering, University of California, Santa Barbara, California 93106

Larry Coldren
Department of Materials, University of California, Santa Barbara, California 93106
and Department of Electrical and Computer Engineering, University of California, Santa Barbara, California 93106

(Received 14 September 2005; accepted 3 April 2006; published 30 May 2006)

In this article we describe the growth, design, and characterization of a 1310 nm lattice-matched vertical cavity laser which take advantage of an AlGaAsSb distributed Bragg reflector and AlInGaAs active regions. The molecular beam epitaxial growth for this structure was particularly challenging due to the various III–V alloys used; in particular, the interfaces between them were observed to be a significant source of macroscopic defects and roughness. The AlGaAsSb–InP interface was seen to control the yield and overall quality of device structures, and so was the focus of the crystal growth optimization. InP heat- and current-spreading layers were utilized to offset the thermal and electrical limitations of the AlGaAsSb mirrors; we optimized the defect density and roughness of these epilayers by studying their dependence on growth temperature and P overpressure. Vertical cavity lasers grown using these optimized approaches and incorporating a thin, selectively etched tunnel-junction aperture were fabricated and tested, and demonstrated promising characteristics. Operating temperatures up to 90 °C with single-mode power in excess of 1.6 mW were observed. Differential quantum efficiency of 64% was seen for our best devices, a record for long-wavelength vertical cavity lasers. © *2006 American Vacuum Society.*
[DOI: 10.1116/1.2200380]

I. INTRODUCTION

Vertical cavity lasers (VCLs) operating in the wavelength space from 1300 to 1600 nm are interesting data communication and telecommunication sources for existing fiber-optic networks, since they take advantage of absorption and dispersion minima in conventional silica fiber; their circular output mode shape, low dissipated power, and efficient direct modulation behavior make them favorable for network applications. VCLs operating at shorter wavelengths (780–980 nm) have demonstrated excellent performance characteristics for short distance communications.[1] In order to translate these successes to the local-, storage-, and metroarea networks, VCLs operating at 1310 and 1550 nm are desired. There have been two general lines of approach for realizing long-wavelength VCLs to this point: GaAs based and InP based. GaAs-based approaches take advantage of AlGaAs/GaAs distributed Bragg reflectors (DBRs) with their associated high index of refraction contrast and thermal conductivity. The optical and current aperturing technology is also well developed, with submicron devices incorporating tapered oxide apertures demonstrating high-speed modulation and high differential quantum efficiency. In order to extend the operation of GaAs-based devices from 980 to 1310 and 1550 nm, less mature active region materials such as GaInN(Sb)As or InGaAs quantum dots must be used.[2,3] These active regions are relatively new, and their reliability at longer wavelengths remains in question.

InP-based approaches take the opposite tack: the active region materials, AlInGaAs and InGaAsP, are well developed, having been deployed in commercial long-wavelength edge-emitting lasers for many years. The DBR and aperturing technology, however, are less well developed. The conventional lattice-matched alloys to InP, AlInGaAs, and InGaAsP do not have sufficient index contrast to be effective options for DBRs with high reflectivity. This has led to a variety of approaches to realize InP-based VCLs, including wafer-fused AlGaAs/GaAs DBRs,[4] metamorphically grown AlGaAs DBRs,[5] and dielectric DBRs.[6] Devices with high operating temperature, useful output power, and good differential efficiency have been demonstrated using each of these techniques.

[a)]Electronic mail: dave.buell@gmail.com
[b)]On leave from Department of Electronics and Telecommunications, Norwegian University of Science and Technology, NO-7491 Trondheim, Norway.

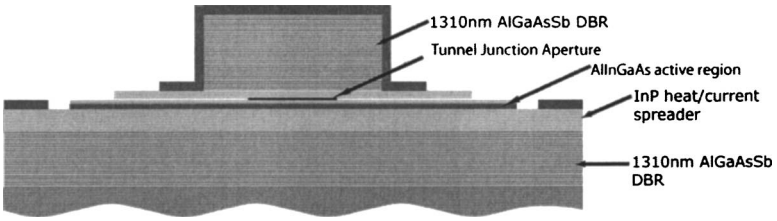

FIG. 1. Vertical cavity laser at 1310 nm with AlGaAsSb mirrors and AlInGaAs active region, with thin AlInGaAs tunnel-junction aperture for current and optical confinement.

In this article we report the results using an alternative approach, in which we take advantage of the InP lattice-matched material AlGaAsSb. Our group has reported VCLs based on this technology before, both at 1550 nm (Ref. 7) and more recently at 1310 nm.[8] Prior results at 1550 nm showed operating temperature of 88 °C and 1.2 mW output power at 15 °C, with 23% differential quantum efficiency. Improvements to the device design and epitaxial growth have led to our most recent results, in which 1310 nm VCLs have been fabricated which operate to 90 °C, have 1.6 mW single-mode output power, and a record differential quantum efficiency of 64%. The molecular beam epitaxial growth optimization is detailed below.

II. MOLECULAR BEAM EPITAXY

The vertical cavity laser structures detailed in this article were grown using molecular beam epitaxy in a Varian Gen-II reactor, with standard EPI-SUMO effusion cells for group III elements and valved, cracked sources for all group V elements. For our laser structures, AlGaAsSb alloys were used as DBRs, AlInGaAs was used for active regions and tunnel junctions, and InP for heat- and current-spreading layers. The optimization of these different alloys, as well as the interfaces between them, was of utmost importance to successful device fabrication. A schematic of a fully fabricated VCL is given in Fig. 1 to illustrate the relationship between the various alloys and their placement in the device structure.

A. AlGaAsSb DBR growth

Lattice-matched $AlAs_{0.56}Sb_{0.44}$ and $GaAs_{0.51}Sb_{0.49}$ has been demonstrated to be a suitable candidate for DBRs in the wavelength span of 1310–1550 nm.[9] We controlled the composition of the AlGaAsSb alloy via short-period superlattices (2.0 nm) with varying duty cycles of AlAsSb and GaAsSb. Using this method we formed alternating 1/4 λ layers of $Al_{0.95}Ga_{0.05}As_{0.54}Sb_{0.46}$ and $Al_{0.30}Ga_{0.70}As_{0.52}Sb_{0.48}$, referred to in this article as 95%AlGaAsSb and 30%AlGaAsSb, respectively. Growth was performed at a temperature of 480 °C as measured using an Ircon optical pyrometer, and a growth rate of 0.35 nm/s. The lattice matching of the ternaries was achieved using the method we have previously reported, in which the beam flux ratio for As/Sb is fixed to ~6.5, and fine-tuning of the composition was done by adjusting the Al and Ga beam fluxes.[10] Stable lattice-matched conditions were possible using this method, with observed x-ray diffraction (XRD) peaks indicating less than 0.01% strain in the growth direction. Minimum defect density and roughness, as measured using atomic force microscopy (AFM), for samples grown using the above parameters were 150 cm^{-2} and 0.17 nm rms, respectively. The bottom (output) DBR for the 1310 nm VCL consisted of 27.5 pairs, while the top (highly reflective) DBR used 39.5 pairs.

B. InP growth diagram

Homoepitaxy of InP, compared to GaAs, has a narrow optimal growth window. Previously we had observed that the defect density in our bulk layers of InP was sufficient to increase optical losses and thus decrease device performance. An investigation of the InP growth diagram for our conditions was thus necessary. We have previously found that InP substrate orientation played a large role in the quality of subsequently grown InP epilayers, with optimum films observed on (001) substrates miscut 0.5° towards the (111)*A* planes. For compatibility with the other requirements of our system, an InP growth rate of 0.15 nm/s was fixed, and other pertinent growth parameters were varied. In Fig. 2 we present the dependence on growth temperature and P_2 beam flux pressure of the macroscopic defect density and rms roughness. In these experiments an InP growth rate of 0.15 nm/s was achieved using an In beam flux of 3.6×10^{-7} Torr.

Growth of InP under 9×10^{-6} Torr P_2 overpressure at a temperature of 465 °C yielded films with defect density equal to 200 cm^{-2} and rms roughness of 0.17 nm for 1 μm thick epilayers. InP which was grown on the optimized AlGaAsSb DBRs described above, however, suffered from increased defect density and roughness. In order to grow the highest quality devices an investigation into the interface between AlGaAsSb and InP was necessary.

1. AlGaAsSb–InP interface

The interface between AlGaAsSb and InP occurred where the bottom DBR and InP heat-current-spreading layer met, as seen in Fig. 1. This interface involved the transition between a quaternary and binary alloy, with no common anions or cations between them. As a result, many different methods for switching from one material to the next could be imagined. Previously, we transitioned from AlGaAsSb to InP by soaking the static AlGaAsSb surface in both As and Sb beams while adjusting the P valve position for InP growth. We then soaked the AlGaAsSb surface under P_2 flux to pump out excess As and Sb for 30 s. InP growth was then initiated. Using this approach (referred to as AsSb soak) occasionally yielded acceptable films, including some of our prior VCL results, but was not sufficiently reproducible for reliable usage. Antimony adatoms present on the static surface tended

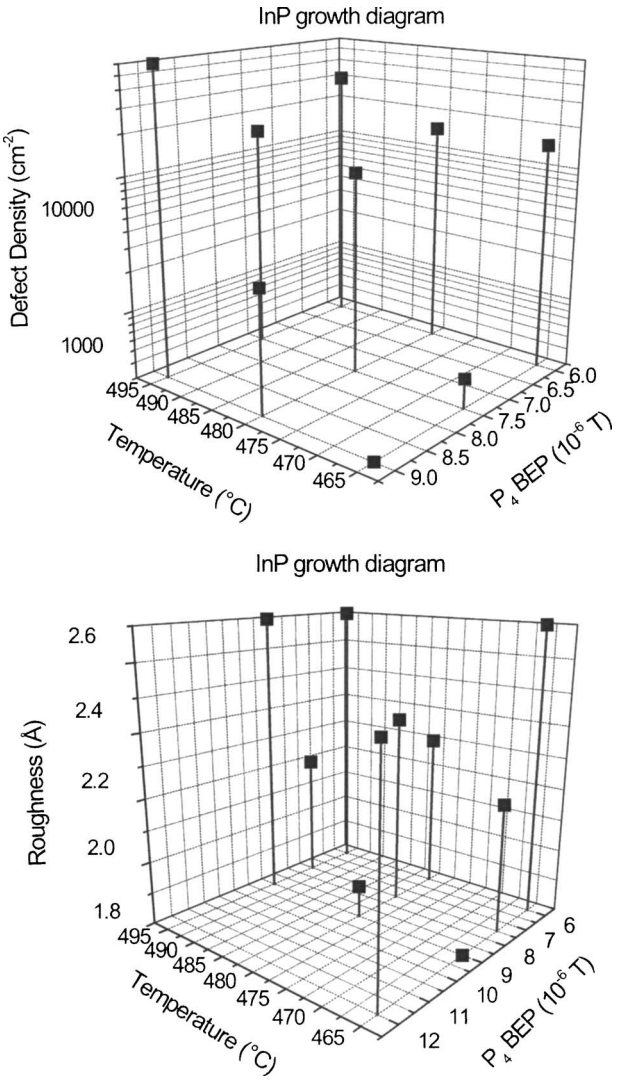

FIG. 2. rms roughness (top) and defect density (bottom) dependence on InP homoepitaxial layers. Growth rate for InP in all cases is 0.15 nm/s.

to remain even with subsequent P_2 soaking, due to the relatively cool growth temperature of 465 °C. This led to the observed defects and roughness. In order to overcome this limitation we developed a transition approach (referred to as P soak) in which P_2 is the only group V species present during the growth pause between AlGaAsSb and InP. This transition used a short initial P_2 soak followed by a thin (2.0 nm) InP buffer layer. This buffer layer was then exposed to the P_2 beam for 60 s to pump out the excess As and Sb still present. Growth of InP continued using the optimized conditions described above. Using this technique we routinely and repeatedly obtained films with low defect density and roughness. In Table I we summarize and compare the two transition methods.

Using this interface transition technique, in conjunction with the optimized AlGaAsSb and InP bulk heteroepitaxy, a full 1310 nm VCL device layer structure was grown. An AFM image of the wafer surface after this 15 μm thick growth is given in Fig. 3. The rms roughness of this surface is 0.31 nm.

TABLE I. Transitions between AlGaAsSb–InP.

AsSb soak	P soak
AlGaAsSb DBR growth	AlGaAsSb DBR growth
Soak AsSb surface with both As_2 and Sb_2 flux—30 s	Soak AsSb surface with only P_2 flux—5 s
Open in shutter, grow according to optimized conditions	Grow 2.0 nm InP buffer layer
	Soak InP buffer layer with P_2 flux—60 s
	Grow remaining InP using optimized conditions
Macroscopic growth results	
Defect density: 5000 cm^{-2}	Defect density: 200 cm^{-2}
rms roughness: 1.5 nm	rms roughness: 0.18 nm

III. VERTICAL CAVITY LASER DEVICE STRUCTURE AND RESULTS

Our 1310 nm VCL structure and design have been detailed elsewhere;[8] the major features are described here, with some of the most pertinent device results provided as well. After MBE growth, the completed all-epitaxial laser structure was fabricated using standard lithographic techniques, with the thin tunnel-junction aperture formed by selectively etching the AlInGaAs with respect to surrounding InP using a solution of citric acid and hydrogen peroxide (10:1 ratio). The devices were then probed on a stage mounted with an InGaAs photodetector, and the light-current-voltage (*L-I-V*) characteristics measured. In Fig. 4 we see *L-I* curves for a range of temperatures, showing continuous-wave (cw) operation up to a maximum of 90 °C. Figure 5 shows the *L-I-V* curves for a device with an aperture diameter of 5 μm at room temperature.

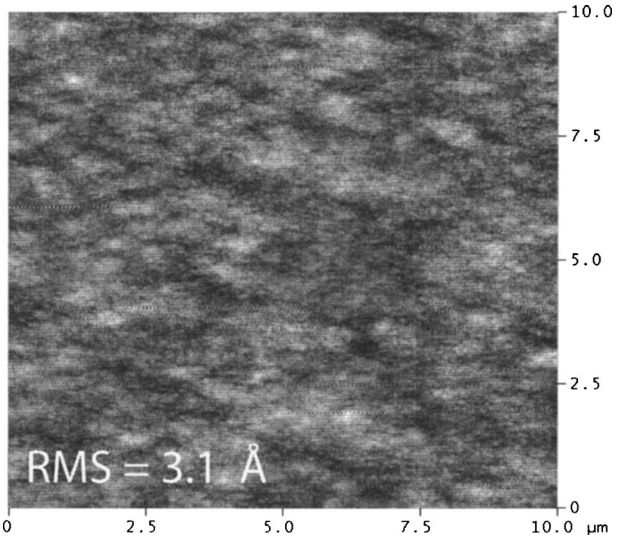

FIG. 3. Atomic-force microscope image of 10×10 μm^2 completed vertical cavity laser layer structure epilayers. The scale in the image is 5 nm. Surface roughness (rms) is 3.1 Å.

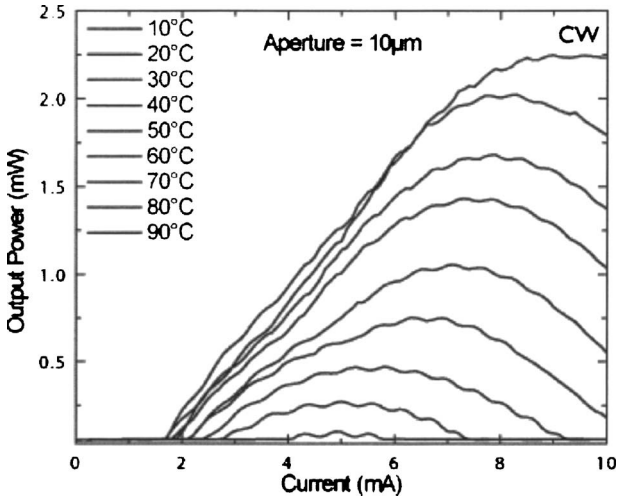

FIG. 4. Light-current curves for a multimode 1310 nm vertical cavity laser operating continuous wave at a range of temperatures. Maximum operating temperature of 90 °C is observed.

This device has single-mode output power greater than 1.0 mW, and differential quantum efficiency of 60%, and other devices exhibited up to 64%. This efficiency is a record for all long-wavelength vertical cavity lasers. The high differential efficiency can be attributed to low excess optical losses in the structure, thanks to the thin tunnel-junction aperture located at the standing wave null of the mode in the optical cavity, along with low free-carrier absorption losses from the mostly *n*-type doping in the structure, and undoped DBRs. The high temperature operation is limited by the active region injection efficiency, which decreased to zero near 120 °C. Rolloff in the output power with drive current is limited by a reduction in injection efficiency with temperature; improvements to the characteristic temperature via redesigning the band structure of the quantum wells and barriers will lead to increased maximum operating temperature for the VCLs. In addition, optimization of the spectral offset between the cavity mode and optical gain peaks should increase the achievable maximum temperature.

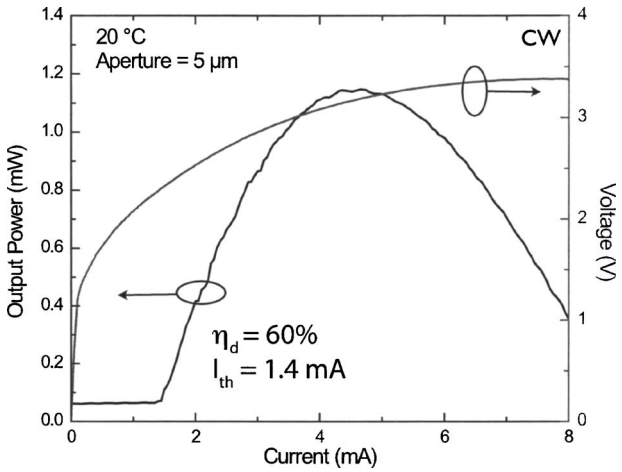

FIG. 5. *L-I-V* curves for a single-mode 1310 nm vertical cavity laser operating continuous wave at room temperature. Maximum output power of 1.1 mW and differential efficiency of 60% are observed.

IV. CONCLUSIONS

Long-wavelength vertical cavity lasers grown all epitaxially on InP substrates can take advantage of AlGaAsSb alloys for highly reflective Bragg mirrors and AlInGaAs alloys for quantum well active regions. The interface between AlGaAsSb and InP has been optimized for minimum defect density and roughness. Growth of complete layer structures with 0.31 nm rms roughness has been demonstrated with low defect density. VCLs at 1310 nm were then fabricated with low-loss thin tunnel-junction apertures for current and optical confinements. Operation at temperatures as high as 90 °C was observed, with single-mode output power above 1.6 mW. Differential quantum efficiency as high as 64% was achieved, a record for long-wavelength vertical cavity lasers.

ACKNOWLEDGMENTS

The authors thank Mr. Geir Myrvågnes for discussion on the AlGaAsSb MBE growth. This work made use of MRL Central Facilities supported by the MRSEC Program of the National Science Foundation under Award No. DMR00-80034 and was funded by NSF under Award No. ECS-0245426.

[1]N. Ueki *et al.*, IEEE Photonics Technol. Lett. **11**, 1539 (1999).
[2]M. Kondow *et al.*, IEEE J. Sel. Top. Quantum Electron. **3**, 719 (1997).
[3]V. Gambin *et al.*, IEEE J. Sel. Top. Quantum Electron. **8**, 794 (2002).
[4]V. Jayaraman *et al.*, IEEE Photonics Technol. Lett. **15**, 1495 (2003).
[5]J. Cheng *et al.*, IEEE Photonics Technol. Lett. **15**, 7 (2005).
[6]R. Shau *et al.*, Electron. Lett. **37**, 1295 (2001).
[7]S. Nakagawa *et al.*, IEEE J. Sel. Top. Quantum Electron. **7**, 224 (2001).
[8]D. Feezell *et al.*, Electron. Lett. **14** (2005).
[9]O. Blum *et al.*, Appl. Phys. Lett. **67**, 3233 (1995).
[10]M. H. M. Reddy *et al.*, Appl. Phys. Lett. **82**, 1329 (2003).

Electrical Design Optimization of Single-Mode Tunnel-Junction-Based Long-Wavelength VCSELs

Manish Mehta, Danny Feezell, David A. Buell, Andrew W. Jackson, Larry A. Coldren, *Fellow, IEEE*, and John E. Bowers, *Fellow, IEEE*

***Abstract*—We present principles for tunnel-junction (TJ) design optimization for use in intracavity contacted long-wavelength vertical-cavity surface-emitting lasers (LW-VCSELs). Using the WKB approximation, we find that layer thicknesses of 10 nm on the n++ side and 10 nm on the p++ side are large enough to maximize quantum tunneling probability and small enough to yield low optical free-carrier absorption loss. We also conjecture that our experimental test structures and actual devices have far lower active acceptor concentration than we expect based on an analytical model. Finally, we calculate the necessary doping levels to enable single-mode operation of LW-VCSELs and incorporate these conditions into a complete optimized model of our VCSELs. Based on optimal I–V curves, we can expect an increase in single-mode output power from 2 to 3.5 mW.**

***Index Terms*—AlInAs, AlInGaAs, current spreading, InP, long-wavelength, tunnel diode, tunnel junction, vertical-cavity surface-emitting laser (VCSEL).**

I. Introduction

TUNNEL junctions (TJ) have found widespread application in high-frequency oscillators and thermophotovoltaic devices since their discovery in 1958 [1]–[3]. More recently, groups have incorporated TJ structures into long-wavelength vertical-cavity surface-emitting lasers (LW-VCSELs) in order to realize reduced optical loss, as well as current and optical confinement. LW-VCSELs offer a low-cost alternative to their in-plane counterparts in the access and metro-area network component market, but performance of these devices has been historically limited by the high resistance and excessive optical loss associated with high acceptor doping levels in the p-type distributed Bragg reflector (DBR) and current spreading layers [4]. In the last several years, groups incorporating TJ structures in LW-VCSELs have demonstrated multimode (MM) output power in excess of 9 mW and single-mode (SM) output power greater than 2.5 mW at 20 °C and 1.5 mW at 70 °C [5]–[9]. Several groups have also reported 3.125-Gb/s SM transmission up to 70 °C [8], [10]. Several other groups have also developed LW-VCSEL structures incorporating TJ layers which are lattice-matched to InP [11], [12].

While groups have presented work on the theoretical modeling and design principles of InGaAs and InGaAsN TJs on GaAs substrates [13], little has been made public about the modeling and design of AlInAs–InP and AlInGaAs–AlInGaAs TJs developed on InP. Moreover, little work has been presented on TJ design for SM applications. The conventional wisdom on TJ growth has been to impress a maximum flux of carbon (C) atoms on a Hall calibration sample of the p++ layer and rely on the measured hole concentration to serve as the experimental limit. Unfortunately, this technique does not provide the most accurate or steadfast TJ design method for several reasons. First, the accuracy of the doping calibration is questionable since the actual AlIn(Ga)As p++ layer thickness (10 nm) is only $\sim 1\%$ of the prepared Hall sample thickness (1 μm). Second, the amphoteric nature of C in AlIn(Ga)As can yield compensation effects reducing the overall hole concentration in the TJ [14]. Finally, since most of the aforementioned groups use an intracavity contact scheme to bypass current conduction through the DBRs, it is necessary that the TJ provides enough lateral spreading resistance to uniformly pump the active region. Designs that fail to take this into account tend to produce MM devices which are not suitable for applications requiring signal propagation longer than several hundreds of meters.

The aim of this paper is to model optimal TJ operation for use in SM LW-VCSELs and incorporate the modeled TJ characteristics with an optimized electrical design for the remainder of the device in order to determine the maximum SM output power for our current structure. In Section II, we present theoretical TJ characteristics based on a model developed by Demassa and Knott [15] and compare modeled TJ characteristics to experimental results. In Section III, we derive the TJ resistivities required for uniform current spreading and SM VCSEL operation over a range of aperture sizes. We proceed to use the model from Section II to determine the TJ doping densities required to achieve these desired resistivities. Since the electrical properties of the TJ are then optimized, Section IV examines physical layer thickness design of the TJ using tunneling probability metrics. We compare the optical loss in the experimental structure and the optimized physical design and quantify the effect of growth aberrations on the optical loss. Section V incorporates the results of the TJ optimization in the previous sections with active region diode characteristics, spreading resistance, heterobarrier voltage, and transport resistances to generate a complete I–V model for the VCSEL. We present two calculated curves—one which closely matches our experimental I–V results and the other which presents a theoretical I–V curve for an optimal device. While some reduction in device voltage arises from changes in device geometry and cavity-length reduction, most of the improvement stems from the TJ optimization presented in earlier sections. Finally, we present the theoretical increase in SM output power and roll-off current associated with optimizing the electrical characteristics of the device.

Manuscript received Febuary 1, 2006; revised March 23, 2006.

The authors are with the Department of Electrical and Computer Engineering, University of California Santa Barbara, Santa Barbara, CA 93106-9560 USA (e-mail: manish@ece.ucsb.edu).

Digital Object Identifier 10.1109/JQE.2006.876713

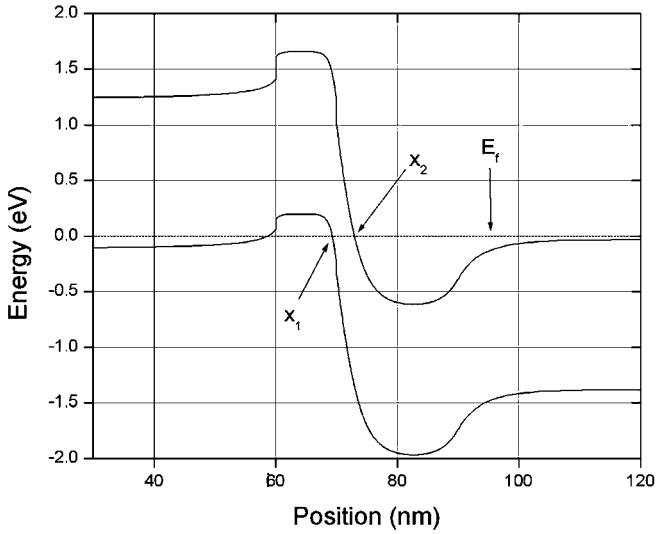

Fig. 1. Band diagram for an p++-AlInAs/n++-InP TJ doped 2×10^{20} cm^{-3} and 5×10^{19} cm^{-3} on the p and n sides, respectively. The points x_1 and x_2 represent the tunneling width limits at the Fermi level at equilibrium. The p side is 10 nm thick while the n side is 20 nm.

II. TJ-Band Diagram, Modeled Characteristics, and Experimental Characteristics

Fig. 1 illustrates the energy-band diagram for an AlInAs–InP TJ doped 2×10^{20} cm^{-3} on the p-side and 5×10^{19} cm^{-3} on the n-side. This particular configuration benefits from a Type-II band alignment which facilitates the degeneracy necessary for TJ operation. The fundamental tunneling current is given by [15]

$$I \equiv A\int [Fc(E)-Fv(E))]^{*}Gc(E)^{*}Gv(E)^{*}z^{*}de \quad (1)$$

where $F_c(E)$ and $F_v(E)$ are the Fermi probability functions in the conduction and valence bands, respectively, $G_c(E)$ and $G_v(E)$ are the density of states functions in the conduction and valence bands, respectively, and z is the tunneling probability. Fig. 1 demonstrates that the stated doping levels place the Fermi level significantly further into the conduction band of the n++ side than the valence band of the p++ side. Since changes in Fermi level will more significantly affect the number of available states in the valence band as opposed to the conduction band, acceptor concentration gradients will predominantly determine the current–voltage (I–V) characteristics of the diode.

A closed-form solution to (1) is given by

$$J \equiv J_p\left(\frac{V}{V_p}\right)\exp\left(1-\frac{V}{V_p}\right) \quad (2)$$

where J_p and V_p are the current density and voltage values corresponding to the peak tunneling current density before the Esaki dip [16]. J_p and V_p have been analytically defined by Demassa *et al.* as [15]

$$V_P \approx \frac{(V_n+V_p)}{3} \quad (3)$$

and

$$Jp = \frac{qm^{*}}{36h^{3}}E_{\perp}D\exp\left[\frac{\pi m^{*1/2}E_g^{3/2}}{2(2)^{1/2}hF}\right]$$

where

$$E_{\perp} = \frac{2^{1/2}hF}{\pi m^{*1/2}E_g^{1/2}}$$
$$F = \left(\frac{q^3}{2\varepsilon}\right)^{1/2} n^{*1/2}V_d^{1/2} \quad (4)$$

where V_n and V_p represent the degree of Fermi-level penetration into the conduction and valence bands on the n and p sides, respectively, m^{*} is the reduced effective mass, D is the overlap integral and can be estimated as V_P, and V_d serves as the diffusion potential estimated by E_g. For simplicity, we assume a homojunction model in our calculations. The staggered lineup of AlInAs–InP TJs simply reduces the diffusion potential and the estimations serve as a worst-case scenario.

We can use (3) and (4) to generate theoretical J–V characteristics for TJs based on doping and bandgap variations and subsequently fit these characteristics to experimental results to deduce the actual doping density of our test structures and devices. Fig. 2 shows J–V characteristics at various bandgap energies for TJs with the expected doping levels mentioned earlier in this section. According to the data, we should observe a negligible 25-mV voltage drop across our AlInAs–InP TJ at a nominal operating current density of 10 kA/cm^2 and reduce the drop even further by using a 1.2Q AlInGaAs–AlInGaAs TJ. The 1.3Q and 1.4Q TJs are instructive for 1.55—μm device design but will severely limit performance in 1.3-μm devices due to band-to-band optical absorption. Groups have seen operating voltage drops on the order of 30 mV in InGaAs-based TJs [17]. The 25-mV voltage drop corresponds to an effective contact resistivity of 2.5×10^{-6} Ω-cm^2, similar to the best p-type contact resistivities and generally accepted n-type contact resistivities [18], [19].

No group developing Al-based TJs for LW-VCSELs has reportedly seen characteristics on par with the values observed in Fig. 2. Our best TJ test structures produce results represented in Fig. 3, with a contact resistivity an order of magnitude larger than the calculated characteristic results ($\sim 2.5\times10^{-5}$ Ω-cm^2). We display the entire forward and reverse bias sweep of the experimental TJ in Fig. 4 to confirm tunneling operation in our devices. We use the peak current density and voltage in all the modeling presented in this work. Fig. 5 shows calculated TJ characteristics more consistent with our VCSEL TJ characteristics. Based on the model, our best test structures show approximate acceptor doping levels of 1×10^{19} cm^{-3}, which is an order of magnitude lower than the designed value. Fig. 5 also shows the impact of 1×10^{18} cm^{-3} changes in acceptor doping levels. Equal changes in donor doping levels yield minimal changes in J–V characteristics.

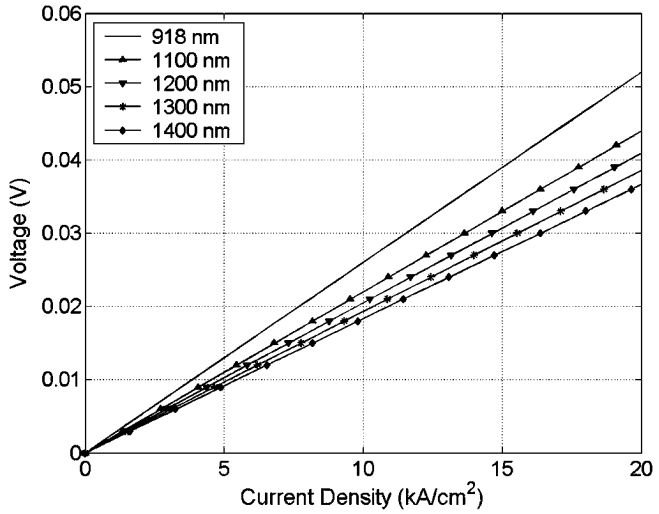

Fig. 2. Calculated variation in characteristics for various band gap TJ characteristics at nominal VCSEL operating current densities (10–20 kA/cm^2). Calculations assume 2×10^{20} cm^{-3} and 5×10^{19} cm^{-3} on the p and n sides, respectively. Recall that the n++ layer thickness is 20 nm and the p++ layer thickness is 10 nm.

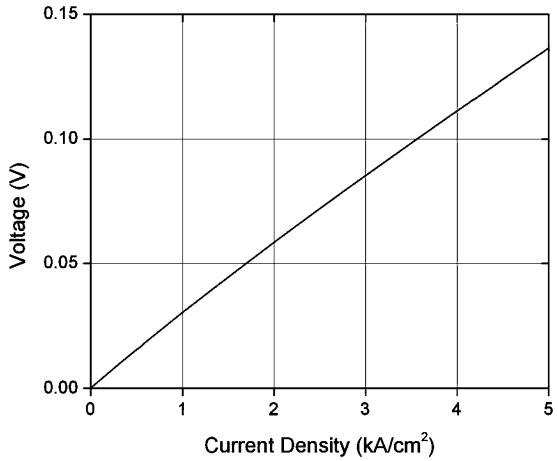

Fig. 3. Measured data for best TJ test structures. Only the reverse bias characteristics are shown to emulate VCSEL I–V characteristics.

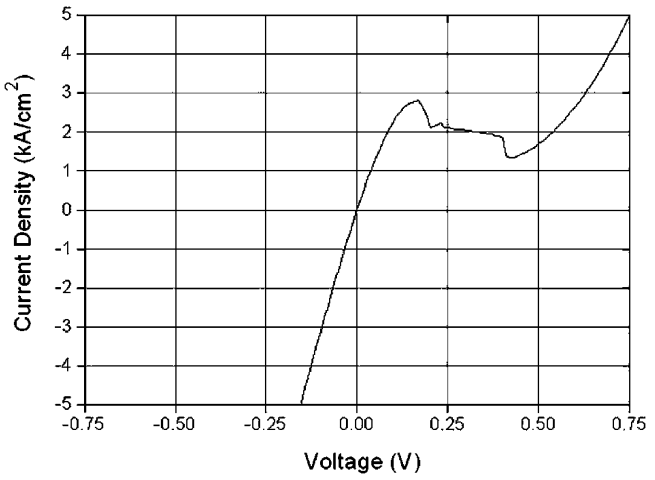

Fig. 4. Forward and reverse bias characteristics of TJ test structure in Fig. 4. Tunneling characteristics are confirmed in quadrant I.

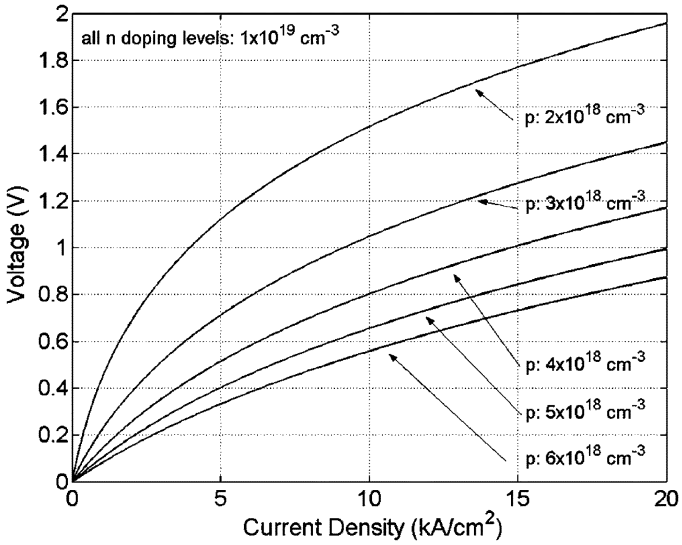

Fig. 5. Calculated J–V curves for TJ structures with lower doping levels than Fig. 2. These curves more closely resemble the experimental data in Fig. 3. The curve shows the large effect of p-doping variation on TJ characteristics. All curves assume n-type doping of 1×10^{19} cm^{-3} and vary p-type doping from 2×10^{18} to 6×10^{18} cm^{-3}.

Several tunnel diode device structures, such as metal–insulator–semiconductor (MIS) devices, take advantage of two-step tunneling associated with deep-level interfacial defects to assist in the tunneling process [20], [21]. Impurities such as Sb at the n++/p++ interface could have the same effect on the TJs examined in this study and, in the process, reduce the absolute resistance of the TJ. Since none of our measured TJs include intentional interfacial impurities, we do not consider the effect of these defects in the modeling of the TJ. Moreover, the mature growth technology associated with the InP-based TJs examined in this work and the onset of tunneling at the origin of the I–V curve lead us to believe that the structure acts as a standard TJ. That being said, we would like to note that further improvements could potentially be made to our TJ through the incorporation of deep level defects at the tunneling interface such as Sb. As a final comment in regards to tunneling mechanisms, we refer to the onset of tunneling at the origin of the I–V curve for the experimental TJ characteristics in Fig. 4. TJ degradation mechanisms involving saturation would manifest themselves as a delay in the reverse bias turn-on characteristics that are not seen in the experimental data.

Actual LW-VCSELs show voltages with even higher extracted resistivities than our best test structures, as will be shown in Section V. Possible reasons for low acceptor levels include nonoptimized C–In and III–V ratios during the epitaxial deposition process and increased dopant diffusion or compensation during growth of the VCSEL structure versus the Hall samples [14]. Furthermore, the electric field gradient will vary for the actual sample when compared with the Hall samples due to the absence of the alternate highly doped layer of the TJ in the Hall sample, presenting another factor which could serve to displace acceptor ions from their primary lattice sites.

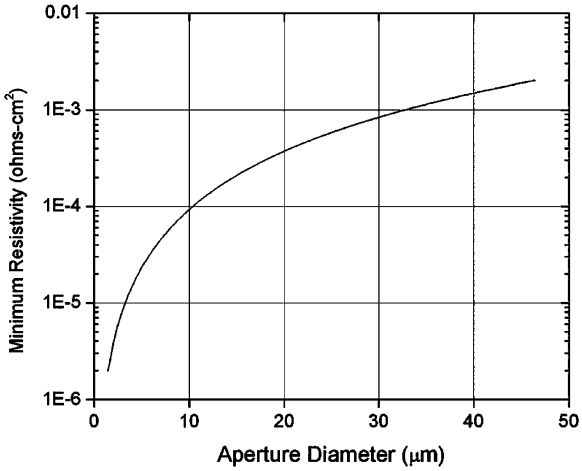

Fig. 6. Minimum TJ resistivity allowed to uniformly spread carriers throughout various diameter TJ aperture.

III. Lateral Current-Spreading Optimization

Given an intracavity contacting scheme, a simple analytic expression to define the current density as a function of distance from the aperture edge is given by [22]

$$J = \frac{V_o}{R_{td}} \exp\left(\frac{x}{\xi}\right), \qquad \xi = \sqrt{l_h^* \sigma_h^* R_{td}} \tag{5}$$

where x is the distance from the aperture edge, R_{td} is the TJ resistivity, l_h is the contact layer thickness, σ_h is the contact layer conductivity, and ξ defines a characteristic length which we will use to determine the optimal resistivity of the current spreading TJ aperture.

In order to realize SM VCSEL operation, the current must spread evenly throughout the TJ aperture. Previous work has shown that, in order for the highly resistive layer to provide uniform current spreading, ξ should be larger than the radius of the current-confining aperture [22]. We hold l_h and σ_h constant at values which optimize the optical loss/resistance tradeoff from the contact layer. Fig. 6 plots characteristic length versus resistivity for our given structural and material parameters and denotes the minimum resistivity necessary to evenly spread carriers in apertures of between 8–20 μm. Any reduction in resistivity from these values will cause current crowding around the edges of the TJ aperture and enhanced MM VCSEL operation. Our VCSEL results corroborate this model as we see more output power in higher order lasing modes rather than the fundamental mode on devices between 12–20 μm [6]. Devices with 8-μm apertures show SM operation and, concurrently, more uniform current distribution. According to Fig. 6, the resistivity threshold for uniform pumping on an 8-μm aperture is 6×10^{-5} Ω-cm^2. While this is a bit higher than our best test structure results, the value is less than what we see in actual devices. Table I shows the p-doping values which correspond to the SM threshold for both 918- and 1200-nm bandgap TJs. We note several observations when considering the data from Fig. 6 and Table I. First, a highly conductive TJ is not the best design for optimized SM performance unless the structure includes an alternate high-mobility layer to spread the carriers uniformly.

TABLE I
Maximum Allowed TJ Doping Levels Which Will Spread Carriers Uniformly Throughout the Aperture for 8-, 12-, 16-, and 20-μm Devices. They Can Also be Thought of as Optimized Doping Levels for SM Device Design

Aperture size (in μm)	Optimized p-doping @ E_g=918 nm	Optimized p-doping @ E_g=1200 nm
8	$5\text{x}10^{18}$ cm^{-3}	$2.3\text{x}10^{18}$ cm^{-3}
12	$3\text{x}10^{18}$ cm^{-3}	$1.5\text{x}10^{18}$ cm^{-3}
16	$2\text{x}10^{18}$ cm^{-3}	$1.1\text{x}10^{18}$ cm^{-3}
20	$1\text{x}10^{18}$ cm^{-3}	$1\text{x}10^{18}$ cm^{-3}

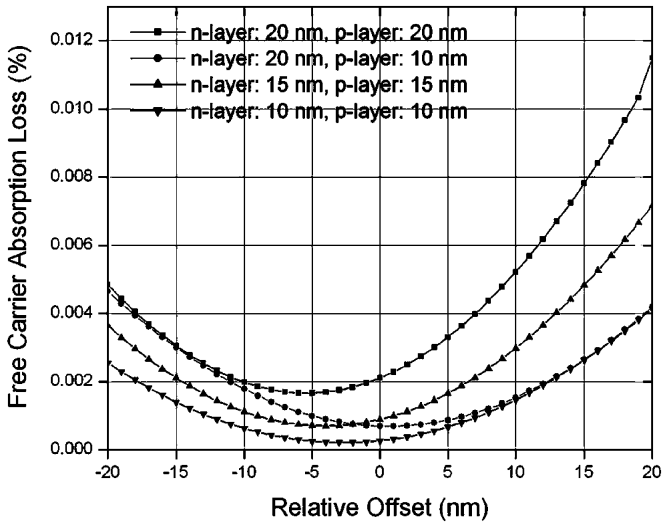

Fig. 7. Free-carrier absorption (FCA) versus relative offset of the n++/p++ TJ interface from a standing wave null. The structure assumes doping levels of 2×10^{18}cm^{-3} and 10×10^{18}cm^{-3} on the p-side and n-side, respectively. The four curves show the loss characteristics for various TJ dimensions. All TJ dimensions illustrated will allow for proper TJ operation.

Second, large devices for use in high-power multimode applications may be better suited for use with current pumping through a DBR which naturally spreads carriers more evenly throughout an aperture than intracavity schemes. However, a highly reflective, highly conductive, and low-loss epitaxial DBR has been difficult to achieve for 1310-nm emitting devices. Solutions such as wafer-bonded devices incorporating conduction through the DBR add an extra voltage component through the bonded interface, and the use of dielectric or metamorphic DBRs eliminates any opportunity to pump current through the DBRs. Therefore, in the case of SM devices, where output power is typically lower, the added free carrier absorption loss and the voltage drops associated with these DBR schemes may limit the benefits of current conduction through the DBR.

IV. WKB Parameter and Tunneling Probability

Before calculating the complete device I–V and L–I characteristics, we define the physical limits of tunneling in order

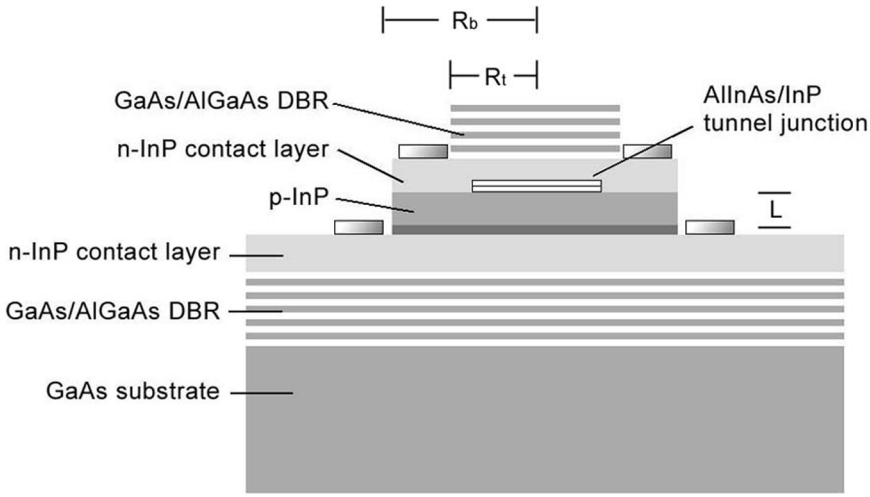

Fig. 8. Basic device structure. R_b represents the bottom contact inner radius and R_t represents the top contact inner radius. These two dimensions define the lateral spreading resistance associated with the intra-cavity contacts. L defines the length of the p-cladding layer.

to minimize optical loss using a metric coined by Mars *et al.*, which is the WKB parameter [13]

$$\text{WKB} \cong 2\int_{x_1}^{x_2} \sqrt{\frac{2m^*}{\hbar^2}(E_c - E_f)dx}. \tag{6}$$

As WKB increases linearly, the tunneling probability z decreases exponentially. The relationship between these parameters can be found elsewhere [13]. The limits of integration x_1 and x_2 are delineated in Fig. 1 and serve as the constructs for the quantum tunneling width. The energy potential barrier is defined as (E_c-E_f) and closely resembles a triangular potential barrier with an energy barrier defined by $(E_g/2 - q\varepsilon x)$, where E_g and ε define the bandgap and electric field, respectively.

The WKB parameter serves as a first-order design metric in determining TJ-layer thickness. The TJ needs to be thick enough so as not to deplete the layers, but as thin as possible to minimize free-carrier optical absorption. Fig. 7 displays the single-pass absorption due to free-carrier losses in the TJ versus the relative offset of the TJ layer from a standing wave null for three-layer thickness variations. We calculate free carrier absorption loss coefficients of 65 cm^{-1} for the p++ side and 20 cm^{-1} for the n++ side for the optimized doping levels on an 8-μm aperture, which is the most likely to provide SM operation, calculated in the previous section [23]. The corresponding optimized doping levels are 5×10^{18} cm^{-3} and 1×10^{19} cm^{-3} on the p-side and n-side, respectively, corresponding to absorption coefficient values of 13 cm^{-1} per 1×10^{18} cm^{-3} and 2.0 cm^{-1} per 1×10^{-18} cm^{-3}, respectively. Zero offset corresponds to the n–p interface placed at a standing wave null. A positive relative offset represents the TJ moving towards the active region of the device. The 20-nm n-layer and the 10-nm p-layer serve as our default test structure values. We can reduce the n-layer thickness from 20 to 10 nm and minimize absorption without any increase in the WKB parameter. We can reduce the n- and p-layer thicknesses even further, but we then begin to see an increase in the WKB parameter and orders-of-magnitude reduction in tunneling probability. The greatest advantage gained from reducing layer thickness and optical loss is improved growth tolerances. We observe an order-of-magnitude increase in loss from growth aberrations on the order of tens of nanometers as we increase the 10-nm TJ layers to 20 nm.

V. Voltage Contribution of Other Sources in an Intracavity Contacted VCSEL Structure

Now that we have theoretically designed the TJ to operate at the lowest possible voltage while still facilitating SM VCSEL requirements, we can incorporate the remaining voltage contributors into a complete electrical model for the device. Fig. 8 shows our complete VCSEL structure. R_t represents the distance from the top contact to the center of the TJ, R_b represents the distance from the lower contact to the center of the TJ, and L represents the thickness of the p-cladding layer. The active region diode, intracavity contact related resistances associated with electron transport from the TJ to the top contact, the bottom contact to the active region, p-cladding layer resistances, and other heterobarrier voltages will also contribute significantly to the overall I–V characteristics of these devices.

The fundamental equation governing the n-contact layer lateral spreading resistance is given by [24]

$$R_{\text{sp}} = \frac{\rho_n}{2L\pi}\ln\left(\frac{R_{\text{t,b}}}{R_a}\right) \tag{7}$$

where ρ_n represents the n-type layer resistivity, $R_{\text{t,b}}$ corresponds to either the top or bottom inner contact radius, and R_a refers to the TJ aperture radius. We calculate the resistance associated with p-cladding layer vertical transport using the basic equation $R = \rho_p L/A$, where A represents the cross-sectional area and ρ_p corresponds to the p-type cladding layer resistivity. Modeled voltage contributions from each of these, given the geometries and thicknesses associated with our experimental structure, are plotted in Fig. 9 for an 8-μm T J aperture. The experimental structure incorporates a 25-μm top inner contact radius and a 46 μm bottom inner contact radius. The values for ρ_n and ρ_p are 3.8×10^{-3} Ω-cm and 0.4 Ω-cm, respectively, based on InP n- and p-type doping levels of 1×10^{18} cm^{-3} and

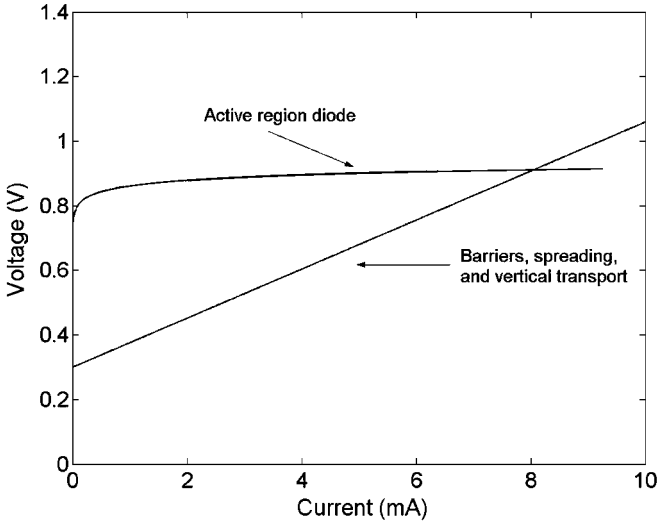

Fig. 9. I–V characteristics of voltage contributions other than the TJ. We include the active region diode characteristic, lateral spreading resistance, vertical transport resistance, and barrier voltage. Device dimensions are 25 and 46 μm for R_t and R_b, respectively, and a 400-nm p-cladding layer.

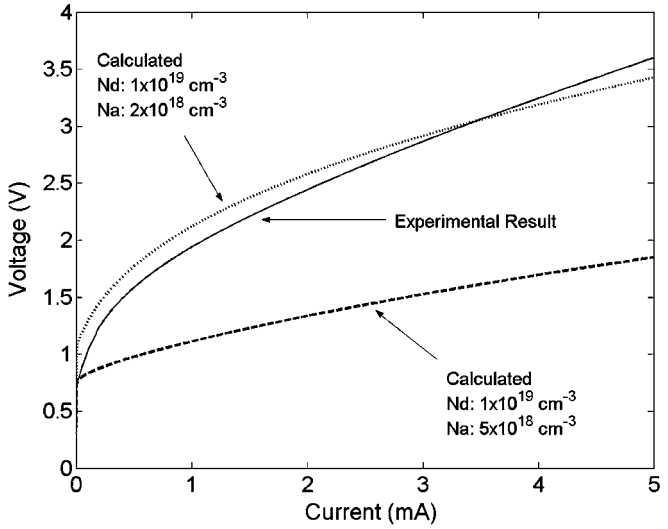

Fig. 10. I–V characteristics for an 8-μm first-generation device versus calculated curves based on the I–V characteristics of the TJ and other factors modeled in this chapter. The top calculated curve shows a nice fit with experimental data while the bottom calculated curve shows optimal I–V characteristics for an 8-μm SM TJ apertured device.

TABLE II
VARIOUS RESISTANCE CONTRIBUTIONS FOR THE FIRST-GENERATION EXPERIMENTAL STRUCTURE VERSUS THE OPTIMIZED DIMENSIONS OF: $R_t = 12\ \mu$m, $R_b = 25\ \mu$m, AND $L = 200$ nm

	Top Contact Spreading Resistance (Ω)	Bottom Contact Spreading Resistance (Ω)	p-Cladding Resistance (Ω)	Hetero-barrier voltage (V)
Experimental Structure	27.1	36.12	32.63	.3
Optimized Structure	16.25	27.1	16.31	0

5×10^{17} cm^{-3}, respectively [23]. The 0.3-V built-in voltage is inherent to the ungraded AlInAs–InP interface between the InP n-cladding and the undoped AlInAs active region layer [25].

We now calculate amount by which we can reduce the voltage contribution of the spreading, transport, and barrier layers by reducing device geometries to sizes still within our fabrication capability. We decrease the top inner contact radius from 25 to 12 μm, decrease the bottom inner contact radius from 46 to 25 μm, reduce the p-cladding layer thickness from 400 to 200 nm, which is a reduction from a full-wavelength layer to a half-wavelength layer, and grade the doping around the hetero-barrier to remove the heterointerface voltage. Table II shows the improvement in differential resistance and voltage calculated at 10 mA for an 8-μm aperture for each of these changes. The optimized geometries reduce the initial voltage drop 0.3 V and improve the overall differential resistance by 36.19 Ω. All differential resistance values are calculated for nominal VCSEL operating current levels, i.e., 10 mA. While the voltage improvement due to geometry optimization is not as large as the improvement afforded through TJ optimization, it is nonetheless important as it nudges the total differential resistance towards 50 Ω, which is a key parameter for devices intended for use in transmission-line systems.

VI. COMPLETE DEVICE MODEL AND SM DEVICE OPTIMIZATION

Now that we have optimized the entire VCSEL design to minimize the voltage contribution of each resistive element in the device while still maintaining uniform current spreading, we can compare I–V models for experimental and theoretically optimized devices and predict the improvement in output power associated with the voltage reduction. An experimental I–V curve for an 8-μm VCSEL is plotted in Fig. 10 along with two calculated curves. All calculated curves assume an 8-μm aperture. The calculated curve which is in strong agreement with the experimental curve is derived using structural and material values equal to those in the experimental structure, which includes an 8-μm-diameter aperture, a 400-nm-thick n-contact layer, and a 400-nm-thick p-contact layer. In order for the curves to closely match, we must reduce the actual acceptor concentration in the p++ AlInAs layer of the TJ to 1.7×10^{18} cm^{-3}. As mentioned in Section II, the overestimated acceptor concentration can arise from many factors, most of which cause large portions of the C content to act as donors rather than acceptors. Low-temperature AlInAs growth as well as C–In ratio and III–V ratio optimization should improve the acceptor concentration in the p++ layers. Other groups developing TJs for use in 1300-nm VCSELs have demonstrated low-voltage devices and confirm that higher acceptor concentrations are possible, although, to the best of our knowledge, none of these groups have designed TJs to optimize SM characteristics.

The maximum acceptor concentration for SM operation as defined by Table I is 5×10^{18} cm^{-3} for an 8-μm device. The second calculated curve in Fig. 10 is a result of combining a TJ with an optimized acceptor concentration and the new device geometries stated in the previous section. This curve presents the optimized I–V characteristics for an 8-μm device. The optimization process reduces the differential resistance from

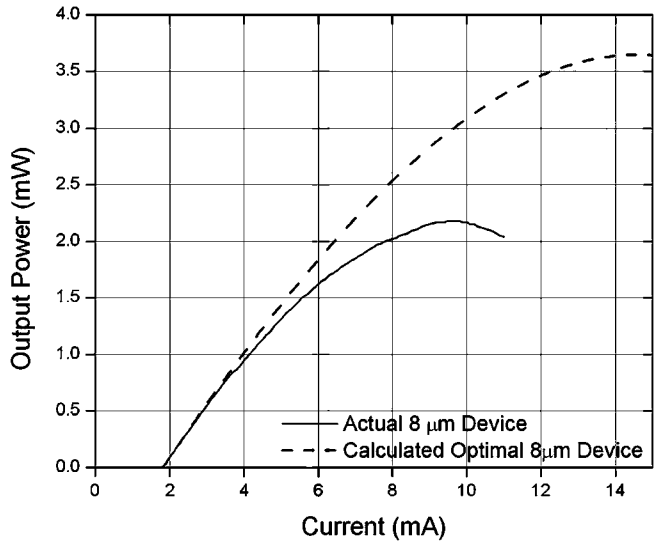

Fig. 11. Perceived improvement in output power through electrical optimization. The calculations are made for an 8-μm aperture diameter at 20 °C.

300 to 150 Ω and allows the devices to operate well under 3 V, which is an important metric in LW-VCSEL design, since most devices are driven by 3.3-V electrical driver circuitry. Given the theoretical improvement in I–V characteristics, we can estimate the potential improvement in output power of the VCSEL, as demonstrated in Fig. 11. We expect the output power to roll over at higher current levels than in the experimental curve due to a slower rate of heating in the active region. The reduction in active region temperature will increase the gain at a given current level. Driving the device at higher current densities will allow excess carriers to contribute directly to stimulated emission and improve the output power of the device. Given a thermal impedance value of 1.289 °C/mW and the LIV characteristics recorded previously [6], we can derive a junction temperature–differential efficiency relationship. We can then apply this relationship to a device exhibiting the optimized I–V characteristics from Fig. 10 in order to predict the differential efficiency at a given current. Using this optimized device design, we see a 1.5-mW increase in output power, which is a significant improvement.

By improving the I–V characteristics, we not only increase the absolute output power, but we also increase the roll-over current of the device. Because the resonance frequency of diode lasers is inherently based on the difference between the drive and threshold currents, increasing the roll-over current will also serve to increase the modulation bandwidth.

VII. Summary

We present a methodology for TJ design and incorporation in SM LW-VCSELs. Using band diagrams and the WKB approximation, we determine the TJ layer thicknesses which optimize tunneling probability and optical loss due to the TJ. We find that our present 20-nm n++-InP layer can be reduced to 10 nm without any loss of tunneling probability.

Once we determine the physical dimensions of the TJ, we examine the effects of varying the doping levels from our expected levels of 5×10^{19} cm^{-3} on the n-side and 2×10^{20} cm^{-3} on the p-side and attempt to match experimental TJ results with calculated curves. While it is evident from inspection that our experimental results do not resemble characteristics of highly degenerate TJs, we quantify the discrepancy as an order of magnitude reduction in acceptor concentration on the p++ side of the TJ. Variations in donor concentration do not prove to have much effect on the operation of InP-based TJs.

While our designed doping levels would yield low voltage devices, the TJs would not support single-mode operation of VCSELs. An 8-μm aperture requires a minimum resistivity of 6×10^{-5} Ω-cm^2 to uniformly inject current into the active region. This resistivity corresponds to an acceptor concentration of 5×10^{18} cm^{-3}, which is more than an order of magnitude less than our design levels. Given this optimized resistivity and doping level, we calculate the I–V and L–I characteristics for an optimized 8-μm device and predict devices operating well under 3 V and SM output powers exceeding 3.5 mW.

References

[1] O. Boriclubecke, D. S. Pan, and T. Itoh, "Fundamental and subharmonic excitation for an oscillator with several tunneling diodes in series," *IEEE Trans. Microw. Theory Tech.*, vol. 43, no. 4, pp. 969–976, Apr. 1995.

[2] O. Kwon, M. M. Jazwiecki, R. N. Sacks, and S. A. Ringel, "High-performance, metamorphic $In_xGa_{1-x}As$ tunnel diodes grown by molecular beam epitaxy," *IEEE Electron Device Lett.*, vol. 24, no. 10, pp. 613–615, Oct. 2003.

[3] L. Esaki, "New phenomenon in narrow germanium para-normal-junctions," *Phys. Rev.*, vol. 109, pp. 603–604, 1958.

[4] D. I. Babic, J. Piprek, K. Streubel, R. P. Mirin, N. M. Margalit, D. E. Mars, J. E. Bowers, and E. L. Hu, "Design and analysis of double-fused 1.55-μm vertical-cavity lasers," *IEEE J. Quantum Electron.*, vol. 33, no. 8, pp. 1369–1383, Aug. 1997.

[5] M. Ortsiefer, S. Baydar, K. Windhorn, G. Bohm, J. Rosskopf, R. Shau, E. Ronneberg, W. Hofmann, and M. C. Amann, "2.5-mW single-mode operation of 1.55-μm buried tunnel junction VCSELs," *IEEE Photon. Technol. Lett.*, vol. 17, no. 8, pp. 1596–1598, Aug. 2005.

[6] V. Jayaraman, M. Mehta, A. W. Jackson, S. Wu, Y. Okuno, J. Piprek, and J. E. Bowers, "High-power 1320-nm wafer-bonded VCSELs with tunnel junctions," *IEEE Photon. Technol. Lett.*, vol. 15, no. 11, pp. 1495–1497, Nov. 2003.

[7] J. Cheng, C.-L. Shieh, X. Huang, G. Liu, M. V. R. Murty, C. C. Lin, and D. X. Xu, "Efficient CW lasing and high-speed modulation of 1.3-μm AlGaInAs VCSELs with good high temperature lasing performance," *IEEE Photon. Technol. Lett.*, vol. 17, no. 1, pp. 7–9, Jan. 2005.

[8] V. Iakovlev, G. Suruceanu, A. Caliman, A. Mereuta, A. Mircea, C. A. Berseth, A. Syrbu, A. Rudra, and E. Kapon, "High-performance single-mode VCSELs in the 1310-nm waveband," *IEEE Photon. Technol. Lett.*, vol. 17, no. 5, pp. 947–949, May 2005.

[9] D. Feezell, D. Buell, and L. Coldren, "InP-Based 1.3–1.6 μm VCSELs with selectively etched tunnel junction apertures on a wavelength flexible platform," *IEEE Photon. Technol. Lett.*, vol. 17, no. 10, pp. 2017–2019, Oct. 2005.

[10] D. Feezell, L. Johansson, D. Buell, and L. Coldren, "Efficient modulation of InP-based 1.3 μm VCSELs with AsSb-based DBRs," *IEEE Photon. Technol. Lett.*, vol. 17, no. 11, pp. 2253–2255, Nov. 2005.

[11] J. Boucart, C. Starck, F. Gaborit, A. Plais, N. Bouche, E. Derouin, J. C. Remy, J. Bonnet-Gamard, L. Goldstein, C. Fortin, D. Carpentier, P. Salet, F. Brillouet, and J. Jacquet, "Metamorphic DBR and tunnel-junction injection. A CW RT monolithiclong-wavelength VCSEL," *IEEE J. Sel. Topics Quantum Electron.*, vol. 5, no. 3, pp. 520–521, May-Jun. 1999.

[12] C. K. Lin, D. P. Bour, J. Zhu, W. H. Perez, M. H. Leary, A. Tandon, S. W. Corzine, and M. R. T. Tan, "High temperature continuous-wave operation of 1.3- and 1.55-μm VCSELs with InP/air-gap DBRs," *IEEE J. Sel. Topics Quantum Electron.*, vol. 9, no. 5, pp. 1415–1421, Sep. –Oct. 2003.

[13] D. E. Mars, Y. L. Chang, M. H. Leary, S. D. Roh, and D. R. Chamberlin, "Low-resistance tunnel junctions on GaAs substrates using GaInNAs," *Appl. Phys. Lett.*, vol. 84, pp. 2560–2562, 2004.

[14] J. Yan, G. Ru, Y. Gong, and F. S. Choa, "Study of P-type carbon doping on $In_{0.53}Ga_{0.47}As$, $In_{0.52}A_{l0.2}Ga_{0.28}As$ and $In_{0.52}Al_{0.48}As$," *Proc. SPIE*, vol. 5260, Applic. Photon. Technol. 6, pp. 446–449, 2003.

[15] T. A. Demassa and D. P. Knott, "Prediction of tunnel diode voltage-current characteristics," *Solid-State Electron.*, vol. 13, pp. 131–131, 1970.
[16] S. M. Sze, *Physics of Semiconductor Devices*. New York: Wiley-Interscience, 1969.
[17] M. Arzberger, M. Lohner, G. Bohm, and M. C. Amann, "Low-resistivity p-side contacts for InP-based devices using buried InGaAs tunnel junction," *Electron. Lett.*, vol. 36, pp. 87–88, 2000.
[18] M. H. Park, L. C. Wang, J. Y. Cheng, and C. J. Palmstrom, "Low resistance ohmic contact scheme (similar to $\mu\Omega\text{cm}^{(2)}$) to p-InP," *Appl. Phys. Lett.*, vol. 70, pp. 99–101, 1997.
[19] C. L. Chen, L. J. Mahoney, M. C. Finn, R. C. Brooks, A. Chu, and J. G. Mavroides, "Low resistance Pd/Ge/Au and Ge/Pd/Au Ohmic contacts to normal-type GaAs," *Appl. Phys. Lett.*, vol. 48, pp. 535–537, 1986.
[20] S. Ahmed, M. R. Melloch, E. S. Harmon, D. T. McInturff, and J. M. Woodall, "Use of nonstoichiometry to form GaAs tunnel junctions," *Appl. Phys. Lett.*, vol. 71, pp. 3667–3669, 1997.
[21] A. M. Andrews, H. W. Korb, N. Holonyak, Jr, C. B. Duke, and G. G. Kleiman, "Tunnel mechanisms and junction characterization in III–V tunnel diodes," *Phys. Rev. B*, vol. 5, pp. 2273–2295, 1972.
[22] J. W. Scott, "Design, fabrication and characterization of high-speed intra-cavity contacted vertical-cavity lasers," Ph.D. dissertation, Elect. Comput. Eng. Dept., Univ. California, Santa Barbara, 1995.
[23] D. I. Babic, "Double-fused long-wavelength vertical-cavity lasers," Ph.D. dissertation, Elect. Comput. Eng. Dept., Univ. California, Santa Barbara, 1995.
[24] E. M. Hall, "Epitaxial approaches to long-wavelength vertical-cavity lasers," Ph.D. dissertation, Mater. Eng. Dept., Univ. California, Santa Barbara, 2001.
[25] J. Piprek, V. Jayaraman, M. Mehta, and J. E. Bowers, "Balanced optimization of 1.31 μm tunnel-junction VCSELs," in *Proc. IEEE/LEOS 3rd Int. Conf. Numerical Simulation of Semicond. Optoelectron. Devices*, Piscataway, NJ, pp. 45–6 2003.

Manish Mehta received the Ph.D. degree in electrical engineering from the University of California, Santa Barbara, in 2006.

He is currently working on the development of mid-infrared semiconductor lasers as a Post-Doctoral Researcher under Dr. Diana Huffaker with the University of New Mexico, Albuquerque.

Danny Feezell received the B.S. degree in electrical engineering from the University of California, Irvine, in 2000, and the M.S. and Ph.D. degrees from the University of California, Santa Barbara, in 2001 and 2005, respectively.

He is currently working on design, fabrication, and characterization of novel GaN-based light-emitting devices as a Post-Doctoral Researcher under Prof. Shuji Nakamura with the University of California, Santa Barbara.

David A. Buell received the Ph.D. degree in materials from the University of California, Santa Barbara, in 2005. His doctoral work focused on InP-based vertical cavity lasers.

He is a researcher of molecular beam epitaxy of III–V and II–IV semiconductors with a focus on optoelectronics and optical phenomena. He is currently researching ZnO at CNRS-CRHEA as a Chateaubriand Fellow.

Andrew W. Jackson recieved the B.A. degree in physics from Princeton University, Princeton, NJ, in 1994, and the Ph.D. degree in materials engineering from the University of California, Santa Barbara, in 1999.

From 1999 to 2002, he worked at Cielo Communications developing the first commercial InGaAsN-based 1.3-μm VCSELs. Since 2003, he has been a Project Scientist with the Electrical and Computer Engineering Department, University of California, Santa Barbara. His research interests are currently focused on materials growth by molecular beam epitaxy. He is the author or coauthor of 30 technical papers and holds seven U.S. patents.

Larry A. Coldren (S'67–M'72–SM'77–F'82) received the Ph.D. degree in electrical engineering from Stanford University, Stanford, CA, in 1972.

After 13 years in the research area at Bell Laboratories, he was appointed Professor of Electrical and Computer Engineering at the University of California at Santa Barbara (UCSB) campus in 1984. In 1986, he assumed a joint appointment with Materials and ECE, and in 2000 the Fred Kavli Chair in Optoelectronics and Sensors. He is also Chairman and Chief Technology Officer of Agility Communications, Inc. At UCSB, his efforts have included work on novel guided-wave and vertical-cavity modulators and lasers as well as the underlying materials growth and fabrication technology. He is now investigating the integration of various optoelectronic devices, including optical amplifiers and modulators, tunable lasers, wavelength-converters, and surface-emitting lasers. He has authored or coauthored over 500 papers, five book chapters, one textbook, and has been issued 32 patents.

Prof. Coldren is a Fellow of the Optical Society of America (OSA) and a past Vice-President of IEEE Laser and Electro-Optics Society (LEOS).

is the Fred Kavli Professor of Optoelectronics and Sensors at the University of California, Santa Barbara, CA. He is also Chairman and Chief Scientist of Agility Communications, Inc. He received the Ph.D. degree in Electrical Engineering from Stanford University in 1972. After 13 years in the research area at Bell Laboratories, he joined UC-Santa Barbara in 1984 where he now holds appointments in Materials and Electrical & Computer Engineering, and is Director of the Optoelectronics Technology Center. In 1990 he co-founded Optical Concepts, later acquired as Gore Photonics, to develop novel VCSEL technology; and in 1998 he co-founded Agility Communications to develop widely-tunable integrated transmitters.

John E. Bowers (S'78–M'81–SM'85–F'93) received the M.S. and Ph.D. degrees from Stanford University, Stanford, CA.

He is the Director of the Multidisciplinary Optical Switching Technology Center (MOST) and a Professor with the Department of Electrical Engineering, University of California, Santa Barbara (UCSB). His research interests are primarily concerned with optoelectronic devices and optical networking. He is a cofounder of the Center for Entrepreneurship and Engineering Management and a cofounder of Terabit Technology and Calient Networks. He worked for AT&T Bell Laboratories and Honeywell before joining UCSB. He has published six book chapters, 350 journal papers, and 600 conference papers and holds 38 patents.

Prof. Bowers is a Fellow of the Optical Society of America and the American Physical Society. He was a recipient of the IEEE LEOS William Streifer Award and the South Coast Business and Technology Entrepreneur of the Year Award.

III. MBE Technology & Devices

C. In-plane Short-Cavity Lasers

Fabrication and molecular beam epitaxy regrowth of first-order, high contrast AlGaAs/GaAs gratings

C. S. Wang,[a] G. B. Morrison, E. J. Skogen, and L. A. Coldren
Department of Electrical and Computer Engineering, University of California, Santa Barbara, California 93106

(Received 14 September 2005; accepted 2 January 2006; published 30 May 2006)

We present a fabrication technique and molecular beam epitaxy (MBE) regrowth of first-order, high contrast AlGaAs/GaAs diffraction gratings for laser emitting at 980 nm. An immersion holography technique is used to uniformly pattern first-order gratings with a pitch of 155 nm. MBE is used to overgrow $Al_{0.75}Ga_{0.25}As$ on etched GaAs gratings. It is found that slow growth rates with optimum arsenic overpressure are necessary to overgrow gratings with low pitting defect densities. These first-order, high contrast gratings are integrated as distributed Bragg reflectors in an edge-emitting laser structure. Single-mode emission at 1 μm with a side mode suppression ratio greater than 30 dB is demonstrated. © *2006 American Vacuum Society.* [DOI: 10.1116/1.2190679]

I. INTRODUCTION

Photonic integrated circuits are providing a solution to the growing demands for low-cost optoelectronics with increased device functionality and improved performance. With lower costs and improved performance, applications for photonic integrated circuits are emerging. For instance, high-efficiency, short-cavity transmitters have recently been developed as part of an optical solution to the growing bandwidth and path-length requirements of chip to chip optical interconnects.[1] These edge-emitting transmitters have higher output powers and bandwidths than conventional vertical-cavity lasers and are therefore able to drive "receiverless" architectures. To accommodate the high power, high-efficiency, and high temperature specifications of an optical interconnect, transmitters operating at a wavelength of 980 nm were fabricated on GaAs.[2]

A key component within these integrated 980 nm transmitters is the distributed Bragg reflector (DBR), which enables single-frequency operation. Fabrication of DBRs for lasers based at 980 nm or shorter wavelengths on GaAs is challenging due to the shorter grating pitch compared to conventional 1550 nm DBRs on InP. For 980 nm DBRs, higher order gratings are used, but these higher order gratings suffer from lower coupling coefficients, larger footprints, and increased loss.[3] Surface gratings and deeply etched gratings have also been used; these take advantage of the large index of refraction difference between semiconductor and air but require very smooth and precise etching techniques and have increased scattering and diffraction losses.[4,5]

In this work, we present an immersion holography technique for the fabrication of first-order gratings. Regrowth over the gratings is accomplished by molecular beam epitaxy (MBE). There have been a few reports of using MBE to regrow gratings, but these generally involve higher order gratings and use lower contrast AlGaAs ($x<0.45$), resulting in a lower grating coupling coefficient κ.[6–8] In order to maximize κ, $Al_{0.75}Ga_{0.25}As$ was overgrown for the realization of strong reflectors with small footprint. The quality of the regrown gratings was studied by varying the growth rate and growth temperatures and evaluated using atomic force microscopy (AFM) and scanning electron microscopy (SEM). These first-order AlGaAs/GaAs DBRs were then successfully integrated into an edge-emitting laser structure.

II. HOLOGRAPHY

We have chosen to use holography over direct e-beam writing to pattern gratings due to advantages of cost, throughput, and simplicity. Figure 1 shows a diagram of the setup. In our holography setup, a HeCd laser emitting at 325 nm is used as the source. The beam is expanded through a pinhole and is incident on a rotational stage consisting of the sample and an optical mirror. The reflection from the mirror creates a standing wave pattern which exposes the photoresist on the sample surface in a spatially periodic manner. The resulting grating pitch Λ is controlled by the stage angle θ by the following equation, $\Lambda=\lambda_{laser}/2 \sin\theta$, as plotted in Fig. 2.

With the 325 nm wavelength of the HeCd laser, a stage angle of $\theta=45°$ results in $\Lambda=\sim 240$ nm, suitable for 1550 nm based applications, as shown by the right stage in Fig. 1. By rotating the sample and mirror relative to the incident light, the grating pitch can be adjusted. At the limiting incident angle of 90°, the pitch can be reduced to 163 nm, but this is an impractical exposure angle and is unsuitable for gratings at 980 nm.

In order to achieve $\Lambda=\sim 155$ nm necessary for first-order 980 nm Bragg gratings, a shorter incident wavelength must be used in the holography setup. However, we have developed a more elegant solution of reducing the effective wavelength of the HeCd source using a prism. As shown by the left stage in Fig. 1, a prism replaces the conventional mirror stage. The sample is adhered to one side of the prism with xylene, which also acts as an index-matching fluid. The expanded laser beam enters the prism through the hypotenuse face of the prism and standing wave patterns are created

[a]Electronic mail: cswang@engineering.ucsb.edu

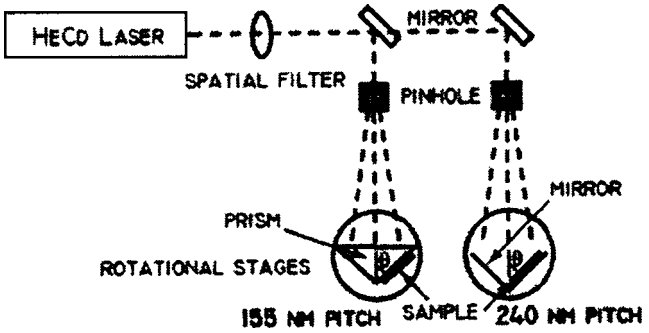

FIG. 1. Schematic of the holography setup. The right stage is used for exposing gratings with ~240 nm pitch. The left stage is used for exposing gratings with ~155 nm pitch through a prism. The sample adheres to the prism by using the index-matching fluid xylene.

from reflections from the two sides of the prism. As shown in Fig. 2, the wavelength of the HeCd source is reduced by $n_{\text{prism}}=1.482$, and the resulting pitch at $\theta=45°$ is ~155 nm. The hypotenuse face of the prism was antireflective coated to prevent unwanted reflections.

To pattern the GaAs wafers, first photoresist was spun onto the samples which were then patterned using the immersion holography technique. Typical exposure energies were 30 mJ. After developing the exposed photoresist, the samples were subjected to a 7 s O_2 plasma ashing to ensure that the semiconductor is clearly exposed at the bottoms of the photoresist gratings. The duty cycle of the gratings can be controlled by the exposure time and power of O_2 plasma ashing. Next, the grating pattern was transferred into the GaAs wafer by using an inductively coupled plasma reactive ion etch with Cl_2-BCl_3-Ar. The target etch depth was 45 nm deep. Figure 3 shows a SEM image of the etched gratings. The gratings are uniform with square shape. Finally, the samples were cleaned for regrowth. The grating pitch can be accurately measured by placing the finished sample back on the prism and measuring the diffraction angle of the incident beam.

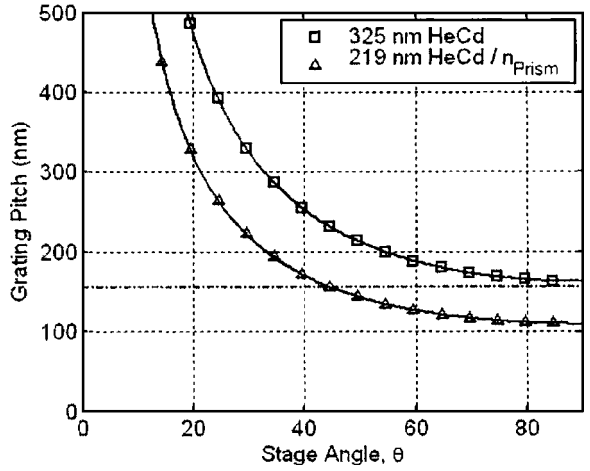

FIG. 2. Grating pitch as a function of stage angle. The HeCd laser source is limited to a minimum pitch of 163 nm. By reducing the wavelength via a prism, a 155 nm pitch is achievable at an angle of ~45°.

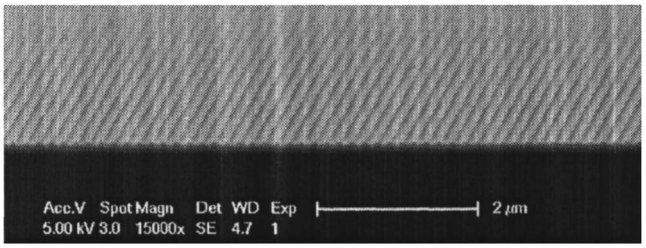

FIG. 3. Scanning electron micrograph of gratings patterned by immersion holography and etched into GaAs.

III. MBE REGROWTH

All growths and regrowths were performed in an ultrahigh vacuum Varian Gen II solid-source MBE system with valved As source. To study the quality of overgrowth on gratings by MBE, the growth rate and growth temperature T_g were varied. The gratings used for these regrowths were fabricated without the use of the prism for simplicity. Gratings were etched into 1 μm GaAs epi templates grown on (100) GaAs substrates. Regions of each sample were covered with Si_xN_y prior to holography and selectively etched in order to obtain both regions with and without gratings. Prior to loading into the MBE chamber for regrowth, the SiN was removed and the samples were subjected to a 1 h UV ozone treatment followed by 30 s 1:2 BHF:DI dip.

Oxide desorption was kept consistent throughout the regrowths. With an As_2 overpressure of 1×10^{-5} (V/III ratio=25), the substrate was heated to a temperature of 620 °C, as measured by an optical pyrometer, upon which (4×2) reconstruction could be seen. The substrate was then held at 625 °C for 2 min before cooling to growth temperature. It was found that holding the substrate hotter or longer resulted in significant surface migration of the GaAs grating tooth, essentially destroying the square grating shape. While not used in this work, including a hydrogen radical cleaning step prior to oxide desorption has been shown to effectively remove oxides and contaminants.[9,10] This would eliminate the need for high temperature thermal oxide desorption to further preserve the grating shape and improve regrowth quality.

Regrowths consisted of first depositing 1 nm of GaAs followed by a 6 nm grade up to $Al_{0.75}Ga_{0.25}As$. After 900 nm of $Al_{0.75}Ga_{0.25}As$, the regrowth finished with a 45 nm grade down to 100 nm of GaAs. Initial regrowths were performed with a V/III ratio of 25. Digital superlattices were used for the AlGaAs which has been found to result in better material quality than compared to analog growth.[8] When regrowing over gratings using growth conditions of 1 μm/h growth rate at $T_g=600$ °C, the resulting epi was rough and had dense pitting defects, as shown in Fig. 4(a). To reduce the pitting defects, the growth rate was slowed and the substrate temperature was varied. Slowing the growth rate has been shown to reduce threading dislocation defects.[8] Similarly, we found that the pitting defect density was reduced for slower growth rates of 0.5 and 0.2 μm/h, as shown in Figs. 4(b) and 4(c). In addition, three substrate temperatures of 585, 600,

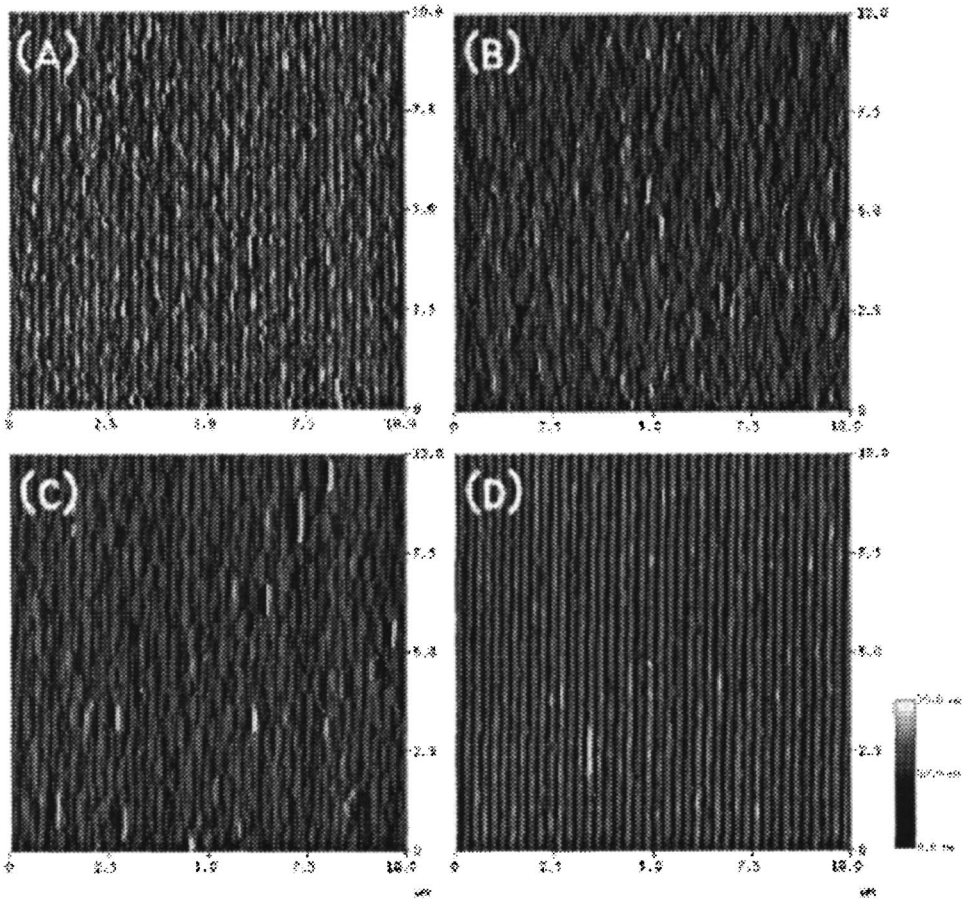

FIG. 4. AFM images of regrown gratings for growths rates of (a) 1 μm/h, (b) 0.5 μm/h, and (c) 0.2 μm/h grown at 600 °C. The sample in (d) is regrown gratings with an initial slow growth rate of 0.2 μm/h at V/III=15, then finished with a 1 μm/h growth rate at V/III=25 grown at T_g =585 °C. 1 μm of $Al_{0.75}Ga_{0.25}As/GaAs$ was regrown over GaAs gratings.

and 615 °C were used to observe the effect of T_g. While not as pronounced, hotter growth temperatures tended to somewhat reduce pitting defects.

While slowing the growth rate and increasing the growth temperature improved growth over grating regions, growth over field regions without gratings became rougher. Field regions grown either at 0.2 μm/h or at 615 °C yielded rms roughness values in excess of 13 Å. It was found that a lower V/III ratio was needed to smooth out the field regions, resulting in rms roughness values of around 3 Å. Lowering the arsenic overpressure did not adversely affect growth over grating regions. The final regrowth condition used was an initial slow growth rate of 0.2 μm/h at T_g=585 °C with a V/III ratio of 15. After 0.5 μm of growth, the cell temperatures were heated and the remainder of the growth occurred at a growth rate of 1 μm/h, also at T_g=585 °C. Figure 4(d) shows an AFM image of regrowth over gratings with the dual growth rate conditions. While the finished growth is not planar, this should not adversely affect the gratings since the surface is significantly far away from the lasing mode. It is more important to note that the pitting defects have been minimized, which would be a larger source of scattering loss.

IV. DEVICE PERFORMANCE

To investigate the performance of the gratings, the gratings were monolithically integrated into a DBR laser structure, with a side-view schematic as shown in Fig. 5. The gain section is 250 μm long; a DBR is used for the rear mirror and a cleaved facet is used for the front mirror. Behind the DBR is active material that serves as a back absorber to prevent reflections back into the cavity.

Complete details of the epitaxial structure and fabrication process can be found in Ref. 2. A centered quantum well structure was used consisting of three InGaAs/GaAs sandwiched between $Al_{0.3}Ga_{0.7}As$ waveguides. A 65 nm GaAs layer above the waveguide serves as the grating and regrowth layer. After patterning and etching gratings using the immersion holography technique, regrowth was performed to overgrow a 1.8 μm thick $Al_{0.75}Ga_{0.25}As$ p cladding. The dual growth rate conditions similar to the one used for Fig. 4(d)

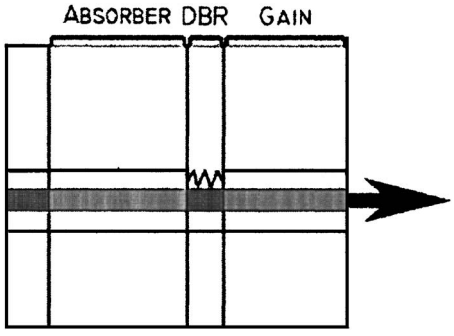

FIG. 5. Side-view schematic of the DBR laser structure.

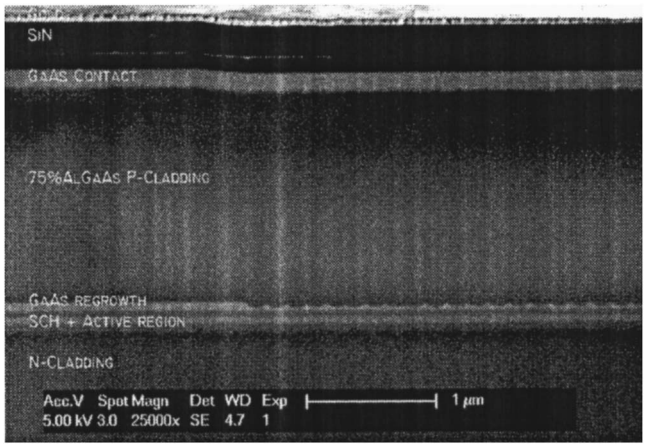

FIG. 6. SEM of regrown laser structure showing both field and grating regions.

were applied for these DBR lasers. Figure 6 shows a SEM of a regrown laser structure, showing both active and grating regions. From the SEM, overgrowth on the gratings has resulted in a somewhat triangular shape. This is most likely due to some diffusion that occurs during the entire regrowth, which has decreased the tooth depth to ~25 nm from a target etch depth of ~40 nm. This slight reduction in κ can be improved by increasing the etch depth and adjusting the duty cycle.

The DBR lasers were tested under continuous wave (cw) operation, and the light and voltage characteristics are plotted in Fig. 7. The devices were operated single mode at 1003 nm with 30 dB side mode suppression, as shown in the inset. A threshold current of 16 mA (J_{th}=2133 A/cm^2) was measured and output powers of 5 mW were achieved with a gain section current of 45 mA.

To calculate the κ of the gratings, the subthreshold spectra of the DBR laser were measured, as shown in Fig. 8. Using the method described by Yee *et al.*, the subthreshold mode spacing was measured to be .49.[11] The simulated effective

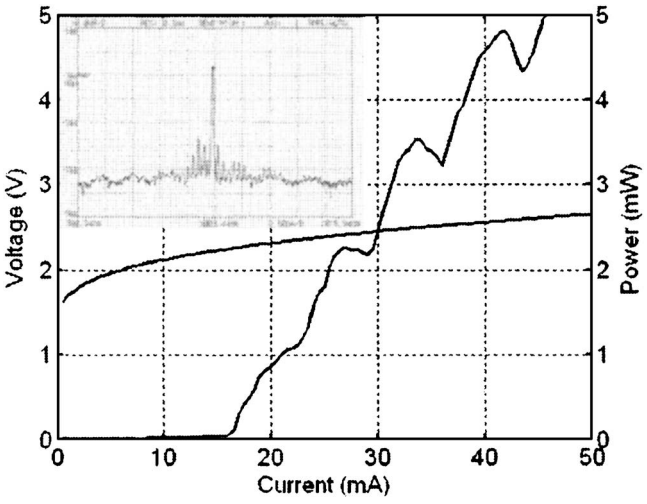

FIG. 7. cw LIV of the DBR laser. The kinks in the power curve are due to mode hops. The inset shows a lasing spectrum of the device biased at 2.5I_{th}.

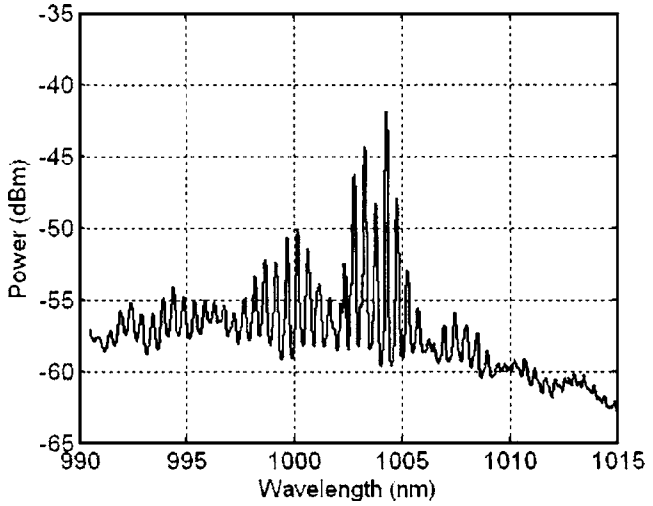

FIG. 8. Subthreshold spectra of the DBR laser biased at 0.98I_{th}.

group index η_{ge} of the laser structure is 3.85. From this, the effective cavity length L_{eff} is 267 μm, which corresponds to a κ of 312 cm^{-1}. From measurements on the SEM, this value is slightly lower than the simulated κ of ~400 cm^{-1} for a triangular shaped grating for a tooth depth of 25 nm. Nevertheless, high-κ gratings have been demonstrated and implemented in a DBR laser structure.

V. SUMMARY

In conclusion, first-order, high contrast AlGaAs/GaAs diffraction gratings have been developed and implemented into a DBR laser emitting at 980 nm. An immersion holography technique has been developed to fabricate uniform gratings, and optimum regrowth conditions by MBE were found to overgrow and fill in the gratings. The gratings were successfully integrated in a DBR laser structure resulting in single-mode emission at 1 μm. While initial results of the DBR laser showed relatively low output powers, this could be improved by increasing the injection efficiency of the material. Additional optimization of the epilayer structure could also be made, particularly band engineering the GaAs regrowth layer to eliminate this hole barrier in the laser section and improve the waveguiding for optimal modal overlap with the active region. Further improvements to the gratings could be made by adding additional hydrogen cleaning and adjusting for diffusion during regrowth.

ACKNOWLEDGMENTS

The authors would like to thank the excellent laboratory support of John English. This work was supported by DARPA under the C2OI program. This work made use of MRL Central Facilities supported by the MRSEC Program of the National Science Foundation under Award No. DMR00-80034.

[1]C. S. Wang, E. J. Skogen, J. W. Raring, G. B. Morrison, and L. A. Coldren, *Proceedings of the International Semiconductor Laser Conference* (IEEE, Piscataway, NJ, 2004), pp. 8–9.
[2]G. B. Morrison, C. S. Wang, E. J. Skogen, D. D. Lofgreen, and L. A. Coldren, Proceedings of the Integrated Photonics Research and Applications, San Diego, CA, 2005, Paper No. IWF2.
[3]G. M. Smith, J. S. Hughes, M. L. Osowski, D. V. Forbes, and J. J. Coleman, IEE Electronics Lett. **30**, 651 (1994).
[4]Y. Yuan, T. Brock, P. Bhattacharya, C. Caneau, and R. Bhat, IEEE Photonics Technol. Lett. **9**, 881 (1997).
[5]D. Hofstetter, B. Maisenhölder, and H. P. Zappe, IEEE J. Sel. Top. Quantum Electron. **4**, 794 (1998).
[6]M. Ilegems, H. C. Casey, S. Somckh, and M. B. Panish, J. Cryst. Growth **31**, 158 (1975).
[7]S. Noda, K. Kojima, K. Mitsunaga, K. Kyuma, K. Hamanaka, and T. Nakayama, IEEE J. Quantum Electron. **23**, 188 (1987).
[8]G. W. Pickrell *et al.*, J. Appl. Phys. **96**, 4050 (2004).
[9]T. M. Burke, E. H. Linfield, D. A. Ritchie, M. Pepper, and J. H. Burroughes, J. Cryst. Growth **175/176**, 416 (1997).
[10]H. Künzel, J. Bōttcher, A. Hase, H.-J. Hensel, K. Janiak, G. Urmann, and A. Paraskevopoulos, J. Cryst. Growth **175/176**, 411 (1997).
[11]H. H. Yee, H. T. Hsu, J. Y. Chang, and P. C. Chen, Proc. SPIE **4216**, 103 (2001).

Short-Cavity 980 nm DBR Lasers with Quantum Well Intermixed Integrated High-Speed EA Modulators

Chad S. Wang[†], Yu-Chia Chang[†], James W. Raring[*], and Larry A. Coldren[†*]
[†]*ECE Dept. University of California, Santa Barbara, CA 93106*
[*]*Materials Dept. University of California, Santa Barbara, CA 93106*

Phone: 805.893.7065, Fax: 805.893.4500, Email: cswang@engineering.ucsb.edu

Abstract: Short-cavity, 980nm DBR lasers with integrated EAMs were designed and fabricated using a quantum well intermixing processing platform. RF bandwidths of 16GHz were achieved and open eyes at 10Gb/s were observed with >7dB dynamic extinction.

1. INTRODUCTION

For photonics to replace electronics in applications such as board-to-board and chip-to-chip level interconnects, there is a clear need for increased speed and efficiency. Vertical cavity lasers have demonstrated high efficiencies, but operation to higher data rates is challenging [1]. We have previously demonstrated high efficiency, short-cavity distributed Bragg reflector (DBR) lasers at 1.55 μm with integrated, high bandwidth (25 GHz) electro-absorption modulators (EAM) [2]. By using a quantum well intermixing (QWI) integration platform, the laser and modulator can be simultaneously optimized for high performance. Recently, 980 nm DBR lasers with quantum well intermixed passive sections have been demonstrated with output powers up to 400 mW [3]. Moreover, intermixed quantum well (QW) EAMs have also shown promise to extend data rates up to 40 Gb/s and beyond [4]. Here, we present a short-cavity, 980 nm, DBR laser using a QWI platform in the InGaAs/GaAs/AlGaAs material system, monolithically integrated with a high-speed EAM demonstrating 16 GHz of 3dB bandwidth.

2. DEVICE

The integrated DBR laser-EAM is designed with 3 sections: gain, front DBR mirror, and EAM, as shown in the side-view schematic of Fig. 1a. A high reflectivity (HR) coating is applied to the rear facet. The gain section of the device is 110 μm long designed for low thresholds and high slope efficiency. The front DBR is 20 μm long, and makes use of deep gratings, targeting a coupling coefficient, (κ), of 650 cm^{-1}. The epitaxial base structure consists of 3 InGaAs/GaAs quantum wells centered between two $Al_{0.3}Ga_{0.7}As$ waveguide layers, as shown in Fig. 1b. The upper waveguide also includes a GaAs regrowth layer followed by a sacrificial InGaP layer. An impurity-free quantum well intermixing process described in [5] was used to monolithically integrate high-speed QW-EAMs with the DBR laser. Selective intermixing of the EAM, DBR, and passive regions of the device was achieved by depositing SiO_2 followed by a rapid thermal anneal (RTA) at 850°C. The gain section of the laser was maintained at the as-grown band-edge, λ_{pl} = 977 nm, by applying a surface fluorination treatment to suppress intermixing. Figure 2a shows the photoluminescence (PL) spectra for the two band-edges used for this work; the EAM and passive regions (λ_{pl} = 949 nm) were intermixed 28 nm from the active band-edge. Following QWI, the sacrificial InGaP layer is removed, and first order gratings are patterned using an immersion holography technique and dry etched into the GaAs regrowth layer [6]. Regrowth of the upper p-cladding and p-contact was performed by molecular beam epitaxy [6]. Ridge waveguides 3 μm wide were patterned, benzocyclobutene (BCB) was defined beneath the EAM contacts for low capacitance, and isolation was accomplished by proton implantation. The wafers were thinned, backside metalized, and cleaved into bars. Subsequently, the front and rear facets of cleaved bars were AR and HR-

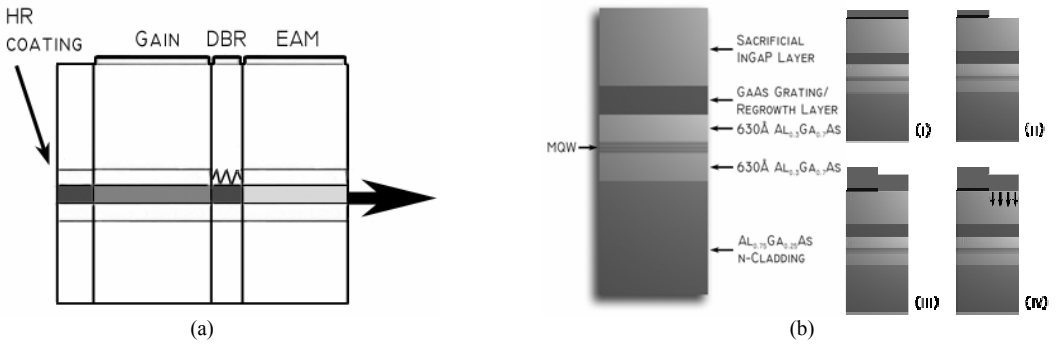

FIGURE 1. (a) Side view schematic of the integrated short-cavity DBR laser-modulator, illustrating the Gain, DBR, and EAM sections. (b) Epitaxial base structure. To the right illustrates the intermixing process used: (i) surface fluorination followed by SiO_2 deposition; (ii) removal of the SiO_2 and fluorination layer; (iii) deposition of a second SiO_2 layer; (iv) RTA to drive vacancies down through the multiple quantum well active region.

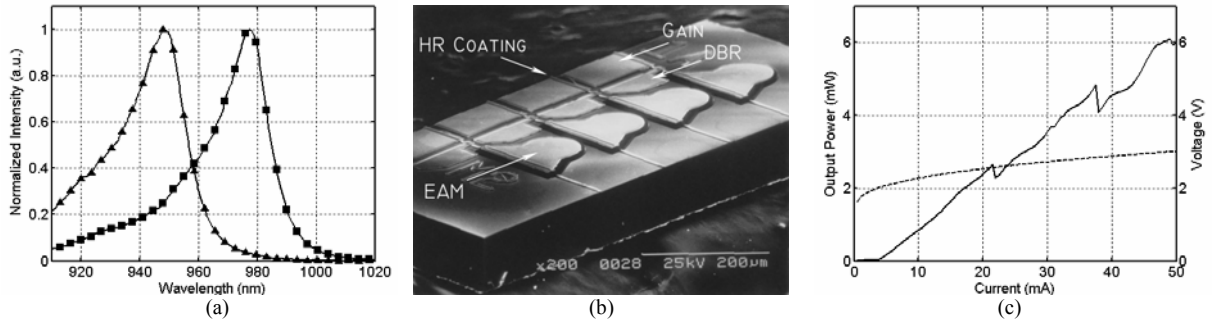

(a) (b) (c)

FIGURE 2. (a) PL spectra for device shown in this work. Symbols indicate active region photoluminescence (squares) and EAM/passive section photoluminescence (triangles). (b) SEM of a fabricated 4-element DBR laser-modulator. (c) Room temperature continuous wave light (solid) and voltage (dashed) characteristics of the integrated DBR laser-modulator.

coated, respectively. Finally, the devices were mounted onto AlN carriers and wire-bonded to RF pads for high-speed testing. A scanning electron micrograph (SEM) of a fabricated 4-element array is shown in Fig. 2b.

3. RESULTS

The DBR laser had a threshold current of 5 mA and demonstrated output powers up to 6 mW at a gain section current of 50 mA, as shown in Fig. 2c. We expect to see higher output powers upon improving the low injection efficiency of these devices. The 125 µm long integrated EAM exhibited over 10 dB of optical extinction with 5 dB/V efficiency, and the small signal 3dB modulation bandwidth was measured to be 16 GHz, as shown in Fig. 3a and 3b, respectively. Large signal digital modulation experiments were performed at 10 Gb/s using a nonreturn to zero pattern and a pseudorandom-bit-sequence of 2^{31}-1. Open eye diagrams were achieved with 7.7 dB dynamic extinction at a DC bias of -2.5 V and a 3 V peak-to-peak swing. Corresponding bit error rate (BER) curves is plotted in Fig. 3c, demonstrating error-free operation at 10^{-9}. Higher data rates were not able to be tested due to equipment limitations.

4. CONCLUSION

We have demonstrated short-cavity DBR lasers emitting at 980 nm with integrated QW-EA modulators fabricated using a QWI platform. The integrated QWI EAMs demonstrated 16 GHz bandwidth and error-free operation at 10 Gb/s, with further optimization possible for increased high-speed performance. With QWI, the band-edge of each section of the device can be individually optimized, resulting in monolithic integration of lasers with high-performance QW-EAMs.

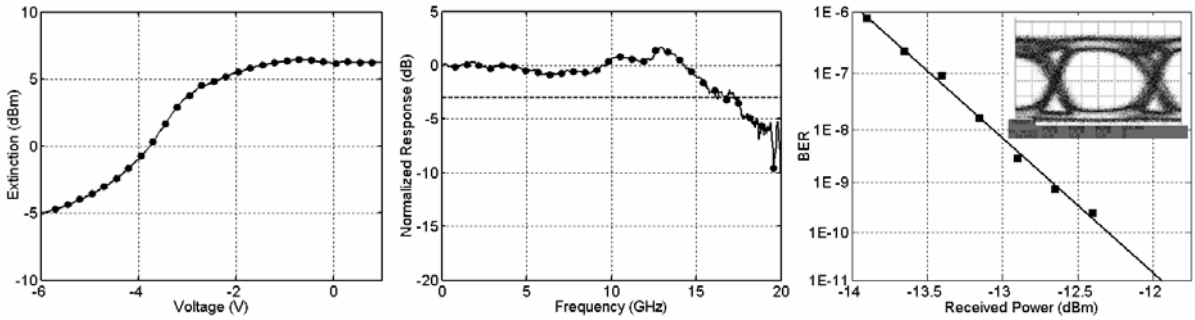

(a) (b) (c)

FIGURE 3. Performance characteristics of a 125 µm long QWI EAM: (a) DC optical extinction, (b) 3 dB modulation bandwidth of 16 GHz, and (c) BER curve and open eye diagram at 10 Gb/s.

5. REFERENCES

[1] N. Suzuki, et al., "25-Gbps operation of 1.1-µm-range InGaAs VCSELs for high-speed optical interconnections," *Optical Fiber Communications Conference*, Technical Digest, paper no. OFA4, 2006.

[2] E.J. Skogen, et al., "Monolithically Integrated Active Components: A Quantum-Well Intermixing Approach," *IEEE J. of Sel. Topics in Quantum Electronics*, vol. 11, no. 2, pp. 343-355, 2005.

[3] K. Song, et al., "High Power 1060 nm DBR Lasers with Quantum Well Intermixed Passive Sections," *Proceedings of the 18th Annual Meeting of the IEEE Lasers and Electro-Optics Society*, pp. 949-950, 23-27 Oct. 2005.

[4] J.W. Raring, et al., "Low Drive Voltage, Negative Chirp 40 Gb/s EA-Modulator/Widely Tunable Laser Transmitter, Using Quantum-Well Intermixing," *Optical Fiber Communications Conference*, Technical Digest, postdeadline paper no. PDP26, 2006.

[5] G.B. Morrison, et al., "980 nm DBR Lasers Monolithically Integrated with EA Modulators for Optical Interconnect Applications," P*roceedings of the Integrated Photonics Research and Applications*, San Diego, CA, paper no. IWF2, 2005.

[6] C.S. Wang, et al., "Fabrication and molecular beam epitaxy regrowth of first-order, high contrast AlGaAs/GaAs gratings," *J. of Vacuum Science and Technology:B*, vol. 24, no. 3, May/June 2006.

IV. Spin-Wave Physics of Quantum Structures

Transient Spin-gratings of Itinerant Electrons in Lightly-doped GaAs Quantum Wells

S. G. Carter, Z. Chen, and S. T. Cundiff
JILA, University of Colorado and National Institute of Standards and Technology, Boulder, Colorado 80309-0440
cartersg@jilau1.colorado.edu

A. S. Huntington and L. A. Coldren
Materials Department, University of California, Santa Barbara, California 93106

Abstract: Spin gratings lasting longer than the carrier lifetime are measured in lightly *n*-doped quantum wells. In a magnetic field, precession of the grating is observed, and diffusion rates are determined by varying the grating period.

OCIS Codes: (320.7130) Ultrafast processes in condensed matter, including semiconductors; (300.2570) Four-wave mixing

The use of spins to store and transmit information requires an understanding of both spin relaxation and transport. In semiconductor systems, time-resolved optical pump-probe measurements are often used to study these phenomena, demonstrating long-lived (tens of nanoseconds) electron spin polarizations that can be transported over distances greater than 100 μm [1]. Transient spin grating experiments are similar to pump-probe measurements but two pump pulses are used to generate a grating of spins with alternating polarizations. For crossed-linear polarized pump pulses, the net polarization varies from right-circular to left-circular, which modulates the carrier spin orientation across the sample. (For co-linear polarized pump pulses, the intensity across the sample is modulated, leading to a population grating.) A delayed probe pulse is diffracted off of this grating until the grating decays due to spin relaxation and diffusion. These transient spin gratings have been measured in undoped GaAs quantum wells (QWs) [2,3], giving the electron spin relaxation times and diffusion rates. Recently, spin Coulomb drag in highly *n*-doped QWs was demonstrated by examining the decay of spin gratings [4]. In these experiments, the spin gratings typically decayed with a time constant on the order of 10 ps, before recombination of the optically generated carriers. This summary describes experiments in lightly *n*-doped GaAs QWs, in which spin gratings can last about 1 ns, long after carrier recombination. In the presence of a magnetic field in the QW plane, the spin grating precesses, leading to a signal that oscillates at twice the precession frequency. The results demonstrate the generation of a spin grating of itinerant electrons and give insight into spin dynamics in semiconductors.

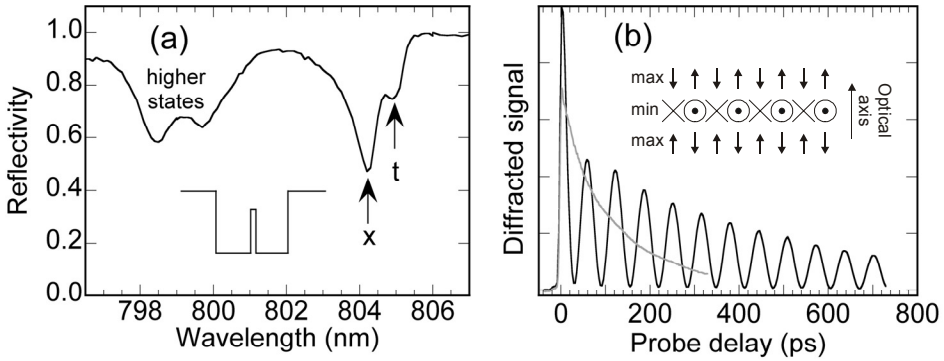

Fig. 1. (a) Sample reflectivity with the lowest exciton (x) and trion (t) states labeled. The QW profile is inset in the graph. (b) Transient population (grey line) and spin (black line) gratings vs probe delay taken with a magnetic field of 2 T. The probe was set to 804.8 nm. The inset displays the spin grating orientation for maximum and minimum signal.

The sample used for these measurements consists of 10 periods of coupled GaAs QWs, with Silicon modulation doping centered in the 41 nm $Al_{0.3}Ga_{0.7}As$ barriers. The coupled QWs are 10 nm and 12 nm in width, separated by a 2.5 nm $Al_{0.2}Ga_{0.8}As$ tunnel barrier [see inset of Fig. 1(a)]. The sample was designed to have an electron concentration of ~2×10^{10} cm^{-2} per pair of wells, with the electron wavefunction extending into both wells. A distributed Bragg reflector is behind the QWs, so the reflectivity of the sample [Fig. 1(a)] is essentially double-pass

transmission. Transient grating experiments were performed with the pumps set to the exciton/trion resonance near 804 nm with a bandwidth of ~4 nm. The linear polarized probe was made spectrally narrow (~0.2 nm) using a pulse shaper and was typically set near the trion resonance.

Figure 1(b) displays transient population and spin gratings in the presence of a 2T magnetic field oriented in the QW plane. The population grating decays with a time constant of 280 ps [5]. For crossed-linear polarized pumps, spins are initially oriented perpendicular to the QW planes but precess about the magnetic field at the Larmour frequency. The inset of Fig. 1(b) displays the changing orientation of the spin grating relative to the probe optical axis. When the spin grating is aligned with the optical axis of the probe (perpendicular to the QW planes), the contrast in the optical susceptibility across the grating is at its maximum. When the spin grating is oriented in the QW plane, the optical susceptibility is uniform for the probe, thus giving no diffracted signal. The field of the diffracted beam oscillates at the Larmour frequency, so the intensity oscillates at twice this frequency. The oscillation frequency in Fig. 1(b), 15.5 GHz, was confirmed to be double the precession frequency by time-resolved Kerr rotation (TRKR) measurements. The spin grating signal can be fit to the square of a decaying cosine, $\left[A\cos(\omega t+\phi)\exp(-t/\tau)\right]^2$. This fit gives a decay time of 0.92 ns.

The population and spin gratings decay due to both relaxation and diffusion according to $\gamma_{pg,sg} = D_{p,s}q^2 + \Gamma_{p,s}$. The population (spin) grating decay rate is γ_{pg} (γ_{sg}), the diffusion rate is D_p (D_s), the relaxation rate is Γ_p (Γ_s), and the grating wavevector is q. The data in Fig. 1(b) was taken with a pump angle of ~4.3° (grating period Λ = 10.7 μm, q = 0.59 μm^{-1}). Measurements were taken for a series of grating spacings with the probe at the exciton (804.2 nm) and the trion (804.8 nm) resonances. The grating decay rate is plotted vs. q^2 in Fig. 2 for (a) the population gratings and (b) the spin gratings. The decay rate appears to be fairly linear with q^2, and the slope is not significantly different for the two probe wavelengths. The slopes give D_p = ~28 cm^2/s and D_s = ~13 cm^2/s, and the intercepts give $1/\Gamma_p$ = 148 ps (350 ps) and $1/\Gamma_s$ = 880 ps (1530 ps) for the probe at the exciton (trion). Since the spin grating decay time is much longer than the population relaxation time (*i.e.* the recombination time), we attribute the spin grating to the itinerant electrons. The dependence of the spin relaxation time on probe wavelength is not well understood. TRKR measurements also show an interesting dependence on probe wavelength with two precession frequencies appearing under some conditions. Further work must be performed to understand this unique behavior.

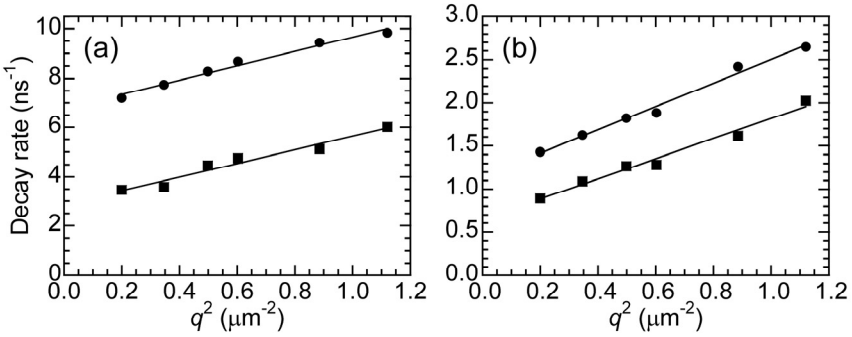

Fig. 2. Decay rate of (a) population and (b) spin gratings as a function of the grating wavevector squared.The probe was set to the exciton (trion) energy for the circles (squares). The lines are linear fits to the data points.

Transient grating experiments provide a useful tool in studying spin dynamics. The technique has a number of advantages over the more common method of TRKR in that the signal is background free and it allows easy measurement of spin diffusion. Until now, measurements have been in systems where the spin gratings decayed rapidly, before carrier recombination. The results in this summary demonstrate spin gratings that last longer than the carrier lifetime, indicating the formation of spin gratings of itinerant electrons. These measurements have also been performed for the first time in a magnetic field, exhibiting oscillations at twice the Larmour precession frequency.

[1] J. M. Kikkawa and D. D. Awschalom, "Lateral drag of spin coherence in gallium arsenide," *Nature* **397**, 139-141 (1999).
[2] A. R. Cameron, P. Riblet, and A. Miller, "Spin Gratings and the Measurement of Electron Drift Mobility in Multiple Quantum Well Semiconductors," *Phys. Rev. Lett.* **76**, 4793-4796 (1996).
[3] S. Adachi, Y. Takagi, J. Takeda, and K. A. Nelson, "Optical sampling four-wave-mixing experiment for exciton relaxation processes," *Opt. Comm*. **174**, 291-298 (2000).
[4] C. P. Weber, N. Gedik, J. E. Moore, J. Orenstein, J. Stephens, and D. D. Awschalom, "Observation of spin Coulomb drag in a two dimensional electron gas," *Nature* **437**, 1330-1333 (2005).
[5] Since the diffracted intensity is proportional to the square of the grating amplitude, the signal decays with time constants half of those given in the text.

Nondestructive Optical Measurements of a Single Electron Spin in a Quantum Dot

J. Berezovsky, M. H. Mikkelsen, O. Gywat, N. G. Stoltz, L. A. Coldren, D. D. Awschalom*

Kerr rotation measurements on a single electron spin confined in a charge-tunable semiconductor quantum dot demonstrate a means to directly probe the spin off-resonance, thus minimally disturbing the system. Energy-resolved magneto-optical spectra reveal information about the optically oriented spin polarization and the transverse spin lifetime of the electron as a function of the charging of the dot. These results represent progress toward the manipulation and coupling of single spins and photons for quantum information processing.

The prospect of quantum computation in conventional material systems has spurred much research into the physics of carrier spins in semiconductor quantum dots (QDs) (*1*).

Center for Spintronics and Quantum Computation, University of California, Santa Barbara, CA 93106, USA.

*To whom correspondence should be addressed. E-mail: awsch@physics.ucsb.edu

An important element necessary for spin-based quantum computing is the readout of the qubit spin state. Previously demonstrated schemes for single spin readout in a QD include optical measurements, such as photoluminescence (PL) polarization (*2*, *3*) or polarization-dependent absorption (*4* *6*). Single spins can also be read out electrically by measuring the spin-dependent probability for an electron to tunnel out of the

dot (*7*). However, these methods are destructive, in that they either remove the spin from the dot or drive transitions in the system with a resonant optical field. In contrast, we describe measurements of a single electron spin using Kerr rotation (KR), in which the spin state is probed nonresonantly, thus minimally disturbing the system. This effective spin-photon interaction has been shown to allow for Schrödinger's cat–type measurements to probe quantum effects such as measurement-induced decoherence and spin squeezing (*8*, *9*), as well as the implementation of quantum information protocols involving spin-photon entanglement (*10*) and optically mediated spin-spin entanglement (*11*–*13*).

In the present work, the electrons were confined to a single charge-tunable QD formed by monolayer fluctuations at the interfaces of a gallium arsenide (GaAs) quantum well (QW). The QD layer was centered within an optical microcavity with a resonance chosen to enhance the interaction of the optical field with the QD at energies well below the lowest interband transition. By the application of a transverse magnetic field, the electron spins can be depolarized in a Hanle-type measurement, thereby yielding information about the spin lifetime.

The magneto-optical Kerr effect results in a rotation of the plane of polarization of linearly polarized light with energy E upon reflection off the sample and is analogous to the Faraday effect for transmitted light. For both effects, the rotation angle is determined by the difference of the dynamic dielectric response functions for left and right (σ^+ and σ^-) circularly polarized light, which are proportional to the interband momentum matrix elements $\langle\psi_c|\hat{p}_x \pm i\hat{p}_y|\psi_v\rangle$, where ψ_c (ψ_v) is a conduction (valence) band state (*14*, *15*), and $\hat{p}_x$ and $\hat{p}_y$ are the components of the electron momentum operator perpendicular to the growth direction. As a result of the microcavity, both reflection and transmission contribute to the measured polarization rotation. For simplicity, we refer only to KR. For a single conduction-band energy level in a QD containing a spin-up electron in a state $|\psi_\uparrow\rangle$, optical transitions to the spin-up state are Pauli-blocked, and the KR angle θ_K is then given by

$$\theta_K(E) = CE \sum_{\alpha=\pm1;v} \alpha|\langle\psi_\downarrow|\hat{p}_x + \alpha i\hat{p}_y|\psi_v\rangle|^2 \frac{E - E_{0,v}}{(E - E_{0,v})^2 + \Gamma_v^2} \quad (1)$$

where C is a constant, and $E_{0,v}$ and Γ_v are the energy and linewidth of the transition involving $|\psi_v\rangle$, respectively. We focus on a single transition in the sum in Eq. 1 and drop the index v. For $\Gamma << |\Delta| << E$, where $\Delta = E - E_0$, we note that $\theta_K \sim \Delta^{-1}$, which decays slower than the absorption line ($\sim\Delta^{-2}$) (*15*, *16*). Therefore, for a suitable detuning Δ, KR can be detected whereas photon absorption is strongly suppressed.

The sample structure (Fig. 1A) is grown by molecular beam epitaxy and consists of a single 4.2-nm GaAs QW in the center of a planar aluminum GaAS ($Al_{0.3}Ga_{0.7}As$) λ-cavity (*17*). The reflectivity of the sample at 10 K (Fig. 1D) shows a cavity resonance centered at 763.6 nm (1.624 eV) with a quality factor of 120. The probe light effectively interacts with the spin many times as it is reflected back and forth within the cavity. As a result, the polarization rotation described by Eq. 1 occurs repeatedly, enhancing the small, single spin KR angle (*18*). Based on previous measurements with similar cavities (*19*, *20*), we expect the KR at the peak of the cavity resonance to be enhanced by a factor of ~15.

The band profile for our structure (*17*), calculated with a one-dimensional self-consistent Poisson-Schrödinger solver, is shown in Fig. 1B. By the application of a bias voltage V_b across the structure, the conduction-band minimum in the QW can be made to plunge beneath the Fermi level, charging first the QDs, then the well itself (*21*, *22*). The onset of this charging occurs around 0.5 V (Fig. 1C) according to the band-structure calculation.

A continuous wave (cw) Ti-sapphire laser (1.654 to 1.662 eV) is focused through a microscope objective (spot size ~ 2 μm) on the sample at temperature T = 10 K to excite electron-hole pairs into the continuum of states in the QW. The carriers then relax into the QDs, and the subsequent PL is collected through the same objective, dispersed in a spectrometer, and detected by a liquid nitrogen–cooled charge-coupled device. In a typical single-dot PL spectrum as a function of the applied bias (Fig. 2A), the sharp features (linewidth ~100 μeV) are characteristic of single-dot PL (*23*), demonstrating the presence of only one QD within the laser focus. Above 0.5 V, a single line is observed at 1.6297 eV, which is attributed to recombination from the negatively charged exciton (trion or X^-) state. Below 0.5 V, this line persists faintly, and a bright line appears 3.6 meV higher in energy because of the neutral exciton (X^0) transition. The presence of the X^- line at $V_b < 0.5$ V implies that occasionally a single electron is trapped in the dot, forming an X^- when binding to an electron and a hole. In addition, a faint line at 1.6292 eV is visible from radiative decay of the biexciton (XX). These assignments of the observed lines are consistent with measurements on

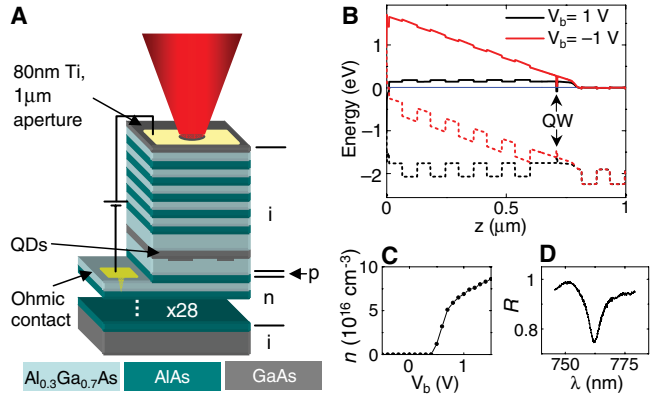

Fig. 1. Sample structure and characterization. (**A**) Schematic of the sample structure. i, n, and p indicate intrinsic (undoped), n-doped, and p-doped regions of the sample, respectively. Twenty-eight repetitions of the AlAs/AlGaAs layers, indicated by x28, are not shown. AlAs, aluminum arsenide. (**B**) The calculated conduction (valence) band profile along the growth direction z shown in solid (dashed) lines. Raising the bias voltage V_b from −1 to 1 V lowers the QW conduction-band minimum past the Fermi level (blue). (**C**) The calculated electron density n in the QW showing the onset of charging at V_b = 0.5 V. (**D**) The reflectivity R of the cavity at T = 10 K versus wavelength λ, with a resonance at 763.6 nm.

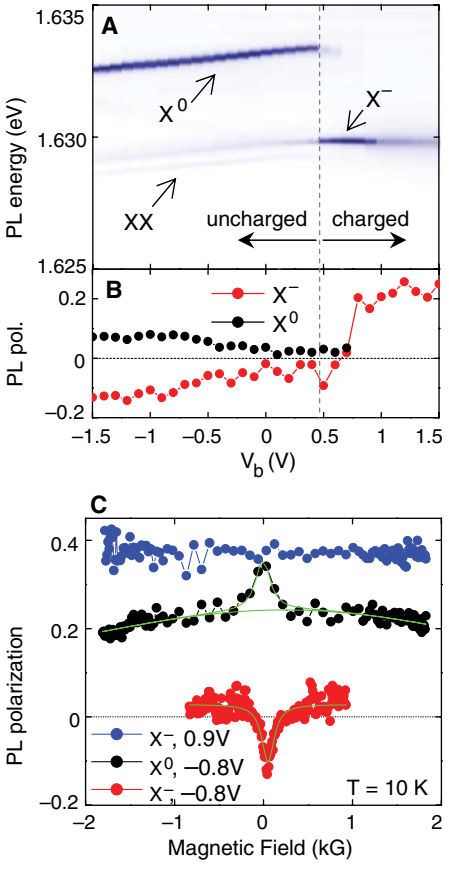

Fig. 2. Single-dot PL and Hanle measurements. (**A**) PL of a single QD as a function of V_b. A jump in the PL energy indicates the onset of QD charging. (**B**) The polarization (pol.) of the X^- and X^0 PL lines as a function of bias. (**C**) Hanle curves in the charged regime (blue) and in the uncharged regime (black and red).

similar structures (*2*, *22*) and are further supported by the linear dependence of the X^- and X^0 lines and the quadratic dependence of the XX line on the excitation intensity. Figure 3C illustrates these three optical transitions. In this QD, we see no evidence of a positively charged exciton.

With circularly polarized excitation, spin-polarized electrons and heavy holes can be pumped into the QD because of the optical selection rules of the GaAs QW (*2*, *24*). For the purposes of this discussion, spin polarization parallel to the optically injected electron spin polarization will be referred to as "spin up" and the opposite spin as "spin down." Information about the spin polarization in the QD can be gained from the polarization of the PL (*2*). The circular polarization of the PL is determined by switching the helicity of the pump from σ^+ to σ^- and measuring the intensity of the σ^+-polarized PL (I^+ and I^-, respectively). The polarization is then defined as $P = (I^+ - I^-)/(I^+ + I^-)$ and is shown for the X^0 and X^- lines in Fig. 2B, in agreement with earlier results (*2*, *22*).

The polarization of the X^- line is determined by the hole spin, as the two electrons in the trion form a spin-singlet state. In the uncharged regime ($V_b < 0.5$ V), the negative polarization of the X^- PL indicates that the heavy hole undergoes a spin flip before recombination in most cases. Hole spin flips may occur either during energy relaxation in the QW (*25*) or by an exchange-mediated electron-hole spin flip (*26*). Regardless of the hole spin-flip process, after the recombination of the X^-, the electron left in the QD is polarized in the spin-up direction. In this way, both optical injection and trion recombination serve to pump lone spin-up electrons into the QD.

When the dot is initially charged near V_b = 0.5 V, the now dominant X^- line remains negatively polarized, resulting in continued pumping of the spin-up state. As the electron density in the QW increases with higher applied bias, the X^- polarization becomes positive, as has been previously observed (*2*, *22*).

In a transverse applied magnetic field, the electron spins precess, depolarizing the PL. The hole spins do not precess (*27*) because the heavy and light hole states are split [by ~20 meV in our sample (*28*)], leading to an effective heavy-hole g factor of zero in the plane of the QW. Hanle measurements on this dot are summarized in Fig. 2C. In the charged regime, at V_b = 0.9 V, no depolarization of the X^- PL is observed, as expected for polarization resulting from the hole spin. The case is markedly different at V_b = –0.8 V, in the uncharged regime. Here, the (negatively polarized) X^- line is depolarized with a half-width $B_{1/2}$ = 80 G. With an estimated electron g factor of g_e = 0.2 (*2*), $B_{1/2}$ = 80 G corresponds to a time-averaged transverse spin lifetime $T_2^* = \hbar/B_{1/2}g_e\mu_B$ = 7 ns, where μ_B is the Bohr magneton and $\hbar$ is Planck's constant h divided by 2π. This sharp Hanle peak has been previously attributed to the electron spin in the QD, before X^- formation (*2*). The X^0 line shows a much broader peak ($B_{1/2}$ = 4.1 kG), with a small narrow component at low field. The broad component is consistent with the radiative lifetime of the exciton (~50 ps) (*4*). The narrow component has a $B_{1/2}$ = 95 G, which is similar to the X^- width. Indeed, this narrow peak is expected if a lone electron in the dot can bind and recombine with a subsequently injected hole. Similar features have been observed in ensemble Hanle measurements in GaAs QWs (*29*).

In the uncharged regime, spin-polarized excitons or electrons can be pumped into the dot. Both optical injection and trion recombination

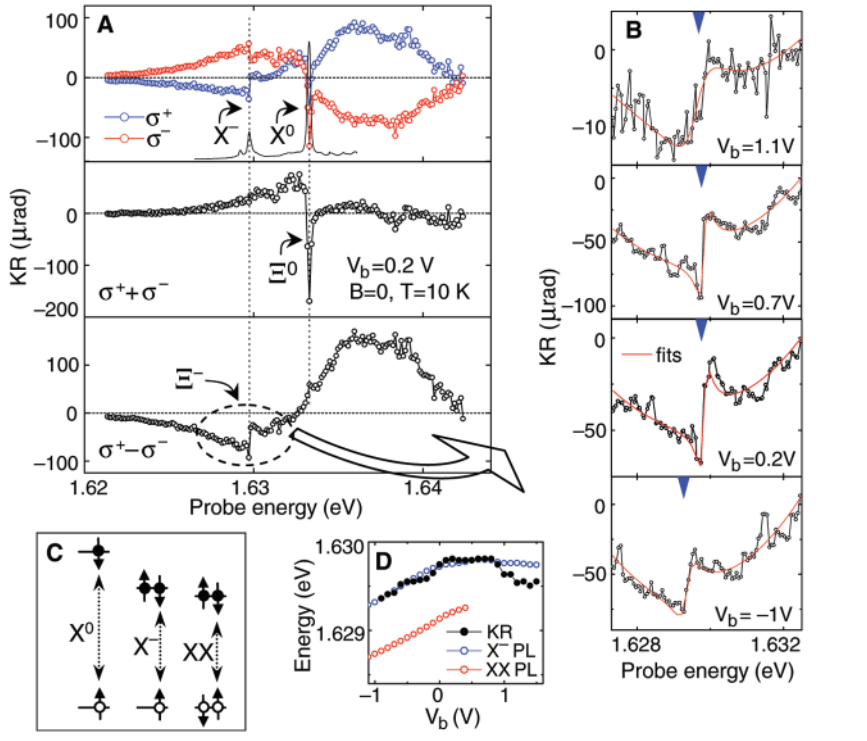

Fig. 3. Single-dot KR spectra. (**A**) Top panel, KR measured with a σ^+- and σ^--polarized pump at V_b = 0.2 V. The PL at this bias is also shown. Middle panel, the sum of the σ^+ and σ^- data showing a spin-independent feature Ξ^0 at the X^0 energy. Bottom panel, the difference of the σ^+ and σ^- data with the feature Ξ^- at the X^- energy circled. The circled feature is shown in more detail in (**B**), as indicated by the large arrow. (**B**) Single spin KR (Ξ^-) at various bias voltages. The blue triangle indicates the energy of the X^- PL line. Fits to the data are shown in red. (**C**) Illustration of three relevant optical transitions. Solid circles represent electrons, and open circles represent holes. (**D**) The agreement between the X^- PL energy and the Ξ^- energy. The biexciton PL energy is also shown for comparison.

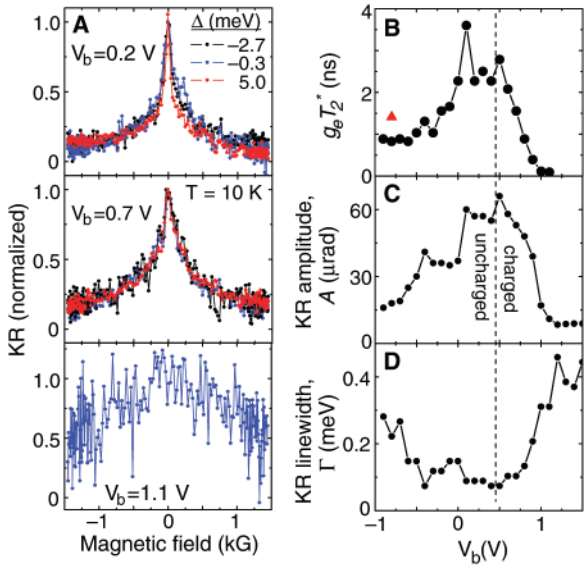

Fig. 4. KR depolarization and analysis. (**A**) KR as a function of transverse magnetic field for various bias voltages. The top two panels show measurements with the probe at various detunings Δ from the X^- energy. (**B**) $g_eT_2^*$ determined from the KR half-width. The red triangle indicates the value obtained from the Hanle measurement. (**C** and **D**) The amplitude and width of the KR Ξ^- feature as a function of applied bias.

serve to pump spin-up electrons. At high bias in the charged regime (V_b = 0.9 V), the PL polarization is due to the hole spin, obscuring any information about the electron spin polarization. To address this issue, we require a more direct probe of the spin polarization.

To probe spins in the dot through KR, we focused a second, linearly polarized, cw Ti-sapphire laser onto the sample, spatially overlapping the pump laser (*17*). The data in the top panel of Fig. 3A show the KR signal as a function of probe energy for σ^+ and σ^- pump helicity. Here, the applied bias is V_b = 0.2 V and the QD is in the uncharged regime. The PL at this bias is also shown, with the X^- and X^0 energies indicated by the dotted lines. These energies coincide spectrally with two sharp features observed in the KR data, which we will refer to as Ξ^- and Ξ^0, respectively. In the bottom two panels of Fig. 3A, the sum and difference of the σ^+ and σ^- data are shown. The feature Ξ^0 at the X^0 energy clearly does not depend on the sign of the injected spin and is similar to features seen in single-dot absorption measurements (*30*). We attribute this peak to polarization-dependent absorption in the QD. We focus here on the (σ^+–σ^-) data, which represent KR due to the optically oriented spin polarization. The feature Ξ^- at the X^- energy only appears in the difference data, indicating that it is due to the injected spin polarization, shown in Fig. 3B at four different bias voltages. For all voltages, the Ξ^- feature is centered at the X^- transition energy, indicated by the blue triangles. We can fit these data to Eq. 1 including only a single transition in the sum, on top of a broad background (red lines, Fig. 3B). From the free parameters in these fits, we determine the transition energy E_0, amplitude A (defined as half the difference of the local maximum and minimum near E_0), and width Γ of the Ξ^- KR feature.

Figure 3D shows E_0 compared to the energy of the X^- PL line as a function of the applied bias. The two energies agree well and show the same quantum-confined Stark shift. Only at the highest bias, where substantial broadening sets in, do we observe a small anti-Stokes shift between E_0 and the X^- PL energy. This effect may be caused by interactions with electrons in the QW. For a single electron spin in the QD ground state, the lowest-energy optical transition contributing in Eq. 1 is the X^- transition (Fig. 3C). Thus, the Ξ^- KR feature is due to the measurement of a single electron spin in the QD. We have repeated this measurement on another QD and observed the same Ξ^- feature, also at the X^- PL energy. The large, broad KR background is likely due to transitions involving excited electron and hole states, which are typically a few milli–electron volts above the lowest transition (*23*).

If present, a KR feature due to the X^0 spin should appear centered at the XX transition energy. The signal-to-noise ratio in our measurement is not high enough to conclusively identify such a feature. Despite the large amplitude of the X^0 PL compared to the X^- PL in the uncharged bias regime (~10:1), the short radiative lifetime of the X^0 state results in a low steady-state X^0 population and therefore in a low KR signal.

By applying a transverse magnetic field B, we can monitor the depolarization of the single electron spin through the KR signal. In contrast to the Hanle measurements described above, the KR probes the spin in the QD directly and nondestructively, as opposed to being inferred from the spin-dependent formation of the X^-. The KR as a function of B is shown for three different bias voltages (Fig. 4A). At V_b = 0.2 V, in the uncharged regime, a narrow peak is observed with a $B_{1/2}$ = 52 G, which is consistent with the X^- Hanle width measured in this regime. At V_b = 0.7 V, where the dot has charged but the PL remains negatively polarized, we measure a somewhat wider KR depolarization curve, with $B_{1/2}$ = 150 G. When the QW is charged further, the spin lifetime decreases as shown at V_b = 1.1 V, with $B_{1/2}$ = 1.4 kG. Assuming an effective electron g factor of 0.2 (*2*), these half-widths correspond to transverse spin lifetimes of 11, 3.3, and 0.8 ns, respectively.

The electron spin depolarization curves measured at probe energies detuned from the X^- transition by an energy Δ are shown in the top two panels of Fig. 4A for Δ = –0.3 meV (at the maximum of the Ξ^- feature), Δ = –2.7 meV (in the low-energy tail), and Δ = +5.0 meV (on the broad, high-energy feature). The curves have been normalized by their peak values, which vary with probe energy, but show identical lineshapes for a given bias. This suggests that, in this entire range of detuning, the KR of the same spin-polarized electron state in the QD is being probed.

Figure 4B shows $g_eT_2^* = \hbar/B_{1/2}\mu_B$ as a function of the applied bias, measured at a probe energy E = 1.6288 eV, near the X^- transition. The dashed line indicates the onset of QD charging. The spin lifetime is largest in the uncharged regime. Here, $g_eT_2^* \sim 3$ ns is consistent with previous measurements (*2*) in which the spin dephasing is attributed to the random, fluctuating hyperfine field (*31*, *32*). As the dot and well are charged, the electron spin lifetime decreases dramatically. This result can be caused by the increasingly rapid capture of a second electron in the dot, which forms a spin-zero singlet state. Also, as discussed below, spin flips with electrons in the QW are likely to be a relevant mechanism in this regime.

The amplitude of the Ξ^- KR signal is shown as a function of V_b (Fig. 4C). A decreases in the charged regime, reflecting the lower spin lifetime. We have argued above that spin-up electrons are pumped into the QD in the uncharged regime. Therefore, the constant sign of the KR over the entire range of bias indicates spin-up polarization in the charged regime as well. Contrary to this observed polarization, the positively polarized X^- PL leaves a spin-down electron in the QD. However, this electron interacts with the bath of electrons in the QW, which is, on average, optically oriented in the spin-up direction. The predominant spin in the QW may be transferred to the electron in the dot via a higher-order tunneling process (*33*). The finite spin-up polarization measured up to a large bias suggests that these electron-electron spin flips dominate over the X^--mediated spin pumping in the charged regime.

As the bias increases above V_b = 0.5 V, the width of the Ξ^- KR feature, Γ, grows by a factor of six, as shown in Fig. 4D. A similar increase in linewidth is seen in the X^- PL in the charged regime. This provides further evidence for an increased coupling of the QD to other electronic states as the charging increases.

By probing a single electron in a QD through KR nonresonantly, we demonstrate a direct measurement of the electron spin with minimal perturbation to the system. As a first application, this method reveals information about spin dynamics in single QDs and constitutes a pathway toward quantum nondemolition measurements and optically mediated entanglement of single spins in the solid state. This scheme may also prove useful for nondestructive measurements in a variety of solid-state qubits, such as electrically gated (*7*) or chemically synthesized (*20*) QDs.

References and Notes

1. D. D. Awschalom, D. Loss, N. Samarth, Eds., *Semiconductor Spintronics and Quantum Computation* (Springer, Berlin, 2002).
2. A. S. Bracker *et al.*, *Phys. Rev. Lett.* **94**, 047402 (2005).
3. A. Ebbens *et al.*, *Phys. Rev. B* **72**, 073307 (2005).
4. T. H. Stievater *et al.*, *Appl. Phys. Lett.* **81**, 4251 (2002).
5. X. Li, Y. Wu, D. G. Steel, D. Gammon, L. J. Sham, *Phys. Rev. B* **70**, 195330 (2004).
6. A. Högele *et al.*, *Appl. Phys. Lett.* **86**, 221905 (2005).
7. J. M. Elzerman *et al.*, *Nature* **430**, 431 (2004).
8. J. M. Geremia, J. K. Stockton, H. Mabuchi, *Science* **304**, 270 (2004).
9. A. Kuzmich, L. Mandel, N. P. Bigelow, *Phys. Rev. Lett.* **85**, 1594 (2000).
10. F. Meier, D. D. Awschalom, *Phys. Rev. B* **70**, 205329 (2004).
11. B. Julsgaard, A. Kozhekin, E. S. Polzik, *Nature* **413**, 400 (2001).
12. M. N. Leuenberger, M. E. Flatté, D. D. Awschalom, *Phys. Rev. Lett.* **94**, 107401 (2005).
13. M. N. Leuenberger, *Phys. Rev. B* **73**, 075312 (2006).
14. D. V. Kupriyanov, I. M. Sokolov, *Quantum Opt.* **4**, 55 (1992).
15. F. Meier, D. D. Awschalom, *Phys. Rev. B* **71**, 205315 (2005).
16. J. R. Guest *et al.*, *Phys. Rev. B* **65**, 241310(R) (2002).
17. Materials and methods are available as supporting material on *Science* Online.
18. M. Sugita, S. Machida, Y. Yamamoto, preprint available at http://arXiv.org/abs/quant-ph/0301064.
19. G. Salis, M. Moser, *Phys. Rev. B* **72**, 115325 (2005).
20. Y. Q. Li *et al.*, *Appl. Phys. Lett.* **88**, 193126 (2006).
21. R. J. Warburton *et al.*, *Nature* **405**, 926 (2000).
22. A. S. Bracker *et al.*, *Phys. Rev. B* **72**, 035332 (2005).
23. D. Gammon, E. S. Snow, B. V. Shanabrook, D. S. Katzer, D. Park, *Science* **273**, 87 (1996).
24. F. Meier, B. Zakharchenya, Eds., *Optical Orientation: Modern Problems in Condensed Matter Sciences* (North Holland, Amsterdam, 1984).
25. R. I. Dzhioev *et al.*, *Phys. Solid State* **40**, 1587 (1998).
26. S. Cortez *et al.*, *Phys. Rev. Lett.* **89**, 207401 (2002).
27. J. G. Tischler, A. S. Bracker, D. Gammon, D. Park, *Phys. Rev. B* **66**, 081310(R) (2002).
28. Y. El Khalifi, B. Gil, H. Mathieu, T. Fukunaga, H. Nakashima, *Phys. Rev. B* **39**, 13533 (1989).

29. R. I. Dzhioev *et al.*, *Phys. Rev. B* **66**, 153409 (2002).
30. A. Zrenner *et al.*, *Phys. Rev. Lett.* **72**, 3382 (1994).
31. A. V. Khaetskii, D. Loss, L. Glazman, *Phys. Rev. Lett.* **88**, 186802 (2002).
32. I. A. Merkulov, Al. L. Efros, M. Rosen, *Phys. Rev. B* **65**, 205309 (2002).
33. J. Lehmann, D. Loss, *Phys. Rev. B* **73**, 045328 (2006).
34. We thank Y. K. Kato for useful advice and discussions and acknowledge support from NSF and the Air Force Office of Scientific Research.

Supporting Online Material
www.sciencemag.org/cgi/content/full/1133862/DC1
Materials and Methods
References

14 August 2006; accepted 1 November 2006
Published online 9 November 2006;
10.1126/science.1133862
Include this information when citing this paper.